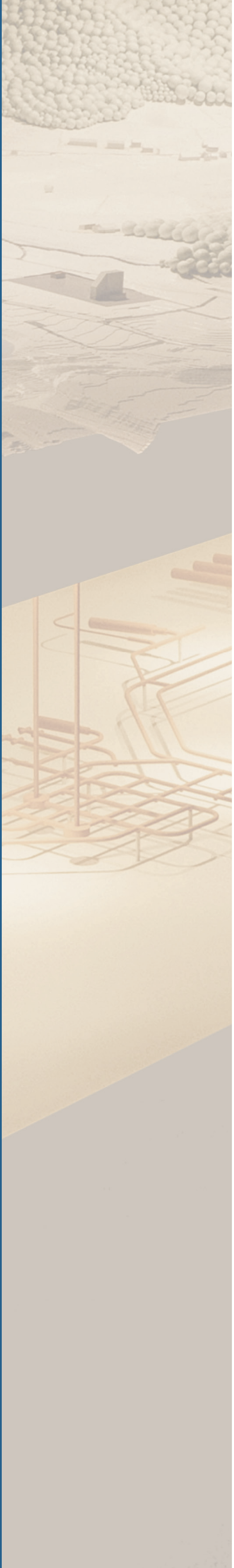

TECHNICAL REPORT 23-10

In-situ Experiments on Bentonite Long-term Stability and Radionuclide Mobility at the Bentonite–Crystalline Interface at Grimsel Test Site

January 2025

Nagra | National Cooperative for the Disposal of Radioactive Waste
Hardstrasse 73 | 5430 Wettingen | Switzerland
T. +41 56 437 11 11 | info@nagra.ch | nagra.ch

nagra.

TECHNICAL REPORT 23-10

In-situ Experiments on Bentonite Long-term Stability and Radionuclide Mobility at the Bentonite–Crystalline Interface at Grimsel Test Site

January 2025

T. Schäfer[1], J. Pingel[1], T. Frank[2] , U. Noseck[2],
H. Seher[2], H. Geckeis[3], Y. Kouhail[3], F. Quinto[3] &
R. Schneeberger[4]

[1] Friedrich-Schiller-Universität Jena, Institute of Geosciences (IGW), Applied Geology

[2] Gesellschaft für Anlagen- und Reaktorsicherheit

[3] Karlsruher Institut für Technologie

[3] Nagra

Nagra | National Cooperative for the
Disposal of Radioactive Waste
Hardstrasse 73 | 5430 Wettingen | Switzerland
T. +41 56 437 11 11 | info@nagra.ch | nagra.ch

ISSN 1015-2636

Table of Contents

List of Tables

List of Figures

List of Acronyms

AFM	Atomic force microscopy
AGA	Amino-G
AMS	Accelerator mass spectrometry
AUC	Analytical ultracentrifugation
BPWO	Bentonite porewater oxidisation
BPWR	Bentonite porewater reduction
CCC	Critical coagulation concentration
C_{cr}	Concentration of radionuclides sorbed on mobile colloids
CEC	Cation exchange capacity
CFM	Colloid Formation and Migration project
C_{fr}	Concentration of radionuclides in the fracture
C_{pr}	Concentration of radionuclides in the rock matrix pores
DDL	Diffusive double layer
DLS	Dynamic light scattering
DOC	Dissolved organic carbon
EC	Electrical conductivity
EDX	Energy-dispersive X-ray
F_{Col}	Immobile colloids sorbed on the fracture wall
FOV	Field of view
FTLA	Finite track length algorithm
GGW	Grimsel groundwater
GRS	Gesellschaft für Anlagen- und Reaktorsicherheit
GTS	Grimsel Test Site
i-BET	In-Rock Bentonite Erosion Test
JGP	JAEA (Japan Atomic Energy Agency) Grouting Project
KIT	Karlsruhe Institute for Technology
KIT-INE	Institute for Nuclear Waste Disposal of the KIT
LCT	Long-Term Cement Studies
LIT	Long-Term In-Situ Test
M_{Col}	Mobile colloids inside the fracture
MW	Mixed water

NTA	Nanoparticle tracking analysis
S_{cr}	Concentration of radionuclides sorbed on immobile colloids
SEM	Scanning electron microscopy
S_{fr}	Concentration of radionuclides sorbed on the fracture surface
SiC	Silicon carbide
S_{pr}	Concentration of radionuclides on pore walls of the rock matrix
URL	Underground research laboratory
vdW	van der Waals (attraction forces)
XRD	X-ray powder diffraction

1 Introduction

1.1 Background

Generating energy through nuclear fission leads to the production of radioactive waste, which can contain uranium, plutonium, so-called "minor actinides" such as neptunium, americium and curium as well as fission and activation products. In particular, the safe disposal of high-level radioactive waste requires its isolation from the biosphere for several hundred thousand years. In line with German safety requirements for the disposal of heat-generating radioactive waste, a site-specific safety case covering an assessment period of one million years must be prepared to demonstrate the safety of the repository concept (EndlSiUntV). In connection with this, one important issue is radionuclide behaviour (the retardation, mobilisation, and potential release and transport of radionuclides) within the disposal zone of the deep geological repository. the primary aim of radioactive waste disposal is to immobilise and contain long-lived radionuclides over a geological timescale in the repository. The internationally agreed concept is to dispose of high-level radioactive waste in deep geological repositories using a multi-barrier system that fulfils different safety functions (Alonso et al. 2005, Yoshida et al. 2005, OECD-NEA 2013)

In the ongoing site selection process, different repository concepts in different host rock formations (rock salt, clay rock and crystalline rock) are currently being comparatively evaluated in Germany. One important part of the evaluation is the application of preliminary safety assessments for each site and the consideration of scenarios that can lead to the release of radionuclides. Repository concepts in crystalline rock, such as the KBS-3 concept in Sweden and Finland, which foresees using a disposal canister with very low corrosion rates in combination with a bentonite buffer as (geo)engineered barriers (SKB 2011), are widely applied.

One relevant scenario, which includes a possible breach of the disposal canister and ensuing radionuclide release, is the intrusion of low-mineralised glacial/meteoric waters into the disposal zone, which can cause erosion of the bentonite barrier (Liu & Neretnieks 2006). Aspects of such a scenario are addressed in the Colloid Formation and Migration (CFM) project, which is performed within the framework of an international consortium at the Grimsel Test Site (GTS), the underground research laboratory (URL) operated by Nagra, the National Cooperative for the Disposal of Radioactive Waste, in the Swiss Alps. The CFM project deals with the relevant processes of bentonite erosion and radionuclide migration in the near field of the geological and engineered barrier system of a deep geological repository constructed in crystalline rock. The focus is on clay-colloid-release mechanisms and the facilitated radionuclide transport investigated in the form of laboratory and in-situ experiments as well as within the context of model developments and applications. This programme is the only combined experimental and modelling research project worldwide performed under in-situ conditions over longer time scales in a URL within an international consortium (https://www.grimsel.com/gts-projects/). The CFM project is supported by German ministries (BMWi/BMUV) within the KOLLORADO-e^3 [1] project, and partners from the Friedrich-Schiller University Jena, the company Gesellschaft für Anlagen- und Reaktorsicherheit (GRS) GmbH, and the Institute for Nuclear Waste Disposal of the Karlsruhe Institute for Technology (KIT-INE) are involved. The outcome of previous studies within the CFM project has been reported (e.g. in Noseck & Schäfer 2020; Huber et al. 2014 and 2016). The present report describes the results of the KOLLORADO-e^3 project.

---

[1] In-situ Experimente zur Bentonit Langzeit-Stabilität und der Radionuklidmobilität an der Grenzfläche Bentonit – Kristallin (FKZ: 02 E 11759A-C).

1.2 Colloid Formation and Migration (CFM) Experiment

To assess the impact of bentonite colloids on the long-term, post-closure safety of a repository in crystalline host rock, a series of field experiments have been carried out in Nagra's underground research laboratory (Grimsel Test Site, GTS) within the framework of the Colloid Formation and Migration project (CFM, Schlickenrieder et al. 2017). CFM is an international project currently joined by BGE (Germany), BMUV (Germany), KAERI (Republic of South Korea), Nagra (Switzerland), NUMO (Japan) and NWS (United Kingdom). Numerous organisations support the CFM project.

CFM further pursues previous GTS colloid studies such as the Grimsel Colloid Exercise (Degueldre et al. 1990) or the Colloid and Radionuclide Retardation Experiment (CRR, Möri 2004). CFM started in 2004 with a first phase dedicated to studying the in-situ boundary conditions, predictive modelling and supporting laboratory programmes in the controlled Area with a focus on the so-called Migration Shear zone (Möri & Blechschmidt 2006). CFM Phase 2 lasted from 2008 to 2013 and was used to enhance the field setup with three new monitoring boreholes and the corresponding instruments in the boreholes and tunnel and to test the robustness of the system while characterising the flow domain. To this end, multiple tracer tests were carried out. Phase 3 started in January 2014 and lasted until 2018. The Long-term In-situ Test (LIT) was initiated in May 2014 with the emplacement of a compacted bentonite ring source containing radionuclide tracers in a central borehole. LIT was overcored in 2019 after an in-situ experiment duration of approximately 4.5 years. CFM Phase 4 was started in 2019 with the implementation of the i-BET (in-situ Bentonite Erosion Test) consisting of roughly 50 kg of Na-dominated bentonite emplaced in a highly fractured and water -conducting interval. Since then, i-BET has been continuously monitored. As i-BET is implemented outside the radioprotection-controlled area, experiments within the CFM project are performed in two distinct areas of the GTS.

1.3 Aims and starting point of the current KOLLORADO-e^3 project

The KOLLORADO-e^3 research programme is based on the outcome of the preceding KOLLORADO-e^2 project. The overall objective of both projects is to shed light on the multitude of different interaction forms and paths between radionuclides, colloids and the rock matrix. The following topics are of Special interest: (i) the erosion behaviour of compacted bentonite in fractured rock, (ii) obtaining a better understanding of the speciation of homologues and radionuclides under the field conditions at the GTS, (iii) the consequences of kinetically controlled adsorption and desorption processes, (iv) the effect of fracture heterogeneity on bentonite erosion and (v) the effect of fracture heterogeneity on flow and non-reactive tracer transport. Aside from the experiments performed in the laboratory as well as under in-situ conditions at the GTS and the application of sensitive analytical techniques, various modelling and simulation approaches were used:

- Benchmark calculations with thermodynamic speciation models and the respective databases;
- Macroscopic 1d/2d models using simplified geometry implementing sorption/desorption kinetics of colloids/radionuclides;
- extension of an available 2d model on bentonite erosion to include heterogeneous flow fields based on random aperture distributions; and
- Comsol multiphysics® to simulate flow and transport of non-reactive tracers in single fractures with complex geometry.

For the computer simulations of the radionuclide transport, two transport codes used for performance assessment were applied: (i) the 1D-transport COFRAME (Reiche et al. 2016), which considers colloid-facilitated radionuclide transport in fractured media using a double-porosity approach and (ii) the transport code CLAYPOS, which simulates one-dimensional radionuclide transport in low-permeable media either in cylindrical or in planar geometry (Rübel et al. 2007).

The Long-term In-situ Test (LIT) at the GTS ran from 2014 to 2018. Its objective was to investigate in-situ colloid formation and mobilisation of radionuclides from a radionuclide-labelled bentonite plug (Schlickenrieder et al. 2017). A radionuclide cocktail filled into glass vials was embedded in a bentonite block, which in turn was emplaced inside a packer system in the GTS, where it was brought into contact with a water-bearing fracture. During the KOLLORADO-e^2 project, samples from observation boreholes and a tunnel surface packer (Pinkel) were continuously taken, analysed and evaluated until the experiment was terminated and overcored at the end of 2018. A series of mock-up tests under inert gas conditions (argon atmosphere) performed in the laboratory using a plexiglass setup were performed within KOLLORADO-e^2 in order to study and quantify bentonite erosion processes. Natural Febex bentonite or a mixture of synthetic montmorillonite and Grimsel groundwater (GGW) were used for this type of experiments to keep it close to the expected LIT scenario. Besides investigating bentonite erosion and radionuclide mobilisation, an additional focus lay on a feasibility study aiming to find a suitable way to conserve the LIT sample during overcoring.

Very low erosion rates and no indication of a gravitational erosion were observed in the LIT (Noseck & Schäfer 2020), which contradicts the outcome of experimental work by SKB and POSIVA in the laboratory on artificial plexiglass fracture setups (Alonso et al. 2019) and the results of our own laboratory experiments with a similar horizontal test setup (Rinderknecht 2017). A key task of KOLLORADO-e^3 was the investigation of possible reasons for the discrepancy of results and notably the influence of accessory mineral phases in the bentonite on the erosion behaviour in laboratory experiments.

During the lifetime of LIT, of the radionuclides ^{45}Ca, ^{75}Se, ^{99}Tc, ^{137}Cs, ^{233}U, ^{237}Np, ^{241}Am and ^{242}Pu, only ^{99}Tc was observed at ultra-trace concentration levels in the observation boreholes (Noseck & Schäfer 2020). Radionuclide migration simulations described in the present report focused on investigating the diffusion of the radionuclides contained in the glass vials in the bentonite. In mock-up tests, release curves could be obtained for ^{99}Tc as well as for ^{237}Np and ^{233}U from the bentonite. Respective 1D model calculations for purely diffusive transport, based on the data and model approaches used for Nagra's long-term safety analysis (van Loon 2014), were carried out with the CLAYPOS code (Rübel et al. 2007). Scoping calculations for diffusion profiles of all radionuclides used in the LIT and in the mock-up test were performed. For the trivalent and tetravalent actinides, the model calculations predicted that during the duration of the experiments, transport should only take place over a few mm (Noseck & Schäfer 2020). Steady-state profiles were expected for radionuclides in oxidised form of e.g. ^{99}Tc, ^{237}Np and ^{233}U. The LIT samples could only be delivered to the radioanalytical laboratories relevant for characterisation with a significant delay due to technical problems during over-coring and cutting, as well as due to the Corona pandemic. A comparison with experimental data that were made available recently will be described and discussed in the present report.

Radiotracer migration experiments under in-situ conditions, notably for elements with low solubilities, usually suffer from high dilution due to dispersion, resulting in concentrations that are difficult to analyse using classic instrumental techniques. By developing and applying appropriate methods on the basis of the extremely detection-sensitive accelerator mass spectrometry (AMS) (Quinto et al. 2017, Quinto et al. 2019), radionuclides could also be determined in the ultra-trace range in samples. Transport of bentonite colloids dispersed in GTS groundwater spiked with relevant radionuclides had been investigated in those studies. AMS analysis allowed for the detection of actinides in the long-term tailings of elution curves at very low concentrations. Those data allowed for the determination of consistent reaction rates, which served as the basis for a forecast of colloid transport at repository scale in the Kollorado-e^3 project. In a series of tracer experiments on colloid- facilitated radionuclide transport at the Grimsel Test Site, the clear influence of kinetics on radionuclide sorption and desorption reactions as well as on colloid filtration was determined. Calculations were carried out with the FRAME-COFRAME programme package (Reiche et al. 2014).

Thermodynamic benchmark calculations were performed within KOLLORADO-e^2 in order to better understand the speciation and thus the transport and retardation effects of homologues and radionuclides under the evolving geochemical conditions in the field experiments at the GTS, particularly the LIT (Kunze et al. 2008). Since an earlier benchmark performed in 2000 (Bruno et al. 2000), updates related to radionuclide-speciation calculations, have been reported in the literature. These are mainly related to new thermodynamic data and more detailed knowledge on groundwater and porewater compositions as well as redox conditions for the scenario of interest. In particular, the conditions at the interface between bentonite and crystalline rock have become more important for the current experiments and have been included into the new benchmark. The speciation of the radionuclides, for example their redox state, is of crucial importance for their mobility, solubility and interaction with colloids in systems in the near- and far-fields of a repository constructed in granite rock. To check (i) the influence of the geochemical conditions on the radionuclide speciation and (ii) the applicability of the currently available databases, benchmark speciation calculations for the six radionuclides used in the LIT(^{75}Se(VI), ^{99}Tc(VII), ^{233}U(VI), ^{237}Np(V), ^{241}Am(III), ^{242}Pu(IV) and ^{232}Th(IV)) in bentonite porewater, Grimsel groundwater and mixed water that forms at the bentonite/crystalline rock interface have been performed within the current project. Assuming a reasonably solid phase, the solubility and the most relevant mobile species for each element in five different model waters have been determined. The initial results of two modelling groups have already been published (Montoya et al. 2022). Depending on the radionuclide, pH values, redox conditions, carbonate, silicate, iron and/or calcium concentrations are decisive for their speciation and maximum concentration, which are determined by the solubilities of the corresponding solid phases. In general, the results of both modelling groups show good agreement. Any differences result from the consideration of different species, for example the existence of silicate complexes for trivalent and pentavalent actinides or the consideration of poly-selenides. However, for both systems the data situation is still uncertain. These benchmark calculations showed, among other things, the possible influence of the silicate concentrations measured in the respective water and porewater as well as the uncertainties in the input data on the radionuclide speciation. Differences arose in the calculation of maximum concentrations for radionuclides, which are required for the planning of radionuclide tracer cocktails for in-situ experiments. These differences are mainly caused by different solubility-determining solid phases and their crystallinity, which the respective experts suggested as relevant for their calculations. Results of all six modelling groups are summarised in the present report.

The specific goals of KOLLORADO-e^3 were to develop an improved mechanistic understanding of the integrity of the bentonite barrier and the colloid-mediated radionuclide transport using advanced spectroscopic and microscopic methods.

Key topics included:

- Laboratory and in-situ studies on bentonite erosion with a focus on the role of accessory mineral abundance in the bentonite;
- Post-mortem analysis of samples from the lit and respective mock-up experiments;
- Analysis of fallout-actinides at the gts in order to gain insight into actinide mobility under given environmental conditions.

Experimental studies were complemented by modelling and simulation studies:

- Benchmark exercise related to radionuclide speciation under experimental conditions relevant for CFM studies;
- Modelling radionuclide migration under the conditions of the LIT at the GTS and laboratory mock-up experiments;
- Upscaling of simulations to repository scales (space and time).

2 Laboratory-scale erosion experiments

As a successor project to the colloidal transport for deep geological repositories for high-level waste (HLW) investigated in the KOLLORADO-e² project (Noseck & Schäfer 2020), small-scale artificial fracture erosion experiments were performed using two different raw bentonite samples (MX-80, GMZ) as well as separate, Na-homo-ionised pure montmorillonite samples (Na-mnt). To this end, the Na-mnt samples were artificially enriched with different amounts and types of accessory minerals (quartz, bassanite, anhydrite) to study their influence on the swelling and erosion behaviour of the material. By means of time-resolved monitoring of the erosion behaviour under laboratory conditions, new nanoparticle detection techniques for bentonite erosion quantification and pressure detection in combination with hydro-chemical monitoring were applied. During the experiments, samples were brought into contact with either low-mineralised natural or modified groundwater extracted from the GTS. Eventually, we aimed for a comparison or survey of transferability of the laboratory data to the large-scale i-BET[2] (In-situ Bentonite Erosion Test) project in the final analysis. The i-BET experiment is part of the CFM project and started at the end of 2018/ beginning of 2019 in order to study bentonite erosion under the URL conditions at the GTS. The i-BET experiment uses a larger cylindrical bentonite source (compacted MX-80 bentonite) with a diameter of 220 mm and a length of 1.15 m (Lanyon et al. 2018).

2.1 Materials and methods

2.1.1 Sample materials

While natural bentonites consist of a large amount of swellable 2:1 (T-O-T) smectite, the material also has variable amounts of naturally admixed accessory minerals such as quartz, feldspar, sulphides, calcite, or gypsum. These typically range within the lower tens of weight per cent and, on average, have a much larger grain-size distribution than the clay particles. While accessory minerals can form porous beds with larger pores through which smaller smectite particles could migrate (Moreno et al. 2011), they also have a much smaller or no surplus charge and can thus influence the swelling behaviour and other properties of the bentonite.

2.1.1.1 Bara-Kade bentonite (MX-80 type)

Bara-Kade® is a Wyoming Na-bentonite trade name commonly referred to as MX-80. Formed by the alteration of rhyolitic tephra and deposited in the Mowry Sea basin (central North America) during the Cretaceous period (Slaughter & Earley 1965), MX-80 bentonite is a natural product found in Wyoming, parts of Montana, and South Dakota (USA) (Xie et al. 2012). Deposited as layers in marine shales, the material is a blend of mostly sodium-/calcium-dominated smectite (around 70/30 wt.%), quartz and feldspar horizons (Karnland et al. 2006, IAEA 2013), mined and milled to mm-sized grains by the American Colloid Company (Minerals Technologies® – ACC®). natural bentonite contains varying amounts of accessory minerals (around 15 ± 5 wt.%), which mainly consist of smectite (85 ± 5 wt.%) or montmorillonite, respectively (Kiviranta & Kumpulainen 2011, IAEA 2013). While an increasing amount of smectite generally leads to a decreased grain-size distribution, it also affects the amount of exchangeable cations and thus the cation exchange capacity (CEC) of the raw material, similar to natural and reduced-charge montmorillonites (Delavernhe et al. 2015). The swelling pressure thus depends on the packing

---

[2] https://grimsel.com/gts-projects/cfm-section/cfm-ibet-in-rock-bentonite-erosion-test

density of the material and can range from 0.2 MPa for lower bulk densities of 1.5 g/cm^3 up to pressures exceeding 10 MPa at 2.1 g/cm^3 (Karnland 2010, Kiviranta & Kumpulainen 2011, IAEA 2013).

MX-80 bentonite was used in the laboratory-scale erosion experiments and for the compacted bentonite rings implemented within the i-BET packer system. Note that within the scope of laboratory-scale erosion experiments, the natural MX-80 bentonite was sieved to a grain size <200 µm and is henceforth referred to as raw MX-80 bentonite. See Tab. 2-1 and Tab. 2-2 for an overview of the mineralogical composition and major chemical properties of the raw bentonite material from the literature.

2.1.1.2 Gaomiaozi (GMZ) bentonite

Originating from the Inner Mongolia autonomous region of China (Ye et al. 2016), the Gaomiaozi, or short GMZ bentonite has been recognised as potential backfill material in deep geological repository programmes for HLW by the Chinese government due to its favourable physical and mineralogical properties (Liu et al. 2004). Deposited in the late Jurassic, the GMZ bentonite formed from continental volcanic sediments, weathered by interaction with groundwater (Liu & Wen 2003, Ye et al. 2010). Containing three major exchangeable surface cations, the smectites of the GMZ bentonite are charged with approx. 45 ± 13% Na$^+$, 22 ± 8% Ca^{2+}, and 9 ± 3% Mg^{2+} based on meq/100g (Ye et al. 2009, Chen et al. 2015). Studies of the swelling characteristics of the GMZ bentonite at full saturation conditions further showed that the relation between the pore ratio and the swelling pressure of the compacted material is independent of initial conditions such as the dry density or the water content of the bulk material (Sun et al. 2013).

Two types of GMZ bentonite (GMZ-001, GMZ-24-200) were applied for our laboratory-scale experiments. At that, the ELF-China project (Funding number: 02E11850E) supplied the material. See Tab. 2-1 and Tab. 2-2 for an overview of the mineralogical composition and major chemical properties of the raw bentonite material taken from the literature.

Tab. 2-1: Mineralogical composition (wt.%) of MX-80, GMZ-001, and GMZ-24-200 bentonite

	MX-80 [1-8, 11]	**GMZ-001** [9-13, 15]	**GMZ-24-200** [14, 15]
Smectite content, thereof Montmorillonite	84.0 ± 5.0 78.2 ± 3.2	74.7 ± 1.5 70.1 ± 8.2	51.3 ± 5.0 48.0
Quartz	4.6 ± 1.6	11.9 ± 3.5	16.0 ± 1.0
Cristobalite/opal	1.3 ± 0.6	10.3 ± 5.9	8.7 ± 5.0
Feldspars	6.1 ± 2.1	8.2 ± 2.7	15.3 ± 2.3
Mica/illite	1.6 ± 1.3	0.8	3.7 ± 0.6
Soluble sulfates	2.3 ± 1.4	-	-
Carbonates	0.8 ± 0.6	7.3	-
Sulfides	0.9 ± 0.3	-	-
Others	-	-	6.9

[1] Kiviranta & Kumpulainen (2011), [2] Steudel (2009), [3] Steudel & Emmerich (2013), [4] Alonso et al. (2019), [5] Fernández et al. (2017), [6] Fernández et al. (2000), [7] Müller-Vonmoos & Kahr (1983), [8] Karnland (2010), [9] Ye et al. (2013) Ye et al. (2016), [10] Sun et al. (2013), [11] IAEA (2013), [12] Chen et al. (2014), [13], [14], [15] Kaufhold et al. (2023)

Tab. 2-2: Main exchangeable cations (%) and CEC (meq/100g) of the investigated bentonites (MX-80, GMZ-001 and GMZ-24-200)

	MX-80 [1-7]	**GMZ-001** [7-13, 14]	**GMZ-24-200** [13, 14]
Na^+ (%)	69.0 ± 13.0	45.0 ± 13.0	28.95
Ca^{2+} (%)	23.0 ± 13.0	22.0 ± 8.0	20.66
Mg^{2+} (%)	11.0 ± 4.0	9.0 ± 3.0	10.49
K^+ (%)	2.0 ± 1.0	4.5 ± 1.5	0.99
CEC (meq/100 g)	73 to 85	71 to 78	50 to 65

[1] Müller-Vonmoos & Kahr (1983), [2] Kiviranta & Kumpulainen (2011), [3] Alonso et al. (2019), [4] Fernández et al. (2017), [5] Missana et al. (2018), [6] Steudel (2009), [7] IAEA (2013), [8] Sun et al. (2013), [9] Ye et al. (2013) , [10] Ye et al. (2009), [11] Chen et al. (2014), [12] Chen et al. (2015), [13] Zhang (2020), [14] Kaufhold et al. (2023).

2.1.1.3 Grimsel groundwater

Low mineralised glacial meltwater was sampled from the GTS at different extraction points (see Fig. 2-1 and Fig. 3-1); JGP11.001 in the case of the i-BET project; BOUS 85.003 extraction borehole, and the LIT Pinkel surface packer in the case of laboratory-scale erosion experiments. In the latter case, the extracted GGW was used to flush the artificial fracture cells and was thus stored in 50 L steel barrels under argon atmosphere during transport and storage. In some of the laboratory-scale erosion experiments, the Ca concentration of the regular GGW was artificially raised to 2 mmol/L, or around 80 mg/L, respectively. The purpose was to exceed the Ca-CCC (critical coagulation concentration) of the clays, according to Seher et al. (2020), by adding $CaCl_2 \cdot 2H_2O$. Tab. 2-3 summarises the main hydro-chemical and colloid-related properties.

Tab. 2-3: Hydro-chemical and colloidal properties of the Grimsel groundwaters applied (study-related data)

	JGP11.001	**BOUS 85.003**	**LIT Pinkel**
Electrical conductivity (µS/cm)	86.0 ± 4.6	80.4 ± 3.2	112 ± 3
pH*	8.5 ± 0.4	7.59 ± 0.05	7.37 ± 0.09
Al (mg/L)	0.011 ± 0.003	<0.015	0.019 ± 0.001
Ca (mg/L)	7.35 ± 0.29	8.09 ± 0.04	5.86 ± 0.46
K (mg/L)	0.3 ± 0.1	0.201 ± 0.005	0.131 ± 0.003
Mg (mg/L)	0.02 ± 0.01	0.0248 ± 0.0002	0.024 ± 0.018
Na (mg/L)	10.84 ± 0.84	8.4 ± 0.05	18.74 ± 0.93
S (mg/L)	3.01 ± 0.65	2.11 ± 0.03	2.63 ± 0.15
Si (mg/L)	4.92 ± 0.46	4.38 ± 0.03	5.48 ± 0.71
F (mg/L)	4.07 ± 0.47	4.27 ± 0.04	6.52 ± 0.18
Cl (mg/L)	0.39 ± 0.17	0.59 ± 0.01	6.97 ± 0.72
SO_4 (mg/L)	9.41 ± 1.93	6.43 ± 0.05	6.39 ± 0.28
DIC[1] (mg/L)	25.67 ± 4.36	29.3 ± 0.2	22.85 ± 8.65
DOC[2] (mg/L)	-	0.32 ± 0.16	0.29 ± 0.2
Median hydrodynamic particle diameter (nm)	134.4 ± 17.9	126.1 ± 34.0	138.3 ± 17.2
Colloid concentration (particles/mL)	2.2 ± 0.6E+07	4.1 ± 1.8E+06	1.6 ± 1.2E+07
Colloid concentration (µg/mL)	0.16 ± 0.04	0.04 ± 0.03	0.12 ± 0.07
Sample batches (n)	5	3	6

* The pH value of low mineralised GGW depends on contact time with atmospheric CO_2. The Natural pH is approx. 8.5 – 9.5 (Schneeberger, Kober et al. 2019). [1]: dissolved inorganic carbon. [2]: dissolved organic carbon

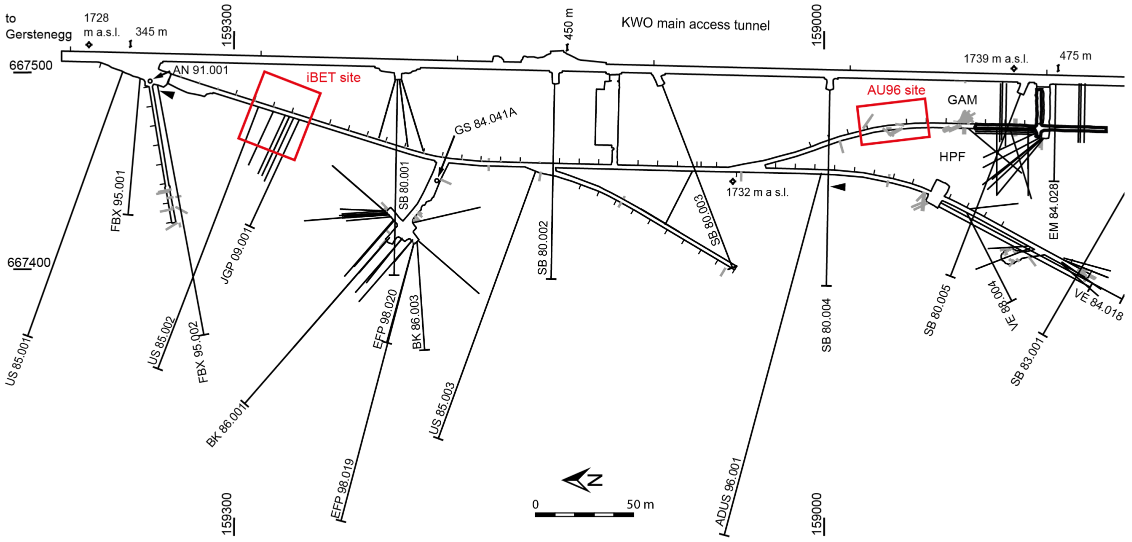

Fig. 2-1: Modified plan of the Grimsel Test Site with relevant areas highlighted in red

Taken from Schneeberger et al. (2019b): A detailed overview of the i-BET borehole layout can be found in Fig. 3-1

2.1.1.4 Purified and sodium homo-ionised montmorillonite

Besides the raw MX-80, GMZ-001, and GMZ-24-200 bentonites, purified and sodium homo-ionised montmorillonites (Na-mnt) were applied as the base material for the artificial erosion experiments. Thereby, a full sodium substitution of the exchangeable cation was performed to provide comparable experimental conditions to previously conducted homo-ionic erosion experiments, e.g. Neretnieks et al. (2009), Kiviranta & Kumpulainen (2011), Steudel & Emmerich (2013), Delavernhe et al. (2015), Eriksson & Schatz (2015), Schatz et al. (2015), Neretnieks et al. (2017), Rinderknecht (2017), Alonso et al. (2018), Alonso et al. (2019). Moreover, Na-mnt shows a different and more pronounced swelling ability compared to, e.g., Na/Ca or purely Ca^{2+}-charged montmorillonites, where this ability is reduced, and the clay tends to flocculate. Enhanced by the large specific surface area of montmorillonite (>500 m²/g) (Müller-Vonmoos & Kahr 1983, Caballero et al. 2005), the Na^{+}-exchanged montmorillonite can be cation-exchanged during the experiments, depending on the mineralogical composition of the samples (e.g. inner change), or the chemical composition of the flushing water (outer change). Containing high amounts of natural montmorillonite, the natural bentonite also contains soluble salts, mainly NaCl and $CaSO_4$, which dissolve upon contact with water (Norrfors et al. 2015). This led to the elimination of contained salts During the homo-ionisation process of the derived clay fraction. X-ray powder diffraction (XRD) and ICP-OES element concentration measurements of the purified and homo-ionised sample material subsequently confirmed a substitution of around 97 ± 2% (see Tab. 2-4). Measurements of the grain-size distribution (Laser granulometry, Fritsch Analysette 22 – NanoTec) were indispensable and performed regularly to guarantee the wanted grain-size distribution of 0.2 to 2 µm (see Fig. 2-2).

Tab. 2-4: Material properties after the purification and homo-ionisation process

	MX-80 (Na-mnt)	**GMZ-001 (Na-mnt)**
Smectite/montmorillonite (%) Thereof Na-mnt (%)	96.9 ± 5.0 98.2 ± 0.2	~100* 97.3 ± 1.7
Others (%)	1.6 ± 0.1 (Al_2O_3) 0.3 ± 0.01 (SiO_2)	-
CEC (meq/100 g)	86.6 ± 0.02	88.5 ± 2.7
D50 grain size dist. (µm)	0.37	0.26
D10 (µm)	0.24	0.14
D90 (µm)	1.0	0.45

* Due to technical issues, a more detailed quantification of the GMZ-001-derived Na-mnt sample was impossible.

In the following, the step-by-step purification and homo-ionisation process is briefly described; further details can be found in Pingel (2025, to be published): (a) Compacted bentonite provided by Posiva is crushed using an agate mortar (Xie et al. 2012) and sieved <200 µm using a nylon sieve, (b) the sieved material is dispersed in deionised water under continuous stirring (approx. 700 rpm) and afterwards the suspension is briefly (15 seconds) sonicated, filtered through a 63-µm nylon mesh and centrifugated for 29 minutes at 2,000 rpm to separate the clay fraction (<2 µm) (Tributh & Lagaly 1986), (c) the supernatant <2 µm is measured by laser granulometry to guarantee the grain-size distribution of 0.2 to 2 µm (see Fig. 2-2), which is a different approach to that of Kiviranta & Kumpulainen (2011), who did the cation exchange on the entire bentonite material. The 0.2-2 µm clay particles containing suspensions were then centrifugated for 20 to 25 minutes at 3,500 rpm to separate the clay material, Na-exchanged with 1 mol NaCl solution (analytical grade) for two hours and settled for 24 hours and centrifugated for 15 minutes at 3,600 rpm. This step was repeated twice to ensure complete Na cation exchange.

According to Karnland (2010), the theoretical structural formula of Na-homo-ionised montmorillonite is: $Na_{0.46}(Al_{3.10}Fe_{0.37}Mg_{0.50})(Si_{7.94}Al_{0.06})O_{20}(OH)_4$.

The Remaining soluble salts were removed by resuspension – centrifugation cycles until the supernatant had an electric conductivity <10 µS/cm. After the final centrifugation step at 3,600 rpm for 1.5 hours, the deposited purified clay materials were collected and freeze-dried.

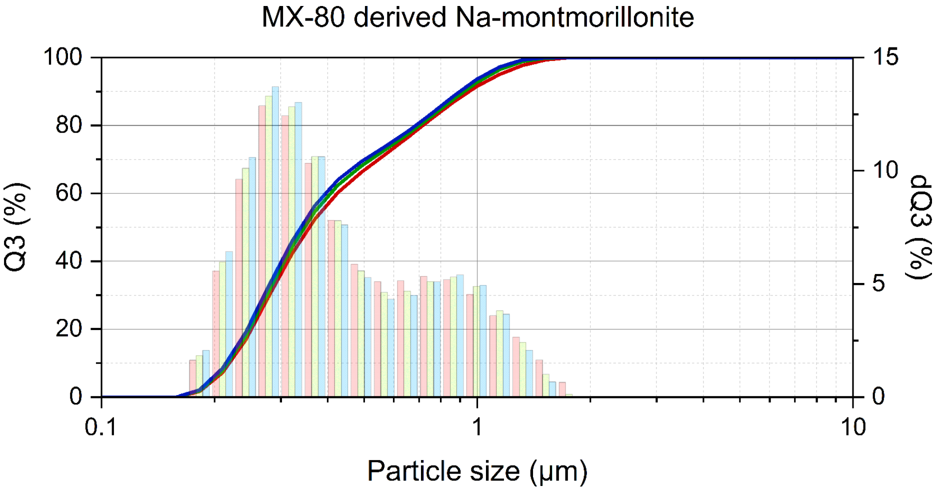

Fig. 2-2: Integral (Q3) and differential (dQ3) grain-size distribution of multiple measurements (single batch) after the purification and homo-ionisation process, exemplarily shown for MX-80-derived Na montmorillonite

2.1.1.5 Sample pellets

To provide a homogeneous distribution of the homo-ionised smectite and the respective accessory material for each pellet, the freeze-dried montmorillonite was crushed into a powder as this was best suited for creating homogeneous pellets.

The sample pellets were manually produced hereafter using a hydraulic KBr-Press (Specac). A target bulk density of 1.8 ± 0.05 g/cm³ was chosen to achieve comparability to previously performed experiments, e.g. Kiviranta & Kumpulainen. The resulting (2011) Svensson et al. (2011), Bouby et al. (2020) pellets had a diameter of 13 mm, a thickness of around 4 mm, and thus a total weight of around 1 g (see Fig. 2-3). Different compositions of raw bentonite (MX-80, GMZ-001, GMZ-24-200) or artificially purified and Na-homo-ionised montmorillonite samples were used to observe the effects of changes on the experimental or sample setup, respectively. Used accessories were thereby selected due to their typical mineralogical occurrence in natural bentonites as well as their chemical composition and similar grain-size distribution to the original and/or purified material:

- Quartz (SF800); Typical and most prominent accessory mineral in natural bentonites with a mean particle-size distribution of 2 µm and a specific surface area of 6.0 m²/g. For a more detailed datasheet, see HPF (2015).
- Bassanite (alpha-AGR40) $CaSO_4 \cdot ½H_2O$, with a mean particle size of 10.8 µm and a specific surface area of 0.8 m²/g; specially created alpha-hemihydrate, based on REA-gypsum (Flue-gas desulphurisation gypsum) and characterised by a high degree of purity (>90%) and cohesiveness (product sheet CASEA GmbH 2013).
- Anhydrite (Micro A - $CaSO_4$), with a mean particle size of around 9.3 µm; Micro A anhydrite is of natural origin (product sheet CASEA GmbH 2018).

While the bulk bentonite has a slightly varying initial water content of 10 to 15 wt.% (see, e.g. IAEA 2013, Sun et al. 2013, Kuusela-Lahtinen et al. 2016), the effective clay density ρ_b can be calculated using the following equation (1), where ρ_d is the dry density of the material (swelling and non-swelling), R_s the fraction of the non-swelling s and, ρ_s: the dry density of the non-swelling mineral:

$$\rho_b = \rho_d \cdot \frac{1-R_s}{(1-(\rho_d \cdot R_s/\rho_s)} \tag{1}$$

2.1.2 Experimental setup

The erosion experiments were conducted using custom-designed, small-scale, dipole flow-through and artificial fracture cells (see Fig. 2-3); additional information can be found in Pingel (2024, to be published). The acrylic glass fracture cells were positioned at a horizontal position (0° angle) for all experiments, with an in- and outflow connection at the top half of the cells. An erosion chamber was milled into the top half of the cell with a diameter of 85 mm and an aperture of 1 mm. Additionally, within the centre of the top tile, a 5-mm-high and 13-mm-wide circular notch was milled out for the sample emplacement. Hence, the free space within the erosion chamber amounts to a total volume of ~5,542 mm^3, excluding the sample space. Placed at the centre of the bottom tile but facing towards the inner side of the erosion chamber, Tekscan pressure sensor foils (Type 5051) with a pressure range of either 1,200, 500, or 150 psi were integrated into the experimental setup. To protect the sensor from the water and prohibit chemical and/or mechanical erosion, a thin polyethylene film (approx.15 μm) was set up between the sensor and the erosion chamber[3]. To provide a continuous water supply for the individual erosion setups, a multi-channel peristaltic pump was used, which was, similarly to Huber et al. (2014), Alonso et al. (2019), set up with a constant flow rate of 50 ± 1 μl/min. Effluents were sampled periodically from the outlet. In contrast, the duration periods of the experiment were chosen based on the individual experimental progression and stopped when no further system changes were observed or expected, respectively.

---

[3] Note that the polyethylene film was tested to have no measurable influence on the sensitivity of the pressure sensors.

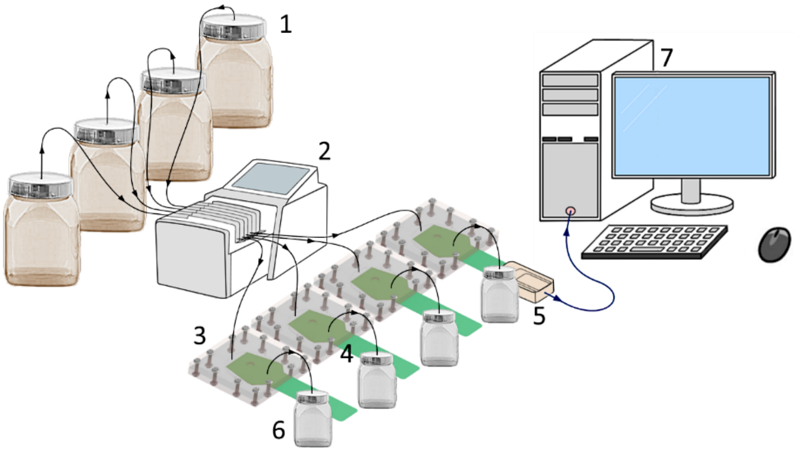

Fig. 2-3: Experimental setup of the laboratory erosion experiments

1) 2,000 mL brown glass PVC container; 2) Watson-Marlow 205S peristaltic pump; 3) artificial fracture cells (see Fig. 2-4 for comparison); 4) TekScan pressure sensor Type 5051; 5) TekScan data reader EH-2; 6) 750 mL PVC container; 7) programme operation and data acquisition computer

2.1.3 Hydro-chemical analysis

To determine the hydro-chemical evolution of the artificial fracture tests and the CFM i-BET setup, chemical analyses were performed on all extracted samples. Samples were stored in a refrigerator until analysis. In preparation for ion-concentration measurements using IC (Integrion-RFIC, ThermoFisher Scientific) and ICP-OES (725ES, Agilent), the liquid samples were pre-filtered by default with 0.45 µm cellulose acetate filters. Acidified samples were additionally retained. However, electrical conductivity, pH, and HCO_3 measurements were performed on unfiltered water samples. HCO_3 was determined by acidimetric titration (Titrino 716 DMS), with the pH value being determined in the process. To verify the plausibility and quality of the measured ionconcentrations, charge-balance calculations were performed. Note that due to the application of different batches of natural or modified Grimsel groundwater (see Tab. 2-3 for comparison) for the artificial erosion experiments, the data of ion analyses are always displayed and referred to as $C-C_0$, where C is the measured concentration of an individual sample and C_0 is the background concentration of the applied GGW. In contrast, hydro-chemical data of the i-BET project are displayed as regular concentration plots due to the single system setup and flow of natural Grimsel groundwater.

2.1.4 Particle characterisation

There is a variety of techniques that can be applied to analyse the size distribution or concentration of nanoparticles in suspensions or solutions; common ones including, e.g. Dynamic Light Scattering (DLS), Scanning Electron Microscopy (SEM), Atomic Force Microscopy (AFM), or the Analytical Ultracentrifugation (AUC). However, as, e.g. Filipe et al. (2010)Hole et al. (2013) or Carr & Wright (2013) point out, each unique technique comes with its individual advantages and disadvantages regarding potentially damaging sample preparations or measurement procedures (e.g. DLS, SEM, AAS) or the necessity of base knowledge of the composition of the sample (e.g. AUC) (Mächtle 2007, Syvitski 2007).

2.1.4.1 Nanoparticle tracking analysis (NTA)

The Nanoparticle Tracking Analysis (NTA) provides some significant advantages over already established analysis techniques such as the DLS (Filipe et al. 2010, Carr & Wright 2013, Carr & Wright 2014). The NTA method captures artificially emitted light scattered from individual particles undergoing Brownian motion. It combines laser-light scattering microscopy with visualisation and recording of nanoparticles in solutions by means of a high-sensitivity sCMOS camera.

In principle, a laser beam with a predefined wavelength (405 – 635 nm) passes through a prism glass pane with an angle of incidence and refractive index so that the laser beam refracts when it reaches the interface between the glass and the liquid sample; see Carr & Wright (2013), Hole et al. 2013. Thus, the nanoparticles in the path and suspension scatter the emitted light, which can be visualised with a microscope using a high sensitivity CCD or sCMOS camera with a frame rate of approximately 30 fps (Hole et al. 2013). This method is briefly presented here.

The particle size range that can be detected using NTA is limited by the refractive index difference between the particles and the solvent in which the material is suspended. The size range for highly refractive index particles (e.g. engineered colloidal Au & Ag) can thus be narrowed down to around 10 – 15 nm, while for lower refractive materials (e.g. clay, silicate, or bio-colloids), the range is approximately 25 – 35 nm, or even 40 nm for weakly scattering material (e.g. polymers) (Carr & Wright 2014, Mehrabi et al. 2017). On the other hand, the upper level for size limits is reached when the Brownian motion of large particles (1 – 2 µm) becomes so slow that it approaches the centering errors of the software, resulting in determination inaccuracies (Carr & Wright 2014). As the method is based on the size analysis of individual particles, enough particles must be analysed to provide a statistically viable dataset. The optimum detection range proclaimed by the manufacturer (Malvern Panalytical 2017) lies between approx. 10^6 and 10^9 particles per mL. As there is a high degree of freedom with regard to customising the settings, comparability and any errors resulting from the individual judgement of the operator have to be taken into account (Filipe et al. 2010). To provide repeatability and reproducibility of the data obtained in this study, Tab. 2-5 lists all the settings for customising, capturing and analysing the measurements.

Tab. 2-5: System (software, hardware) settings applied for all NTA measurements conducted

Setting		**Value**	**Note / function**
NTA Version		3.4	
Camera Type		sCMOS	
Laser Type		Blue405 nm	Wavelength 405 nm
Viscosity		0.888 – 0.889 cP	Water
Temperature		25.0 °C	Constant measurement temperature
Delay		2 s	Idle period after injection
Capture		5 s, 25 FPS	Video recording, 125 frames
Repetitions		29	Total of 30 measurements
Capture:	Screen Gain	2.0	
	Camera Level	11	
Process:	Screen Gain	10.0	
	Detection Threshold	5	
Advanced:	Min. Track Length	Auto	
	Blur Size	Auto	
	Max. Jump Distance	17.0	
Hardware:	Camera Shutter	1,500	
	Camera Gain	500	
	Histogram	0 – 12,000	

NTA provides data without bias towards larger particle distributions due to its individual particle record. However, as the estimation of the diffusion coefficient relies on the accurate trajectory of the particles' Brownian motion, a sufficient number of tracks are necessary to generate a precise value of the step length, based on which the particle size can be determined (Carr & Wright 2014). Due to a smaller scattering volume, smaller particles in particular can have a limited presence time within the field of view (FOV), causing an artificial broadening of the size distribution, even though the estimated mean size remains accurate (Carr & Wright 2014). However, this reduction in accuracy can be mathematically modelled, e.g. by the finite track length algorithm (FTLA) and compensated Saveyn et al. (2010). Additional merits include the low sample volume of down to 250 µl and the wide temperature control range between 5 °C below and up to 50 °C above the ambient temperature.

For comparability purposes, measured particle concentration and calculated mass concentration data shown in the results are not rectified with regard to the individual background level of the GGW, but are shown as the actually measured or respectively calculated values due to the known concentrations in the GGWs used. However, the approximated colloidal "background" masses of the applied GGWs volume that was run through the individual setups was additionally calculated and presented in addition to the data to avoid miscaptions (see Tab. 2-3 for comparison). Nevertheless, in the attempt to quantify the colloidal masses of the individual samples, and thus also the upscaling approaches, the colloidal masses of the natural GGW background were considered and subtracted.

2.1.4.2 Erosion quantification

The approach published by Mehrabi et al. (2017) was applied to the NTA-based quantification of the eroded bentonite masses. In the above-mentioned study, the linear relation of calculated and measured particle concentrations was investigated and NTA measurements for solutions above 1.0E+08 particles/mL were found to be prone to overestimate particle concentration. Therefore, calibration curves had to be made for each new suspension investigated. Hence, system calibration measurements for the applied materials, namely MX-80, GMZ-001, and FEBEX-derived clay colloids (FEBEX bentonite applied for e.g. CIEMAT studies (Missana et al. 2011)), were conducted and showed a good correlation regarding the calculated or targeted concentration values and those measured (see Fig. 2-4). Furthermore, the investigation revealed that in the case of the colloidal smectite material, the appliance of the NTAsoftware in-built FTLA algorithm (finite track length) further improved the precision of the method, leading to an overall average deviation of approx. ± 10% concerning the target values.

To quantify the eroded mass concentration m_c of a measurement or sample, respectively, the approach after Mehrabi et al. (2017) considers the particle-size distribution histogram, which is created based on the NTA measurements conducted and their respective settings. Created by the NTA standard software (NanoSight v3.4), the experimental summary files show the proportional distribution of the total particle number across the particle-size distribution histogram in a given size range (bins) (Mehrabi et al. 2017). Those bins range from 5 nm for the raw data to 1 nm when applying the FTLA. the average number concentration in each bin was then multiplied by its associated (spherical) particle diameter d_i and from that the respective particle volume $\bar{v}_{c,i}$ was obtained. Considering a typical particle density ρ for montmorillonite of around 2.35 g/cm³ (e.g. Duda et al. 1990), the masses calculated for each bin were summed up:

$$m_c = \rho \sum_{i=1}^{n} (\bar{v}_{c,i} \frac{1}{6} \pi d_i^3) \tag{2}$$

In an approach to quantify the mass erosion within the system, individual sample mass concentrations were further applied to calculate the total mass loss over time. Considering the total or sequential time and the flow rates of the applied experiments, mass balances were calculated for all experiments using a quadrature interpolation of individual experimental sequences.

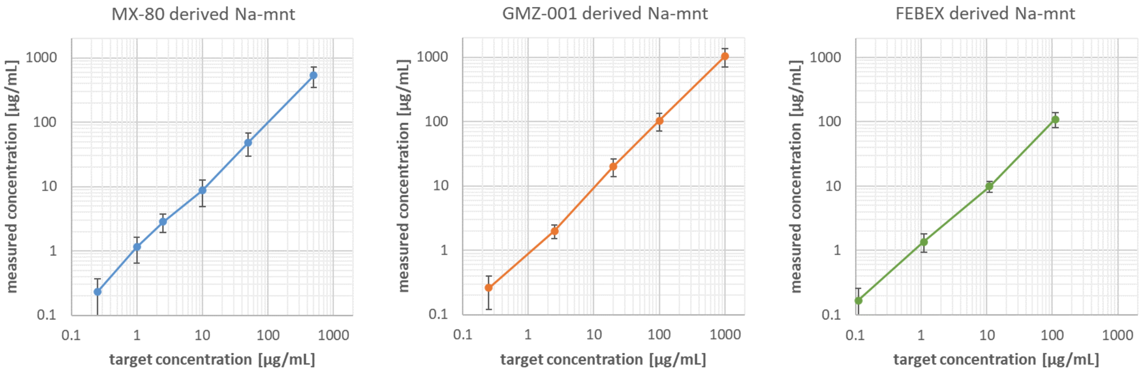

Fig. 2-4: NTA calibration measurements for MX-80, GMZ-001, and FEBEX-derived clay colloids

Median hydrodynamic particle diameters derived for MX-80 are: 130.5 ± 27.9 nm; for GMZ-001: 177.5 ± 9.0 nm; and for FEBEX: 142.7 ± 15.7 nm

2.1.5 Swelling pressure

To measure the temporally resolved pressure evolution within the artificial erosion cells, Tekscan® pressure sensor foils were implemented into the experimental setups. Thereby, pressure foils with different levels of sensitivity (Type 5051; 1,200, 500, and 150 psi) were applied, each chosen for the pressure expected from the samples used. Each pressure sensor was calibrated using lead weights with a progressive (linear) increase of 1 to 35 kg to provide the most accurate pressure measurement possible. Calibration curves showed an estimated error of approx. 5%. The pressure data were read out during the experiments using Tekscans standard I-Scan software. Here, different pressure values were measured in situ, including the contact pressure, which describes the total force relative to the pressure contact area upon the pressure sensor, or the peak pressure values measured at a single sensor. Th software compiled all settings, data, and system adjustments, including the calibration of the sensors and the pressure properties.

2.1.6 Cation exchange capacity

Due to the low amount of extractable sample material after the erosion experiment (<1 g), the Cu(II)-trien-method was applied after and adapted by to even be able to determine the cation exchange capacity (CEC) of a Meier & Kahr (1999), Dohrmann et al. (2012) small clay sample of <100 mg. The CEC measurements for all samples included the cation exchange composition determined through ICP-OES.

2.2 Results – Influence of accessory minerals and water composition on clay erosion

Different material compositions were used to investigate the swelling and erosion behaviour of natural bentonites or purified Na-mnt samples derived therefrom, mixed with accessory minerals of varying quantity. Contact water was either GGW or Ca-enriched GGW.

2.2.1 Case 1: Raw bentonite

For the first case, different raw bentonite samples (MX-80, GMZ-001, and GMZ-24-200) were used as a reference for later experiments on Na-homo-ionised montmorillonite samples. All samples were set up under equal conditions with a pellet density of 1.8 ± 0.05 g/cm³ and were flushed with a constant flow of 50 ± 1 µL/min. See Tab. 2-6 for an overview of all parameters of Case 1:

Tab. 2-6: Overview of essential properties for the erosion experiments conducted for Case 1

Note that the smectite content and accessory minerals match the data in Tab. 2-1.

Applied material	**MX-80**	**MX-80**	**GMZ-001**	**GMZ-24-200**
Grimsel groundwater Applied	BOUS (regular)	BOUS (2 mmol/L Ca)	Pinkel (regular)	Pinkel (regular)
Experimental run time (days)	56	119	77	77
Total pellet weight (g)	1.41	1.40	1.22	1.22
Pellet thickness (mm)	5.73	5.99	4.97	4.99
Pellet volume (mm³)	760.27	794.78	659.13	662.71
Bulk density (g/cm³)	1.85	1.77	1.85	1.84
Smectite content (wt.%)	84 ± 5	84 ± 5	79 ± 8	~55
Smectite content (g)	~1.2	~1.2	~1.0	~0.7
Accessory minerals (wt.%)	16 ± 5	16 ± 5	21 ± 8	~45
Accessory minerals (g)	~0.2	~0.2	~0.2	~0.6
Effective clay density (g/cm³)	1.63	1.57	1.47	1.0

2.2.1.1 Swelling and pressure propagation

MX-80 brought into contact with regular GGW showed the fastest and most pronounced swelling of all raw bentonite samples applied, reaching the borders of the swelling chamber ($r = 36$ mm) within 28 days (see Fig. 2-5). In comparison, the raw MX-80 sample, flushed with the Ca-modified GGW, showed the least pronounced swelling behaviour of the raw bentonites, reaching a maximum swelling radius of approx. 17 mm, presumably due to the cation-exchange-induced lower swelling capability of Ca-exchanged montmorillonites.

With a tear-shaped swelling towards the outlet, the GMZ-001 bentonite showed highly visible erosion streaks emerging from the start of the experiment. However, a fine band of more transparent material was visible at the very edge of the ring. After 56 days, the GMZ-001 bentonite reached a maximum average swelling radius of around 29 ± 4 mm. In comparison, the GMZ-24-200 bentonite reached a maximum average swelling radius of 21 mm after 35 days. Similarly, as observed for the GMZ-001 bentonite, visible erosion streaks towards the outlet could be seen from the start of the expansion but were more pronounced for this experiment.

Exemplified in Fig. 2-5, the image series shows different time steps during the erosion experiments of the raw bentonites. While some air enclosures can be seen within the swollen material for all experiments, likely due to trapped air between the pellet and the notch, similar air enclosures have already been reported by, e.g. Alonso et al. (2019).

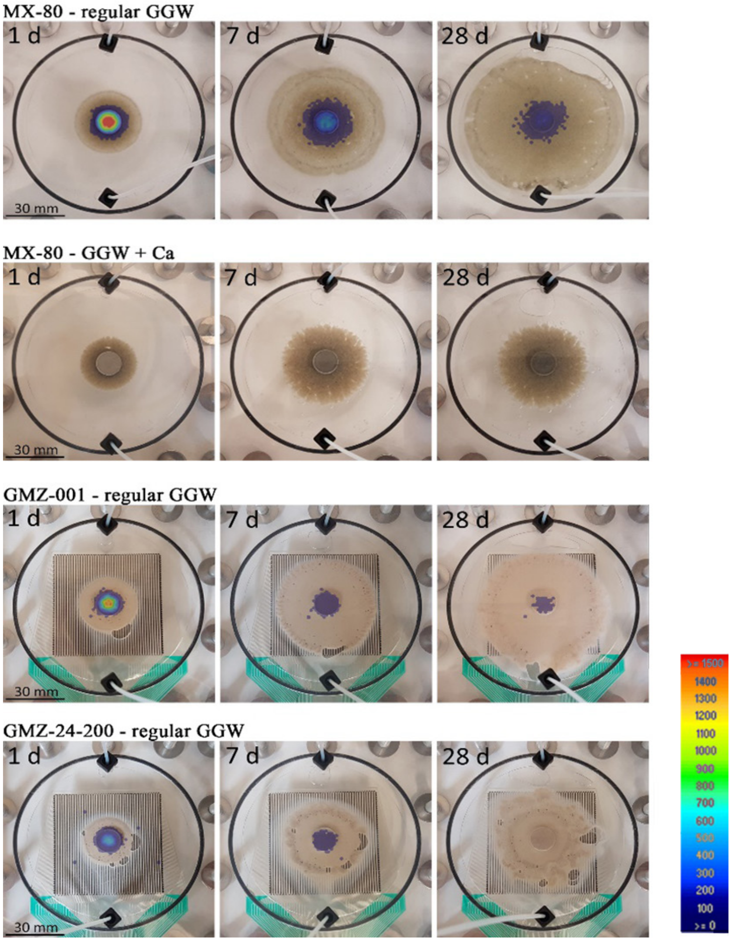

Fig. 2-5: The view from above of different time steps for the applied raw bentonite samples is underlaid with the mapped pressure propagation (kPa). Note that the pressure data plot for raw MX-80 flushed with regular GGW was compiled in a re-run attempt of the same setup

2.2.1.2 Hydro-chemical evolution

During the experiments, no significant changes in electrical conductivity were observed for any of the experiment eluates. Additionally, measured pH for all extracted samples showed stable values of 7.57 ± 0.04 (raw MX-80, GGW), 7.29 ± 0.06 in the case of the Ca-modified GGW setup; 7.15 ± 0.07 in the case of the raw GMZ-001 and 7.2 ± 0.05 in the case of the GMZ-24-200.

Concerning the temporal hydro-chemical evolution, cation and anion concentrations were determined in all eluates. The temporal ion evolution in Fig. 2-6 is presented as C-C_0, where C resembles the measured sample concentration and C_0 is the GGW background concentration.

Linked to the predominant Na/Ca cation exchange process, all setups show an initially raised sodium concentration with values of up to 6.0 ± 0.03 mg/L in the case of raw MX-80 and are flushed with Ca-modified GGW. However, a steady decline can be seen in all setups afterward. While the GMX bentonites and the MX-80 (GGW) setup reached values slightly above their respective Na-GGW background concentration of approx. 1 mg/L after about 40 to 60 days, the Ca-modified MX-80 setup reached a sodium concentration within proximity to the background level after around 120 days. In the case of the raw GMZ-001 bentonite, a concentration peak can be seen around Day 40 of the experiment. This can be due to an increased exchange of surface cations at the time, as it corresponds to a decline in the Ca concentration, respectively. However, based on macroscopic visual inspections, no clear changes for the gel layer could be observed. The occurrence of an interior or structural change on the microscopic level while the experiments are ongoing cannot be ruled out.

In the case of calcium, mainly constant concentrations were measured for the setups flushed with regular GGW (natural GGW background concentration: BOUS approx. 8 mg/L or 0.2 mmol/L, Pinkel approx. 7.4 mg/L or 0.18 mmol/L, see Tab. 2-3). As Ca was stripped from the contact water due to cation exchange, $C\text{-}C_0$ values were slightly decreased (approx. -1 mg/L) and reached background values after approx. 60 days. Due to the artificially increased Ca concentration of the GGW in the second MX-80 bentonite setup, a more pronounced cation exchange of the Ca can be observed to reach a negative $C\text{-}C_0$ peak of -8.2 ± 0.3 mg/L after 49 days. For Mg and K (data not shown), initial concentration values were slightly above the GGW background level and reached near-background values over the course of the experiments.

Concerning chloride or fluoride anions, no significant changes were observed in sample eluates flushed with regular GGW. However, a distinct peak was measured for the raw MX-80 sample flushed with the Ca-modified GGW ($CaCl_2$addition), with a negative $C\text{-}C_0$ concentration of -10.2 ± 0.1 mg/L after 49 days (see Fig. 2-7). Furthermore, a pronounced sulphate release of up to 3.5 ± 0.1 mg/L was observed in the case of the raw MX-80 bentonites but not for the GMZ bentonites, which can likely be attributed to the content of soluble sulphates within the raw MX-80 material (see Tab. 2-1).

The dissolved organic carbon (DOC) content was also measured to investigate its potential influence on erosion behaviour as described by, e.g. Geckeis et al. (2004). While generally low (BOUS: 0.32 ± 0.12 mg/L; BOUS + Ca: 1.03 ± 0.04 mg/L; Pinkel: 0.29 ± 0.2 mg/L), DOC concentrations between 0.39 and 1.78 mg/L were measured for a selected number of samples. However, higher concentrations within the sampled water are likely due to the natural origin of the raw bentonites, as clay minerals tend to have some amount of natural organic constituents (approx. 0.4 ± 0.2 wt.%) Geckeis et al. (2004)Kumpulainen & Kiviranta (2011).

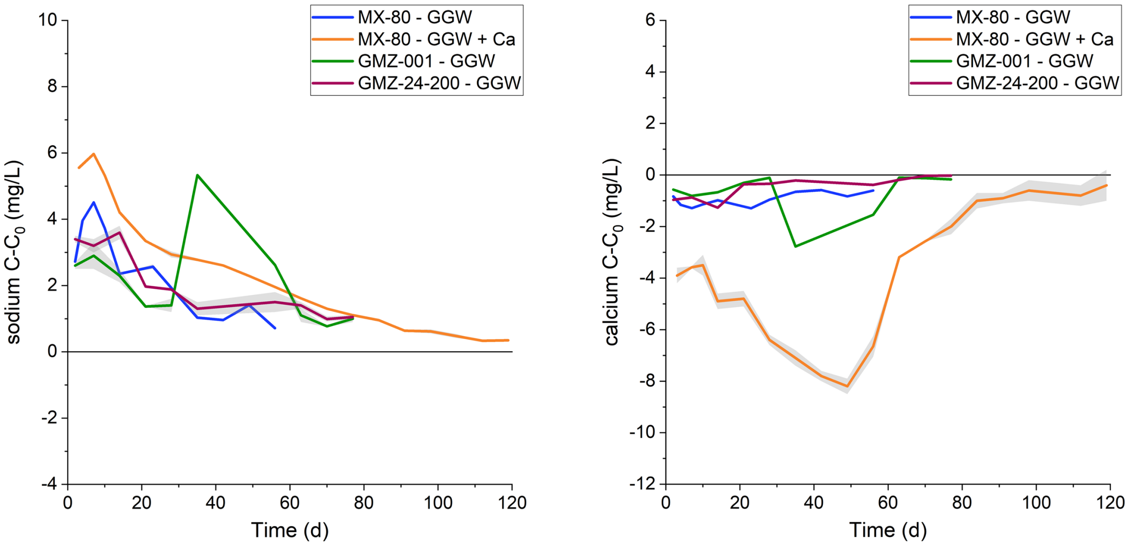

Fig. 2-6: Changes in concentration (mg/L) of major cations (Na, Ca) for the different raw bentonite samples over time, plotted as C-C_0. Grey-shaded areas represent the standard deviation of the measurements. For Mg and K, see Pingel (2025, to be submitted). C_0 values can be found in Appendix A.2

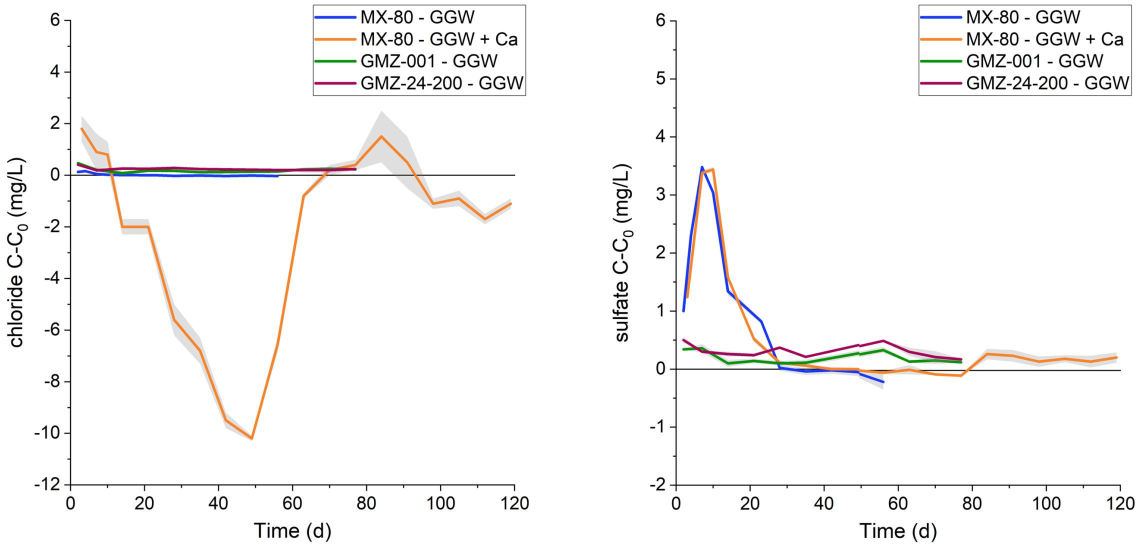

Fig. 2-7: Changes of chloride and sulphate concentration (mg/L) for all setups for Case 1, plotted as C-C_0. C_0 values can be found in Appendix A.2

2.2.1.3 Colloid characterisation and mass erosion

As a crucial parameter for determining the erosion masses, Fig. 2-8 exemplifies the measured hydrodynamic size distributions for two of the MX-80 (GGW) setups with respect to the particle concentration. Average size values were measured to be around 101.4 ± 28.9 nm in the case of MX-80 in GGW, 150.0 ± 33.4 nm in the case MX-80 in Ca-modified GGW, 147.5 ± 31.7 nm in GMZ-001 and 181.4 ± 51.3 in the case of the GMZ-24-200 bentonite, respectively. A tendency towards larger size distributions is observed for all experimental setups over time.

Particle concentration measurements showed values of 5.1 ± 1.6E+08 particles/mL for MX-80 with regular GGW, 7.7 ± 4.2E+06 particles/mL for the Ca-modified GGW, which is within the GGW background concentration (4.1 ± 1.8E+06 particles/mL; BOUS), and slightly higher average particle concentrations of 2.4 ± 1.7E+09 per mL (GMZ-001) and 2.2 ± 1.5E+09 per mL (GMZ-24-200) within the first 60 days of the experiment. Afterwards, a decrease of around one order of magnitude was observed, likely related to an intentional flow-stop of three weeks (days 35 to 56), which gave the GMZgels additional time for cation exchange to stabilise the system. Note that as stated in Section 2.1.4.1, colloidal particle concentrations presented were not rectified concerning the individual background level of the GGWs but are shown as the actually measured values due to the known concentrations in the GGWs used (applies ff.).

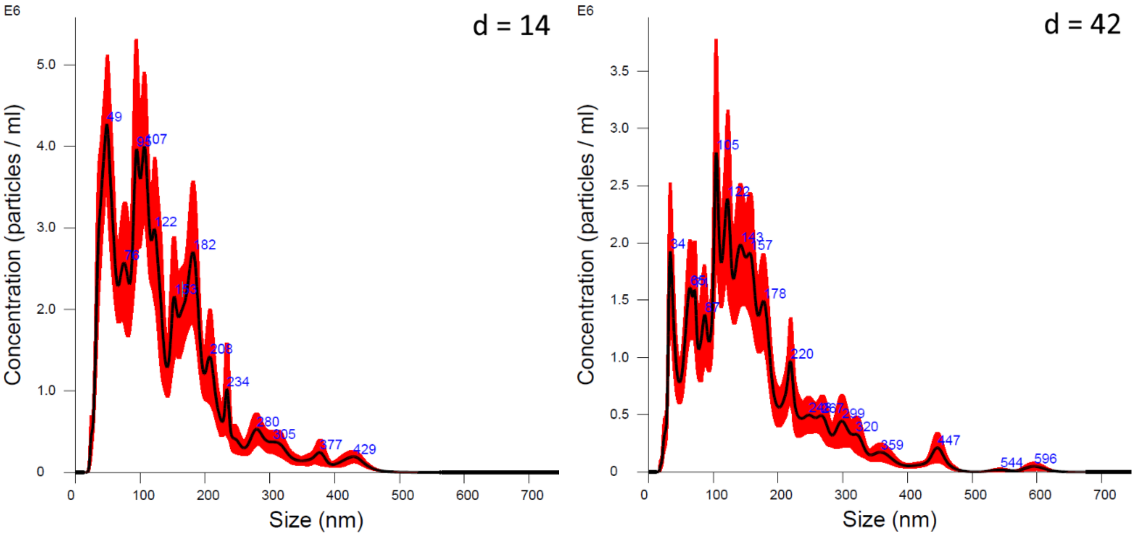

Fig. 2-8: Average FTLA concentration – size plots of the MX-80 (GGW) setup after 14 (left) and 42 days (right)

The eroded clay fraction mass was quantified according to Mehrabi et al. (2017). When taking into account the time and flow rates applied, the total estimated clay erosion was calculated to be 0.8 wt.% in the case of MX-80 brought into contact with regular GGW, of which 0.01 wt.% can be related to the natural GGW background. In the case of the Ca-modified GGW setup, a total mass 0.1 wt.% was calculated, with 0.03 wt.% descending from the applied GGW. While a total colloidal mass of 12.6 wt.% was calculated in the case of the GMZ-001 and 32.6 wt.% in the case of GMZ-24-200 bentonite, the relative GGW background only amounts to approx. 0.001 wt.% each, with respect to the originally emplaced mnt masses of the samples (see Fig. 2-9). To reconcile the erosion rates observed in Case 1, the lateral gel/water contact of the radial swelling extension was used as surface area to determine the surface-area-normalised erosion rates:

- MX-80 – GGW = 0.25 ± 0.11 kg/m²/a
- MX-80 – GGW + Ca = 0.021 ± 0.016 kg/m²/a
- GMZ-001 – GGW = 2.33 ± 1.8 kg/m²/a
- GMZ-24-200 – GGW = 5.9 ± 3.33 kg/m²/a

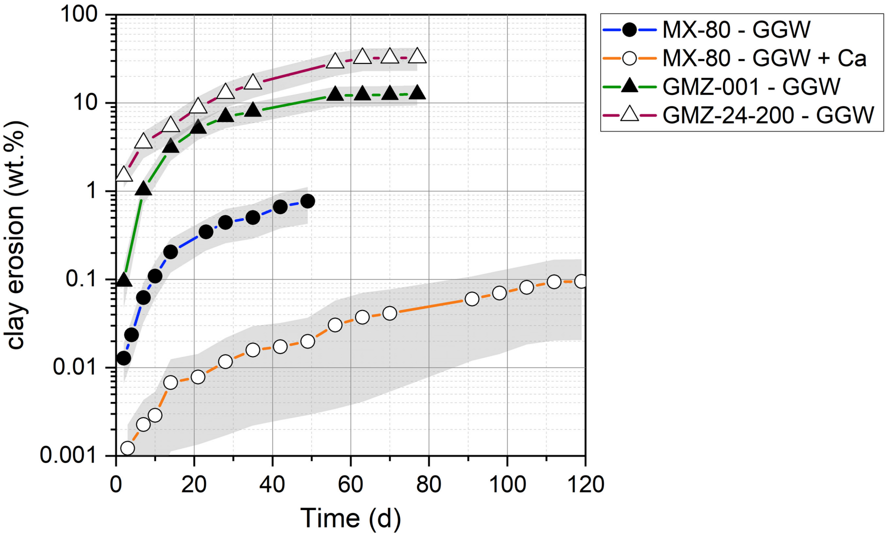

Fig. 2-9: Calculated relative mass loss of clay (wt.%) over time for all setups, including the natural GGW background masses

2.2.1.4 CEC and exchangeable cation composition

Different segments were harvested from the remaining material after each experiment to investigate possible differences in the CEC and exchangeable cation composition between the sample core and the inner and outer parts of the swollen ring (see Fig. 2-13). Thus, a smaller 64 mg and a larger 96 mg comparative sample were investigated from each harvested segment. In this context, the core segment always represented the notch of the emplaced sample (r = 6.5 mm), while the radii of the inner/outer ring boundaries were approx. 25, 10, 18 and 18 mm for the raw MX-80 flushed with regular or Ca-modified GGW and the GMZ-001 or GMZ-24-200 setup, respectively.

Concerning the start of the experiment on the raw material, differences in the CEC values were measured. Due to the higher smectite content of around 80 wt.%, the raw MX-80 and GMZ-001 bentonite were determined to have higher CEC values of 77.8 ± 1.9 and 79.0 ± 0.1 meq/100g, respectively, matching typical values described in the literature (e.g. Kumpulainen & Kiviranta 2011). Due to the lower smectite content of around 55 wt.%, the GMZ-24-200 bentonite showed a lower CEC of 56.9 ± 0.8 meq/100g (see Tab. 2-7).

During or after the experiments, respectively, CEC values partly changed for the materials and segments harvested. While the core segments of the raw MX-80 flushed with regular GGW CEC value rose slightly to 84.0 ± 1.4 meq/100g, no significant changes were observed for the core segments of the raw MX-80 flushed with Ca-modified GGW or the GMZ-001 bentonite. However, in the case of the GMZ-24-200 bentonite, values decreased to 32.0 ± 9.3 meq/100g. Furthermore, both the MX-80 and GMZ-001 setups showed a declining gradient of the CEC from the core towards the outer ring segment, likely linked to a decrease in smectite redistribution during swelling. Daniels et al. (2021) saw a redistribution of smectite via quantitative XRD analysis and interpreted the observations to result from the migration of nanoparticulate smectite through a more silica-rich matrix of the bentonite substrate. The data for the rising CEC values in the case of the GMZ-24-200 bentonite towards the outer ring segment specifically indicate the occurrence of this process (see Fig. 2-5).

The exchangeable cations sodium, calcium, potassium, and magnesium of the harvested material were more closely investigated (see Tab. 2-7). In addition, strontium was measured to determine a possible Sr-carbonate dissolution during the experiments. The exchangeable Na content at the start of the experiments showed a significant decrease in all segments flushed with regular GGW after the experiments. Vice versa, the outer ring segments showed a significant surface cation exchange in favour of Ca with up to 78% in the case of MX-80 and GMZ. Likewise, the GMZ-24-200 bentonite setup showed a less pronounced but still measurable exchange of its surface cations in favour of Ca (approx. 25 to 54%), likely due to the lower initial CEC of around 57 meq/100g. Concerning magnesium, slightly increased concentration values were measured for all raw bentonites. However, a slightly higher increase was measured for the core and inner ring segments. Although subordinary, the MX-80 bentonite flushed with regular GGW showed an overall decrease in the K-concentration. GMZ bentonites showed an increase within their core segments but a declining gradient towards their respective outer segments. In the case of the MX-80 sample flushed with Ca-modified GGW, a significant Na/Ca exchange was measured for all segments harvested (up to 86.5 ± 0.2% for the inner ring segment), likely due to the greater availability of calcium, but also the longer experimental run time of this experiment. Conversely, Na, K, and Mg concentrations were measured with significantly reduced values in comparison. However, a slight increase in the Mg-concentration was observed concerning the base level measured. While Sr was measured to have a relatively low abundance in the raw MX-80 (0.2 ± 0.1%) and GMZ-24-200 and GMZ-001 bentonites (0.6 ± 0.1%), slightly increased values were measured for all setups, which were especially pronounced for the outer ring segments of the MX-80 and GMZ-001 bentonites. Reaching values of up to 1.5 ± 0.1%, a marginal Sr-carbonate precipitation was detected.

The results indicate that even under the GGW conditions, the low but present calcium concentration is stripped of the contact solution via cation exchange, although the experimental duration (56 – 77 days) is not sufficient to achieve equal cation composition for all three sample depths (core, inner ring, outer ring). In the case of the experimental duration of the GGW + Ca experiment (119 days), equilibrium cation composition was achieved.

Tab. 2-7: CEC (meq/100g) and element concentrations (%) of the major exchangeable cations for different segments of all applied bentonites in Case 1, flushed with either regular or Ca-modified GGW

	CEC [meq/100 g]	**Na** [%]	**Ca** [%]	**K** [%]	**Mg** [%]
MX-80 (raw)	77.8 ± 1.9	74.3 ± 3.3	20.3 ± 0.01	1.0 ± 0.02	4.1 ± 0.01
GMZ-001 (raw)	75.6 ± 0.6	66.2 ± 2	21.2 ± 0.1	0.6 ± 0.1	11.4 ± 0.1
GMZ-24-200 (raw)	56.9 ± 0.8	67.2 ± 3.4	22.2 ± 0.1	1.0 ± 0.02	9.4 ± 0.3
MX-80 – GGW (core)	84.0 ± 1.4	48.7 ± 3.2	41.7 ± 0.1	1.0 ± 0.02	7.9 ± 0.1
MX-80 – GGW (inner ring)	76.2 ± 0.4	32.8 ± 2.2	57.4 ± 0.2	0.7 ± 0.03	8.2 ± 0.02
MX-80 – GGW (outer ring)	60.0 ± 0.1	14.6 ± 1.9	76.5 ± 0.4	0.6 ± 0.1	7.0 ± 0.1
MX-80 – GGW + Ca (core)	74.9 ± 1.1	5.9 ± 2.2	84.8 ± 0.3	0.7 ± 0.04	8.0 ± 0.04
MX-80 – GGW + Ca (inner ring)	77.1 ± 0.4	6.2 ± 2.1	86.5 ± 0.2	0.6 ± 0.03	7.1 ± 0.02
MX-80 – GGW + Ca (outer ring)	74.6 ± 0.9	7.2 ± 2.1	86.2 ± 0.2	0.6 ± 0.1	5.6 ± 0.02
GMZ-001 (core)	78.9 ± 0.1	58.9 ± 3.8	26.1 ± 0.2	1.1 ± 0.03	13.1 ± 0.1
GMZ-001 (inner ring)	71.0 ± 4.0	25.4 ± 2.4	57.3 ± 0.1	0.7 ± 0.01	15.2 ± 0.1
GMZ-001 (outer ring)	67.0 ± 1.9	14.3 ± 2.1	78.1 ± 0.5	0.7 ± 0.04	5.4 ± 0.03
GMZ-24-200 (core)	32.0 ± 9.3	58.5 ± 8.6	25.3 ± 0.02	2.4 ± 0.3	13.4 ± 0.1
GMZ-24-200 (inner ring)	40.2 ± 2.2	44.0 ± 9.0	40.2 ± 0.2	2.7 ± 0.1	12.5 ± 0.04
GMZ-24-200 (outer ring)	47.7 ± 0.4	33.3 ± 7.7	53.5 ± 0.4	2.3 ± 0.1	10.2 ± 0.03

2.2.2 Case 2: Na montmorillonite

To investigate the swelling and erosion behaviour of Na-mnt (MX-80), samples were pressed to a pellet density of 1.8 ± 0.05 g/cm³ and flushed with a constant flow rate of 50 ± 1 µL/min. In addition to the regular GGW approach, two identical experiments were conducted to investigate the interim cation exchange stages after 7 and 14 days, respectively (see Tab. 2-8).

Tab. 2-8: Overview of major properties for the conducted erosion experiments for Case 2

Applied Material	**100% (MX-80) Na-mnt**	**100% (MX-80) Na-mnt**
Grimsel groundwater Applied	BOUS (regular)	BOUS (2 mmol/L Ca)
Experimental run time (days)	56	119
Total pellet weight (g)	0.99	0.98
Pellet thickness (mm)	4.03	4.06
Pellet volume (mm³)	534.76	539.41
Bulk density (g/cm³)	1.84	1.82
Smectite content (wt.%)	100	100
Smectite content (g)	0.99	0.98
Effective clay density (g/cm³)	1.83	1.81

2.2.2.1 Swelling and pressure propagation

Both setups show a similar fast-swelling extension, reaching an average radial swelling distance of around 23 mm within the first ten days. In contrast, the purified Na-mnt sample flushed with Ca-modified GGW kept swelling afterwards, reaching a mostly constant value of around 26 mm after 35 days, while the pellet flushed with regular GGW showed a significant decrease in its average radial swelling distance between Days 10 and 35, due to a complete washout or erosion of the material, respectively. Concerning their visual appearance, both samples developed a similarly transparent ring, with the inner regions being opaquer than the outer ones. Slightly detectable, fringy edges developed at the gel/water interface of the Ca-modified setup, while the regular GGW setup showed a primarily smooth transition. Furthermore, after around ten days, the regular GGW setup became increasingly transparent due to the visible erosion of the material, the latter leading to a complete disappearance of the sample material after around 35 days. The measured contact pressures showed a similar behaviour within the initial phase of both experiments, both reaching an initial peak of 961 kPa (regular GGW) and 929 kPa (Ca-modified GGW) with a continuous decrease afterwards. Correspondingly, the regular GGW setup reached zero contact pressure after 35 days, whereas the Ca-modified setup showed a pressure plateau between Days 10 and 35 (approx. 130 kPa) and declined to lower pressures afterwards but did not reach zero pressure within the experimental time frame.

2.2.2.2 Hydro-chemical progression

Due to the different Ca concentrations of the applied GGWs, the different high background levels affected the electrical conductivities of both setups for Case 2. While showing initial peak values of up to 244 µS/cm (regular GGW) and 692 µS/cm (Ca-modified GGW), both immediately declined towards their respective GGW background level (regular GGW: 80 ± 1 µS/cm; GGW + Ca: 485 ± 2 µS/cm) within the first ten days. However, both setups showed an ongoing but retarded decline of their respective electrical conductivity between days 10 and 56, reaching a continuously stable system afterwards. Concerning pH, the regular GGW approach showed a slightly higher pH between 7.5 and 7.8, and less pronounced changes with an average pH of 7.3 ± 0.1 in the case of the Ca-modified GGW.

Regarding The GGW background concentration of sodium, the C-C_0 values of both setups showed an initial peak of up to 38 mg/L in the Ca-modified GGW setup and 31 mg/L in the regular GGW setup due to initial cation exchange processes. After ten days, significantly lower Na concentrations were measured for both setups, but these did not reach the respective background level (see Fig. 2-10). Furthermore, in the case of the modified GGW approach, the Na concentration showed a continuous decline over the whole experimental duration but did not reach the background concentration even after 120 days. In contrast, the Na concentrations briefly rose in the case of the Na-mnt sample in regular GGW, coinciding with the visible erosion period observed between days 10 and 35 (see. Fig. 2-10). Hence, a second peak of up to 12.5 ± 0.4 mg/mL was measured. This must be interpreted with the following data on Al and Si.

In contrast to the released sodium, measured Ca concentrations showed significantly decreased values with respect to the applied GGWs, thus indicating a cation-exchange-driven extraction of the Ca concentrations of the GGWs. The regular Ca concentration (initially around. 8 mg/L or 0.2 mmol/L) of GGW (BOUS) was almost wholly stripped, reaching a negative C-C_0 peak of -7.65 ± 0.01 mg/L after 23 days. However, due to the total erosion of the sample, no exchangeable surface cations remained after 35 days; thus, GGW background concentrations were reached afterwards. Showing an even more pronounced extraction of the Ca concentration, a decreased calcium C-C_0 of -9.0 ± 0.2 mg/L was measured for the modified GGW setup after 40 days. However, the exchange process was slower than the regular GGW approach and more extended, likely due to the higher calcium availability in the artificially Ca-modified GGW (approx. 80 mg/L, or 2 mmol/L). In the latter case, the background concentration of the applied GGW was not reached after 120 days, which was comparable to the Na observations and indicated an ongoing cation exchange process.

Concerning Mg and K, no significant changes were observed. Even though the material was purified and Na-homo-ionised, a minor exchange of remaining K and Mg was observed for the regular GGW through slightly increased values during the erosion phase of the setup.

While no Al and Si concentration changes were observed for the artificially Ca-modified GGW approach, distinct peaks for both ions can be seen for the regular GGW approach. As the concentration peaks correlate with the erosion event observed for the setup, it is likely that the increased Al and Si concentrations are due to undissolved clay colloids that were not sufficiently filtered during the sample preparation (<0.45 µm filters, see Section 2.1.3), as both elements are structural components of the eroded montmorillonite. However, with respect to the structural formula of montmorillonite and measured Si/Al ratios of 10:1 or more, the released colloids seem to be non-stoichiometric clay phases or aggregates with additional minerals such as accessory quartz.

In the case of chloride, high initial concentrations were measured, peaking at up to 55.8 ± 0.6 mg/L in the case of the Ca-modified GGW setup, concerning the background concentration of the applied GGWs. A rapid decline of Cl concentrations towards the GGW values was observed in both cases. Furthermore, extraction of the Cl concentration was measured for the Ca-modified GGW setup, reaching a negative C-C_0 peak of -9.1 ± 0.4 mg/L after 49 days. An adjustment within proximity of the applied GGW was reached shortly after (after around 60 days, data not shown). The difference in the observed behaviour was likely due to the different high initial chloride concentrations resulting from the artificially added $CaCl_2$, thus leading to different adjustment phases of the systems.

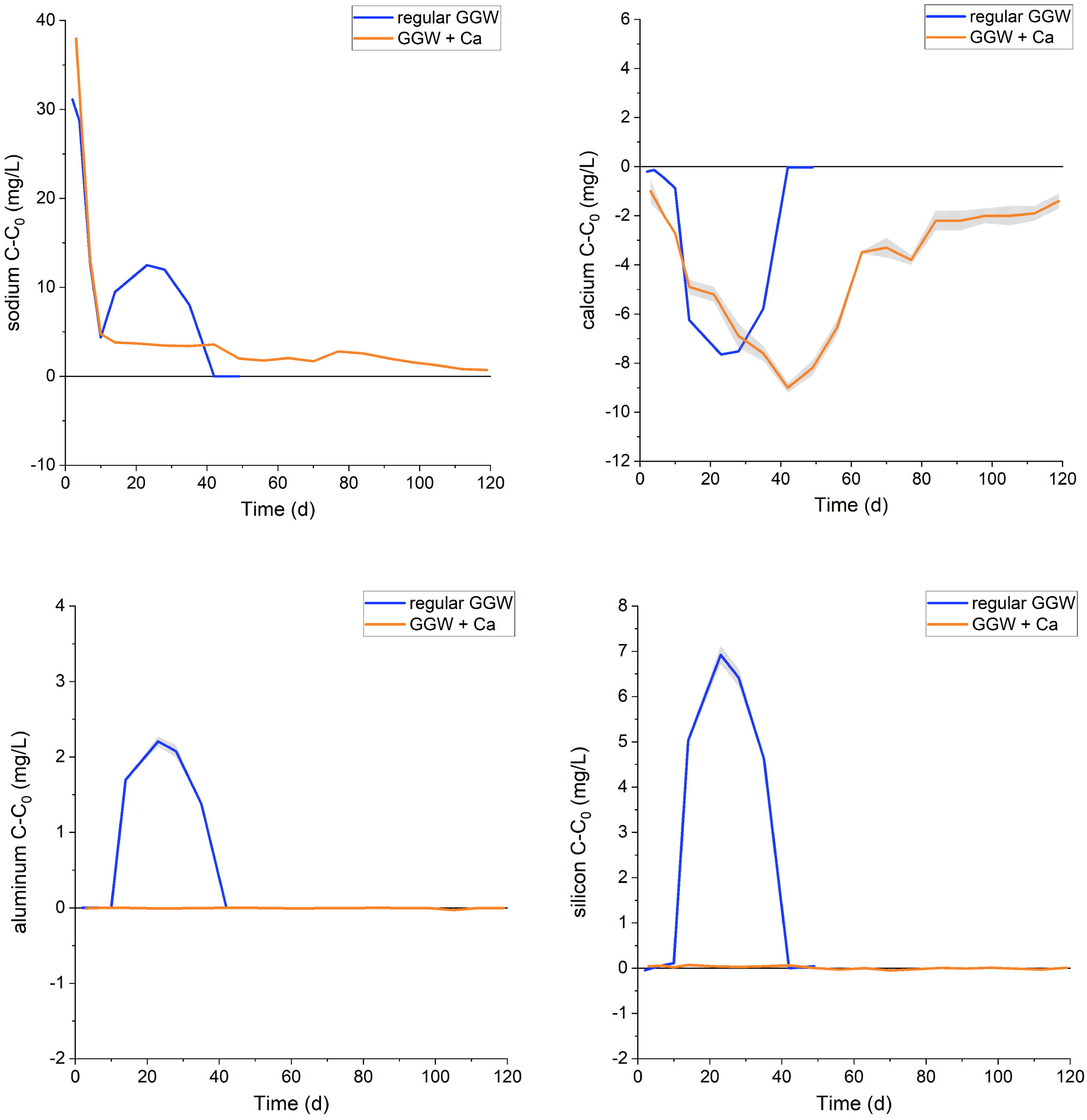

Fig. 2-10: Changes in concentration (mg/L) of major cations (Na, Ca, Al, and Si) for the purified Na-mnt samples in Case 2, flushed with either regular or Ca-modified GGW. C_0 values can be found in Appendix A.2

Due to the purification and Na-homo-ionisation of the sample material, no major SO_4^{2-} changes were observed. However, both setups showed slightly increased concentrations concerning their applied GGWs, having an average $C-C_0$ value of 0.15 ± 0.03 mg/L in the regular and 0.11 ± 0.05 mg/L in the case of the Ca-modified GGW setup. As for sulphate, no significant changes were observed for F^-, with values measured within the proximity of the applied GGWs (4.28 ± 0.19 mg/L).

Background measurements of the applied Namontmorillonites showed a DOC concentration of 0.15 mg/L. Similar to the raw bentonite samples for Case 1, low amounts of DOC were found in the samples for Case 2 during the experiment, ranging between 0.5 and 0.7 mg/L, which is within the range of the measured background concentration of the applied GGWs (0.32 ± 0.12 mg/L, BOUS; 1.03 ± 0.04 mg/L, BOUS + Ca). However, during the visible clay erosion of the regular

GGW setup, higher values of up to 4.37 mg/L were measured, indicating a coherence of the DOC and the integrity of the system. For the data presentation on the time-dependent Cl, SO_4 or F concentration, see Pingel (2025, to be submitted).

2.2.2.3 Colloid characterisation and mass erosion

Median hydrodynamic particle diameters of 134 ± 23 nm (regular GGW) and 150 ± 60 nm (Ca-modified GGW) were measured. These values were larger but still within the proximity of the measured background value of regular GGW with 126 ± 34 nm. Concerning the period of high erosion during the regular GGW setup, measured size distributions were not significantly influenced.

As indicated by the visible erosion, both setups showed significantly different erosion behaviours concerning the released colloid concentrations (see Fig. 2-11). While the artificially Ca-modified GGW showed an overall stable particle erosion of 4.9 ± 2.2E+06 particles/mL, which is only slightly above that of the applied GGW (4.1 ± 1.8E+06 particles/mL), the visible clay erosion of the regular GGW approach was also evident in the measured colloidal concentration of up to 4.2 ± 0.1E+11 particles/mL between days 7 and 35. As the clay sample was eroded, lower concentrations of around 2.0E+7 particles/mL were measured after 42 days.

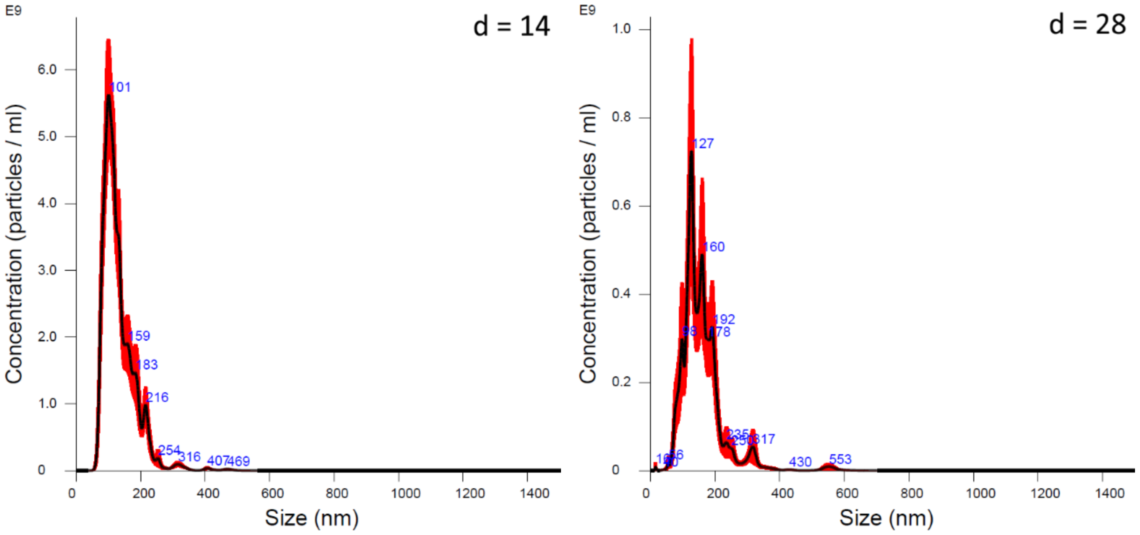

Fig. 2-11: Average FTLA concentration – size plots of the regular GGW setup after 14 (left) and 28 days (right)

Accordingly, different mass concentrations or rates were calculated for both experiments, respectively. In the case of the Ca-modified GGW setup, low erosion rates of 0.09 ± 0.08 µg/mL were calculated, which can be upscaled to approx. 0.012 ± 0.01 kg/m²/a (or 0.011 ± 0.01 kg/m²/a, when considering the GGW-induced colloidal background mass) in accordance with the radial swelling extension and flow rates applied. However, significantly higher mass concentrations were quantified for the regular GGW approach. Coinciding with the particle concentration peak, a mass concentration peak of 1784 ± 524 µg/mL was calculated after 14 days. Considering the applied constant flow rate and duration of the experiment, a total erosion of 97.6 wt.% can be calculated for the regular GGW approach, matching the visible complete erosion of the system.

In contrast, the low erosion rates of the Ca-modified GGW account for a mass loss of around 0.1 wt.% (see Fig. 2-12). The colloidal background masses of the applied GGWs amount to approx. 0.0002 wt.% (regular GGW setup) or 0.005 wt.% (GGW + Ca setup) of the total calculated masses, with respect to the initial mntmasses of the samples.

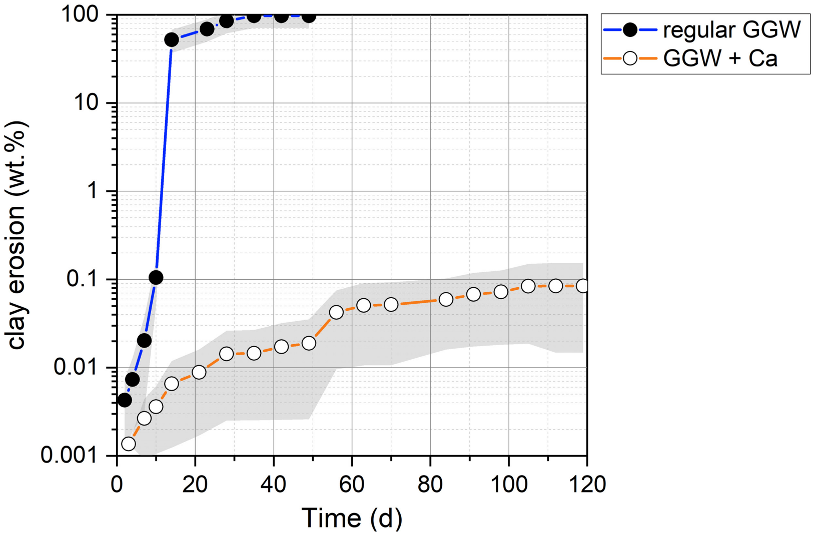

Fig. 2-12: Calculated relative mass loss of clay (wt.%) over time for all setups for Case 2, including the natural GGW background masses

2.2.2.4 Post-mortem analyses

As the background level of Na and Ca was not reached for the Ca-modified GGW setup within the duration period of the experiment (119 days), this indicated an ongoing cation exchange process. In addition, two identical setups were run for seven and fourteen days to observe the time-dependent cation exchange of the Na-mnt material during interim stages of the experiment in the Ca-modified GGW. As for Case 1, different segments of the swollen material were sampled to investigate possible differences in the respective areas (see Fig. 2-13). Thus, a smaller 64 mg and a larger 96 mg sample were investigated from each segment sampled. Note that different segments were selected qualitatively and mainly based on visual differences within the swollen material. In the case of the Na-mnt flushed with Ca-modified GGW, the radii of the inner/outer ring boundaries were approx. 12, 15 and 15 mm after 7, 14 and 119 days, respectively. Due to the pronounced erosion, no further CEC investigation could be made for the regular GGW setup, as no material was left after the experiment.

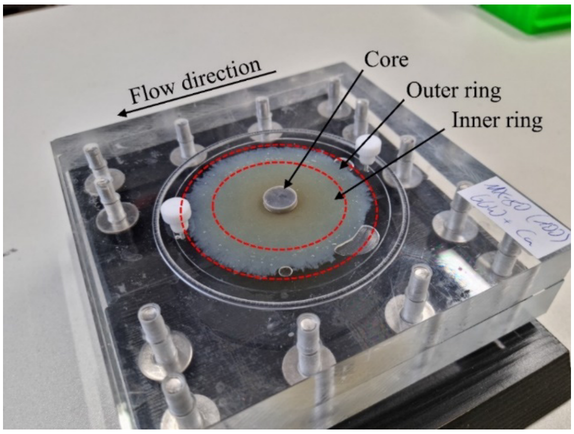

Fig. 2-13: As indicated by the dashed red lines, the image illustrates the different segments sampled for the CEC and exchangeable cation composition after the experiments

2.2.2.5 Scanning electron microscopy (SEM)

Even though the mass quantification in Section 2.2.2.3 shows almost quantitative erosion (97.6 wt.% of the initially implemented clay mass) in accordance with the visible inspection under regular GGW, a Scanning Electron Microscopy (SEM, Zeiss Ultra Plus) was conducted. This investigation method was additionally coupled with Energy-Dispersive X-Ray (EDX, Bruker X-Flash 6/30 SD-detector) analysis to ascertain whether any montmorillonite flakes remained in the harvested samples after the experiments. As a result, clay aggregates were found in the harvested chamber water after the iteration of the regular GGW setup or within the harvested sample material (see Fig. 2-14). As illustrated, the aggregates appeared somewhat bloated, while individual, smaller, and more platelet-shaped montmorillonites were attached to the surfaces of the aggregate.

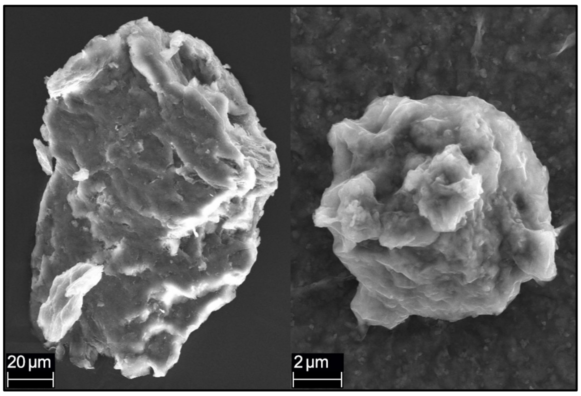

Fig. 2-14: SEM images of montmorillonite aggregates found in the remaining erosion chamber water after the iteration of the regular GGW setup (left) and in the inner ring segment harvested after 14 days (right)

2.2.2.6 CEC and exchangeable surface cations

As the samples were made from purified smectite or montmorillonite, respectively, the initial (unused) material was measured with a higher CEC (86.6 ± 0.1 meq/100g) in comparison to the raw MX-80 bentonite used in Case 1 (see Tab. 2-7 for comparison). Two trends were observed concerning the measured CEC: CEC values for the segments were initially higher after 7 days (core segment up to 94.9 ± 0.6 meq/100g) and 14 days (core segment up to 96.9 ± 0.3 meq/100g). the CEC then decreased with the duration of the experiment, starting at the core segment and progressing towards the outer ring segment (see Tab. 2-9).

While the initial MX-80-derived material has a high grade of Napurification (98.2 ± 0.2%, see Tab. 2-4), the cation exchange proceeded at a different pace, regarding the different segments harvested (see Tab. 2-9). the core segment thus showed a minor exchange of Na after seven days, with still 96.7 ± 0.3%, or 20 mg/g, while in the outer ring segment, close to 1/6 of Na was exchanged to Ca after seven days (82 ± 0.01% or 16 mg/g Na to 16 ± 0.01% or 5.6 mg/g Ca). This trend continued after 14 days, where only around 60% Na-exchangeable cation remained. Meanwhile, the core segment still showed a much higher concentration of sodium (96.2 ± 1.2%, or 19 mg/g), likely due to the slower diffusion process and the high radial swelling distance of the sample. Over time, most surface cations were exchanged for the energetically more favourable Ca, reaching 85 to 90% for all segments after 119 days. The hydro-chemical measurements indicate a still ongoing exchange and adjustment process of the system concerning the Ca-modified GGW (see Section 2.2.2.2), supported by a remaining approx. 7% of sodium after 119 days.

Likely due to the more favourable valence of Mg, slight increases were measured after 7 and 14 days (approx. 1.5 to 5%) with respect to the initial material. With a gradient of higher values towards the core segments, these values increased after 119 days (approx. 3 to 5%). In the case of potassium, no significant changes were observed over time, with overall low values measured for all segments.

The data presented in this section are in line with the selection coefficients for cation exchange and show rather slow kinetics in compacted purified montmorillonite.

Tab. 2-9: CEC (meq/100g) and element concentrations (%) of the major exchangeable cations for different segments of the purified and Na-homo-ionised montmorillonite samples, flushed with Ca-modified GGW

	CEC [meq/100 g]	**Na** [%]	**Ca** [%]	**K** [%]	**Mg** [%]
Initial material	86.6 ± 0.1	98.2 ± 0.2	0.8 ± 0.01	0.1 ± 0.01	0.9 ± 0.03
Core (7 days)	97.2 ± 0.3	96.7 ± 0.3	1.5 ± 0.03	0.2 ± 0.01	1.6 ± 0.03
Inner ring (7 days)	94.9 ± 0.6	94.7 ± 0.5	3.6 ± 0.04	0.2 ± 0.01	1.6 ± 0.1
Outer ring (7 days)	90.7 ± 0.1	82.0 ± 0.01	16.0 ± 0.01	0.2 ± 0.01	1.8 ± 0.01
Core (14 days)	96.9 ± 0.3	96.2 ± 1.2	1.8 ± 0.1	0.2 ± 0.01	1.8 ± 0.1
Inner ring (14 days)	92.1 ± 1.3	92.6 ± 0.4	5.4 ± 0.2	0.2 ± 0.01	1.8 ±0.1
Outer ring (14 days)	91.1 ± 0.1	62.5 ± 0.01	35.3 ± 0.01	0.2 ± 0.01	2.0 ± 0.01
Core (119 days)	83.1 ± 0.7	8.7 ± 0.02	85.5 ± 0.3	0.4 ± 0.03	5.2 ± 0.04
Inner ring (119 days)	80.5 ± 0.4	7.3 ± 0.04	88.1 ± 0.1	0.4 ± 0.01	4.1 ± 0.04
Outer ring (119 days)	79.8 ± 0.3	6.8 ± 0.1	89.9 ± 0.5	0.4 ± 0.01	2.8 ± 0.04

2.2.3 Case 3: Na-mnt with accessory quartz

For Case 3, we investigated the swelling and erosion behaviour of the purified and Na-homo-ionised montmorillonites (MX-80- or GMZ-001-derived) by adding different amounts of quartz powder. This included selecting 10 or 20 wt.% quartz powder to represent typical accessory ranges in natural bentonites (e.g. IAEA 2013). The quartz powder added (type SF800, see Section 2.1.1.5) was chosen due to its similar average grain-size distribution of around 2 µm with respect to the applied clay. As for Cases 1 and 2, samples of equal mineralogical composition were flushed with either regular or Ca-modified GGW (see Tab. 2-3) to investigate possible differences in their swelling and erosion behaviour. In total, five experiments were conducted (see Tab. 2-10).

Tab. 2-10: Overview of major properties for the conducted erosion experiments for Case 3

Applied material	**80/20* Na-mnt (MX-80)**	**90/10 Na-mnt (MX-80)**	**80/20 Na-mnt (MX-80)**	**90/10 Na-mnt (MX-80)**	**90/10 Na-mnt (GMZ-001)**
GGW applied	BOUS (regular)	BOUS (regular)	BOUS (2 mmol/L Ca)	BOUS (2 mmol/L Ca)	Pinkel (regular)
Exp. Run time (days)	56	56	119	119	77
Total pellet weight (g)	1.02	0.96	1.01	1.02	0.75
Pellet thickness (mm)	4.34	4.08	4.32	4.37	3.18
Pellet volume (mm^3)	575.51	541.27	573.39	580.16	422.08
Bulk density (g/cm^3)	1.78	1.77	1.76	1.76	1.78
Smectite content (wt.%)	80	90	80	90	90
Smectite content (g)	0.82	0.86	0.81	0.92	0.68
Accessory quartz (wt.%)	20	10	20	10	10
Accessory quartz (g)	0.20	0.10	0.20	0.10	0.08
Effective clay density (g/cm^3)	1.45	1.60	1.44	1.55	1.61

* 80/20 is equal to a weight mass ratio of 80% Na-mnt and 20% quartz powder.

2.2.3.1 Swelling and pressure propagation

While the samples set up in Case 3 showed a similar initial radial swelling propagation within the first five days, they showed different swelling behaviours for the following individual setups. In the case of the GMZ-001 Na-mnt sample mixed with 10 wt.% quartz powder, the setup reached its maximum radial swelling distance after around 10 days ($r = 16$ mm), which was the smallest radial swelling distance of all samples in Case 3. Comparing this to the MX-80-derived samples mixed with either 10 or 20 wt.% quartz powder, samples with regular GGW showed a slightly higher maximum radial swelling distance after 10 days ($r \approx 24$ mm) in comparison to those flushed with Ca-modified GGW.

However, as observed for the samples flushed with regular GGW in Case 2, a visible erosion event started after around 10 days for all samples flushed with regular GGW in Case 3. Initially identifiable by means of an emerging whitish ring (quartz powder) at the gel/water interface, this state marked the maximum radial swelling distance, with the clay being continuously washed out afterwards. As the area of whitish rings progressively increased towards the respective sample cores, all clay material was washed out over time, leaving only the framework/skeleton of quartz grains behind (see Fig. 2-15, day 28). Note that the visible erosion started after around 10 days in the case of both MX-80-derived samples, with a total wash-out of clay between days 28 and 35. The latter is in line with the observed hydro-chemical and colloidal changes (see Sections 2.2.3.2 and 2.2.3.3) and changes in pressure values. In the case of the GMZ-001-derived sample, the visible erosion started earlier (around day 7), with highly visible erosion streaks emerging, similar to those observed in Case 1. In the case of the MX-80-derived samples flushed with Ca-modified GGW, the radial swelling continued until maximum average radial swelling distances of 25 mm (90/10) and 22 mm (80/20) were reached.

These data clearly show that the addition of accessory minerals (here quartz powder with an average size of 2µm) has no significant effect on the overall erosion mechanism of Na-mnt.

With respect to the measured pressure distribution, the MX-80-derived samples reached an initial contact pressure peak within the first 24 hours. Thereby, as expected, samples with a higher initial smectite content (90 wt.%) also showed higher pressure peaks with 738 (regular GGW) and 592 kPa (GGW + Ca), respectively. In comparison, those with an initially lower Na-mnt composition (80 wt.%) were measured with 525 and 479 kPa, respectively. The pressure continuously decreased over time, reaching zero pressure after 35 days in contact with regular GGW, whereas no zero pressures were reached within the experimental time of 119 days in the case of Ca-modified GGW. In contrast, the 90/10 GMZ-001-derived sample showed a much less pronounced initial contact pressure peak of 289 kPa, followed by a continuous decrease afterwards. Even though the pressure decreased at a comparatively slower pace, zero pressure was reached after 14 days due to the faster clay erosion with respect to the MX-80-derived samples.

The total contact pressure loss is attributed to the quantitative erosion of swelling 2:1 clay minerals in the experiments, leaving the quartz powder skeleton behind.

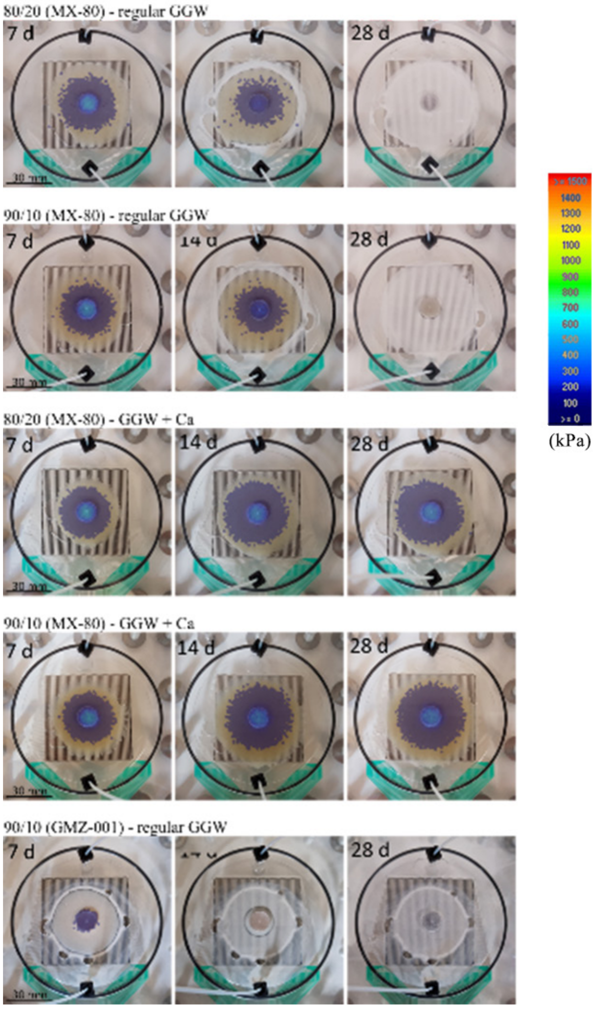

Fig. 2-15: View from above on different time steps for the applied setups for Case 3, underlaid with the mapped pressure propagation (kPa)

2.2.3.2 Hydro-chemical progression

As for Cases 1 and 2, different high electrical conductivities (ECs) were measured for the setups due to the different GGWs (BOUS, BOUS + Ca, Pinkel, see Tab. 2-3 for comparison) applied. While samples flushed with Ca-modified GGW were measured with an initially high but EC of 490 ± 5 µS/cm that stabilised after approx. 10 days, towards the middle and later stages of the experiment, an initially high value of up to around 690 µS/cm was measured for both setups. A slightly decreasing trend could be observed for both setups until approx. day 60, correlating with further hydro-chemical changes observed (see, e.g. Fig. 2-16 or Fig. 2-17). A similarly pronounced initial conductivity peak of 268 µS/cm (90/10) with an exponential decrease to around 88 µS/cm after 10 days was observed for the MX-80 regular GGW setup. A stable EC was reached after around 35 days (79.2 ± 0.1 µS/cm). With a less pronounced but visible initial peak (112 µS/cm), the GMZ-001-derived sample also showed a similar exponential decrease to the background EC values. In this case, continuously stable values were reached after around 28 days, coinciding with the hydro-chemical propagation (see, e.g. Fig. 2-16 or Fig. 2-17) and the visible erosion of the system (see Fig. 2-15).

Similar to the measured EC, variations were observed concerning the pH propagation of the individual setups in Case 3. These variations were mainly observed during the erosion events of setups contacted with regular GGW (days 7 – 35). Note that overall, lower pH values were measured for samples flushed with Ca-modified (pH 7.3) and Pinkel (pH 7.4) GGWs in line with their respective pH values.

Concerning the Na concentration, an initial C-C$_0$ peak was measured for all setups for Case 3. the MX-80-derived samples generally showed a more pronounced peak with concentration values of around 30 to 35 mg/L with respect to the applied GGW (see Fig. 2-16). While this initial peak quickly decreased for all samples within the first 10 to 20 days, samples flushed with regular GGW showed a second peak during their respective erosion events, indicating the release of Na-exchanged clay colloids <450 nm as shown later for e.g. the Al signal.

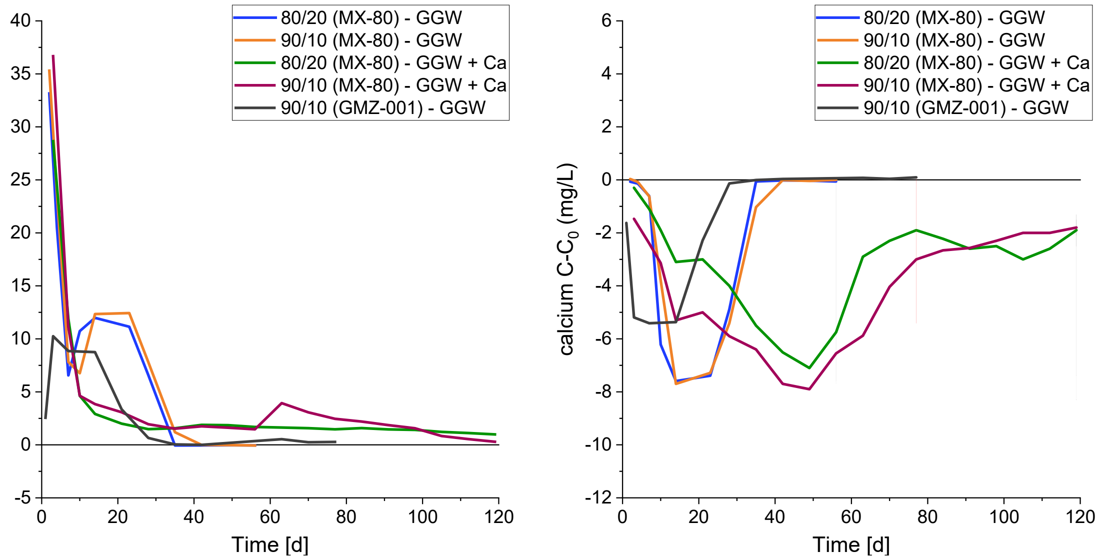

Fig. 2-16: Changes in the Na (left) and Ca concentrations plotted as C-C$_0$ (mg/L) for all samples for Case 3, flushed with either regular or Ca-modified GGW

C$_0$ values can be found in Appendix A.2.

In contrast to sodium, the measured Ca concentration in the contact water was reduced shortly after the beginning of the experiments in all setups. As a result, similarly pronounced C-C_0 values of around -8 mg/L were measured for the MX-80-derived samples (see Fig. 2-16). However, due to erosion and cation exchange processes, maximum extraction was reached for regular GGW samples between 10 and 28 days, (see Fig. 2-18 for comparison). The Ca-modified GGW samples showed a much longer Ca extraction during the experiments, peaking at around 49 days. As indicated by the visible swelling and erosion behaviour, the GMZ-001-derived sample showed an earlier Ca extraction immediately after the beginning of the experiment. While it resembled the rapid progression of the MX-80-derived samples flushed with regular GGW, the Ca extraction was less pronounced with a maximum C-C_0 value of -5.41 ± 0.01 mg/L after 7 days. Due to the total erosion of clay in the regular GGW setups, background Ca concentrations were reached after approx. 30 to 35 days. Prolonged negative C-C_0 values for samples brought into contact with Ca-modified GGW indicate an ongoing cation exchange process even after 119 days.

In the case of potassium, no significant variations were observed for the samples flushed with Ca-modified GGW. However, coinciding with the observed erosion, slightly increased K concentrations were measured for both MX-80-derived samples <0.2 mg/L flushed with regular GGW. Noticeably, the GMZ-001-derived sample showed a much more pronounced initial peak of up to 0.35 ± 0.02 mg/L (day 3), which coincided with the earlier erosion of the setup. As for potassium, measured Mg concentrations did not show significant variations for the setups flushed with Ca-modified GGW. C-C_0 values increased by around 0.4 to 0.5 mg/L during the erosion process as a result of setups flushed with regular GGW.

In the case of Al and Si, significantly increased concentration values were measured during the erosion of the samples flushed with regular GGW. As observed in Case 2, this is likely linked to non-sufficient filtering of the samples (<0.45 µm) due to the high particle concentration of the respective samples (see Fig. 2-17). In contrast, no considerable changes were observed for the Ca-modified GGW systems.

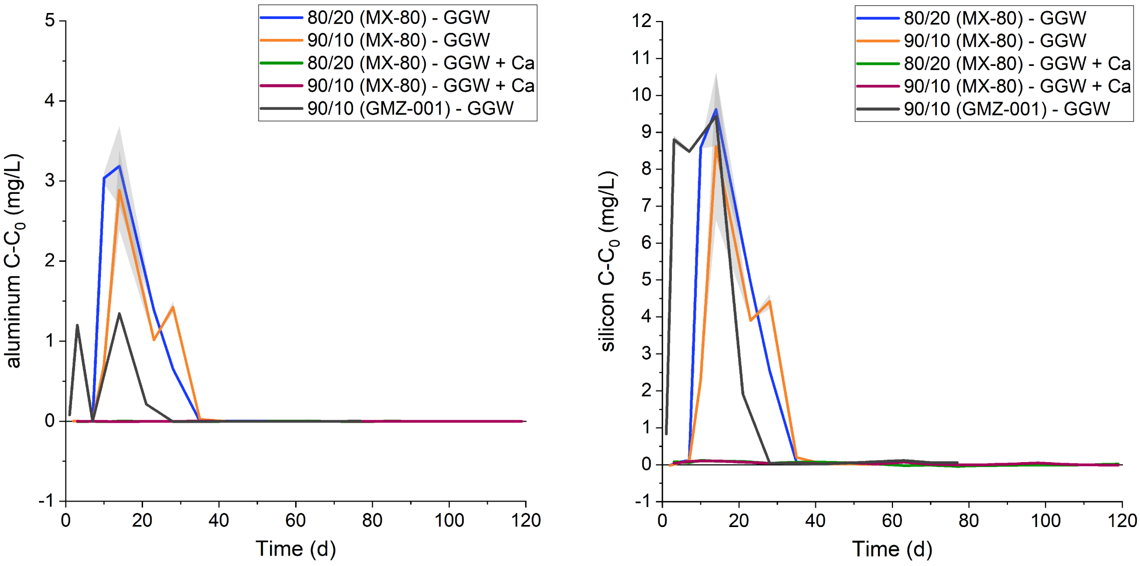

Fig. 2-17: Changes of aluminium and silicon concentration plots as C-C_0 (mg/L) for all samples for Case 3, flushed with either regular or Ca-modified GGW

C_0 values can be found in Appendix A.2.

Similar to the initial peak of Na, an initial high C-C_0 Cl concentration of around 50 mg/L was measured for all MX-80-derived samples, followed by a significant decline toward the GGW background concentration within the first 14 days. However, while the Na-mnt samples flushed with regular GGW remained within proximity of the applied GGW afterwards, samples flushed with Ca-modified GGW were further stripped for their Cl concentration until around 60 days into the experiment, which is comparable to the observations made for the GGW + Ca in Case 2.

In the case of SO_4^{2-}, no significant variances (approx. ± 0.3 mg/L within the applied GGWs) were observed for the MX-80-derived samples. However, in one exception, the GMZ-001-derived sample was measured to have an increased C-C_0 sulphate concentration of up to 2 mg/L during its initial phase or major erosion, respectively (around day 28). For the data presentation on the time-dependent Cl, SO_4 or F concentrations, see Pingel (2024, to be submitted).

2.2.3.3 Colloid characterisation and mass erosion

For the most part, stable average hydrodynamic diameters were measured for the 80/20 (MX-80) samples flushed with either regular (140.7 ± 20.7 nm) or Ca-modified (147.2 ± 45.6 nm) GGW. While a tendency towards larger particle sizes was observed for both cases, this was especially pronounced for the Ca- modified GGW setup. Similar observations were made for the 90/10 (MX-80) samples, where Ca-modified GGW shifted towards larger grain-size diameters with time (regular GGW: 129.1 ± 22.0 nm, GGW + Ca: 159.3 ± 50.2 nm). In contrast, the median hydrodynamic diameter of the 90/10 (GMZ-001) sample showed an initial peak of up to 187.5 ± 5.7 nm (day 3), and median size gradually decreased afterwards.

A pronounced particle release was detected for all regular GGW samples within the first 35 to 42 days (see Fig. 2-18). Thereby, particle concentrations of up to 3.7 ± 0.4E+11 per mL were measured for the 90/10 (MX-80) – GGW sample after 10 days. Matching the visible erosion, the 90/10 (GMZ-001) – GGW sample showed increased particle concentrations from the start, which decreased after around 20 days. In contrast, the measured concentration peaks of the 80/20 and 90/10 (MX-80) – GGW samples were delayed by a few days, in line with the visible erosion. All three setups showed slightly increased concentration values after the major erosion events with respect to their applied GGW (BOUS: 4.1 ± 1.8E+06 and Pinkel: 1.6 ± 1.2E+07 particles/mL), indicating some delayed clay particles release.

In contrast, both MX-80 Ca-modified GGW setups generated a much lower particle emission (on average, 80/20: 5.9 ± 2.9E+06 and 90/10: 6.0 ± 6.3E+06 particles/mL), which lies within proximity of the applied GGW (BOUS + Ca) or even lower in the case of the natural Pinkel GGW. Regarding the particle concentration of the 90/10 (MX-80) sample flushed with Ca-modified GGW, measured low initial concentrations were followed by a steady concentration increase until a peak value of 4.2 ± 0.8E+08 particles/mL was reached after 63 days.

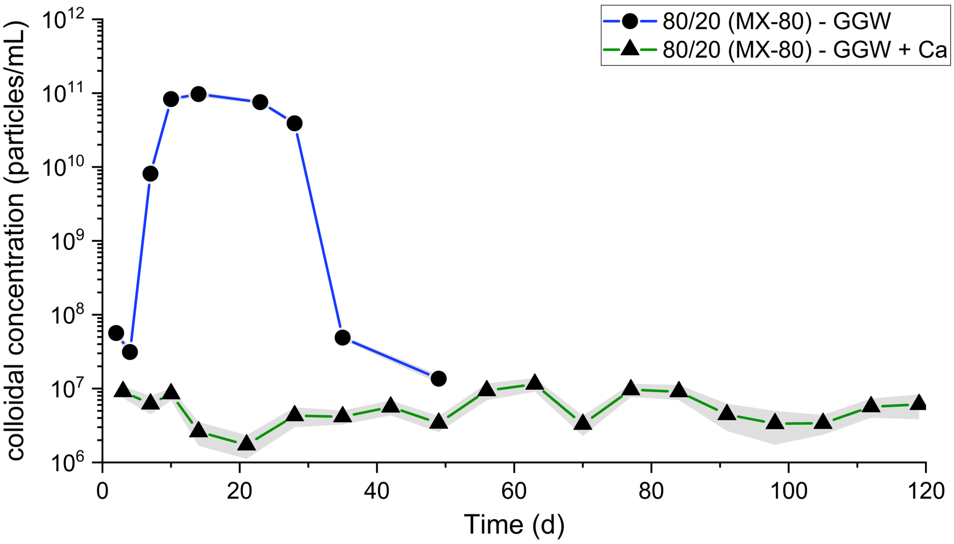

Fig. 2-18: Measured colloidal particle concentration per mL for all setups for Case 3

GGW background: 4.1 ± 1.8E+06 (BOUS) & 1.6 ± 1.2E+07 particles/mL (Pinkel)

Calculations of eroded clay masses for MX-80-derived Na-mnt samples, mixed with either 10 or 20 wt.% quartz, were calculated with peak concentrations of up to 630 µg/mL, resulting in an approximated loss of 98.0 and 98.1 wt.% of their initial smectites. Of these, approx. 0.02 wt.% was associated with the applied GGW background. Likewise, the GMZ-001-derived sample was calculated to lose 94.1 wt.% of its initial clay material (of that, approx. 0.03 wt.% originated from GGW), which also matched the highly visible erosion streaks inside the swelling chamber after the end of the experiments (see Fig. 2-15). In contrast, the setups flushed with Ca-modified GGW were calculated to have a much less pronounced mass erosion with an approximated loss of 0.1 wt.% in the case of the 80/20 (MX-80) and 1.6 wt.% in the case of the 90/10 (MX-80) sample, of which approx. 0.04 wt.% were associated with the applied GGW background masses. With respect to the mostly invariant mass concentrations (see Fig. 2-18), radial swelling extension and flow rates applied, steady erosion rates of 0.019 ± 0.027 kg/m²/a (or 0.013 ± 0.019 kg/m²/a, when considering the GGW background) could be calculated for the 80/20 (MX-80) – GGW + Ca setup. For Further details, see Pingel (2025, to be submitted).

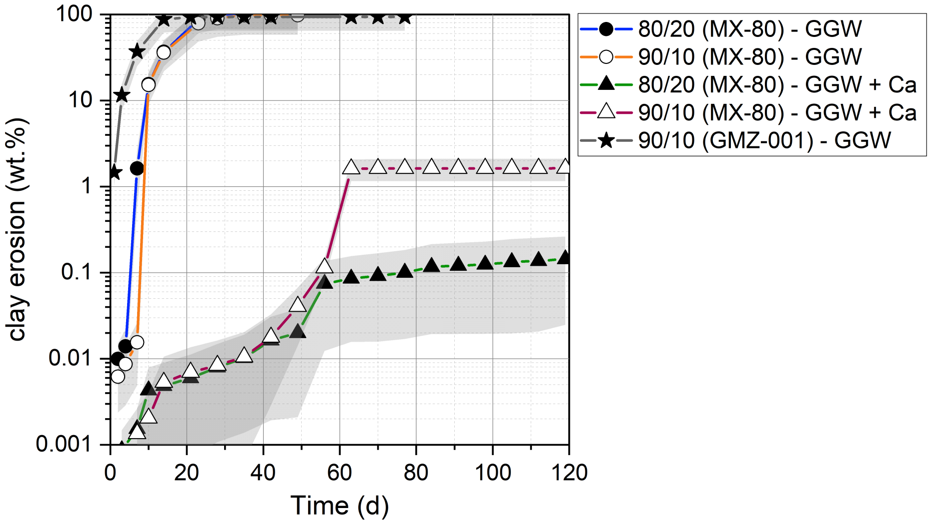

Fig. 2-19: Calculated relative mass loss of clay (wt.%) over time for all setups for Case 3, including the natural GGW background masses

2.2.3.4 Element correlation approach

A correlation approach with respect to the ICP-MS data (Al, Si, and Mg) was conducted as a further data treatment step. In line with the NTA particle measurements, 0.45µm was not sufficient to remove the colloidal fraction before hydro-chemical analysis. Therefore, the data for Case 3 was selected as their Na-mnt pellets were mixed with quartz (see Tab. 2-10), making a potential differentiation of colloidal species more feasible. An increased particle emission correlates with increased Al, Si and Mg concentrations during the pronounced erosion event (around days 7 to 35). Moreover, based on the mol-weight of the elements and the structural formula of montmorillonite (see Section 2.1.1):

$(Na, Ca)_{0.33}(Al, Mg)_2(Si_4O_{10})(OH)_2 \cdot nH_2O$, the approximated amount of montmorillonite is shown in Fig. 2-20b). Considering relative mol weights of: Al ≈ 7.3 wt.%; Si ≈ 30.5 wt.%; Mg ≈ 6.6 wt.%, it is shown that the expected Al/Si ratio (~1/4) correlates well with the measured data, while the measured Mg concentration falls short. The latter, however, is likely due to the variation of Mg by the montmorillonite cation exchange process. As Fig. 2-20 further indicates, most Si can be related to clay-colloid release during the erosion peak. However, with a declining tailing towards later stages of the erosion event (around days 20 to 35) and subsequently growing discrepancies between the approximated amount of montmorillonite and the surplus ($C-C_0$) of silicon, an additional release of quartz colloids is indicated.

To further investigate the correlation of Al and Si within the system, Fig. 2-21 additionally plots all measured data for Case 3. A mostly congruent correlation of all MX-80-derived setups can be seen, highlighted by the added linear fit curve (slope = 2.94 ± 0.09; $R^2 = 0.992$), while the GMX-001-derived sample shows an increased Al/Si ratio in favour of silicon. This however may be due to different structural formulas of the raw MX-80 and GMZ-001 bentonites or montmorillonites, respectively (see e.g. Tab. 2-1, or (IAEA 2013)).

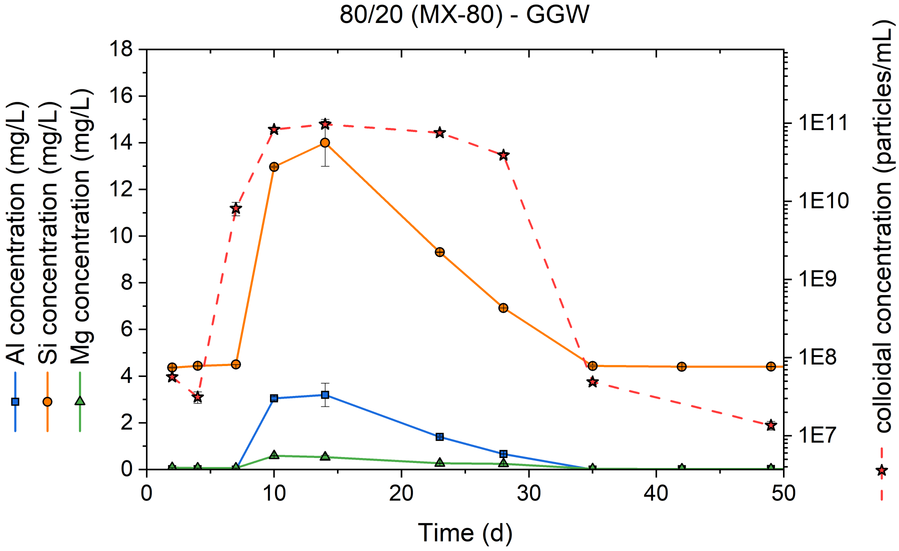

Fig. 2-20: Al, Si, and Mg concentrations for 80/20 (MX-80) – GGW setup and measured colloidal concentration as a function of time

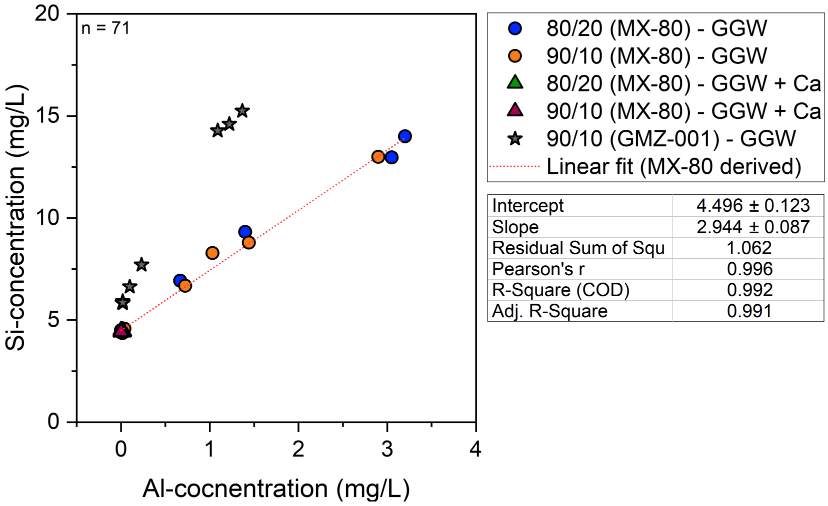

Fig. 2-21: Correlation diagram of measured Al- and Si-concentrations for all samples taken for Case 3

Most data points cluster around 0 mg/L Al-concentration

2.2.3.5 Post-mortem – microscopy

As the samples brought into contact with regular GGW showed pronounced erosion (approx. 94 to 98 wt.% of the initially implemented clay mass), we investigated only the quartz framework and surface that remained after the experiments in detail. As indicated by the images of, e.g. the 80/20 (MX-80) – GGW sample in Fig. 2-22, flakes and clusters of smectite were found within the remaining quartz porous network by SEM. Remaining clay aggregates being attached onto or stuck between the quartz minerals could thus partially explain the missing mass percentage of the quantification approach.

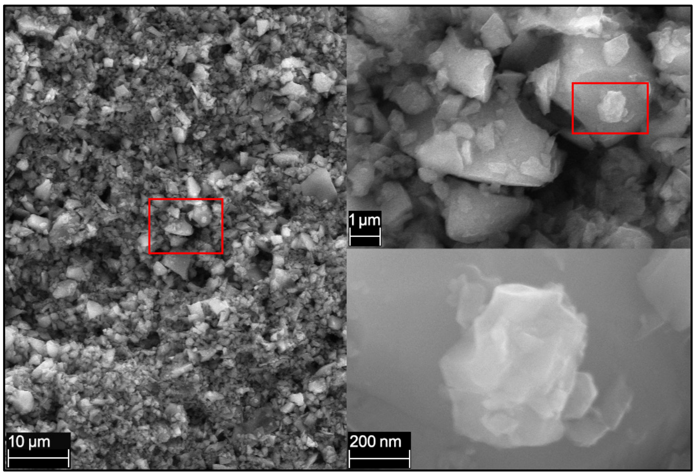

Fig. 2-22: SEM images of the remaining 80/20 (MX-80) – GGW sample after 56 days, showing a small montmorillonite cluster attached to a quartz grain after the erosion experiment

2.2.3.6 CEC and exchangeable cation composition

From the remaining material of the samples contacted with Ca-modified GGW, different segments (core, inner ring, and outer ring) were taken after 119 days (see Fig. 2-13 for comparison). In this case, the radii of the inner/outer ring boundaries of the 80/20 and 90/10 setups, flushed with Ca-modified GGW, were both approx. 18 mm.

In comparison to the pure Na-mnt material, the samples have progressively lower CEC values in conjunction with the amount of added quartz powder, which is as expected. In this context, CEC values of 86.6 ± 0.1 meq/100g (initial Na-mnt), approx. 75 meq/100g (90/10), and approx. 65 meq/100 g (80/20) were measured, respectively (see Tab. 2-11). Concerning the different segments harvested, lower CEC values were also measured for the outer ring segments, likely due to an erosion-induced higher abundance of quartz. Independently of the investigated segment, the smectite surface was mostly exchanged for Ca in both setups. However, as opposed to the initial amounts of montmorillonite added, approx. 70% of the 80/20 (MX-80) and approx. 85% of the 90/10 (MX-80) samples were exchanged in favour of Ca. The effect of different amounts of montmorillonite can be seen by comparing the calcium C-C_0 data in Fig. 2-16. Accordingly, the segments of the 80/20 sample show higher Na concentrations (approx. 20 to 25%) than the 90/10 sample (approx. 10%). Despite suffering from significant erosion, CEC and exchangeable cation composition measurements for the remains of the samples flushed with regular GGW showed very low values of around 3 meq/100g, additionally supporting the quartz-dominated skeleton remaining after the experiments were concluded.

Tab. 2-11: CEC (meq/100g) and element concentrations (%) of the major exchangeable cations of the MX-80-derived Na-mnt sample (segments), mixed with either 10 or 20% quartz and flushed with Ca-modified GGW after 119 days

	CEC [meq/100 g]	**Na** [%]	**Ca** [%]	**K** [%]	**Mg** [%]
80/20 (MX-80) (core)	66.3 ± 0.3	22.4 ± 0.2	73 ± 0.5	0.4 ± 0.01	4.2 ± 0.1
80/20 (MX-80) (inner ring)	67.5 ± 1.6	24.1 ± 0.2	72.1 ± 0.03	0.3 ± 0.03	3.4 ± 0.1
80/20 (MX-80) (outer ring)	62.2 ± 1.4	23.7 ± 0.1	73.3 ± 0.04	0.3 ± 0.01	2.5 ± 0.1
90/10 (MX-80) (core)	74.5 ± 0.7	9.6 ± 0.1	85.1 ± 0.4	0.4 ± 0.01	4.8 ± 0.03
90/10 (MX-80) (inner ring)	76.2 ± 0.2	10.3 ± 0.02	85.4 ± 0.3	0.4 ± 0.01	3.8 ± 0.04
90/10 (MX-80) (outer ring)	73.2 ± 1	12.7 ± 0.03	84.1 ± 0.2	0.4 ± 0.01	2.7 ± 0.04

2.2.4 Case 4: Na-mnt with internal Ca carrier

In the fourth case, Na-homo-ionised montmorillonite was mixed with 10 wt.% of quartz powder (see Case 3 for comparison). Furthermore, different amounts of bassanite (hemihydrate) or anhydrite were added to the samples, acting as a soluble Ca carrier. The conceptional idea was to release Ca through dissolution of bassanite or anhydrite over time and allow it to reach the CCC internally to avoid erosion. While the same quartz powder (SF800) was used as for Case 3, the 10 wt.% value was selected to represent a typical amount found in natural bentonite (e.g. IAEA 2013 or Tab. 2-1). In total, six experiments were conducted using either MX-80- or GMZ-001-derived Na montmorillonite. As for all artificial erosion experiments, a continuous flow of regular GGW (Pinkel) at a constant flow rate of 50 µL/min was applied (see Tab. 2-3).

2.2.4.1 Swelling and pressure propagation

The fastest radial swelling was observed for the MX-80 bentonite containing 2 wt.% of bassanite. The average radial swelling into the open aperture peaked at around 25 mm after 21 days. Due to the onset of the erosion event, similar to the observed swelling behaviour of regular GGW samples in Case 3, the expansion significantly decreased afterwards, reaching zero after 56 days (see Fig. 2-23). Successively slower and less extensive swelling extensions were observed with increased Ca carrier addition of MX-80. the 10 wt.% bassanite and 5 wt.% anhydrite samples showed a similar swelling pace and final radial extension of around 25 mm after 70 days. With a slightly faster and larger average radial extension, the 5 wt.% bassanite sample reached approx. 30 mm after the same time.

A different swelling behaviour was observed for the GMZ-001-derived samples mixed with bassanite. While both samples showed a generally more reduced swelling extension than the MX-80-derived samples, a more considerable swelling extension was observed for the 2 wt.% bassanite sample, peaking at r = 14 mm after 14 days. However, due to the beginning of a pronounced erosion event (see 2 wt.% bassanite – MX-80 for comparison), a rapid loss of the clay components of the samples was observed, reaching zero after 35 days. In contrast, no significant swelling extension was observed for the 5 wt.% bassanite sample, which reached its peak average radial swelling distance (approx. 7 mm) after 24 hours.

With respect to the previous experiments (Cases 1 to 3), the setups for Case 4 showed the lowest peak pressure (contact pressure) values up to 324 kPa for the 2 wt.% bassanite (MX-80), 264 kPa for the 5 wt.% bassanite (MX-80) and 220 kPa for the 10 wt.% bassanite (MX-80) samples, respectively. In general, the pressure was correlated positively with the smectite content. Slower pressure decreases with time were observed than in Cases 1 to 3. While the 5 and 10 wt.% bassanite samples reached a pressure plateau of approx. 40 kPa after around 60 days and no zero pressure within the experimental timeframe, the 2 wt.% bassanite sample reached zero pressure after 56 days, matching the visual erosion of clay from the system.

Similar behaviour was observed for the GMZ-001-derived samples. The peak contact pressures were initially measured with 216 and 200 kPa for the 2 and 5 wt.% bassanite samples, respectively, followed by a continuous pressure decrease over time. Here, no zero pressure was reached for the 5 wt.% bassanite sample, but a comparatively higher-pressure plateau of around 100 kPa was seen after 21 days (see MX-80-derived samples). However, zero contact pressure was reached for the 2 wt.% bassanite sample following the visible clay erosion after 35 days.

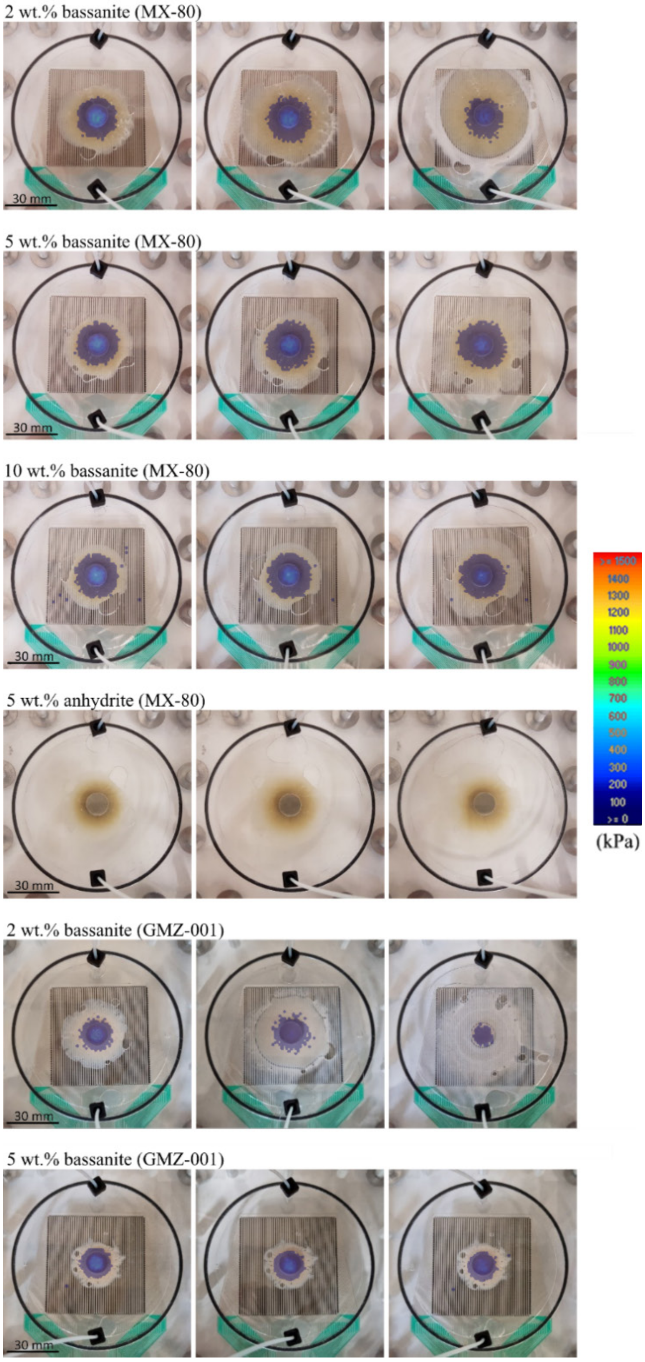
2 wt.% bassanite (MX-80)

5 wt.% bassanite (MX-80)

10 wt.% bassanite (MX-80)

5 wt.% anhydrite (MX-80)

2 wt.% bassanite (GMZ-001)

5 wt.% bassanite (GMZ-001)

Fig. 2-23: View from above on different time steps for the applied setups for Case 4, underlaid with the mapped pressure propagation (kPa)

2.2.4.2 Hydro-chemical progression

As observed in Cases 2 and 3, a high initial EC was measured for all sample setups for Case 4. the MX-80-derived samples thus showed a more pronounced initial peak of 294 ± 8 µS/cm (day 3), compared to the less pronounced but still visible peak of up to 192 µS/cm for the GMZ-001-derived samples. However, the initially high values were followed by a swift EC decrease within the first 20 days towards values of the applied GGW (Pinkel: 110 ± 3 µS/cm) (samples approx. 113.3 ± 4.1 µS/cm). Variations were mainly measured for the 2 wt.% bassanite samples during this period, likely due to the simultaneous clay erosion. pH values showed minor variations over time, and all samples ranged within proximity of the applied GGW (7.37 ± 0.09). However, slightly decreased values were measured for the 2 wt.% bassanite samples (MX-80, GMZ-001) during the erosion period (around Days 10 to 40).

Similar to Cases 2 and 3, Initial Na peaks were measured for all samples extracted in Case 4 (see Fig. 2-24). The MX-80 samples were measured with $C\text{-}C_0$ values of up to 37.4 ± 0.3 mg/L (5 wt.% bassanite, day 3), while the GMZ-001 samples peaked at 16.8 ± 0.1 mg/L (5 wt.%, day 3). Afterwards, all samples showed a rapid decline in Na concentrations towards that of the GGW (Pinkel). In contrast to the Na concentration, the Ca concentration of both 2 wt.% bassanite samples (MX-80, GMZ-001) showed a significant decline briefly after the start of the experiments with negative $C\text{-}C_0$ peak values of -4.90 ± 0.01 and -4.48 ± 0.01 mg/L after 35 and 21 days, respectively (see Fig. 2-24). This Ca stripping correlates well with the visible erosion of both samples, and zero $C\text{-}C_0$ values were reached for both setups after the extensive loss of clay material from the systems.

Samples mixed with higher contents of the soluble Ca carrier showed a different behaviour concerning the measured Ca concentration. There, especially the MX-80-derived samples showed an initial Ca peak concerning the applied GGW, with $C\text{-}C_0$ values of 2 to 3 mg/L in the case of the 5 wt.% bassanite and anhydrite samples and almost 5 mg/L in the case of the 10 wt.% bassanite sample. This initial release of calcium can be linked to the incrementally higher amounts of added bassanite or anhydrite, respectively, and a higher release of calcium due to the dissolution in contact with the applied GGW. However, as the experiments proceeded, the initially higher Ca concentrations declined towards values within proximity of the applied GGW.

In the case of potassium and magnesium (see Fig. 2-25), no significant changes were measured for the 5 and 10 wt.% samples over time. However, as observed for the artificial samples for Cases 2 and 3, concentration peaks were measured for the 2 wt.% bassanite samples, correlating with their respective phase of erosion.

Distinct concentration peaks were measured for aluminium and silicon for the 2 wt.% mixed bassanite samples during their respective erosion events (see Fig. 2-26 also Fig. 2-10, Fig. 2-17 and for comparison). The higher concentrations are likely due to emitted quartz and/or montmorillonite being insufficiently filtered (<0.45 µm) during the post-processing due to the high particle concentrations.

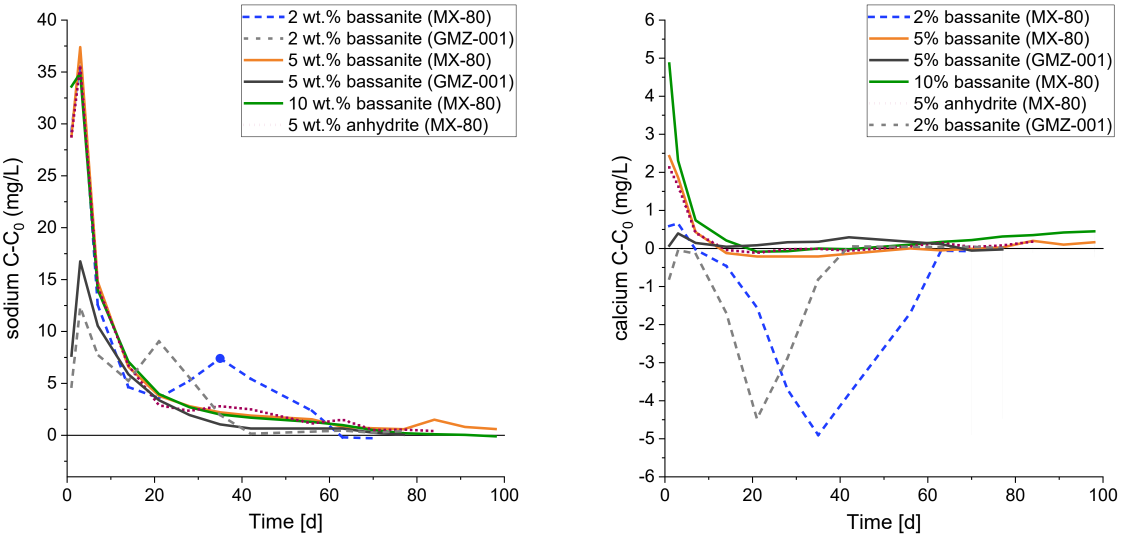

Fig. 2-24: Changes in Na concentration plotted as C-C$_0$ (mg/L) (left) and Ca concentrations (right) for the samples for Case 4 brought into contact with regular GGW. C$_0$ values can be found in Appendix A.2

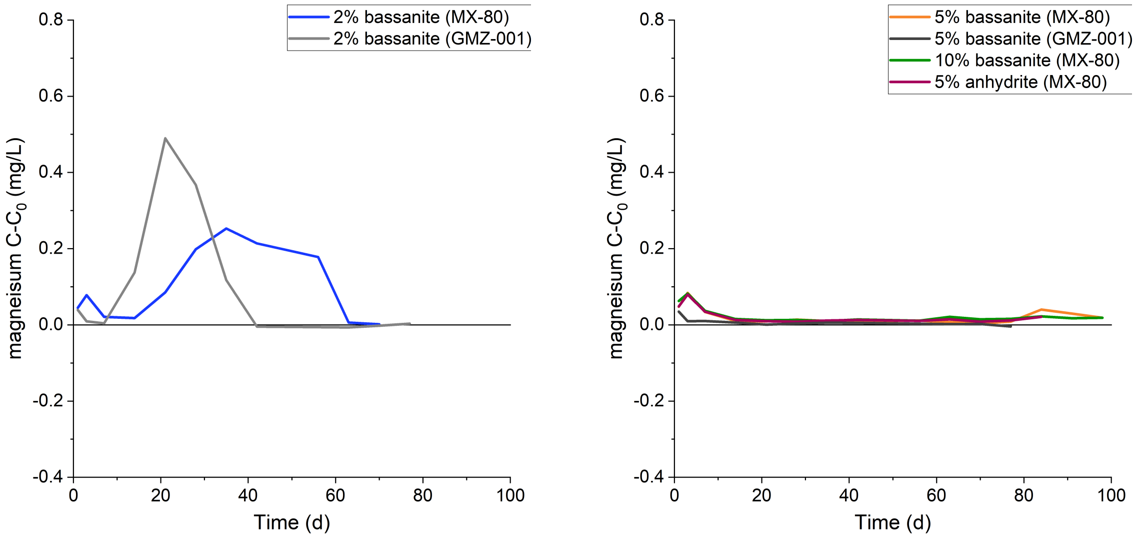

Fig. 2-25: Changes in magnesium concentration plotted as C-C$_0$ (mg/L) for the samples for Case 4, flushed with regular GGW. C$_0$ values can be found in Appendix A.2

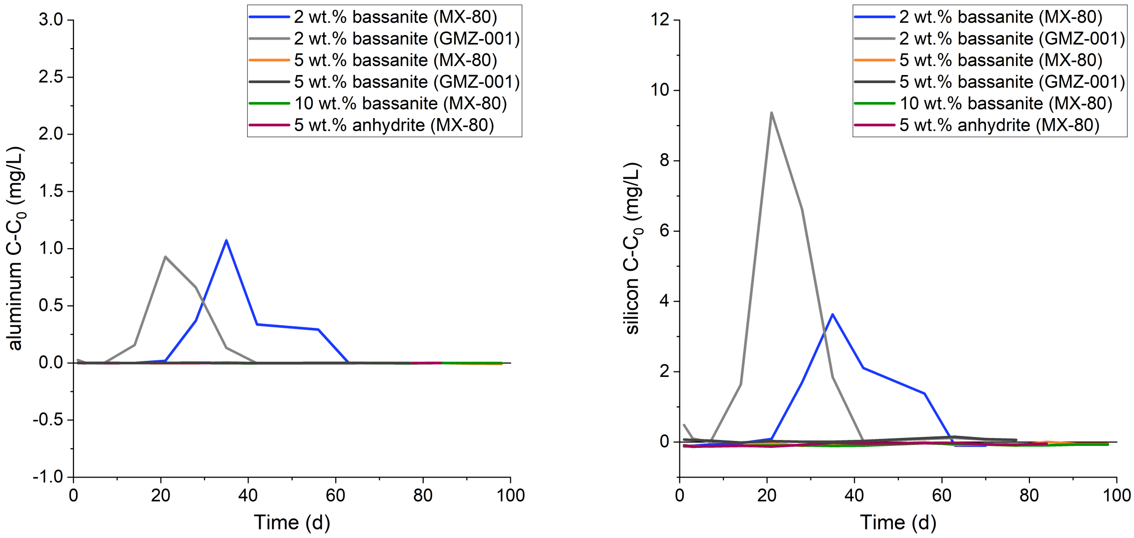

Fig. 2-26: Changes in aluminium and silicon concentrations plotted as C-C$_0$ (mg/L) for the samples for Case 4, flushed with regular GGW. C$_0$ values can be found in Appendix A.2

In the case of chloride, major initial peaks were measured for the MX-80-derived samples, with C-C$_0$ values of up to 52.65 ± 0.4 mg/L in the case of the 2 wt.% bassanite sample after 3 days (see Fig. 2-27). However, these initial peaks were followed by steep concentration declines, asymptotically reaching GGW background concentration ($C = C_0$) after around 14 to 21 days. In contrast, and in accordance with the observations made in Case 3, the GMZ-001-derived samples did not show any initial Cl peak whatsoever.

As expected, all samples were measured with high initial SO_4^{2-} concentration peaks caused by the dissolution of the accessory Ca carrier (see Fig. 2-28). In the case of the MX-80-derived samples, successively higher initial peaks were measured for samples with higher amounts of added bassanite or anhydrite, respectively. Thus, the 2 wt.% bassanite samples showed the least pronounced concentration peaks with respect to the applied GGW (9.83 ± 0.08 mg/L, day 7), while the 5 wt.% samples showed similar values of around 16 mg/L and up to 19.12 ± 0.1 mg/L for the 10 wt.% bassanite sample. More pronounced and slightly faster, the GMZ-001-derived samples were measured with initial C-C$_0$ peak values of up to 23.27 ± 0.05 mg/L (5 wt.% bassanite sample, day 3). However, all sample setups were later measured with progressively decreasing concentration curves toward the applied GGW. In this context, the 5 and 10 wt.% Ca carrier samples never reached the background concentration during the experimentation period. the decreasing concentration curves thus resemble horizontal asymptotes, indicating an ongoing but gradual dissolution of bassanite or anhydrite, respectively.

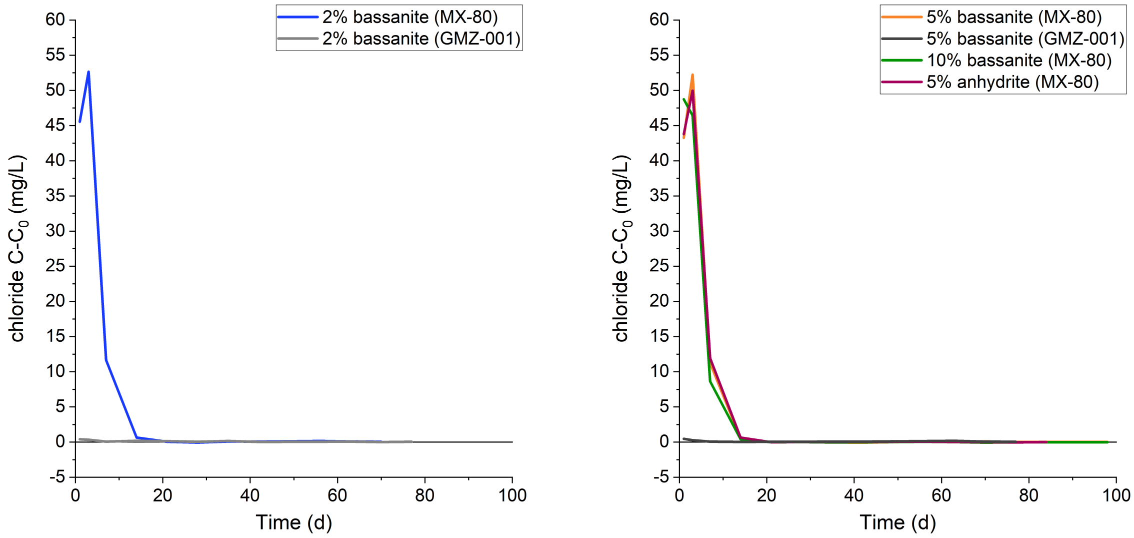

Fig. 2-27: Changes in chloride concentration plotted as C-C$_0$ (mg/L) for the samples for Case 4, flushed with regular GGW

C$_0$ values can be found in Appendix A.2

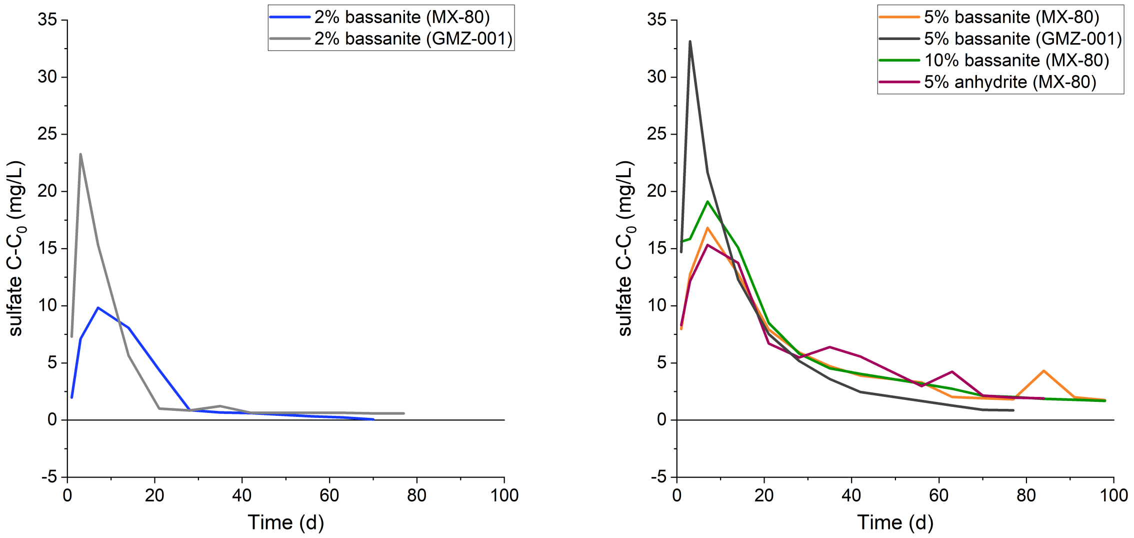

Fig. 2-28: Changes in sulphate concentration plotted as C-C$_0$ (mg/L) for the samples for Case 4, flushed with regular GGW

C$_0$ values can be found in Appendix A.2.

2.2.4.3 Colloid characterisation and mass erosion

NTA size distribution analysis for the MX-80 setup revealed median colloid sizes of 157 ± 20 nm and a slight increase over time, while the GMZ-001 median was determined to be 149 ± 16 nm and showed a slight decrease. In the case of the 2 wt.% bassanite samples, similar hydrodynamic size distributions with little variances were measured.

In the case of the 5 wt.% bassanite samples, an increase of the hydrodynamic diameter was observed after around 7 days for the MX-80-derived samples, reaching plateau values of 200 to 220 nm between days 21 and 56. The GMZ-001-derived sample was measured with average values of approx. 148 ± 24 nm with a slightly increasing trend over time.

The trend of average size increase was even more pronounced in the MX-80 sample mixed with 10 wt.% bassanite. While starting with average values as low as 84 ± 15 nm after 4 days, median hydrodynamic diameters towards the end peaked at 287 ± 30 nm after 56 days. Whereas the 5 wt.% anhydrite sample showed fluctuating values of approx. 173 ± 32 nm, the setup stabilised at around 160 nm towards the end of the experiment.

As indicated by the visual observations (see Section 2.2.4.1), different progressions of colloidal concentrations were measured for the setups for Case 4 (see Fig. 2-29). While the 2 wt.% bassanite setups showed high (1.1 ± 0.5E+10 particles/mL, GMZ-001) or low (2.8 ± 0.4E+07 particles/mL, MX-80) initial particle concentrations, respectively, both setups were measured with significantly increased particle concentrations of up to 8.6 ± 0.5E+10 (GMZ-001) and 1.9 ± 0.6E+10 (MX-80) particles/mL during the observed erosion events. This coincides with the pronounced Ca extraction. Losing their primary share of clay material due to erosion, concentration values measured for both setups decreased towards GGW levels (1.6 ± 1.2E+07 particles/mL, Pinkel) at the end of the experiments. A much lower and more stable particle release was observed for the GMZ-001 + 5 wt.% bassanite sample. With an initial peak concentration of 7.2 ± 0.7E+08 particles/mL, the system quickly adjusted towards colloid concentrations comparable to that of the GGW (approx. 4.2 ± 1.8E+07 particles/mL). In the case of the 5 wt.% bassanite (MX-80) sample, however, a comparably more variable colloid release was observed. While showing a much lower initial colloid concentration of approx. 1.0E+07 particles/mL, which matched the applied GGW, increased values were measured between days 4 and 56, peaking at 2.1 ± 0.6E+08 particles/mL after 28 days. However, the GGW background level was again reached after 77 days within the experiment. Furthermore, an exceptionally steep incline was measured afterwards (day 84), plateauing at approx. 2.0E+08 particles/mL until the end of the experiment, likely caused by advective erosion of the gel layer within proximity of the outlet (see Fig. 2-23) due to the large swelling extension (r = 30 mm).

In Experiments with 10 wt.% bassanite or 5 wt.% anhydrite, an overall low particle concentration in the range of the GGW was detected. Thereby, average particle concentrations of 3.3 ± 4.2E+07 and 1.2 ± 0.8E+07 particles/mL were measured for the 10 wt.% bassanite and 5 wt.% anhydrite setups, respectively. Subsequently, no significant particle emission was induced for either of the systems. However, in the case of the 10 wt.% bassanite sample, at least two events of increased particle emissions were indicated at days 35 and 70, with measured values increasing by around one order of magnitude. As for the late increase of the 5 wt.% (MX-80) sample, these short concentration pulses were likely induced by advective erosion of small clusters of particles within close vicinity of the chamber's outlets (see swelling progression in Fig. 2-23).

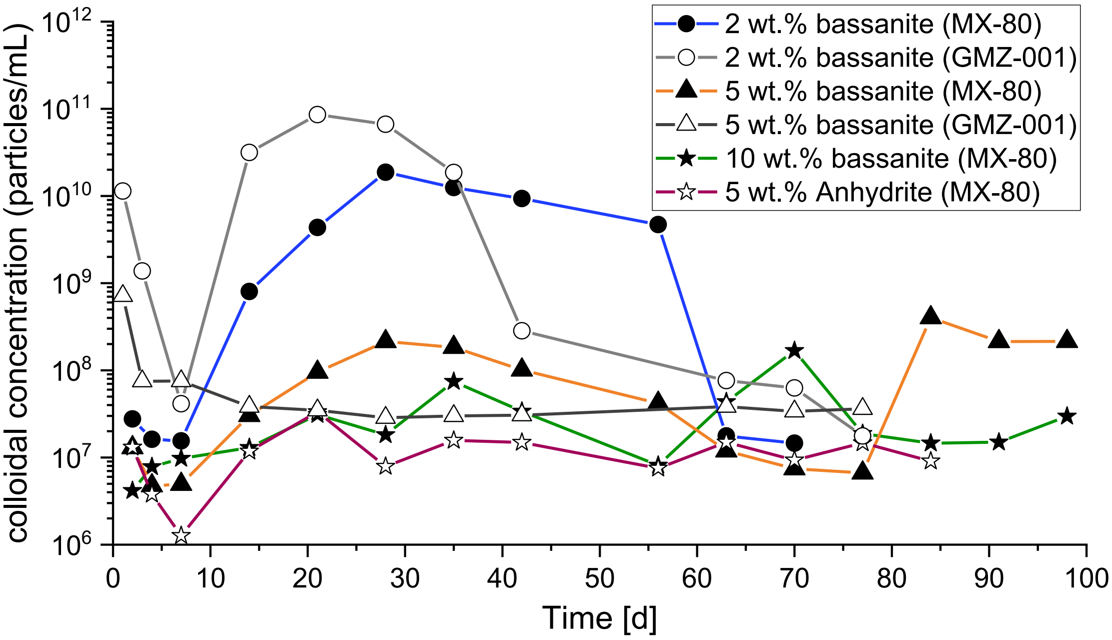

Fig. 2-29: Measured colloidal particle concentration per mL for all setups for Case 4

GGW background: 1.6 ± 1.2E+07 particles/mL (Pinkel)

Based on the colloidal number concentrations (Fig. 2-29), their mass concentrations were calculated (not shown separately). High erosion rates of up to 475 µg/mL were calculated for the 2 wt.% bassanite (GMZ-001) setup during the erosion event, and a total clay loss of 81.2 wt.% was calculated. Brownish shimmer indicated that some montmorillonite remained in the erosion chamber after the end of the experiment (see. Fig. 2-23, and Fig. 2-32 for comparison). In the case of the 2 wt.% bassanite (MX-80) sample, a total clay loss of 60.3 wt.% was calculated (see Fig. 2-30).

With an increase of soluble Ca carrier mixed into the samples, lower erosion mass concentrations were measured. The 5 wt.% bassanite (GMZ-001) sample also showed an initial peak of 6.69 ± 2.81 µg/mL, followed by a continuous decline towards mass concentrations of approx. 0.6 ± 0.3 µg/mL after 7 days, which is slightly above the applied GGW background concentration (0.12 ± 0.07 µg/mL). In this case, an overall mass loss of 0.5 wt.% was calculated, of which approx. 0.1 wt.% was contributed by the natural GGW background. In contrast, the 5 wt.% bassanite (MX-80) sample was calculated with initial low mass concentrations of 0.16 ± 0.11 µg/mL, followed by an increase over time, which peaked at 5.09 ± 2.19 µg/mL after 28 days and decreased towards the GGW background level after 77 days. Following the measured particle concentrations, a concentration plateau was calculated at the end of the experiment with approx. 4.3 µg/mL (see Fig. 2-29 for comparison). A total clay erosion of 1.8 wt.% was calculated for the 5 wt.% bassanite (MX-80) setup after 98 days, of which approx. 0.1 wt.% can be accounted for due to the natural GGW background.

In the case of the 10 wt.% bassanite and 5 wt.% anhydrite samples, average mass concentrations of 0.86 ± 1.31 (10 wt.% bassanite) and 0.29 ± 0.21 µg/mL (5 wt.% anhydrite) were calculated, adding up to an estimated mass loss of 0.8 and 0.2 wt.% in the experimental time frame, respectively. Thus, approx. 0.1 wt.% was of natural GGW origin. Based on the documented data, the following erosion rates can be approximated (note that the maximum colloidal masses were used for the upscaling approach, including the colloids introduced by the applied GGWs (see Case 1 for comparison)):

- 5 wt.% bassanite (MX-80) = 0.21 ± 0.21 kg/m²/a
- 5 wt.% bassanite (GMZ-001) = 0.28 ± 0.47 kg/m²/a
- 10 wt.% bassanite (MX-80) = 0.034 ± 0.024 kg/m²/a
- 5 wt.% anhydrite (MX-80) = 0.07 ± 0.11 kg/m²/a

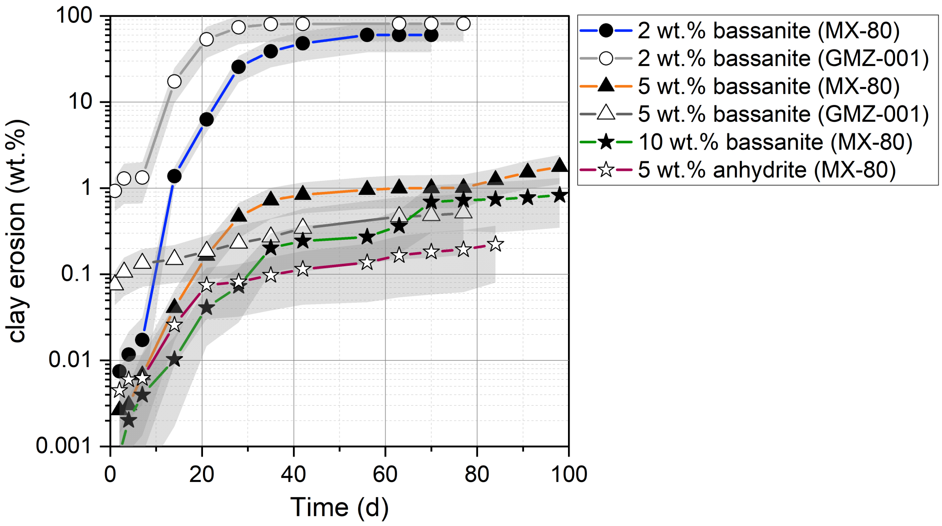

Fig. 2-30: Calculated relative mass loss of clay (wt.%) over time for all setups for Case 4, including the natural GGW background masses

2.2.4.4 Ca carrier solubility, abundance, and speciation

The dissolution of hemihydrate bassanite ($CaSO_4 \cdot ½H_2O$) or anhydrite ($CaSO_4$) led to an appropriate calcium release during the erosion experiments conducted in Case 4. In retrospect, the Ca carrier dissolution is also relevant for the raw MX-80 bentonite material applied in Case 1, as it contains a natural amount of gypsum. Hence, the dissolution kinetics of the Ca minerals can change the hydro-chemical environment to more closely resemble the Ca-CCC of the applied montmorillonite.

An aqueous transformation of soluble anhydrite or hemihydrate (bassanite) into dihydrate (gypsum), and eventual dissolution, is described by Christensen et al. (2008). There, Ca sulphates such as gypsum, bassanite and anhydrate are moderately soluble in water, ranging between 12 and 18 mmol/L at temperatures between 15 and 25 °C (e.g. Klimchouk 1996, Lebedev 2015, Zaier et al. 2021). Dissolution further depends on grain size and pressure conditions where the solubility is inversely proportional to the particle size/surface area. With respect to e.g. gypsum, Hulett (1901), Dundon & Mack (1923) describe it as increasing for radii <1 µm, while it is mostly invariant for particles >1 µm (Lebedev & Kosorukov 2017). Experimental studies of Lebedev & Kosorukov (2017) further showed that maximum solubility values of 18.2 mmol/L were reached for r = 0.2 to 0.5 µm, while minimum values were observed for r > 1 µm, subsequently becoming increasingly independent from the particle size. Furthermore, gypsum is different from most solutes in that it reveals a retrograde or inverse temperature-dependent solubility behaviour (e.g. Rolnick 1950, Dai et al. 2017, Lebedev & Kosorukov 2017). Hence, gypsum shows a rising solubility between 0 and 25 °C, but a decreasing solubility at temperatures >25 °C. Additionally, at higher temperatures and increasing ambient pressure, the hydrate mineral state (gypsum) transforms into the non-hydrate (anhydrate) state due to the loss of minerally bound water, which may be a relevant consideration with respect to the safety case for the post-closure safety of the repository. In contrast, however, the solubilities of bassanite and anhydrate that correspond with the thermal conditions (Klimchouk 1996, Christensen et al. 2008) describe the dissolution rate of bassanite with 4.0 ± 0.9E-5 mol/m^2 s with a hemihydrate content of 90%, which is similar to the one applied in Case 4. the dissolution rate of anhydrate is given with approx. 3.2 mol/m^2 s (Palandri & Kharaka 2004). Moreover, dissolution is described as a diffusion-controlled process which is further influenced by the amount of dihydrate or gypsum, respectively, where higher amounts of gypsum reduce the dissolution rate (Brandt & Bosbach 2001).

Concerning the dissolution kinetics of the Ca carriers, a closer look was taken at the example of hydro-chemical data obtained from the 2 wt.% bassanite (MX-80) experiment. In a first step, the measured Ca concentration was plotted in accordance with the calculated $C-C_0$ (see Fig. 2-31, left). The calculated sulphate $C-C_0$ line was additionally inserted to show the bassanite-dissolution-induced sulphate concentration over time. Based on this information and assuming sulphate as a conservative tracer, the bassanite-related calcium (27.6 wt.%) was calculated for each sample (Fig. 2-31, right). In a final step, the total amount of available calcium in the system was plotted, including the constant GGW (Pinkel) background concentration (5.86 ± 0.46 mg/L) and the bassanite-related calcium.

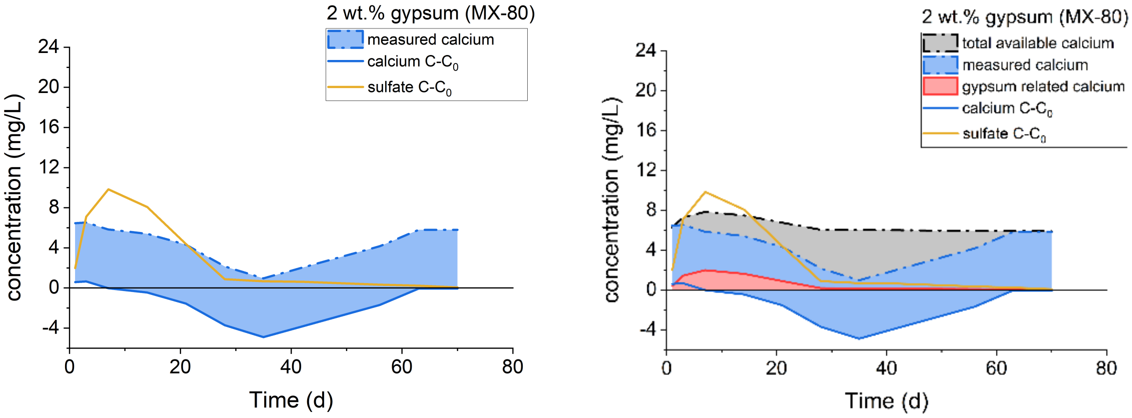

Fig. 2-31: Step-by-step illustration of the calculation approach of bassanite-dissolution-related calcium release, exemplarily shown for the 2 wt.% bassanite (MX-80) setup

Furthermore, backward calculations of the implemented Ca carrier were conducted with respect to the sulphate $C-C_0$ data, to see if the Ca carrier was fully dissolved during the experiments. As a result, calculations of e.g. 2 wt.% bassanite showed a quantitative dissolution. However, as the Ca concentration data suggest, the sulphate dissolution was not fully completed for the 5 or 10 wt.% Ca carrier (MX-80) experiments (see Fig. 2-31), amounting to dissolution values between approx. 60 and 70 wt.% for the 5 and 10 wt.% experiments, respectively.

Due to the Ca carrier dissolution and dependency on the initial amount implemented, different calcium peak heights were calculated for all setups (around 0.2 to 0.35 mmol/L). Restraining the particle release at a qualitatively derived threshold of around 0.2 ± 0.05 mmol/L, erosion increased for all experiments as soon as this value was undercut. On the other hand, an increased particle release could be observed as soon as the Ca concentration decreased below this threshold due to cation exchange processes. However, this increase differed between the individual setups. It was likely linked to the pace of surface cations exchanging at a certain point (see Na/Ca exchange ratios Tab. 2-12 listed in for comparison). Subsequently, if a certain ratio of Na/Ca surface composition were to be provided as a result of a sufficient amount of calcium, erosion rates would stabilise at comparably lower rates within the time frame of the experiment.

In this context, the 100% Na-mnt (MX-80) sample (weight 1 g) for Case 2 brought into contact with GGW (BOUS) at a constant flow rate of 0.05 mL/min is considered an illustrative case. Concerning the measured CEC (86.6 ± 0.2 meq/100g)[4], the theoretically necessary total amount of 17.32 ± 0.04 mg of calcium per gram of montmorillonite can be calculated to exchange all surface cations in favour of calcium $(m_a = 40.08\ u)$, whereas m_a is the molar mass of calcium and the number of charge (+2):

$$\text{Ca (mg/cmol)} = m_a/2/100 \tag{3}$$

Concerning the Ca background concentration (GGW in Case 2 around 8.1 mg/L), the necessary amount of Ca would be provided after flushing around 2,100 mL of GGW or 29 days, respectively. The observed erosion started after around 7 to 10 days for the regular GGW setups for Cases 2 and 3, leading to an insufficient total Ca supply of approx. 4.0 to 5.8 mg/L.

With respect to Case 4, the total amount of Ca supplied by e.g. bassanite complies to a total amount of 13.8 mg of bassanite-related Ca in the case of e.g. the 5 wt.% bassanite (MX-80) setup. With respect to the Ca concentration of the applied GGW (5.86 ± 0.46 mg/L) and the flow rates applied (0.05 mL/min), the calculated amount of necessary calcium to fully exchange Na to Ca would have been reached within 7 days, theoretically. However, as this neglects the non-instantaneous or progressive dissolution of the Ca carriers, shown in Fig. 2-31, the required time to provide the necessary amounts of calcium for full cation exchange ignoring the effective diffusion in the compacted bentonite can be expected to be:

- approx. 32 days in the case of the 2 wt.% bassanite setups,
- approx. 24 days in the case of the 5 wt.% bassanite setups,
- approx. 21 days in the case of the 10 wt.% bassanite setup, and
- approx. 23 days in the case of the 5 wt.% anhydrite setup.

As the experiments lasted 70 to 100 days, a total Ca supply of around 30 to 50 mg is theoretically provided by the applied GGW, thus significantly exceeding the necessary amount. However, quantities of calcium measured in the effluents of the regular GGW approaches showed that not all Ca theoretically provided by the applied GGW was in fact available for the cation exchange. Also, for instance in the case of the 2 wt.% bassanite samples, erosion started after around 10 to 14 days. At that time, only half of the necessary amount of Ca would have been supplied to the systems (approx. 7 to 8 mg), which is in turn also represented in the exchange ratios of Tab. 2-12 and observed in the pronounced erosion events. In the cases of the 5 or 10 wt.% bassanite samples, though, increased particle releases were observed after around 14 to 21 days, but with significantly lower concentrations in the range of approx. 10^7 to 10^8 particles/mL. Hence, around 13 or 14 mg of Ca were supplied after 21 days, leading to increased erosion stability, which is also represented in the cation exchange ratios measured (see Tab. 2-12).

---

[4] 1 meq/100 g = 1 cmol/100 g

The results obtained with an artificial soluble Ca carrier (bassanite) added to the compacted bentonite show, that an addition of 5 wt.% can reduce significantly erosion of homoionic Na-mnt. Higher additions, e.g. 10 wt.% bassanite, do not increase the stability of the bentonite and 2 wt.% are not sufficient to prevent significant erosion most probably due to the Ca release kinetics that take time to reach the Ca-CCC within the bentonite.

For dissolved Ca species analysis, two samples (7 and 14 days) of the 5 wt.% bassanite (MX-80) were chosen applying the geochemical solver PHREEQC using the ThermoChimi (eDH_electron_v9B0) database. The results show experimental pH values of the samples (7.44 and 7.47) and a total calcium molarity of 1.5E-04 and 1.4E-04, respectively. free Ca^{2+} was the predominant species with 96.8% after 7 days and 97.2% after 14 days. While species like $CaSO_4$, CaF^+, $CaCl^+$, and $CaOH^+$ were considered less abundant, only at pH >10, the relative abundance of $CaOH^+$ significantly increases.

2.2.4.5 Scanning electron microscopy (SEM)

Fig. 2-32 illustrates the subjectively perceived higher amount of clay particles between the remaining quartz framework, as compared to the 80/20 (MX-80) – GGW setup for Case 3 (see Fig. 2-22 for comparison), which corresponds with the difference in erosion quantification of around 60 to 80 wt.% (Case 4) and approx. 98 wt.% (Case 3), respectively. Moreover, no traces of bassanite minerals were found within the framework, which corresponds with the expected full dissolution based on the dissolution kinetics of the hemihydrate after 77 days (see Section 2.2.4.4 for comparison).

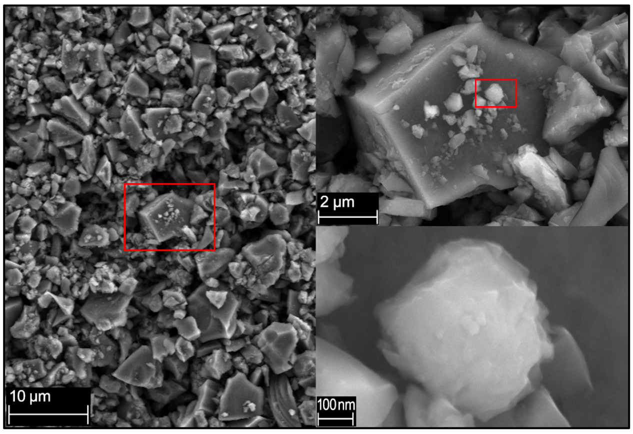

Fig. 2-32: SEM images with increasing magnification levels of the remaining 2 wt.% bassanite (MX-80) sample after 77 days, showing various clusters and individual clay particles attached on and between larger quartz grains (type SF800) after the erosion experiment

2.2.4.6 Cation exchange capacity (CEC) and exchangeable surface cations

As for the post-mortem analysis of Cases 1 to 3, different segments were sampled (see Fig. 2-13) to determine the CEC and exchangeable cation composition over time. No outer ring segment of the 5 wt.% bassanite (GMZ-001) setup was sampled due to the low swelling progression. In Case 4, the radii of the inner/outer ring boundaries were approx. 10 mm in the case of the 5 wt.% bassanite (MX-80) and 2 wt.% bassanite (GMZ-001) setups, 8 mm in the case of the 10 wt.% bassanite and 5 wt.% anhydrite (MX-80) setups and approx. 5 mm in the case of the 5 wt.% bassanite (GMZ-001) setup. Furthermore, samples were harvested after 77, 84 and 98 days (see Tab. 2-12).

Compared to the initial CEC value of the MX-80-derived Na-mnt (86.6 ± 0.1 meq/100g), the MX-80-based sample mixed with 5 wt.% bassanite showed slightly reduced CEC values (approx. 80 meq/100g) for all investigated segments (see Tab. 2-12). Within this context, a slightly higher CEC value for the outer ring segment is assumed to be likely due to the swelling of clay, redistribution of material, and, thus, a higher abundance of montmorillonite compared to the inner and core segments. A similar trend can also be seen for the 10 wt.% bassanite and 5 wt.% anhydrite samples. A significantly increased CEC value was determined for the partially Ca-exchanged outer ring segment of the 5 wt.% anhydrite sample with close to 100 meq/100g. Due to its different swelling behaviour, the 5 wt.% bassanite (GMZ-001) sample was measured to have slightly lower CEC values with an increasing gradient towards its harvested core segment (around 70 to 75 meq/100g). However, Ca exchange was measured to be more advanced with values of approx. 92%.

Regarding the exchangeable cation composition, all sample segments show a predominant shift in favour of Ca (see Tab. 2-12), as expected. Thereby, the core segments generally showed higher Ca/Na exchange ratios in comparison to the inner and especially the outer ring segments. This is in contrast with the previous artificial sample setups for Cases 2 and 3 with a Ca source supplied via the GGW contact. In turn, measured Na concentrations show increased values towards the outer ring segments for Case 4, peaking at 51% for the anhydrite sample. As Mg was only introduced by the applied GGW, higher values were measured for the inner and outer ring segments, compared to the core segment of all setups.

As the 2 wt.% bassanite samples showed an increased erosion behaviour, significantly lower CEC values were measured due to the lower amount of montmorillonite. Thereby, the MX-80 based sample remnants were measured with a higher CEC (18.3 meq/100g) compared to 15.4 and 6.6 meq/100g, measured for the inner and outer ring segments of the GMZ-001-based sample in line with the calculated mass losses of around 60 and 80 wt.% (see Section 2.2.4.3 for comparison).

Tab. 2-12: CEC (meq/100g) and element concentrations (%) of the major exchangeable cations for different segments (core, inner ring, outer ring and the final days of the experiments in parentheses for the MX-80 and GMZ-001 bentonites) derived samples for Case 4

	CEC [meq/100 g]	**Na** [%]	**Ca** [%]	**K** [%]	**Mg** [%]
100% Na-mnt GMZ-001 (initial material)	88.5 ± 2.7	97.3 ± 1.7	1.9 ± 0.01	0.4 ± 0.01	1.35 ± 0.01
MX-80 2 wt.% bassanite (remains, 77 days)	18.3 ± 0.1	42.9 ± 0.1	43.5 ± 0.1	0.8 ± 0.1	12.0 ± 0.1
MX-80 5 wt.% bassanite (core, 98 days)	80.5 ± 0.3	10.7 ± 0.1	85.2 ± 0.3	0.3 ± 0.01	3.6 ± 0.03
MX-80 5 wt.% bassanite (inner ring, 98 days)	80.4 ± 1.1	13.7 ± 0.1	81.3 ± 0.1	0.3 ± 0.01	4.6 ± 0.1
MX-80 5 wt.% bassanite (outer ring, 98 days)	82.3 ± 0.1	21.6 ± 0.01	73.1 ± 0.01	0.3 ± 0.01	4.7 ± 0.01
MX-80 10 wt.% bassanite (core, 98 days)	75.7 ± 1.3	3.5 ± 0.01	94.3 ± 2.5	0.2 ± 0.01	1.9 ± 0.01
MX-80 10 wt.% bassanite (inner ring, 98 days)	80.9 ± 2.1	8.4 ± 0.02	86.9 ± 0.8	0.3 ± 0.01	4.3 ± 0.2
MX-80 10 wt.% bassanite (outer ring, 98 days)	89.1 ± 0.1	17 ± 0.01	78.7 ± 0.01	0.3 ± 0.01	3.6 ± 0.01
MX-80 5 wt.% anhydrite (core, 85 days)	82.5 ± 0.9	12.3 ± 0.1	83.4 ± 0.9	0.3 ± 0.1	3.8 ± 0.1
MX-80 5 wt.% anhydrite (inner ring, 84 days)	81.2 ± 1.9	20.4 ± 0.5	74.9 ± 0.5	0.3 ± 0.01	4.2 ± 0.1
* MX-80 5 wt.% anhydrite (outer ring, 84 days)	98.4 ± 0.1	<51	45.6 ± 0.01	0.2 ± 0.01	3.0 ± 0.01
GMZ-001 5 wt.% bassanite (core, 77 days)	75.4 ± 0.4	0.8 ± 0.1	91.8 ± 0.3	1.6 ± 0.01	5.6 ± 0.02
* GMZ-001 5 wt.% bassanite (inner ring, 77 days)	70.6 ± 0.1	<0.6	91.4 ± 0.1	1.6 ± 0.1	6.2 ± 0.1

Tab. 2-12: Cont.

	CEC [meq/100 g]	**Na** [%]	**Ca** [%]	**K** [%]	**Mg** [%]
* GMZ-001 2 wt.% bassanite (inner ring, 77 days)	15.4 ± 0.1	<10.6	70.4 ± 0.1	0.7 ± 0.1	17.2 ± 0.1
* GMZ-001 2 wt.% bassanite (outer ring, 77 days)	6.6 ± 0.1	<11.2	68.5 ± 0.1	0.5 ± 0.1	18.6 ± 0.1

* Single sample measurement due to insufficient amounts of material acquired after the experiment; error-prone data. Due to the low amount of extracted material, Naconcentrations were below the detection limit.

2.3 Discussion

2.3.1 Swelling behaviour and pressure evolution

The main forces acting in bentonite gels are gravitation, buoyancy diffusion, electrical diffusive double layer (DDL) repulsion, and van der Waals (vdW) attraction forces (Neretnieks et al. 2009), which are balanced by friction if particles are inducted to move (e.g. applied flow rates or swelling). Thus, only the DDL force is influenced by water composition. in waters with low ionic strength below the CCC, DDL force dominates over vdW forces, and particles repel each other (Neretnieks et al. 2009). In a high ionic strength environment, however, the diffusive layer is compressed, and vdW attraction forces can overcome the repulsion forces over a short distance, leading to coagulation and formation of more erosion stable cohesive gel (Neretnieks et al. 2009). Considering high particle concentrations (e.g. compacted bentonite), forces are described to be even more considerable, with expansion rates being balanced by repulsion and friction of particles against water (Neretnieks et al. 2009). While the swelling ability of the different setups depended on the initial mineralogical composition, it was also observed to be severely influenced by the hydro-chemical environment in which the samples were placed. Hence, higher Ca concentrations generally led to better long-term stability and less erosion. natural or artificial interior Ca suppliers (bassanite, anhydrite) retard the swelling capability. With respect to the bentonite sources, lower swelling capacity was observed for the GMZ-001 compared to MX-80 derived Na-mnt , which has also been reported by Sun et al. (2013).

Regarding the visual expansion and erosion behaviour of artificial sample pellets, measured pressure data did not necessarily monitor non- or ongoing erosion processes within the respective systems. Even though high initial pressure data (first 24 h) represented the beginning of the swelling process for all samples in contact with water, they were also measured with decreasing contact pressures over time due to the radial extension of the gel into the artificial fractures. However, in some cases, and especially in the case of significant erosion events, pressure losses or even zero-pressures did correlate with the loss of swellable material (montmorillonite). In other cases, especially for the samples flushed with Ca-modified GGW, decreasing pressure values were also measured, even though no significant erosion of clay was observed. This indicates the spatial (re)distribution of the swelling material within the fracture cells and thus decreased local pressures rather than a loss of clay. Nevertheless, measured pressure data for the raw bentonites and the derived Na-mnt samples taking the estimated compaction density corresponded to literature data (e.g. Agus & Schanz 2008, Karnland 2010, IAEA 2013).

The target density of 1.8 ± 0.05 g/cm³ was achieved for all sample pellets applied in the laboratory-scale erosion experiments. However, variations within this range could lead to slight differences in pressure-related data. Although the TekScan® pressure sensors were linearly calibrated and applied for their expected pressure range, minor errors of approx. 5% must be considered. Furthermore, compiled pressure maps were not equal to the total radial expansion of the swollen gel due to the lower detection limit of the pressure sensors applied (see, e.g. Fig. 2-5).

Another factor to consider, potentially impacting the swelling behaviour and friction on the expanding material, is the surface roughness of the applied acrylic glass cells. Thereby, surface roughness can be described as the fluctuation around a specific reference height of a solid surface, larger than the interatomic distance (Rahimi et al. 2012). Concerning the main components of a granitic rock, quartz, Na- and K-rich feldspars have mostly smooth surfaces compared to rougher Ca-rich feldspars. With respect to the applied acrylic glass, however, a minor restraining impact can be expected due to a polished surface with a roughness of <0.2 µm as described in Stoll et al. (2016), which is even smaller than the 0.2 to 25 µm, considering the processing treatment of such surfaces (CNC lathe), in accordance with DIN (2002).

2.3.2 Hydro-chemical evolution

Initially increased Na concentrations in solution are a result of Na/Ca exchange processes from the Na-exchanged montmorillonites. Over time, Na concentrations asymptotically reach background GGW levels, and K^+ and Mg^{2+} were measured with similar background concentrations in the applied GGWs (approx. 0.2 mg/L), while Mg concentrations on the exchanger increase due to the higher selectivity of the montmorillonite for divalent cations.

Increased Sr concentration in the raw GMZ bentonites indicates precipitation of Sr carbonates such as $SrCO_3$, which aligns with the higher initial carbonate abundance of the base material (see Tab. 2-1), although such changes were not observed for MX-80. No changes were observed for F^-; hence, no CaF_2 precipitation is indicated, and the Ca concentration is fully controlled by CE processes.

When considering the aluminium and silicon data shown e.g. in Fig. 2-10 and/or in Fig. 2-17, it can be seen that the Al/Si ratio correlates with the ratio to be expected from montmorillonite (e.g. Keller 1956, and/or the structural formulae of montmorillonite). This is especially pronounced in experiments for Cases 2 to 4, where a highly congruent correlation of Al/Si ratios indicates a primary release of clay colloids. While Al/Si ratios of around 1/4 were measured for all MX-80 setups, decreased ratios in favour of silicon were observed for the 90/10 (GMZ-001) setup of Case 3 and the 2 wt.% bassanite (GMZ-001) setup for Case 4, indicating an additional release of silica-based colloids.

Having measured only low amounts of DOC in selected contact waters for Cases 1 and 2, these concentrations are attributed to natural organic matter (Schäfer et al. 2004) present in the GGWs (BOUS: 0.32 ± 0.12 mg/L; BOUS + Ca: 1.03 ± 0.04 mg/L; Pinkel: 0.29 ± 0.2 mg/L) and were too low to have an impact on erosion.

2.3.3 Cation exchange capacity (CEC) and exchangeable cation composition

With the primary Na/Ca exchange over time, the systems showed a subsequent decrease in the CEC. While samples with higher Na concentrations also showed higher CEC values, samples with increasingly higher Ca concentrations showed decreasing CEC values, indicating an influence on the Cu exchange during the Cu(II)-trien method, except for the base material (initially purified and Na-homo-ionised montmorillonite) with a CEC value of 87 meq/100g. Another possible explanation for the increased CEC values of Na-mnt samples could be a size partitioning during the swelling process leading to larger surfaces and therefore CEC values. In the cases of pronounced mass loss, low CEC values of approx. 3 to 15 meq/100g were observed, indicating at least minor amounts of clay left within the erosion chambers in accordance with the SEM observations.

Based on the preparation procedure, salts were removed from the initial material during the purification process, thus ensuring the measurement of low ECs (< 10 µS/cm) after the final centrifugation step (see Section 2.1.1.4). Hence, remnant NaCl is minimised. Nevertheless, salt enrichment during the freeze-drying process of the material cannot be fully ruled out; thus, it is not directly associated with the MX-80-derived Na-mnt. Discrepancies of the swelling behaviour, cation exchange and erosion processes observed for MX-80 and GMZ-001 derived from Na-mnt setups, respectively, could indicate different clay layer charges while the CECs of the Na-mnts with 86.6 ± 0.02 and 88.5 ± 2.7 meq/100 g, respectively, are very comparable (see Tab. 2-4).

Due to the higher selectivity coefficient of Ca over Na, the cation exchange trends favouring the divalent cations (Ca, Mg) observed are expected and need to be modelled for the different stages of swelling (compaction density) given different densities and therefore effective diffusion coefficients.

2.3.4 Ca carrier solubility

A positive correlation could be given for the peak concentration of Ca with respect to the added amount of Ca carrier mineral phase. Concerning the Ca-CCC of montmorillonite colloids determined experimentally by Seher et al. (2020) taking into account the measured pH in the erosion experiments of ~7.5, the Ca-CCC would presumably be around 1.2 ± 0.5 mmol/L. The added 2 or 5 wt.% of bassanite plus the natural Ca background concentration of the GGWs, seemed sufficient to temporarily stabilise the systems with an overall Ca concentration of only 0.2 ± 0.05 mmol/L. As the erosion experiments were conducted at low flow rates (water replacement rate around every 2 hours), prolonged GGW residence times may also beneficially enhance system integrity, even at lower Ca concentrations. However, as the results for Case 4 showed, a Ca exchange of roughly 40 – 50% was eventually insufficient to stop erosion (see 2 wt.% bassanite setups, Case 4).

Sulphate concentrations taken as a conservative indicator for the bassanite dissolution indicate an incomplete dissolution for the 5 and 10 wt.% Ca carrier experiments. From the observations made in this study based on the observed low particle erosion of the 5 and 10 wt.% in the Ca carrier setups, it could be hypothised that a Na/Ca threshold or critical value enhances erosion stability. This is an open question for the new EVIDENT project to be tackled also from a modelling perspective.

It should be noted that ions have specific effective diffusion coefficients with pore size and compaction-dependent anion exclusion (Engelhardt 1960).

Based on the experiments for Case 4 with artificial Ca carriers, the natural gypsum content of the raw MX-80 bentonite (Case 1) was likely the reason for the lower particle release in comparison to the raw GMZ bentonites, which show no or other Ca carriers such as carbonates, calcite, micas and plagioclase/feldspar (see Tab. 2-1). Hence, dissolution kinetics and Carelease of these phases must be investigated in future studies. Other factors to consider include the pressure-dependent Ca carrier solubility, which is described to increase up to 5 times under the same hydro-chemical and temperature conditions between 1 and 1,400 bar (Dai et al. 2017). Furthermore, gypsum and anhydrite solubility are also very sensitive to the ionic strength of the contact water, due to a decrease in activity coefficients of the solute ions (i.e. Ca^{2+} and SO_4^{2-}). Thereby, higher ionic strength leads to stronger ion interactions and, thus, a higher solubility (Dai et al. 2017).

2.3.5 Particle characterisation and erosion quantification

Particle-size distribution analysis showed clay colloids of around 150 ± 50 nm in diameter released for artificial and raw bentonite samples. However, tendencies towards larger hydrodynamic particle diameters during the experimental duration were observed for all setups, whereas this tendency was especially pronounced for the Ca-modified GGW. Compared to the NTA data, DLS measurements for the raw MX-80 samples showed larger average particles increased approx. 100 to 150 nm in size. For polydisperse particle-size distributions such as the raw MX-80 DLS, which is based on bulk scattering a signal tail towards larger particle sizes (Filipe et al. 2010), these distributions are better displayed by a single particle method such as NTA (Hoo et al. 2008).

Erosion mass quantification was performed using the approach of Mehrabi et al. (2017) for NTA data. Concentration calibration data (see Fig. 2-7) show that the aspect ratio of the clay particles has a minor effect on concentration estimation. However, deviation errors of the calibration curves (approx. ± 10 wt.%) and high standard errors of the individual measurements (standard errors regularly up to 50%) pose relatively high uncertainties for the NTA-based mass quantification approach. Concerning the calculated clay loss of around 60% (MX-80-derived) and 80 wt.% (GMZ-001-derived) of the 2 wt.% bassanite samples in Case 4, the different behaviours pose the question whether montmorillonites of different origins (MX-90, GMZ-001) can have, based on their layer charge, different erosion behaviours. Furthermore, natural colloidal backgrounds of the applied GGWs were observed to account for up to 38% of the total calculated erosion masses, especially pronounced for the setups with low erosion rates (see e.g. Cases 1 – 3, GGW + Ca). In comparison, the influence of GGW-introduced colloids to the overall calculated masses was negligible in cases where natural GGW was applied, and the erosion was more pronounced.

Regarding a potential upscaling of the approximated erosion mass loss, stable erosion rates for the raw bentonites in Case 1 contacted with regular GGW are:

- Raw MX-80 – GGW (Case 1) = 0.25 ± 0.11 kg/m²/a
- Raw GMZ-001 – GGW (Case 1) = 2.32 ± 1.79 kg/m²/a
- Raw GMZ-24-200 – GGW (Case 1) = 5.88 ± 3.32 kg/m²/a.

While setups flushed with Ca-modified GGW showed lower erosion rates:

- Raw MX-80 (Case 1) = 0.014 ± 0.011 kg/m²/a
- Na-mnt (Case 2) = 0.011 ± 0.010 kg/m²/a
- 80/20 (MX-80) (Case 3) = 0.013 ± 0.019 kg/m²/a

The 5 wt.% bassanite setups for Case 4 have similar values as the raw bentonites for Case 1, at least for MX-80:

- (MX-80) = 0.21 ± 0.21 kg/m²/a
- (GMZ-001) = 0.28 ± 0.47 kg/m²/a

Such upscaled values lie within the reported values of e.g. Smith et al. (2017) who describe similar erosion rates of a few kg/m²/a or Neretnieks et al. (2017), who state mass loss by sedimentation with 0.2 to 0.6 kg/m²/a with the restriction of considering small apertures of 0.1 mm and a non-zero dipping angle. Regarding potential temporal influences of the aquatic environment or pH (~7.5) on the particle stability and size distribution of the extracted samples, no significant changes in particle-size distribution or concentration were observed for the same samples of raw MX-80 bentonite over time. Furthermore, no changes in the zeta-potential were observed for the samples within the same pH range (approx. -40 ± 3 mV).

2.4 Summary and conclusions

The most considerable radial extension was observed for the raw MX-80 bentonite, flushed with regular GGW (Case 1, $r \approx 36$ mm). This is higher in comparison to similar fracture approaches, e.g. Rinderknecht (2017), Alonso et al. (2019) ($r \approx 20$ mm), but lower than the free swelling ability reported by Neretnieks et al. (2009) ($r \approx 45$ mm). As opposed to this, the 100% Na-mnt (MX-80) sample achieved a maximum radial swelling distance of $r \approx 26$ mm when flushed with Ca-modified GGW. The following results could be identified to control the swelling and erosion behaviour:

1. Regarding the erosion experiments conducted with regular GGW, the naturally occurring gypsum content of the raw MX-80 bentonite in combination with the natural GGW Ca concentration was sufficient to reduce erosion.
2. Setups with artificially Ca-enriched GGW (2 mmol/L) showed that erosion stability correlates with a Ca concentration "tipping point" of around 0.2 ± 0.05 mmol/L, below which the particle erosion was enhanced. If the available Ca concentration was above this threshold for a prolonged time (around 14 to 21 days), a sufficient Ca exchange stabilised the gel layer.
3. Increasing amounts of soluble Ca-containing accessory minerals reduced the swelling ability of the respective samples via calcium cation exchange. In the case of the artificial Na-mnt samples, 2 wt.% of added hemihydrate were insufficient to supply the gel with an adequate amount of calcium, thus leading to an increased clay erosion. Whereas 5 wt.% of added Ca carrier bassanite was sufficient to supply an adequate amount of calcium, 10 wt.% addition did not further improve the erosion stability.
4. Non-reactive accessory mineral quartz (10 or 20 wt.%) powder with an average grain size of 2µm had no impact on swelling or erosion behaviour.
5. Montmorillonites from different sources (here, MX-80 or GMZ-001) developed different swelling and erosion behaviours with GMZ-001-derived Na-mnt showing generally higher erosion.
6. As expected, the contact pressure depended on the smectite/montmorillonite content and the exchangeable cation composition with higher pressures for the Na form. With respect to the particle characterisation of the extracted samples, progressively larger hydrodynamic diameters were observed for all experiments over time, likely due to the release of smaller particles during earlier stages of the experiments.
7. A clear correlation of structural Al, Si and Mg (e.g. Al/Si ratio of 1/4) and the approximated colloidal masses indicate a primary release of clay colloids for the MX-80-derived samples. However, with respect to the mineralogical composition of the raw bentonites and the GMZ-001 pellets, the decrease in Al/Si ratios measured (1/7 or lower) suggest a considerable emission of non-clay colloids.

3 Large-scale GTS in-situ experiment in the context of i-BET

As part of the ongoing Colloid Formation and Migration (CFM) project, which is being conducted at the Grimsel Test Site (GTS), the In-Rock Bentonite Erosion Test (i-BET) was launched on 14th December 2018 within the framework of GTS Phase IV. The CFM project is dedicated to repository-relevant in-situ experiments (i.e., large-scale, long-term) regarding colloid formation and its impact on radionuclide transport (Schneeberger et al. 2019a). To this end, bentonite rings were made of Bara-Kade bentonite (MX-80 type), manufactured by Sorvikivi Oy and contracted by Posiva Oy (Schneeberger et al. 2019a). This allowed studying a larger volume (total of 51.3 kg) of compacted bentonite in a natural flow field within a crystalline fracture system.

As part of the project series, i-BET can be seen as a follow-up project of the previously conducted Long-term In-Situ Test (LIT), with the exception that it does not involve the use of radionuclide tracers. The focus of i-BET is on characterising the loss of bentonite in a natural flow field, i.e. at a larger scale than the laboratory environment within the KOLLORADO-e^3 project (see previous Chapter 1) or similar laboratory-scale approaches such as Neretnieks et al. (2017), Rinderknecht 2017, Alonso et al. (2019). Furthermore, i-BET focuses on bentonite loss rather than colloid formation and associated radionuclide migration. A higher bentonite density and thus higher swelling pressures were established in comparison with the LIT (Schlickenrieder et al. 2017). Within the scope of this study, changes in the hydro-chemical conditions and colloid load of extracted groundwater samples over 1,400 days were investigated to quantify erosion masses.

3.1 i-BET site

Previously used for silica sol and cement injection experiments and overcoring trails, i-BET was set up in the boreholes previously drilled in connection with the JAEA Grouting Project (JGP) and Long-term Cement Studies (LCS) (see Fig. 2-1). The site was selected as it was already well characterised within the framework of the former JGP experiment (Lanyon et al. 2018, Schneeberger et al. 2019a). In the context pf the LCS, a central borehole (JGP 11.003) was overcored to a diameter of 220 mm and a total depth of 11.5 meters (Schneeberger et al. 2019a). Due to the expansion of the diameter compared to CFM-LIT, a bentonite with greater density and higher effectiveness could be emplaced (Schlickenrieder et al. 2017, Lanyon et al. 2018). Surrounding the central borehole, three monitoring boreholes (CFM 18.001, 18.002, and 18.003) were drilled to achieve a hydraulically well-connected system (see Fig. 3-1) (Lanyon et al. 2018, Schneeberger et al. 2018). This additionally allowed the characterisation of the near-field hydraulic regime by monitoring hydraulic pressure in test intervals and groundwater sampling to detect bentonite loss (Schneeberger et al. 2019a). As previous studies had considered the influence of flow velocity on mass loss (e.g. Schatz et al. 2013, Schatz et al. 2015), the hydraulic flow field around the source could be enhanced by manually injecting water through the monitoring boreholes, thus making it possible characterise changes in flow paths and estimate flow velocity (Schneeberger et al. 2019a). Placed vertically below the bentonite source, CFM 18.002 can also be used to monitor bentonite mass loss due to gravimetric sedimentation. As tests in inclined synthetic laboratory-scale fractures have shown, mass loss from bentonite plugs can increase in subvertical fractures by sedimentation or gravitation. In addition(Schatz et al. 2015), CFM 18.001 and CFM 18.003 are located in close but horizontal proximity to JGP 11.003, making it possible to identify the extent of the gel front around the bentonite source.

Located in the central Aar granite, the system contains many natural fractures (Schneeberger et al. 2016). Described to "strongly vary along strike", faults intersecting JGP 11.003 have apertures of up to 5 mm and are partially filled with gouge material, which can lead to highly channelled flow paths within the system (Schneeberger et al. 2019a). Performed mainly within the scope of the JGP experiments, hydraulic tests showed connectivity between

JGP 11.003 and the far-field extraction borehole JGP 11.001, located 2000 mm south of the central borehole (Schneeberger et al. 2018). Due to the newly drilled boreholes, increased connectivity between the source and the monitoring boreholes was observed, and the dipole distance was reduced by 250 mm (Schneeberger et al. 2019a). During the experiment, eluates were periodically extracted from the CFM boreholes, applying different flow rates. Detailed hydraulic characterisations of the near-field, including the monitoring boreholes, are described in Schneeberger et al. (2018).

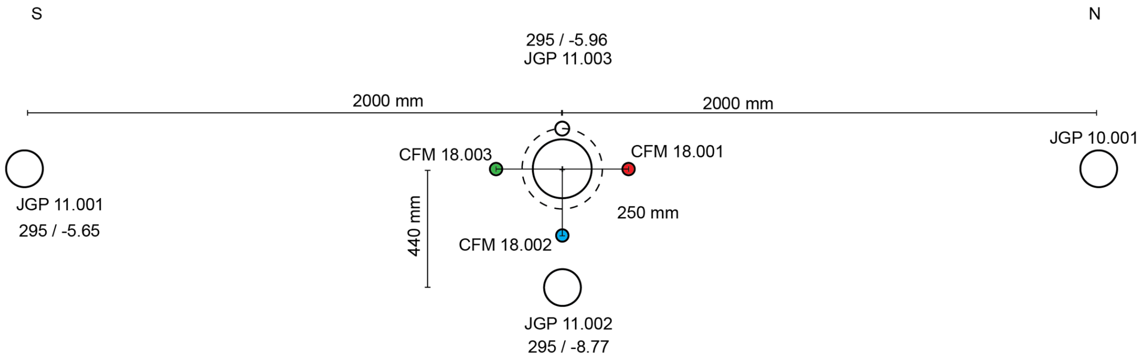

Fig. 3-1: Borehole layout of the i-BET project

Modified after Schneeberger et al. (2019a). Three extraction boreholes (CFM18.001, CFM18.002 & CFM18.003) were set up around a central bentonite source borehole (JGP 11.003). Additionally, the sketch shows three far-field extraction boreholes (JGP 10.001, JGP 11.001 & JGP 11.002) located beneath or towards the south and north, respectively. Note that the colour code of the three extraction boreholes will be maintained in the following.

Implemented in JGP 11.003, a double packer system was set up as bentonite source (see Fig. 3-2). The hydraulic packers have a total diameter of 194 mm, including an additional packer sleeve to avoid damage in connection with the faults observed alongside the borehole. The sealing length is 1,000 mm and the interval length between the packers is 1,942 mm. Emplaced around a steel mandrel and with an individual thickness of 150 mm, the bentonite source rings have a total length of 1,050 mm. Additionally, two resin lines were assembled for injection and backflow. Bentonite and testing interval positions were selected according to the locations of more extensive aperture fractures logged during the previous JGP (Lanyon et al. 2018, Schneeberger et al. 2019a).

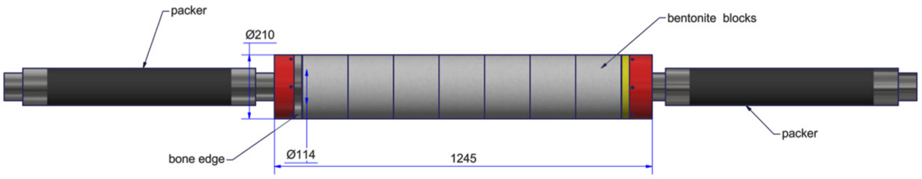

Fig. 3-2: Sketch of the double packer system implemented in the central borehole (JGP 11.003)

Image taken from Schneeberger et al. (2019a).

The implemented bentonite rings were made from Bara-Kade bentonite (MX-80 type), manufactured by Sorvikivi Oy and contracted by Posiva Oy (Schneeberger et al. 2019a). The material had an initial moisture saturation degree of 16.9 wt.% (reference Be-Wy-BT0018-1-Bl-R) and was highly compacted with a bulk density of 1.87 g/cm³, leaving a porosity of 0.39 (Schneeberger et al. 2019a). In total, seven cylindrical bentonite rings with an inner diameter of 114 mm, an outer diameter of 210 mm, and a total mass of 51.3 kg were installed within the segment (Schneeberger et al. 2019a). For the hydro-chemical characterisation of the i-BET setup, an on-site GeoMonitoring cabinet for pH and Eh, electrical conductivity, turbidity, and a bypass for extracting sample water were installed. Refer to Schneeberger et al. (2019a) for a more detailed characterisation of the i-BET site.

3.2 Experimental sectioning/splitting

With the description of the setup of the GTS in-situ experiment in Section 3.1, multiple sections were subdivided following significant system changes (see Fig. 3-3):

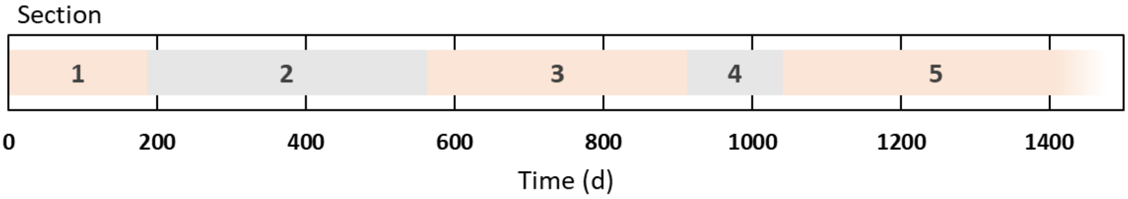

Fig. 3-3: Subdivision of i-BET sections. day 0 equals the day of i-BET setup implementation (14th December 2018)

Section 1 – Setup and initial phase

- Sequence: days 0 to 186
- Implementation of the bentonite source: 14th December 2018
- Manual sampling from the extraction boreholes (CFM18.001 to CFM18.003), starting 34 days after implementation

Section 2 – Autosampler

- Sequence: days 186 to 563
- Implementation of an autosampler system (GeoSwitch) with an applied extraction flow rate of 0.1 mL/min

Section 3 – Flow rate reduction

- Sequence: days 563 to 913
- Change to a lower extraction flow rate of 0.024 mL/min

Section 4 – Technical failure

- Sequence: days 913 to 1,041
- Implementation of a new pH probe (day 913)
- Technical failure of the autosampler led to multiple extraction stops with stagnant flow conditions between days 942 and 979 (see Fig. 3-4)

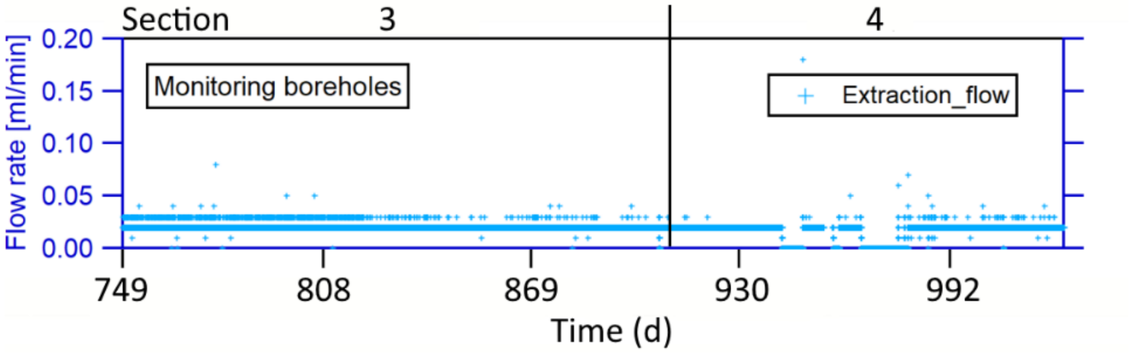

Fig. 3-4: Extraction flow rates of the i-BET system for parts of Phases 3 and 4

Modified from Rösli (2021)

Section 5 - Recirculation

- Sequence: days 1,041 to 1,419
- Remobilisation of settled sediments within monitoring boreholes
- Water recirculation with a constant flow rate of 5 mL/min within a closed-circuit system (total volume: 453 mL)
- Short-term increase of extraction flow rates between 5 and 20 mL/min and extraction volume of 300 mL per sample (see Fig. 3-5)

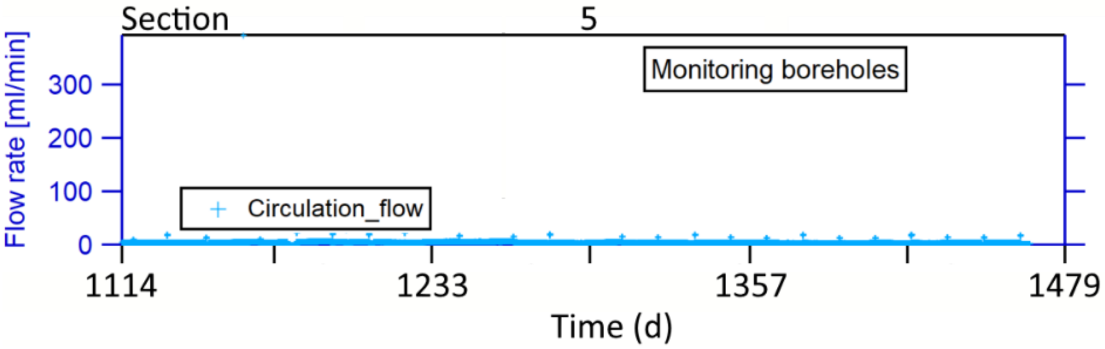

Fig. 3-5: Extraction flow rates of the i-BET system for parts of Phase 5

Modified from Gisinger (2022)

The Grimsel groundwater was sampled from the far-field JGP11.001 extraction borehole (see Fig. 3-1) for background measurements with varying flow rates over time (see Fig. 3-6).

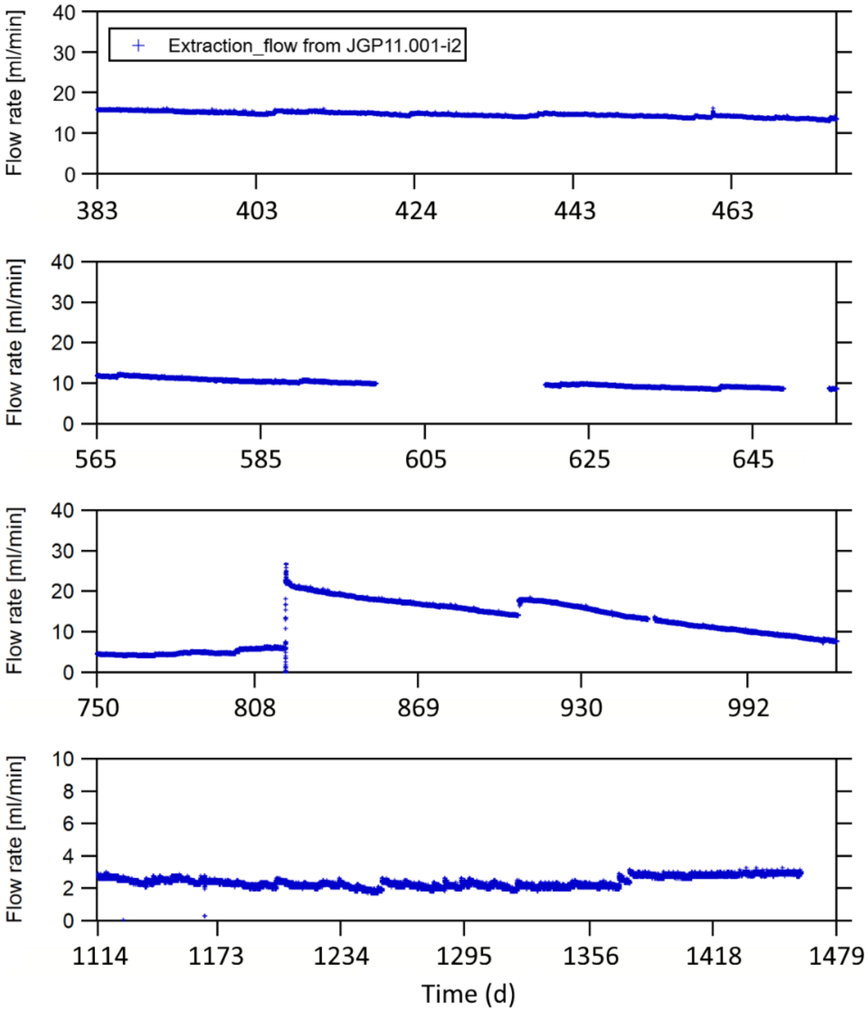

Fig. 3-6: Flow rates of the JGP11.001 far-field extraction borehole for different time intervals of the i-BET experiment

Modified from Rösli (2020); Rösli (2021); Gisinger (2022)

Note that the i-BET experiment is still running. Thus, the data presented in Chapter 3 solely represent the devolution of i-BET from Days 34 to 1,419.

Furthermore, the hydro-chemical analyses presented in this chapter were plotted as regular concentration graphs as only one kind of regular (natural) Grimsel groundwater flows through the system. This is in contrast to the laboratory-scale erosion experiments of Chapter, where different batches of GGW were used during the course of the experiments and C-C_0 plots were applied for better comparability.

3.3 Results

3.3.1 Hydro-chemical evolution

Initially, all extraction boreholes were measured with a similar EC of around 120 ± 5 µS/cm, which is higher than the background measured at JGP11.001 (86.0 ± 4.6 µS/cm). While measured EC values of the horizontally placed CFM18.001 and CFM18.003 extraction boreholes increased later (with respect to the central bentonite source borehole JGP11.003, see Fig. 3-1), EC values for CFM18.002 (sedimentation borehole) remained mostly consistent in Phase 1 (see Fig. 3-7). However, a pronounced increase was measured for all boreholes when implementing the autosampler to the system (start of Phase 2, day 186), with peak EC values of up to 604 µS/cm for CFM18.003 (day 214). After a short adjustment, mostly invariable EC values of around 120 ± 20 µS/cm (CFM18.002) and 270 ± 20 µS/cm (CFM18.001, CFM18.003) were measured for Phases 2 and 3. A significant increase, however, was measured for all boreholes within Phase 4, likely due to the failure of extraction flow and thus, an accumulation of ion concentration. Here, peak EC values of 1,083 µS/cm were measured for CFM18.002 after 997 days. After the reset of the autosampler (day 983) and the start of recirculation (Phase 5, day 1,041), EC significantly decreased and re-adjusted close to the previously measured values of around 145 ± 25 µS/cm. An overview of the hydro-chemistry of the natural GGW for i-BET, measured at the far-field extraction borehole JGP11.001, is listed in Section 2.1.1.3, Tab. 2-3.

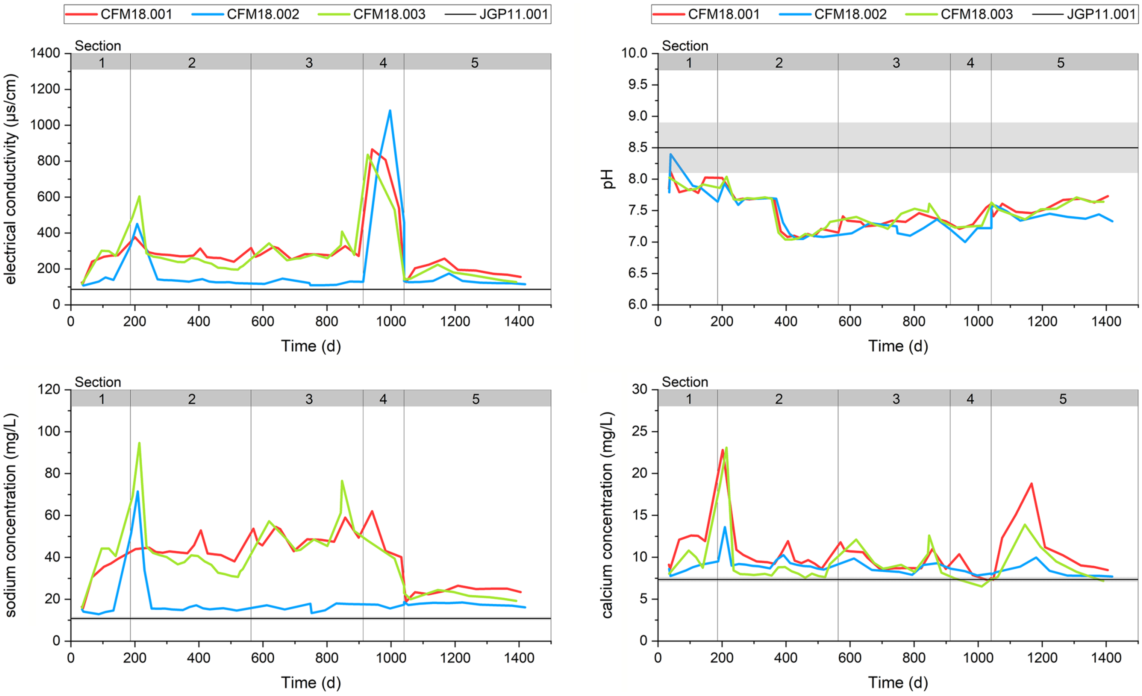

Fig. 3-7: Changes in electrical conductivity for the i-BET setup over time (upper left); time-dependent pH changes (upper right); [Na] concentration over time (lower left); and [Ca] concentration over time (lower right)

(JGP11.001 background: EC: 86.0 ± 4.6 µS/cm, pH: 8.5 ± 0.4, [Na] = 10.84 ± 0.84 mg/L, [Ca] = 7.35 ± 0.29 mg/L). The timeline on top separates the different phases defined in Section 3.2.

In contrast to the EC values, extracted samples initially showed higher pH values of around 8.0 ± 0.2 for all extraction boreholes, slightly decreasing towards pH 7.7 ± 0.1 over time. However, a sudden decline was observed after 369 days, with values reaching approx. pH 7 for all boreholes.

With respect to the sodium concentration, similarly low initial values of 15.9 ± 0.7 mg/L were measured for all extraction boreholes, which is slightly above the GGW background concentration of 10.84 ± 0.84 mg/L. Afterwards, the Na concentrations of the horizontally placed CFM18.001 and CFM18.003 boreholes continuously increased, while CFM18.002 did not indicate a different connectivity to the central borehole. A notable increase of Na concentrations was measured for CFM18.001 and CFM18.003 after the change in extraction flow rate (day 563). The extraction borehole CFM18.002 did not follow the trend, showing generally low Na concentrations of around 15 ± 2 mg/L. While no changes could be correlated to the extraction failure of Phase 4, the start of recirculation (Phase 5) decreased the Na concentrations measured for CFM18.001 and CFM18.003 until they closely resembled that of CFM18.002 (approx. 20 ± 5 mg/L). As for Na, the Ca concentrations show an initial increase for the horizontally placed extraction boreholes, while CFM18.002 was measured with a stable Ca concentration of approx. 9 mg/L within Phase 1. Switching to the autosampler system, pronounced concentration peaks were measured for all extraction boreholes at the beginning of Phase 2 (up to 23.08 ± 0.05 mg/L, CFM18.008, day 214), likely due to a system disturbance by the implementation process and thus an accumulation of loose material within the extracted samples. For the ongoing experiment, however, no major changes were indicated in Phases 2 to 4. Ca concentrations mainly ranged around 10 ± 2 mg/L. However, a significant increase was measured for CFM18.001 and CFM18.003 during Phase 5. The measured Ca concentration peaks in Phases 2 and 5 are more pronounced for CFM18.001 and CFM18.003, indicating a positional or gravitational influence.

In the case of potassium, initial K-concentration values were measured within close proximity of the natural GGW (0.3 ± 0.1 mg/L), followed by an increase during Phase 1 for all samples (see Fig. 3-8). However, at the transition to Phase 2 and shortly after an adjustment, low but continuously stable K-concentration values of around 3 ± 1 mg/L were measured for all extraction boreholes until the end of Phase 3. note that a minor but still visible increase can be seen after the reduction of the extraction flow rate after 563 days (at the beginning of Phase 3). Likely induced by a valve failure paired with stagnant flow conditions, leaching electrolyte solution (3M KCl) led to a significant concentration increase in Phase 4, peaking at up to 275 ± 1 mg/L for CFM18.002 and approx. 180 ± 20 mg/L for CFM18.001 and CFM18.003, respectively. Similar observations were made for chloride (not shown here).

However, as the extraction was restarted on day 983, pre-failure K-concentration values were measured towards the end of Phase 4. With the start of recirculation (Phase 5), increased K concentrations of around 7.2 ± 5.0 mg/L were measured.

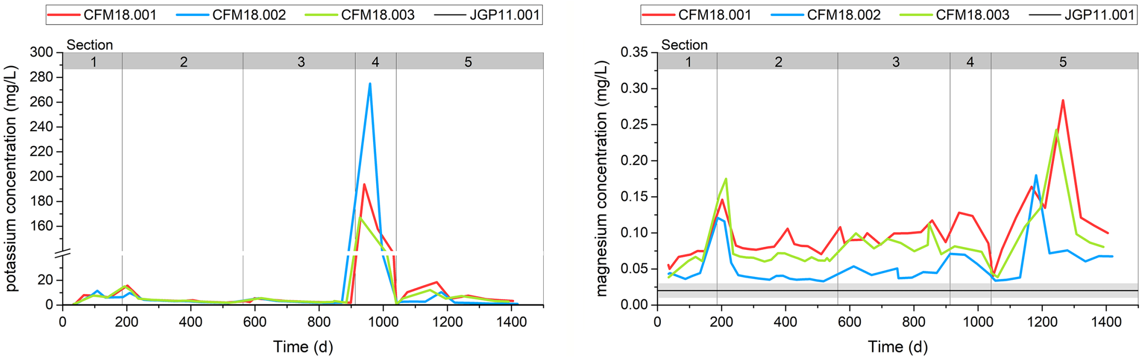

Fig. 3-8: Potassium concentration (left) and Magnesium concentration (right) for all extraction boreholes of the i-BET setup over time. Note the break in the concentration axis due to a significant peak in Phase 4

(JGP11.001 background: [K] = 0.3 ± 0.1 mg/L [Mg] = 0.02 ± 0.01 mg/L)

In the case of magnesium, Mg concentration values were measured to be slightly higher than the GGW background but remained low overall. higher values were measured in the horizontal boreholes, especially in connection with Ca concentrations. Interestingly, after the artificial potassium pulse, higher Ca and Mg concentrations were detected, indicating an induced cation exchange process.

With respect to the silicon concentrations measurements, no major variances were observed between the extraction boreholes. Values were mostly around 10 ± 2 mg/L (see Fig. 3-9), which is nearly double the value of the natural GGW flowing through the i-BET setup (4.92 ± 0.46 mg/L). Correlating with the implementation of the autosampler system, a distinct peak of concentrations up to 25.73 ± 0.04 mg/L (CFM18.001, day 202) was measured for the horizontally placed boreholes. Aside from this peak, a slightly increasing trend was observed for all boreholes within Phases 1 and 2, followed by a continuous decrease. Interestingly, overall Si-concentration values resembled those measured at the JGP10.001 far-field extraction borehole (11.46 ± 0.75 mg/L), which was previously disturbed by silica sol and cement injection experiments (see Section 3.1 for comparison).

As for silicon, no major differences were observed for aluminium concentrations with respect to the different extraction boreholes (see Fig. 3-9). Overall, continuously low Al concentrations between 0.01 and 0.03 mg/L were measured, which is close to the natural GGW (0.011 ± 0.001 mg/L). However, sharp Al-concentration peaks of up to 0.061 ± 0.001 mg/L were measured for CFM18.002 and CFM18.003 at the transition to Phase 2 and during the extraction failure (Phase 4).

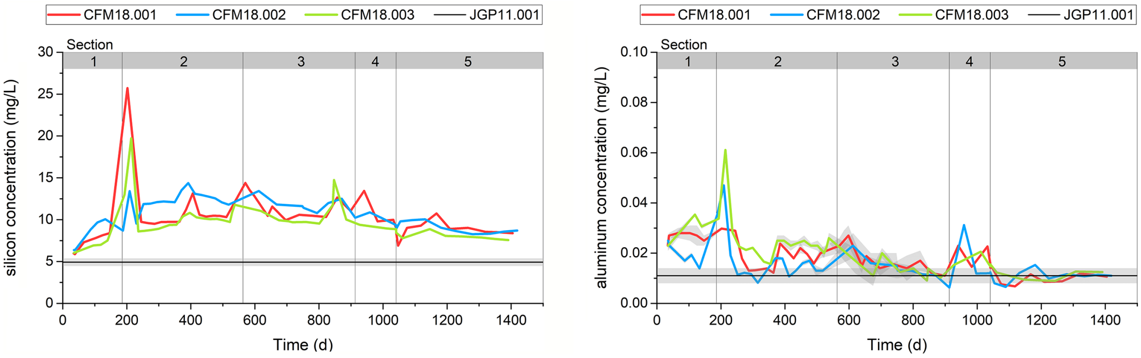

Fig. 3-9: Si concentrations (left) and Al concentrations (right) for all extraction boreholes of the i-BET setup over time

(JGP11.001 background: [Si] = 4.92 ± 0.46 mg/L; [Al] = 0.011 ± 0.003 mg/L)

With a similar initial sulphate concentration of around 20 mg/L, the individual extraction boreholes also showed a similar evolution for EC and Na. Overall, higher sulphate concentrations were measured for CFM18.001 and CFM18.003 during Phases 1 to 4 (approx. 73.8 ± 19.0 mg/L), compared to CFM18.002 (approx. 12.9 ± 2.6 mg/L), presumably due to its proximity to the GGW (9.41 ± 1.93 mg/L). While distinct sulphate concentration peaks were measured during the implementation of the autosampler for CFM18.002 and CFM18.003, CFM18.001 and CFM18.003 also showed a significant decrease in sulphate concentration after the recirculation, likely due to a higher dilution with GGW.

While CFM18.001 and CFM18.003 were measured with increasing sulphate concentrations during Phase 1, CFM18.002 only peaked during the implementation of the autosampler. Distinct sulphate concentration peaks were measured for CFM18.002 (116.6 ± 0.1 mg/L, day 207) and CFM18.003 (163 ± 2 mg/L, day 214) at the beginning of phase 2, but not for CFM18.003, which in turn showed a small decrease. Also similar to the Naconcentration and the EC, CFM18.002 was measured with SO_4^{2-} concentrations when in close proximity to the natural GGW (9.41 ± 1.93 mg/L).

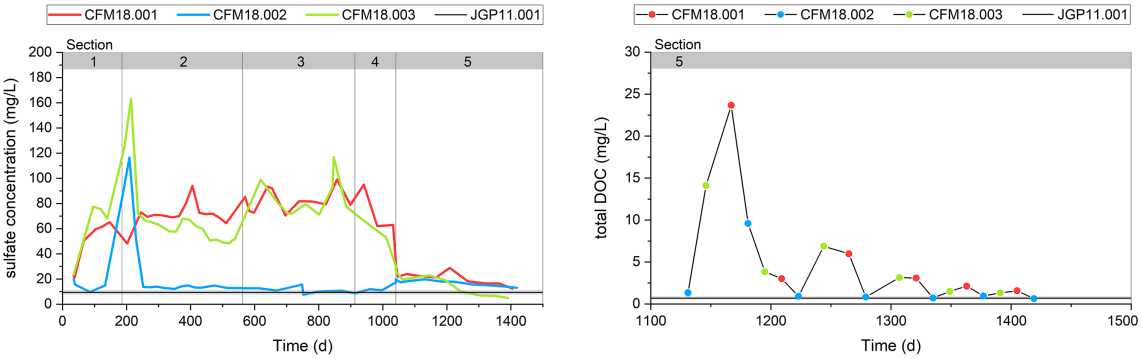

Fig. 3-10: Sulphate concentration (left) and total dissolved organic carbon (right) for all extraction boreholes of the i-BET setup over time

(JGP11.001 background: sulphate = 9.41 ± 1.93 mg/L, DOC for samples 103 to 123 (days 1,131 to 1,419) = 0.7 ± 0.2 mg/L)

Concerning the extraction failure between Days 913 and 983 (Phase 4), an accumulation of greyish-greenish sediments was observed within the turbidity cell and manually extracted sample water. As this indicates microbiological activity, DOC measurements were conducted for the GGW and multiple extracted samples. an overall low DOC concentration was measured for the GGW with approx. 0.7 ± 0.2 mg/L. However, while a slightly increased DOC value of 5.0 mg/L was measured for CFM18.002 after 829 days (just before the extraction failure), significantly increased DOC concentrations were measured during the extraction failure, peaking at up to 216.8 mg/L for CFM18.002 after 959 days.

Furthermore, DOC was also measured for samples of Phase 5, as the recirculation aimed to (re-)mobilise particles within the system. While a low initial DOC concentration of around 1.3 mg/L was measured coming out of Phase 4 (CFM18.002, day 1,131), the increased flow rates during Phase 5 (5 to 18 mL/min) also shortly increased the total DOC, peaking at up to 23.6 mg/L for CFM18.001 (day 1,167). Afterwards, a gradual decrease of the DOC concentration was measured. However, increased flow rates of up to 20 mL/min were applied, which corresponds with the measured particle concentrations.

3.3.2 Colloid characterisation and mass erosion

In addition to the hydro-chemical characterisation of the i-BET samples, particle characterisation (hydrodynamic diameter and particle concentration) was conducted, with a subsequent calculation approach of the eroded mass, performed by applying the NTA method (see Section 2.1.4).

Concerning the median hydrodynamic particle diameter, overall, no major variances were measured for the extraction boreholes over time within the GGW background of 134 ± 18 nm (see Fig. 3-11). Slight changes can be seen during the transitions of Phases 2 – 3 and 4 – 5, where system changes likely initiated minor remobilisation of sedimented particles. Illustrated in Fig. 3-12, a slight narrowing of the measured hydrodynamic size distribution was measured shortly before (d = 857 days) and during the failure of extraction flow (d = 983 days) (Phase 4). Concerning the more undisturbed Phases 2 and 3, an overall decreasing trend for the measured average hydrodynamic diameter is indicated. With respect to the individual boreholes over time, though, CFM18.001 was measured with an overall average of 121 ± 16 nm, CFM18.002 with 126 ± 18 nm and CFM18.003 with 127 ± 14 nm, indicating no major influence of gravity or the positioning on the hydrodynamic diameter of released colloids.

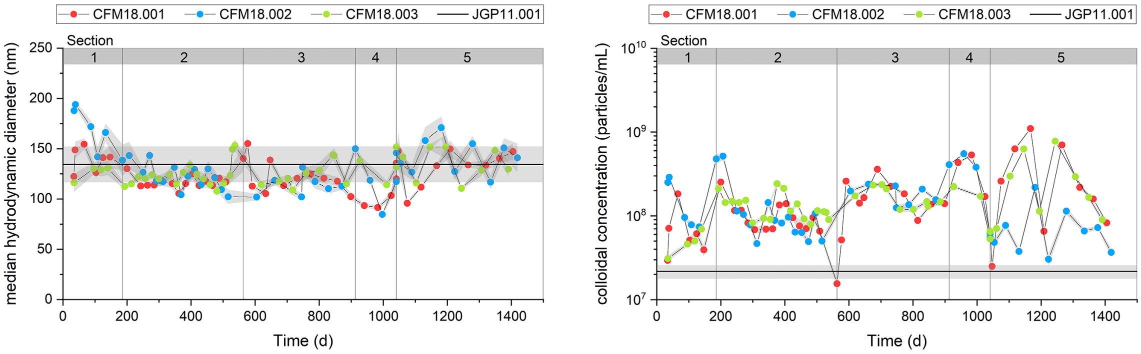

Fig. 3-11: Median hydrodynamic particle diameter (left) and measured colloidal concentrations per mL (right) for the three CFM extraction boreholes over time, including the natural GGW background. The timeline on top separates the different phases defined in Section 3.2 (JGP11.001 background: d_{mean} = 134 ± 18 nm; 2.2 ± 0.4E+07 particles/mL)

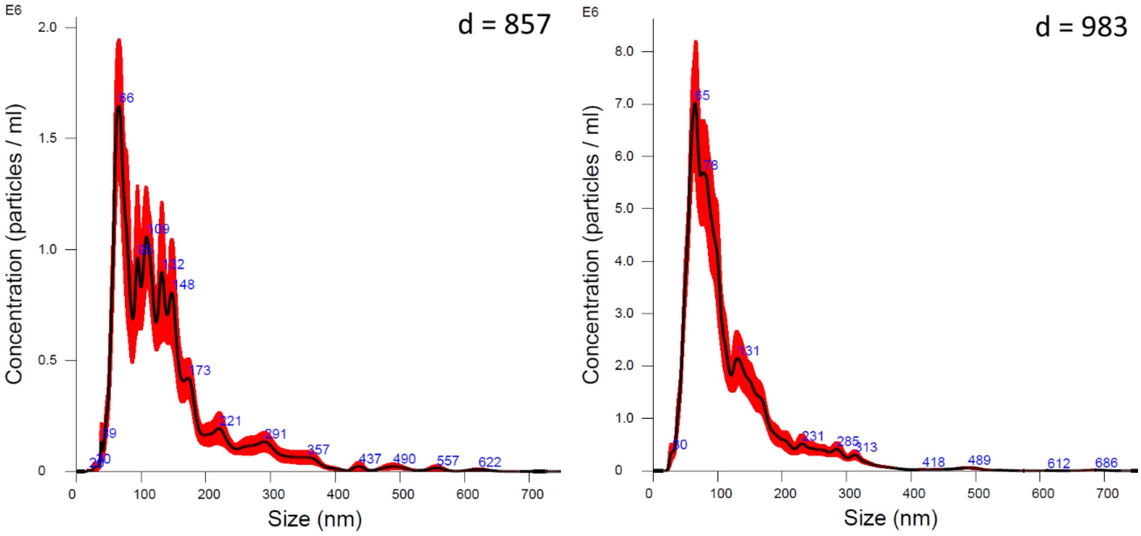

Fig. 3-12: Average FTLA concentration – size plots of the CFM18.001 extraction borehole shortly before (day 857) and during the failure of extraction flow (day 983)

More pronounced changes were observed for the particle concentrations measured (see Fig. 3-11). While the CFM18.002 extraction borehole was measured with an initial peak concentration of 2.5 ± 0.2E+08 particles/mL, the laterally placed extraction boreholes (CFM18.001, CFM18.003) were measured to have a concentration that was around one order of magnitude below that of CFM18.002 (approx. 3.0E+07 particles/mL). Towards the end of Phase 1, values from all three boreholes converged to approx. 8.1 ± 4.5E+07 particles/mL. Likely due to the implementation of the autosampler, a brief but pronounced increase can be seen at the beginning of Phase 2, with particle concentrations of up to 5.2 ± 0.6E+08 particles/mL (CFM18.002, day 207). Afterwards, particle concentrations adjusted to similar values as observed in later stages of Phase 1 (approx. 1.2 ± 0.8E+08 particles/mL). However, with the changing extraction flow rate (start Phase 3), CFM18.003 measurements revealed a brief reduction of its particle concentration. With the start of Phase 3, particle concentrations slightly increased with similar values measured for all extraction boreholes (approx. 1.8 ± 0.6E+08 particles/mL). Due to the extraction failure and thus an accumulation of particles in Phase 4, increased particle concentrations were measured for CFM18.001 and CFM18.002, peaking at 5.5 ± 0.2E+08 particles/mL (CFM18.002, day 959), followed by a pronounced concentration decrease after the reboot of the system. With the start of recirculation in Phase 5, particle concentration values increased, especially for laterally placed extraction boreholes, peaking at up to 6.3 ± 0.2E+08 particles/mL for CFM18.003 (day 1,146). Towards the end, particle concentrations decreased towards low values of approx. 1.0 ± 0.5E+08 particles/mL, which is still above the measured background value of 2.2 ± 0.4E+08 particles/mL. With respect to the individual boreholes, similar average particle concentration values were measured: CFM18.001: 1.8 ± 2.1E+08 particles/mL, CFM18.002 particles/mL: 1.5 ± 1.4E+08 and CFM18.003: 1.6 ± 1.4E+08 particles/mL. Note that the data for the colloidal particle concentrations and the calculated colloidal masses shown in Fig. 3-11 and Fig. 3-13 were not rectified with respect to background level of the GGW but are shown as the actually measured/calculated values due to the known concentrations in the GGW of the setup (see Tab. 2-3).

Based on the particle concentration, approximated erosion masses for all extraction boreholes (see Fig. 3-13) were calculated. higher erosion masses were calculated for CFM18.002 at the very beginning (4.26 ± 0.63 µg/mL, day 35), correlating with the higher particle sizes and concentrations measured. in comparison, CFM18.001 and CFM18.003 were calculated to be

0.15 ± 0.06 µg/mL (day 34) and 0.2 ± 0.1 µg/mL (day 35), respectively, which is close to the values of the GGW (0.16 ± 0.04 µg/mL). The consecutive erosion masses calculated for each borehole approached similar values during Phases 2, 3, and 4. No pronounced increase was observed during the implementation of the autosampler (transition from Phase 1 to 2). However, a rather continuous decreasing trend was detected until the end of Phase 2, with values approaching those of the natural GGW (approx. 0.45 ± 0.25 µg/mL). Likely due to the change in extraction flow (0.1 to 0.024 mL/min), a distinct increase of calculated erosion masses for the transition of Phases 2 and 3 with an average erosion rate of around 2.0 ± 1.5 µg/mL was observed. Further correlating with the variable particle concentrations measured for Phases 4 and 5, similar increasing and decreasing trends were calculated, peaking at up to 15.2 ± 4.8 µg/mL for CFM18.001 (day 1,167). While mass concentration was higher due to the extraction failure in Phase 4 (up to 8.3 ± 2.8 µg/mL, day 913), CFM18.002 was also calculated with an overall lower mass concentration during Phase 5. Towards the end, erosion masses progressively adjusted towards lower concentrations of around 1.0 ± 0.5 µg/mL for all extraction boreholes.

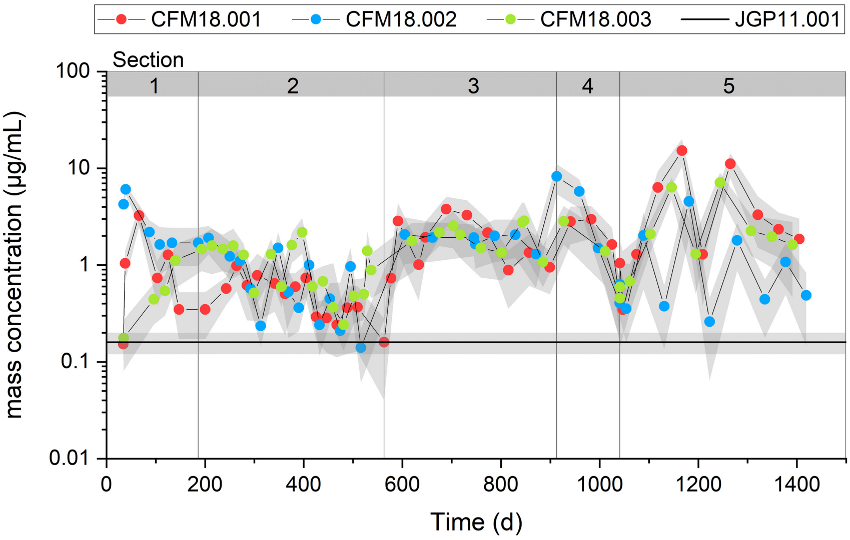

Fig. 3-13: Calculated erosion masses per mL for all three CFM extraction boreholes samples, including the GGW background (JGP11.001) of around 0.16 ± 0.04 µg/mL

3.3.3 Upscaling approach on erosion masses and barrier integrity

After characterising the particle-size distribution, concentration, and a subsequent estimation of the erosion masses of all extracted samples, the following chapter extrapolates the data for an approximation of material loss over time concerning the implemented i-BET setup. Thereby, multiple steps are presented to archive a collective approximation model on the erosion rates under consideration of both the natural and implemented system environment.

3.3.3.1 Linear interpolation considering applied extraction flow rates

In a first step, calculated erosion masses of Fig. 3-13 were summed up as cumulative masses for each extraction borehole over time, taking into account the applied extraction flow rates (see Section 3.2 for comparison). Fig. 3-14 illustrates distinct changes in particle releases concerning the defined phases. Thereby, an early adjustment phase (Phase 1) is characterised by a comparably high erosion mass of 81.3 ± 23.0 mg/a (linear interpolation). After implementation of the autosampler system (Phase 2), the erosion rate gradually decreases (by around 41.4 ± 19.1 mg/a on average) and the system stabilises in Phase 3 with overall erosion rates of around 19.3 ± 8.8 mg/a. As no extraction was applied during Phase 4 due to a technical failure, cumulative masses stagnated between days 942 and 979. Afterwards, due to the applied recirculation of extracted water, erosion masses shortly increased to around 55.6 ± 21.5 mg/a during Phase 5. However, similar to Phase 3, erosion masses stabilised at a rate of around17.2 ± 9.3 mg/a afterwards as the system adjusted to the new flow conditions of the applied recirculation.

Note that as the cumulative masses were calculated by considering the applied extraction flow rates, they do not represent the total groundwater flow rates that the i-BET setup is exposed to.

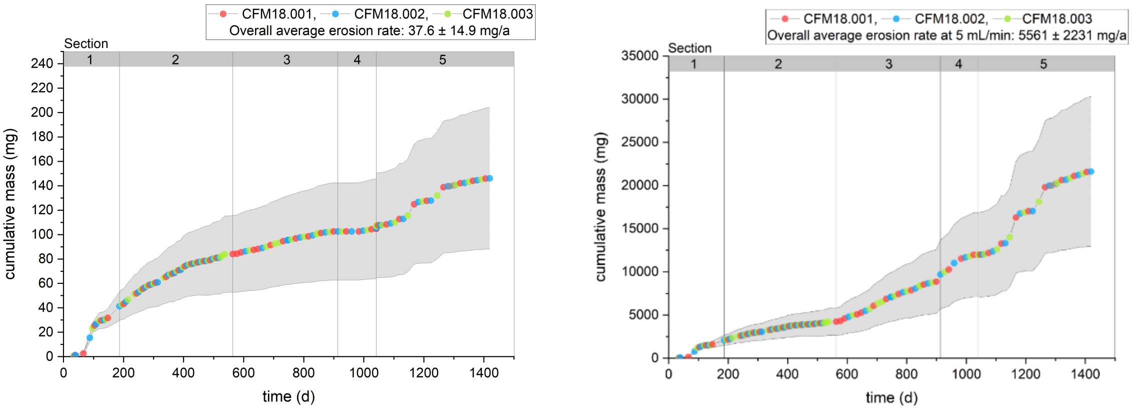

Fig. 3-14: Combined cumulative masses of CFM18.001, CFM18.002, and CFM18.003 based on the extraction flow rates applied (left) and combined cumulative mass for all extraction boreholes (right), including the natural GGW background using an estimated system flow rate of 5 mL/min

3.3.3.2 Extrapolation with estimated system flow rates

In order to extrapolate the approximation model to a more realistic and holistic system approach, cumulative erosion masses were calculated under consideration of the estimated total system flow rates of either 2, 3 or 5 mL/min, which are described to be expected within the setup (e.g. Schneeberger et al. 2018). This was done to better contemplate the i-BET setup within the natural fracture system instead of artificially applied extraction flow rates. While the influence of the individual system changes (e.g. change of extraction flow rate between Phases 2 and 3, or failure of extraction flow in Phase 4) could be observed, cumulative masses were seemingly higher due to the higher total system flow rates considered.

While erosion rates are mostly linear during the undisturbed Phases 2 and 3, Phase 2 was calculated with a significantly lower average erosion rate (2092 ± 971 mg/a, in the case of 3 mL/min) in comparison to Phase 3 (5699 ± 2504 mg/a). This is likely due to dilution effects caused by the reduction of the extraction flow rate between Phases 2 (0.1 mL/min) and 3 (0.024 mL/min). Furthermore, Phase 4 shows a significantly increased erosion rate compared to the previous phases, likely induced by system disturbances due to the implementation of a pH probe and the extraction failure between days 942 and 979 (material accumulation). An adjustment after the reboot of the system towards the end of Phase 4 (see Fig 3.14 for comparison) was observed. With respect to the recirculation of Phase 5, high erosion rates of around 7,000 mg/a were calculated for the initial phase of the recirculation, with an estimated flow rate of 5 mL/min and considering enhanced short-term recirculation flow rates of up to 20 mL/min. Thereby, distinct increases were observed for the CFM18.001 extraction borehole, correlating with a short-term extraction failure after around 1,150 days and adjustments to the hydraulic lines after around 1,250 days. In the long run, the system adjusts to mostly invariant erosion rates of 4,291 ± 2,331 mg/a, despite continuous recirculation with increased flow rates.

Considering the different total system flow rates, average erosion rates can be approximated with:

- 2 mL/min = 2,224 ± 893 mg/a
- 3 mL/min = 3,337 ± 1,339 mg/a
- 5 mL/min = 5,561 ± 2,231 mg/a

However, as the maximum measured particle concentrations were considered and thus the calculated colloidal masses included the masses introduced by the natural GGW, the data had to be reassessed with respect to the GGW background. As a result, the upscaled natural background concentration of the GGW could be calculated as follows:

- 2 mL/min = 168.2 ± 42.1 mg/a
- 3 mL/min = 252.3 ± 63.1 mg/a
- 5 mL/min = 420.5 ± 105.1 mg/a

Thus, the reassessed average erosion rates could be approximated with:

- 2 mL/min = 2,056 ± 851 mg/a
- 3 mL/min = 3,084 ± 1,276 mg/a
- 5 mL/min = 5,141 ± 2,126 mg/a

3.3.3.3 Upscaling under consideration of the interface area

In a last step, the interface area was implemented in the approximation model to estimate the mass loss over time with respect to the contact area (m²) of the bentonite or gel (see Fig. 3-15). the calculated erosion rates were integrated with respect to the interface area of the initially implemented bentonite source blocks and the aperture distribution of the intersecting fracture network, or the approximated gel/water interface within the open fracture system. to archive this, all relevant fractures intersecting the i-BET setup were considered. As reported in Schneeberger et al. (2016), various faults with apertures of up to 5 mm were revealed by TVlogging[5] of JGP11.003. Excluding hairline fractures with aperture widths (<0.5 mm), a total of eight fractures intersecting the source rings with a combined aperture width of 16 mm were identified. Based on this, a total interface area of the bentonite source rings (r = 105 mm) and the open fractures with 10,555.8 mm² or 0.01056 m² was calculated. Assuming an average gel swelling distance of 30 mm and therefore contact diameter increase, the contact area would be 13,571.7 mm² or 0.01357 m². The radial swelling extension of 30 mm is based on laboratory-scale erosion experiments (see e.g. , r = 36 mm), and observations described in Rinderknecht (2017), Alonso et al. (2019) (average gel swelling of 15 to 20 mm in-fracture apertures of 1 to 2 mm) and the free swelling ability of raw MX-80 bentonite of around 45 mm as reported by Neretnieks et al. (2009).

---

[5] Note that detailed information of the TV-logging has not been published yet, but was made available for this study by personal communication.

Tab. 3-1 shows the estimated average erosion rates as a function of system flow rates and interface areas and additionally in relation to the total mass of the implemented bentonite source (51.3 kg).

Tab. 3-1: Estimated average erosion rates with respect to the initial source-ring-/ or gel-layer-fracture interface area over time (vertical time lines 1-3, Fig. 3-14) and total erosion time in relation to the total mass of the implemented bentonite MX-80 bentonite source (51.3 kg) and the approximated bentonite/gel and gel/water interface area (vertical time line 4-6, Fig. 3-14)

Line #:	**Estimated system flow rate**	**Bentonite ring / fracture plane interface** [kg/m²/a]	**Gel layer / fracture plane interface** [kg/m²/a]
1	2 mL/min	0.19 ± 0.07	0.15 ± 0.06
2	3 mL/min	0.30 ± 0.12	0.23 ± 0.09
3	5 mL/min	0.49 ± 0.19	0.38 ± 0.15
4	2 mL/min	263.5 ± 109.1	338.6 ± 140.2
5	3 mL/min	175.6 ± 72.6	225.7 ± 93.4
6	5 mL/min	105.4 ± 43.6	135.4 ± 56.0

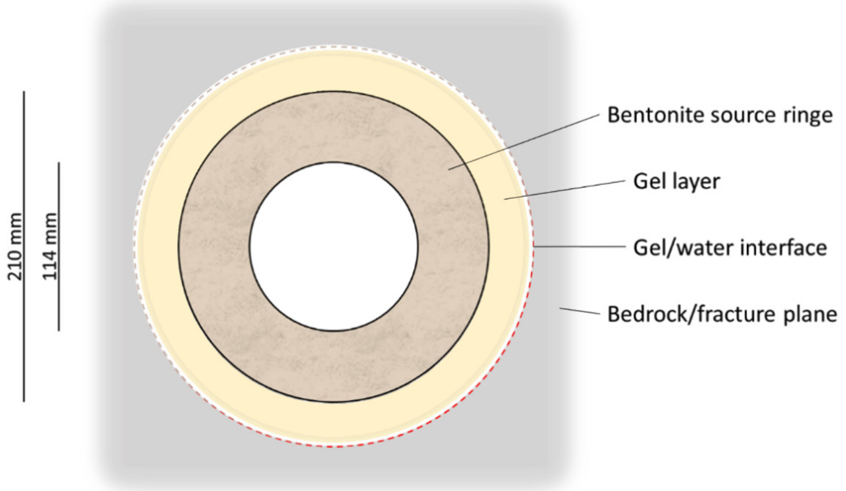

Fig. 3-15: Scheme illustrating the interface area of the implemented bentonite source ring and the approximated gel layer extension of around 30 mm into a fracture plane[6]

---

[6] Note, that the approximated values for the correction (kg/m²/a) include the reassessment with respect to the natural GGW background concentration.

3.4 Discussion

3.4.1 Hydro-chemical evolution

Major differences can be seen with respect to measured ion-concentrations (e.g. Na, Ca, Mg, SO_4, see Section 3.3.1) and the ECs between the laterally placed CFM18.001 and CFM18.003 and the CFM18.002 extraction borehole placed underneath, which was measured with overall lower values of around 100 to 150 µS/cm (see Fig. 3-7). While small-scale variances of hydraulic conductivity have already been reported by Schneeberger et al. (2019b), tracer tests conducted by Schneeberger et al. (2018) found the dipole between CFM18.002 and JGP 11.003 to be well connected. Our results, however, indicate poor hydraulic conductivity between the bentonite source and CFM.18.002, which could explain the constantly lower ion-concentrations measured (e.g. Na, SO4) in Phases 2 and 3 of CFM18.002. Concerning K, peak values of nearly three orders of magnitude above the GGW background were likely caused by a malfunction of the bypass valve, switching between the GeoMonitoring cabinet and the sample extraction. Thus, eluates likely came into contact with the implemented pH probes (Hamilton Polilyte Plus), which can release both KCl electrolytes and organics (glycerol). The latter would also explain the increased DOC concentrations measured in Phase 4.

With respect to other (trace) elements measured, a sudden increase in concentration was observed for Ba, B, Cu, Zn and Lu after recirculation (Phases 5 and 6). As these increases correlate with the increased flow rates applied, concentrations can likely be related to a direct release from the bentonite source. This is supported by (Bouby et al. 2020), who reported minor fractions of BaO, B_2O_3, ZnO or La_2O_3 to be components of the raw MX-80 bentonite. Furthermore, Cu(II)-trien investigations of the raw MX-80 (see Section 2.2.1.4) also confirmed a barium concentration of around 0.02 wt.% within the material, making this a possible scenario.

Concerning the overall surplus silicon of 10 ± 2 mg/L (see Fig. 3-9) with respect to the GGW background (4.92 ± 0.46 mg/L), measured Siconcentrations did not comprehensively represent the course of measured colloidal concentrations. As the eluates were filtered with 0.45 µm cellulose-acetate filters during sample preparation, a quantitative backwards calculation of erosion masses with respect to the structural formula of montmorillonite (see Section 2.1.1 for comparison) was not possible. However, especially with respect to the multi-mineral composition of the implemented MX-80 bentonite, a release of non-clay colloids such as accessory quartz must be considered.

When correlating the concentration of Ca and/or Ba with respect to fluoride, the precipitation of CaF_2 and/or BaF_2 as secondary phase minerals has already been reported for the GTS (Seher et al. 2020). Thereby, fluoride acts as a conservative tracer, as it is only present within the GGW and there is no F^- sorption onto the clay minerals. However, no major variances were observed for the fluoride concentration, which was primarily measured within proximity of the GGW (4.07 ± 0.47 mg/L), except for a peak correlating with the implementation of the autosampler.

While sampling and analysis procedures were conducted continuously during the nearly four years of the i-BET[7], the operational commitments of varying operators may have led to systematic errors with respect to sampling and analysis techniques. For instance, no HCO_3^- measurements were conducted within the first year or 38 samples, respectively, leading to high errors (>5%) in ion balances for the respective samples. Furthermore, due to the high natural pH of the GGW (8.5) and changes in contact with atmospheric CO_2, pH values were no proper tools for indicating major system changes, especially with respect to particle erosion. Hence, pH values significantly depended on sample storage and measurement routines; a sudden decrease of pH at day 369 was likely induced by a changing operator and/or sample storage procedure.

---

[7] Note that the iBET experiment was still running after the last sample considered for this study.

3.4.2 Particle characterisation and erosion quantification

While variations in element concentrations were observed for system changes (see Section 3.2 for comparison), distinct changes were also observed regarding the measured particle concentrations, whereas the median hydrodynamic diameter mostly kept constant (see Fig. 3-11). Thereby, slightly larger distributions were observed for CFM18.002 in the initial phase of the experiment, likely due to an adjustment of the system. The extraction failure of Phase 4 enabled an accumulation of particles in the system leading to higher particle concentrations and overall smaller size distributions were measured. Due to the increased flow rates applied during the recirculation in Phase 5, an initial decrease of particle size, with a simultaneous increase in particle concentration, was observed. Thus, a (re)mobilisation of sedimented particles of smaller size ranges is indicated. Differences in the measured particle concentrations may also be influenced by the different applied extraction flow rates due to a higher or respectively lower sample dilution or advective energy. Thereby, short-term variations of both the particle size distribution and concentration were induced by the changed extraction flow rate after day 563 and were more pronounced for the horizontally placed CFM18.001 and CFM18.003 extraction boreholes.

Considering the higher flow rates of the background extraction borehole (JGP11.001) compared to the monitoring boreholes (CFM18.001 to CFM18.003), an impact on the measured background concentrations cannot be ruled out. While JGP11.001 was set off with around 20 – 25 mL/min, extraction was conducted with successively lower flow rates of down to approx. 5 mL/min over time (see Fig. 3-6) due to technical reasons.

While the calculated cumulative masses showed some differences for the differently positioned extraction boreholes (see Fig. 3-13), the overall erosion concentration approximated for the CFM18.002 extraction borehole placd underneath was only slightly smaller (approx. 1.5 ± 0.6 μg/mL) in comparison to the laterally placed CFM18.001 (approx. 2.0 ± 1.0 μg/mL) and CFM18.003 (approx. 1.7 ± 0.4 μg/mL) extraction boreholes, thus not clearly indicating a potential gravitational or positional influence. Furthermore, individual extraction boreholes seemed similarly affected by system changes such as the implementation of the autosampler (transition of Phases 1 to 2) or the failure of extraction flow (Phase 4) indicated by similar trends for the measured particle concentrations. Continuous logging, however, was very valuable to identify disturbances such as the short-term extraction failure after approx. 1,150 days and the adjustments to the hydraulic lines (installation of a fluorometer and GeoNode to monitor the boreholes) after around 1,250 days. These changes are clearly visible within the cumulative NTA data (see Fig. 3-14) and especially pronounced for the CFM18.001 and CFM18.003 boreholes.

Neretnieks et al. (2017) described the material loss or erosion to be up to 2 to 3 times higher for sloped fractures compared to horizontal fractures, even when considering expected highest water velocities. Furthermore, loss could even occur without water flowing or seeping in vertical fractures if clogging was prevented by continuous removal of eroded material. As further stated by Neretnieks et al. (2017), erosion rates depend on the water velocity, aperture width of the fracture, the radius of extension of the swollen gel layer, and eventually, the ion-concentration of the contact water. However, for fractures with a narrow aperture width (0.1 mm), gravity-induced agglomeration during migration (residence-time-dependent) could reasonably limit the material loss, as such flocs could fill substantial volumes of the rock or fracture network, respectively Neretnieks et al. (2017), Neretnieks et al. (2017) pointed out that this was important, as Ca-dominated clays form strong aggregates which seem to attain reposing slopes of approximately 45° (friction angle). This is further supported by the latest findings of Posiva[8], where sub-horizontal faults were found to have minor influence on erosion for small fracture apertures.

---

[8] DilBi II project, results not published yet. Information gained by personal communication. (https://igdtp.eu/)

A study of Alonso et al. (2019) describes the particle mobilisation (in the case of artificial fracture cells) under water-flow conditions with low velocities to be as low as <0.02% of the initially implemented clay fraction. Furthermore, erosion by sedimentation was investigated under stagnant conditions and found that sedimentation was not observed along fracture slopes, when fracture apertures were <0.4 mm. According to performance assessment studies of Posiva OY & SKB (2017), erosion rates were estimated to range between 500 and 1,500 kg/m²/a mass loss from laboratory synthetic fracture experiments in low saline water, which translates to upscaled erosion rates of a few kg/m²/a (Smith et al. 2017). These are only slightly higher erosion rates than the approximated erosion rates of our extrapolation approach (see Tab. 3-1). Furthermore, Neretnieks et al. (2017) described erosion rates of around 0.2 to 0.6 kg/a for their model, which is close to our approximated values but neglects the interface area and is calculated for a smaller aperture width of 0.1 mm, while we consider only fractures with an aperture width of >0.5 mm. Executed in artificial fracture cells (here with filter frits instead of an open fracture), Bouby et al. (2020) described that erosion via low mineralised groundwater flow was found to range between 0.01 and 0.25 kg/m²/a for raw MX-80 bentonite and Na/Ca- and Na-exchanged clay material, where the latter is similar to our upscaling approach, assuming lower flow rates of 2 mL/min.

3.5 Summary and Conclusions

The following observations could be summarised for the in-situ bentonite erosion experiment:

1. As the long-term sampling campaign results suggest, no major gravitational erosion influence was observed concerning the bentonite source (JGP11.003) and extraction boreholes (CFM18.001 to CFM18.003).
2. A continuous particle erosion from the bentonite source was observed, with colloidal concentrations generally above the background concentration of the natural GGW (2.2 ± 0.4E+07 particles/mL). average particle concentrations of the extraction boreholes and the approximated erosion masses, respectively, were determined to be: CFM18.001 = 1.8 ± 2.1E+08 particles/mL and 2.0 ± 1.0 µg/mL, CFM18.002 = 1.5 ± 1.4E+08 particles/mL and 1.5 ± 0.6 µg/mL, and CFM18.003 = 1.6 ± 1.4E+08 particles/mL and 1.7 ± 0.4 µg/mL.
3. In most cases, an increase in particle concentration correlated with an increase in erosion masses. However, increased particle concentrations, especially pronounced during the artificial system disturbances, did not always resemble higher erosion masses. Thus, changes in the particle-size distribution rather indicated a (re)-mobilisation of smaller particle fractions (<100 nm).
4. Concerning the recirculation approach of Phase 5, sedimentation within the tubing was merely indicated. The increase observed for the sedimentation borehole (CFM18.002) is negligible with respect to the laterally placed CFM18.001 and CFM18.003 boreholes. Therefore, no significant gravimetric erosion has been seen under the experimental i-BET conditions so far. Unfortunately, the possibility of observing gravimetric erosion is additionally limited by the poor hydraulic connectivity of CFM18.002 to the bentonite source and i-BET setup as a whole.
5. Concerning the gel/water interactions, data suggest an adjustment of the system and increased erosion stability over time with a sufficient supply of exchangeable calcium and progressively smaller particles eroded from the interface. However, this contrasts with the progressive increase in average hydrodynamic diameters observed for the laboratory-scale erosion experiments in Section 2.2.1.

6. The long-term sampling from i-BET with multiple extraction boreholes provided a broad database with converging calculated erosion rates in comparison to work performed by Smith et al. (2017), Neretnieks et al. (2017). Thus, we were able to estimate an average mass loss within the system, making the NTA method a valuable tool for a non-destructive approximation of erosion progression and subsequent barrier integrity. However, as the method relies on point-specific borehole data, a precise determination of material loss should always be verified by direct investigative methods such as overcoring, as done in the CFM-LIT project (Schlickenrieder et al. 2017, Lanyon et al. 2018). Such cores can then be compared to the NTA approach, e.g. be CT-scanned to validate the actual material loss.

4 Post-mortem analyses of long-term experiments

As mentioned above, the long-term in-situ test (LIT) ran within the CFM project at the Grimsel Test Site (GTS) from 2014 to 2018. The experiment consisted of compacted bentonite (FEBEX and Zn-labelled montmorillonite) rings. Glass vials containing a radionuclide tracer cocktail mixed with bentonite gel were emplaced into the bentonite rings. These were installed in a well characterised water-conducting fracture at the GTS via a packer system, and bentonite colloids and tracers were monitored for the duration of this long-term experiment (Noseck & Schäfer 2020). In 2021, the bentonite rings, including a part of the adjacent granitic fracture, were overcored, and part of the sample was transferred to laboratories of the Institute for Nuclear Waste Disposal of the Karlsruhe Institute of Technology (KIT-INE) for post-mortem analysis.

Parallel to in-situ studies, analogous laboratory experiments were carried out with so-called mock-up experiments, one of which was set up without radionuclides and one with radionuclides. The following sections describe the results of post-mortem analysis of mock-up and in-situ experiments. In order to allow for the analysis of radionuclides down to ultra-trace concentration levels, the Accelerator Mass Spectrometry (AMS) was applied. In this context, partial method development was necessary and is also described. For details on experimental setups, see (Noseck & Schäfer 2020).

4.1 Experimental and analytical development

4.1.1 AMS analysis of radionuclides in long-term in-situ studies

Due to radiation protection constraints for experiments at the GTS, activity levels for radionuclide tracers employed within the framework of in-situ tracer tests are limited. Furthermore, some of the radionuclides are expected to show high retention in the granodiorite shear zone, as well as slow diffusion through bentonite emplaced in the LIT. Due to these conditions, ultra-trace level concentrations are expected for the radionuclide tracers, especially in Grimsel groundwater (GGW), and solid phase samples were collected months or years after the start of the experiments. It is also important to note that often, only limited sample amounts were available from in-situ radionuclide tracer tests. A highly sensitive analytical method was therefore required for ultra-trace determination of radionuclides in LIT samples. The samples of groundwater mixed with small portions of bentonite porewater (mixed water, or MW) collected at LIT boreholes were to be analysed with regard to the retention and near-field release of the radionuclide tracers ^{99}Tc, ^{233}U, ^{237}Np, ^{242}Pu and ^{241}Am. Furthermore, a similar challenge was faced in the first attempt to determine the possible presence of ^{236}U, ^{237}Np and ^{239}Pu, resulting from global fallout, in groundwater samples collected at several boreholes of the GTS. A description and preliminary outcomes of these studies are given in the following section paragraphs.

This analytical challenge was addressed with AMS that provides detection efficiency for actinide nuclides and ^{99}Tc at the level of around 1×10^4 atoms (25 ag) and 3×10^6 atoms (0.5 fg) per sample, respectively (Steier et al. 2010, Quinto et al. 2019). This level of sensitivity allows determining long-lived and rare radionuclides at concentration levels far below the detection limits of ICP-MS, making the complementary use of these two mass spectrometric techniques an appropriate analytical strategy for in-situ radionuclide tracer tests (Quinto et al. 2017). The sensitivity of AMS stems from the acceleration of the actinide ions to MeV energy and the stripping processes at the terminal of the accelerator, providing both the strong reduction of tailing interferences and the destruction of molecular ions generating isobaric background. These are the main mechanisms allowing ultra-trace analysis of the actinides. In the actual studies, the AMS measurements of the actinides were carried out at the VERA laboratory (Vienna Research Accelerator facility at the University of Vienna) and involved helium-stripping of the actinides to the 3+ charge state at 1.65 MV terminal voltage and an additional 90° magnet in the analyser installed in front of a Bragg-type energy detector (Winkler et al. 2015). The groundwater samples were prepared and measured according to the multi-actinide analysis procedure in which actinides are concentrated from the sample matrix via iron hydroxide co-precipitation and measured sequentially without previous chemical separation from each other (Quinto et al. 2015).

The described background suppression mechanisms are, however, not sufficient to allow for an accurate ultra-trace determination of ^{99}Tc in environmental samples. In fact, while the stripping process dissociates the molecular isobar ^{98}Mo^{1}H^{-}, the stable daughter and atomic isobar ^{99}Ru still represents the majority of ions with mass 99 u in the AMS beam. In this case, an additional filtering device had to be employed. A Gas-Filled analysing Magnet System (GAMS) can provide the physical separation of atomic isobars on the basis of their atomic number, as in the case of $_{43}$Tc and $_{44}$Ru. For such heavy neighbouring nuclides, the relative difference in the nuclear charge is minimal and, therefore, a sufficiently high kinetic energy is required to allow for the significantly different deflection in the gas-filled magnet. Such conditions were achieved with the high energy AMS setup at the Maier-Leibnitz Laboratory (MLL) in Munich, which featured a 14 MV tandem accelerator (Koll et al. 2019). Using this, an analytical method was developed to determine ^{99}Tc at concentration levels of fg/g in 7 MW samples (approx. 1.7 mL volume) (Quinto et al. 2019).

In 20 MW additional samples, the concentration of the radionuclide tracers ^{99}Tc, ^{233}U, ^{237}Np, ^{242}Pu and ^{241}Am was determined with AMS. At the same time, to estimate a possible "shear zone" background, Grimsel groundwater (GGW) samples from the tailing of the two previous in-situ radionuclide tracer tests, namely CFM 12-02 and CFM 13-05 (see ref. Huber et al. 2016) were analysed. These two sample preparation approaches were applied for the two aforementioned sample systems. The MW samples (1.6 to 10 mL volume) were split in halves: one was submitted to the sample preparation described in Quinto et al. (2019) for ^{99}Tc analysis and one for actinide nuclide determination according to the method described in Quinto et al. (2015). A novel approach was employed for the GGW samples (500 mL volume), in which the group of actinide tracers was separated from ^{99}Tc with a TEVA® resin chromatographic column (TRISKEM International) with a sample-loading solution in 0.1 M HCl. For these samples, the lowest concentration of ^{99}Tc was expected and, therefore, instead of splitting the sample in halves, the tracers were extracted from the sample with the maximum available volume. At low acidity, the high selectivity of quaternary ammonium salts of TEVA® for the pertechnetate anion TcO_4^-, over actinide species enables quantitatively retaining Tc on the column while eluting the group of the actinides (Horwitz et al. 1995). The Tc and actinide fractions obtained via this method were then submitted to the AMS sample preparation procedures described in Quinto et al. (2015) and Quinto et al. (2019), respectively. With these procedures, concentrations down to approx. 2×10^5 atoms/mL for ^{99}Tc and approx. 6×10^4 atoms/mL for ^{233}U could be determined with AMS in the GGW and MW samples (Quinto et al., in preparation).

4.1.2 Characterisation of post-mortem mock-up and LIT samples

So-called mock-up experiments have been conducted at the KIT-INE laboratories to study bentonite erosion in an artificial horizontal fracture setup to simulate the intrusion of groundwater in the near-field of a repository with bentonite as a geo-engineered barrier. A ring of compacted FEBEX bentonite (40 mm inner diameter, 80 mm outer diameter, and 25 mm height; the composition of the bentonite is described in Noseck & Schäfer 2020) was emplaced between two Plexiglass plates spaced apart by a 1 mm height aperture to simulate a parallel fracture around the bentonite (Fig. 4-1). Groundwater from the Grimsel Test Site, pumped through the fracture at a flow rate of 50 µL/min, led to bentonite swelling and formation of a gel in the aperture. In the following sections, the results of the post-mortem analysis of two mock-up tests are described, one of which was conducted without radionuclides and performed under air (Mock-up experiment 1), and another spiked with the same radionuclides as used for the LIT, conducted under an argon atmosphere (Mock-up experiment 2).

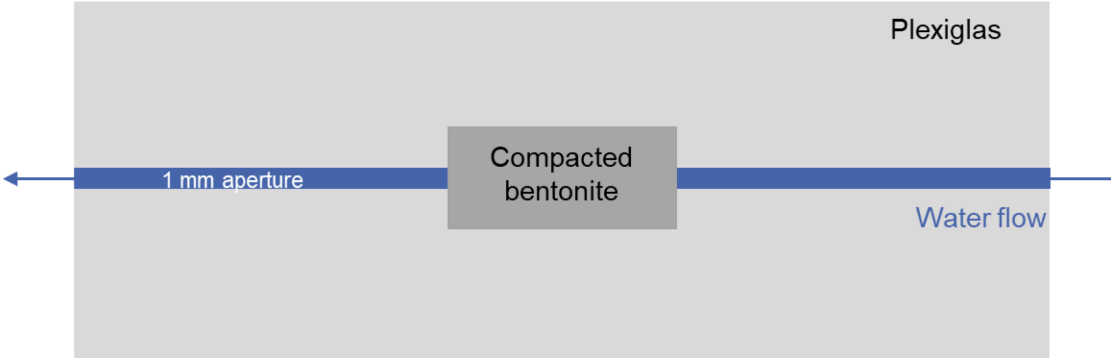

Fig. 4-1: Mock-up experiment setup

4.1.2.1 Sample preparation for the analysis of the bentonite gel structure

Different sample preparation techniques were considered for the post-mortem analysis to be able to preserve the 1-mm gel structure formed around the bentonite ring in the aperture.

The use of an epoxy resin (Araldit 2020, Huntsman International LLC) was proposed in the Kollorado e2 final report (Noseck & Schäfer 2020) for the sample preparation of the mock-up experiments. The same resin was used for the overcoring of the LIT at the Grimsel test site and was thus further investigated. Leftover bentonite rings from the LIT were ground using a mortar and pestle to create a fine powder. This powder was mixed with MilliQ water to prepare a bentonite slurry that was poured onto a Plexiglas sheet to mimic the gel structure of the mock-up test gels. Eight circular gel structures with a diameter of approximately 40 mm and a thickness of 1 mm were prepared on the Plexiglas sheet and left to dry. Afterwards, these bentonite gel samples were wetted with 4 solutions of water and ethanol (100% water, 60% water and 40% ethanol, 30% water and 70% ethanol, and 100% ethanol) in order to simulate the mock-up bentonite in various wetting conditions and with the use of ethanol to dry the bentonite before the injection of the resin. The resin was then poured onto these bentonite gel samples and left to dry for 24 hours before separating the gels trapped in the resin from the Plexiglas with a scalpel. The samples wetted with 70% and 100% ethanol remained intact within the resin and could easily be separated from the Plexiglas sheet, while the samples containing less ethanol were not completely embedded in the resin and broke up during the separation.

A further resin embedding test was made with a circular bentonite gel sample (diameter: 160 mm; thickness: 1 mm) between two sheets of Plexiglas in order to simulate the conditions of the mock-up test. The Araldit resin was injected between the plexiglass sheets (after injection of 50 mL of ethanol at a flow rate of 0.1 mL/min) using a peristaltic pump with a flow rate of 0.5 mL/min and then left to harden for 48 hours. Under these conditions, the resin did not adhere homogeneously to the plexiglass surface and damaged the gel structure that could not be recovered entirely. Therefore, the approach to preserve the bentonite gel by applying a resin could not be used.

After these tests, another sampling technique was used consisting of drilling a hole into the Plexiglas upper plate using a tip of 16 mm, down to a distance of approximately 10 mm away from the sample before overcoring the last 10 mm using a hollow drill device. this way, as can be seen in Fig. 4-3a and b, samples were collected from both the bentonite ring and the gel layer, which was more or less undisturbed, before opening the Plexiglas setup to retrieve more samples. The gel was then mapped into subsections with an optical microscope with a resolution of 200 µm, as shown in Fig. 4-2c and d.

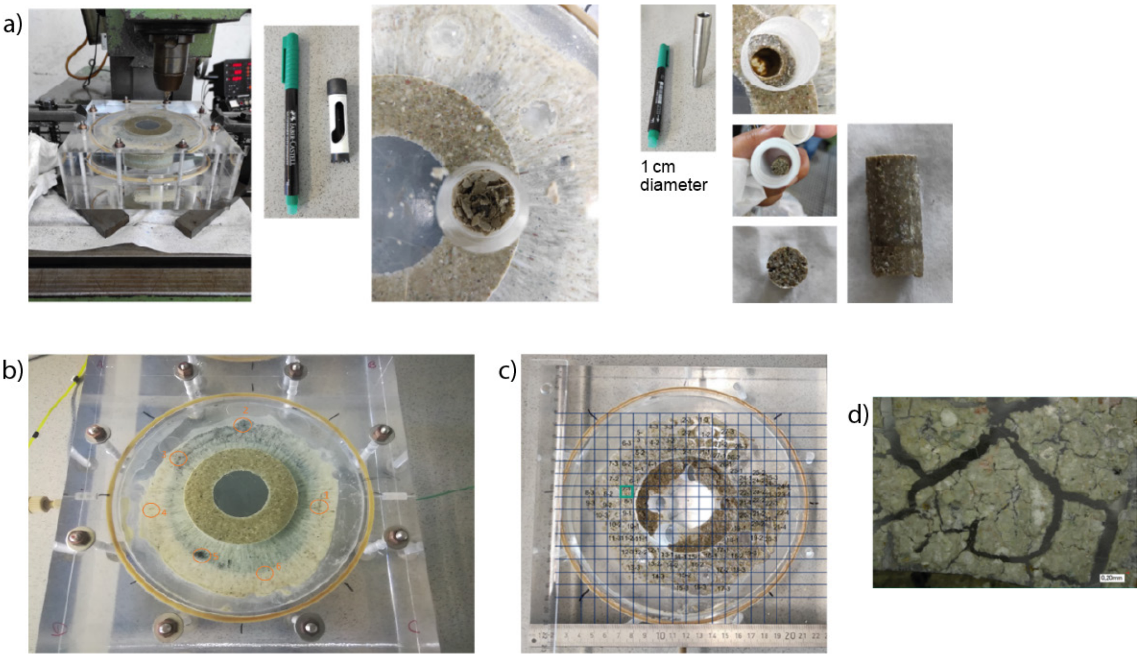

Fig. 4-2: Sampling technique used for the inactive mock-up experiment for (a) the bentonite ring; (b, c) gel samples; and (d) optical microscopy mapping of the gel

4.1.2.2 Sample preparation for the analysis of the bentonite segments adjacent to tracer vials in mock-up experiment 2

A piece of bentonite of approx. 3 cm x 2 cm x 1.5 cm containing the broken vial of Mock-up experiment 2 was sampled using disposable plastic tweezers and embedded in an acrylic resin, Epofix®, as depicted in Fig. 4-3. The sample was then abraded with silicon carbide (SiC) paper in a glove bag to remove 5 mm of resin that did not contain any bentonite. The bentonite embedded in resin was then abraded from the extremity far away from the vial in layers of 20 to 100 µm with pieces of SiC paper until reaching the broken vial.

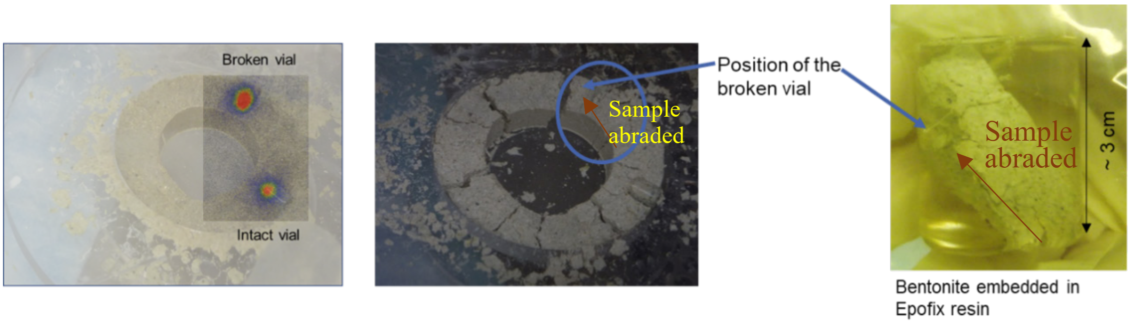

Fig. 4-3: Selection of the bentonite piece that was embedded in resin for the abrasive peeling process

In total, 254 samples were collected over a 2 cm distance. A selected group of 50 samples representative for the entire segment was submitted for analysis. The SiC papers containing the bentonite powder were then transferred into 50 mL centrifuge tubes and mixed with 30 mL of nitric acid 4 M in order to desorb the radionuclide tracers from the bentonite samples. After a contact time of two days, the samples were centrifuged to separate the bentonite powder from the supernatant. The supernatants were then collected, evaporated to dryness on a hot plate and diluted in HNO_3 (2%) for (SF)-ICP-MS analysis. ^{237}Np and ^{233}U were detected by (SF)-ICP-MS in each investigated sample while the concentrations of ^{99}Tc, ^{241}Am and ^{242}Pu were below the detection limit of the instrument.

In addition to this desorption step, some of the leached bentonite samples were submitted to total digestion with concentrated hydrofluoric acid and aqua regia. The residues were transferred to Teflon beakers where 5 mL of concentrated hydrofluoric acid were added. The samples were first heated to 180 °C until almost complete evaporation to dryness, then 5 mL of aqua regia were added and the samples were reheated to 180 °C until evaporation to almost complete dryness before being taken up in HNO_3 (2%). These samples were also analysed by (SF)-ICP-MS. The concentrations of all the radionuclides were below the detection limit of the instrument in these samples, meaning that the desorption with 4 M nitric acid quantitatively desorbs the radionuclides.

4.1.2.3 Sample preparation for the characterisation of LIT post-mortem samples

For the post-mortem analysis of the LIT, the granodiorite containing the bentonite rings was overcored and cut into slices. The first LIT sample, which consisted of a disk of the granodiorite core (30 cm diameter and 3 cm thick, taken 15 cm from the bentonite rings spiked with the radionuclide tracers) did not contain radionuclides and was used to test the sampling procedure for the analysis of the active LIT samples. The bentonite ring was cut out from the granodiorite using an oscillating multi-tool saw. Samples were then drilled from the bentonite ring to obtain fine powders (Fig. 4-4). The powders were subsequently characterised by SEM-EDX and XRD, subsequently digested with hydrofluoric acid and aqua regia and submitted to (SF)-ICP-MS for elemental composition analysis as described above for the mock-up sample. Some residues left undissolved after the digestion were analysed using SEM-EDX.

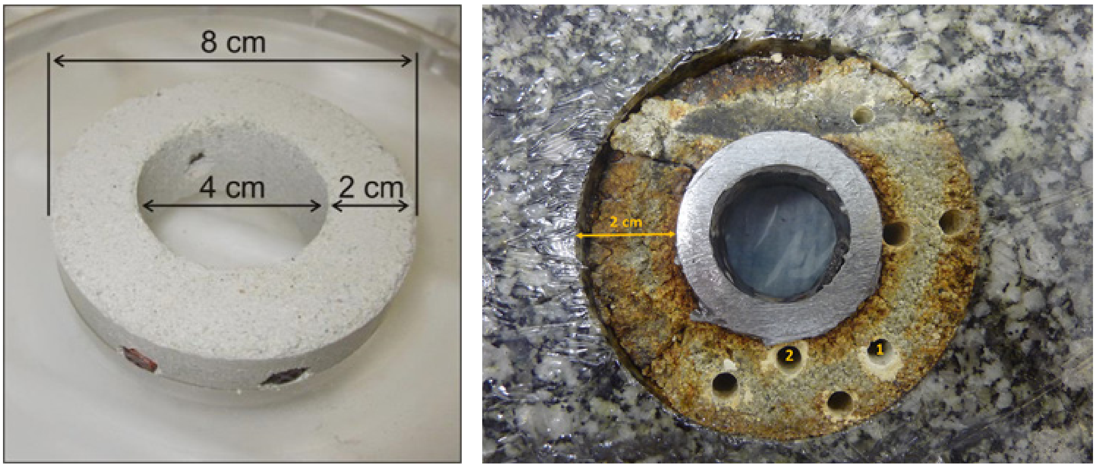

Fig. 4-4: Pristine bentonite ring and LIT sample

4.2 Results of mock-up experiments

4.2.1 Mock-up experiment 1

mock-up experiment 1 with FEBEX bentonite ran for six years. After this time, the gel formed in the aperture extended over the whole plexiglass fracture volume available in the setup, and a ring with a darker coloured material could be clearly observed (Fig. 4-5).

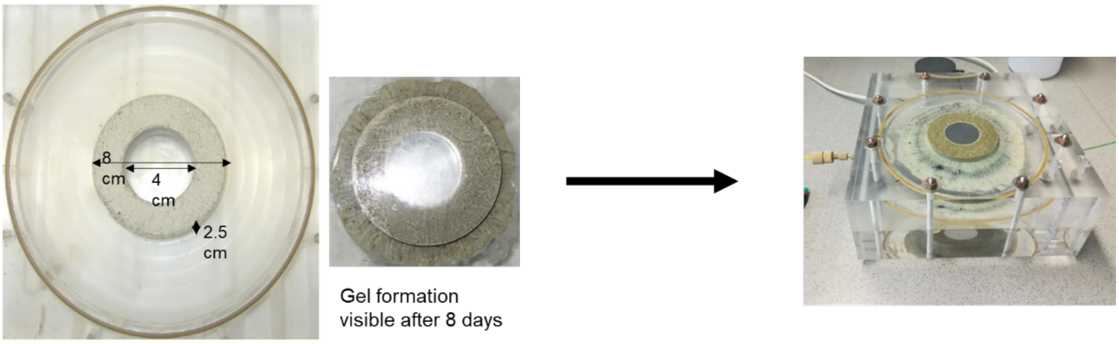

Fig. 4-5: Gel formation in the mock-up experiment

From left to right: initial setup before the erosion experiment, gel formation after 8 days, and setup after 6 years.

Coarse grains of accessory minerals of various colours were visible in this gel and were sampled for SEM-EDX analysis. As shown in Fig. 4-6b and c, SEM-EDX analysis suggests the presence of Si-, Mg- and Al-containing particles, which could be silica and feldspars as expected for the FEBEX bentonite. The samples presenting darker spots contained, in addition to silica and feldspars, about 1% of iron and 15% of titanium that could correspond to ilmenite, as in the case of sample 5. The Respective areas are indicated in Fig. 4-6a, and the elemental composition as analysed by EDX is depicted in Fig. 4-6c.

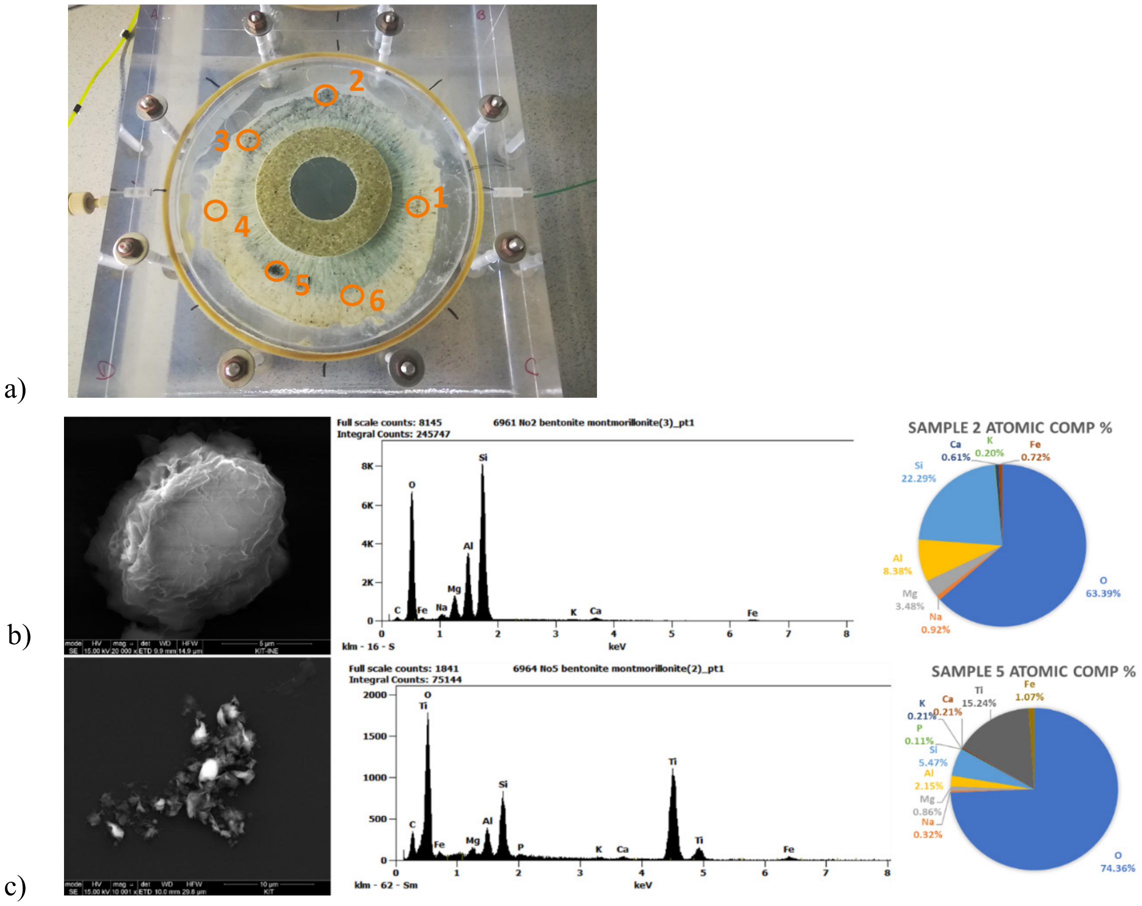

Fig. 4-6: Gel samples collected (a) and SEM-EDX pictures and spectra of Samples 2 (b) and 5 (c)

Some minerals that were originally present in the bentonite such as gypsum could not be identified, most likely due to the dissolution during the erosion experiment as suggested by the elevated SO_4^{2-} concentrations detected in the collected water samples (Noseck & Schäfer 2020). Other less soluble accessory phases were found in the ring (i.e., pyrite as seen in Fig. 4-7).

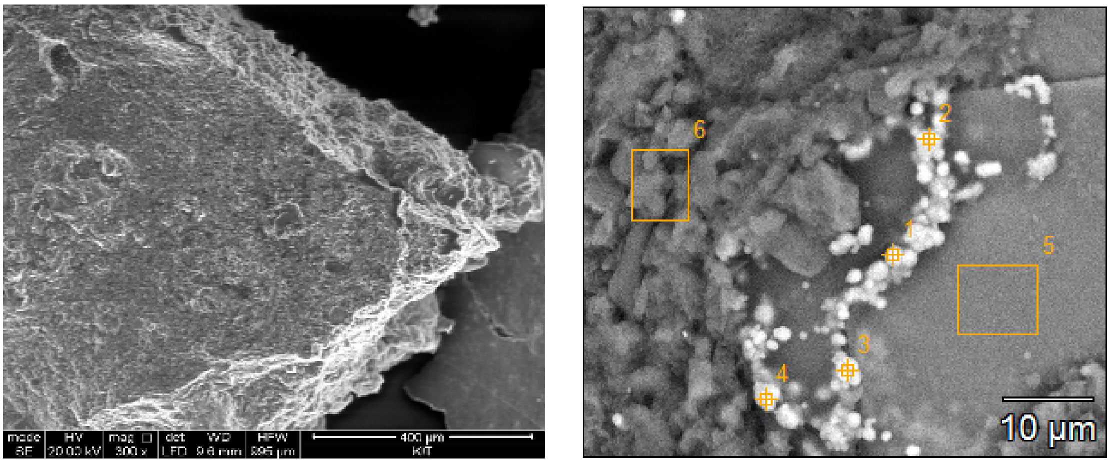

Fig. 4-7: Evidence of pyrite in the bentonite gel detected by SEM-EDX

4.2.2 Mock-up experiment 2

An experiment similar to Mock-Up Experiment 1 was performed with a bentonite mixed with Zn-labelled montmorillonite, a cocktail of radionuclide tracers (containing ^{241}Am(III), ^{137}Cs(I), ^{242}Pu(III), ^{45}Ca(II), ^{75}Se(IV), ^{99}Tc(VII), ^{233}U(VI), and ^{237}Np(V)) and a conservative tracer, Amino-G. This mix was added to a bentonite slurry and inserted into open glass vials placed within the bentonite ring. This experiment was carried out in an argon glove box for five years. The Plexiglas cell containing this radioactive mock-up test was opened around two years after the end of the experiment for post-mortem analysis. Approximately equal parts of the bentonite ring and the gel adhered to the top and bottom plates of the cell, respectively, as seen in Fig. 4-8).

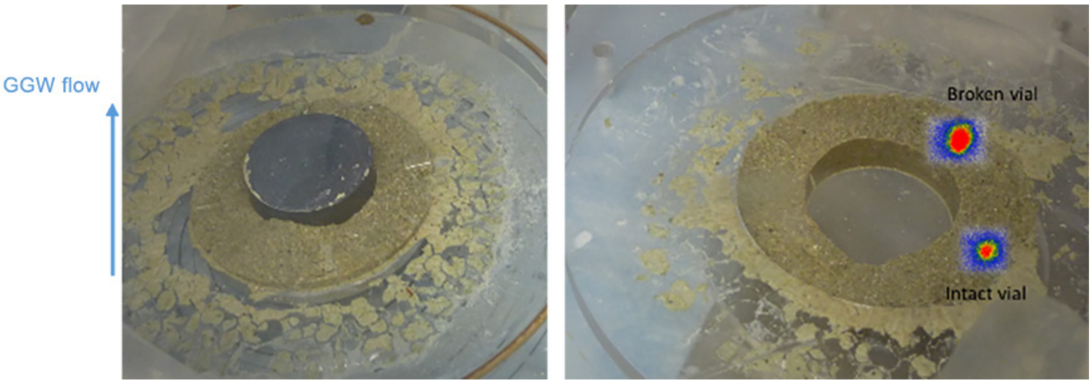

Fig. 4-8: Photo of the erosion cell of the FEBEX experiment after opening. The photo on the left shows the lower part of the cell. Autoradiography is superimposed to the photo on the right of the upper part of the opened bentonite ring

Two of the four vials were found to be intact, and two others were broken due to the increasing pressure during the experiment. Autoradiography was performed on the ring to detect gamma emitters, namely ^{241}Am and ^{137}Cs. Particle emissions were adsorbed by the overlying bentonite layer (Fig. 4-8). For the intact vial, the radiation spot was relatively small with a thickness of a few mm around the vial. In the case of the broken vial, the spot was irregularly shaped and had a larger diameter compared to the intact vial. The extension of the radiation spot could not be directly correlated with a radionuclide diffusion length due to the dispersion and scattering of the gammarays prior to reaching the superimposed autoradiography plate.

In order to investigate the diffusion profiles of the radionuclide tracers with higher accuracy, two segments of the bentonite ring were collected, one adjacent to a broken vial and the other one adjacent to an intact vial. These segments were then submitted to the sample preparation and analysis described in the following paragraphs.

The concentration of radionuclides in the investigated bentonite samples adjacent to the broken vial ranged from 1 to 10 ng/g for ^{237}Np and from 0.1 to 1.2 ng/g for ^{233}U (Fig. 4-9 and Fig. 4-10, respectively). The concentration profiles appeared to be constant within the experimental scattering of the data over a distance of 2 cm away from the vial except for one sample that had levels of 318 ng/g and 43 ng/g of ^{237}Np and ^{233}U, respectively. This sample was shown to be rich in iron, with a concentration of 599 μg/g compared to levels of 1.2 to 20.5 μg/g in the other samples. The enhanced actinide levels could thus be explained by a preferential sorption to an iron mineral, potentially pyrite. Even though strongly scattering concentration data could be seen in the vicinity of the vial, flat concentration profiles up to 2 cm could also be seen. Scattering could be explained by tracer sorption to local pyrite grains as discussed above and/or heterogeneities in diffusive pathways, which could be dominant in the early phase of inhomogeneous saturation and swelling. Nevertheless, the flat concentration profiles were reproduced qualitatively by respective diffusion modelling calculations (see Section 6.3.3). Apparently, the outflow of ^{237}Np and ^{233}U from the vial reached a steady state over the 5-year duration of the experiment. These results were supported by the observation of a breakthrough of both radionuclides in the outlet of the packer during the experiment (Noseck & Schäfer 2020). The high mobility pointed to the existence of Np and U in their oxidised states V and VI, respectively, which was also visible in the measurement of the other samples described below. This indicated that redox conditions were at least not reducing enough to transfer all Np into the tetravalent state and could be different to the respective conditions in the LIT.

In all abrasive peeling bentonite samples adjacent to the broken vial, no ^{241}Am and ^{137}Cs could be detected by gamma spectrometry.

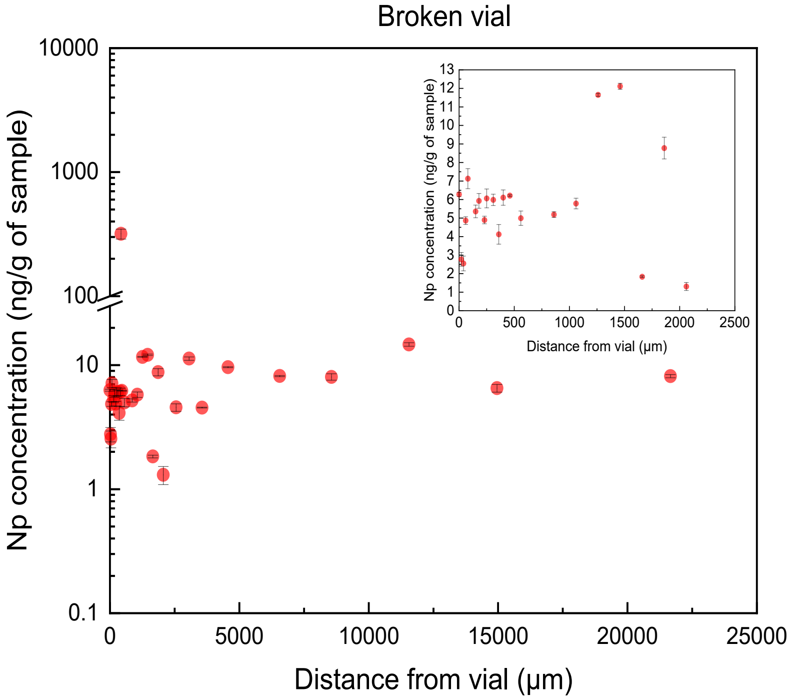

Fig. 4-9: ^{237}Np concentration profile in the FEBEX bentonite samples adjacent to the broken vial (log scale) for a distance up to 25,000 µm from the vial. The insert shows a zoom of the Np profile (linear scale) up to 2,500 µm

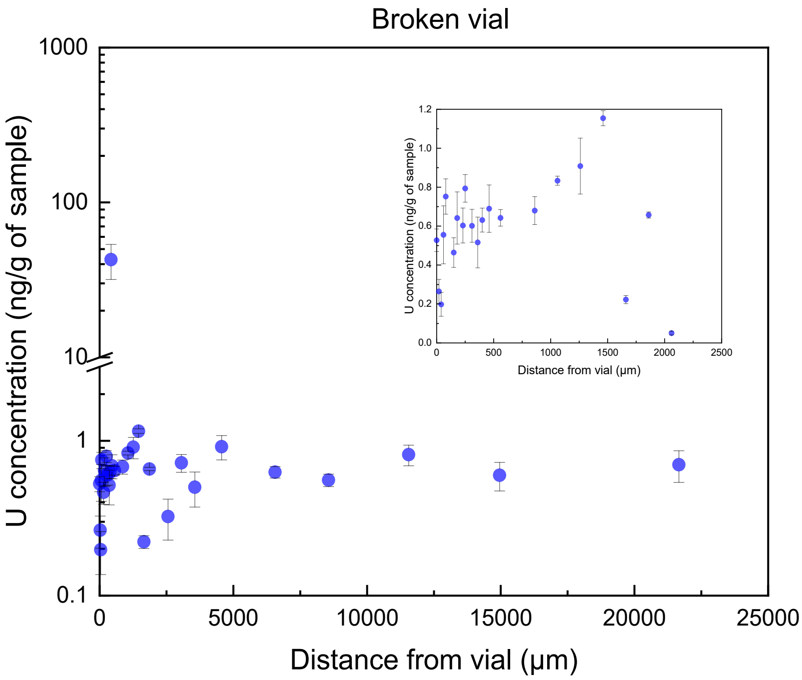

Fig. 4-10: ^{233}U concentration profile in FEBEX samples adjacent to the broken vial (log scale) for a distance up to 25,000 µm from the vial. The insert shows a zoom of the U concentration profile (linear scale) until 2,500 µm

The abrasion of a bentonite segment adjacent to an intact radiotracer vial was performed following the same procedure described in the previous paragraph. In total, 280 samples were collected over 2 cm segment. An inactive vial containing only bentonite without tracers was located at the other end of this bentonite segment.

The concentrations of radionuclides in these bentonite layers ranged from 0.7 to 19 ng/g in the sample for ^{237}Np and between 0.1 and 5 ng/g for ^{233}U (Fig. 4-11 and Fig. 4-12, respectively). Data show significantly stronger scattering compared to the samples collected in the vicinity of the broken vial. However, radionuclide concentrations 2 cm away from the vial lay in a similar range for both segments, at 8 and 10 ng/g for ^{237}Np and at 0.7 and 0.5 ng/g for ^{233}U, respectively. These flat concentration profiles could be reproduced by diffusion model simulations and indicated that a steady state for the diffusive transport of both radionuclides was achieved over the 5-year duration of the experiment. The concentrations of ^{241}Am and ^{242}Pu in the samples already analysed with (SF) ICP-MS will be further analysed with accelerator mass spectrometry (AMS) that allows measuring levels of radionuclides as low as 25 atoms/sample (Steier et al. 2010) and also acquire diffusion profiles for these elements in the bentonite segments adjacent to the broken and intact vial samples.

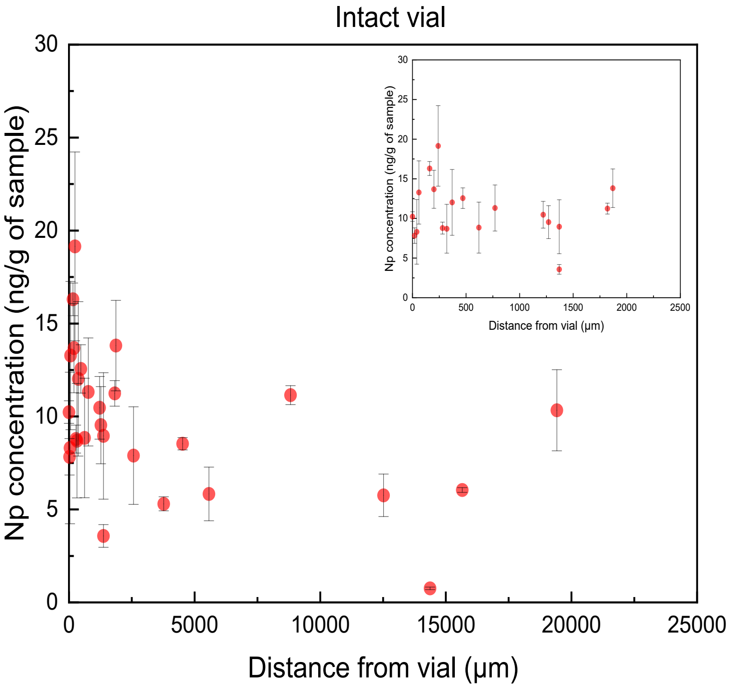

Fig. 4-11: ^{237}Np concentration profile in the bentonite layer adjacent to the intact tracer vial over a distance of up to 25,000 µm from the vial. The insert shows a zoom for the Np profile (linear scale) up to 2,500 µm

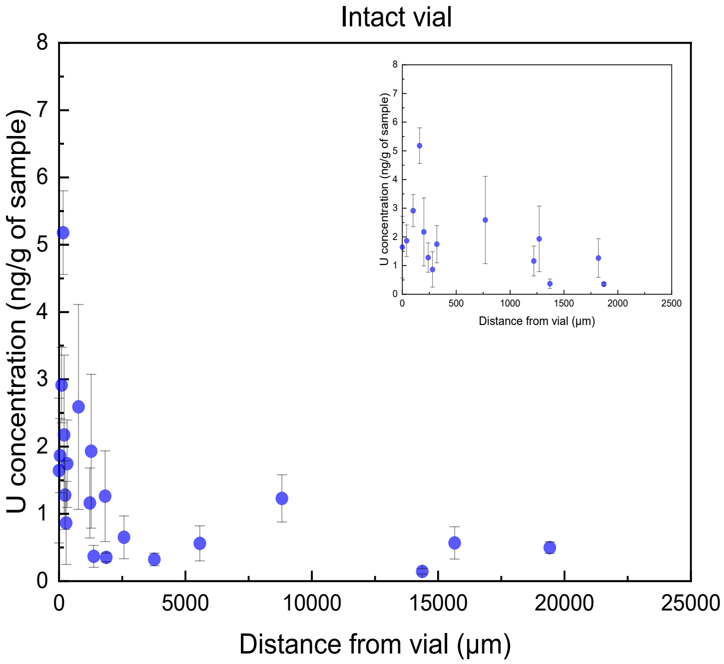

Fig. 4-12: ^{233}U concentration profile in the bentonite layer adjacent to the intact vial over a distance of up to 25,000 µm from the vial. The insert shows a zoom for the U profile (linear scale) up to 2,500 µm

To determine the "source term" of the radionuclides released into the bentonite, it was necessary to analyse the radionuclide tracer content of the remaining bentonite within the glass vials. Preliminary investigations showed that, e.g. in the second intact vial, only 121 mg of the initially inserted 222 mg of bentonite remained in the vial. During the experiment, intruding water apparently led to bentonite swelling and subsequent extrusion of almost half of the initially present bentonite with associated radiotracers. Initial radionuclide analyses of the bentonite slurries turned out to be inconclusive, pointing to problems with the analytical procedure and will be repeated. Another vial present in the LIT sample will also be analysed to obtain a better understanding of the number of radionuclides left in the vials.

4.3 Results for the Long-Term In-Situ Test (LIT)

4.3.1 Post-mortem characterisation of bentonite segments

Various segments of the bentonite ring prepared from the LIT after overcoring and transporting to the KIT-INE laboratories was characterised for mineralogical composition with SEM-EDX and XRD. This chapter describes the characterisation of a segment that was assumed to be unaffected by the radionuclide tracers introduced during the LIT. Results were similar to those obtained in the mock-up experiments (see Section 4.2.1). However, minerals containing copper (97) and sulphur could be identified in addition.

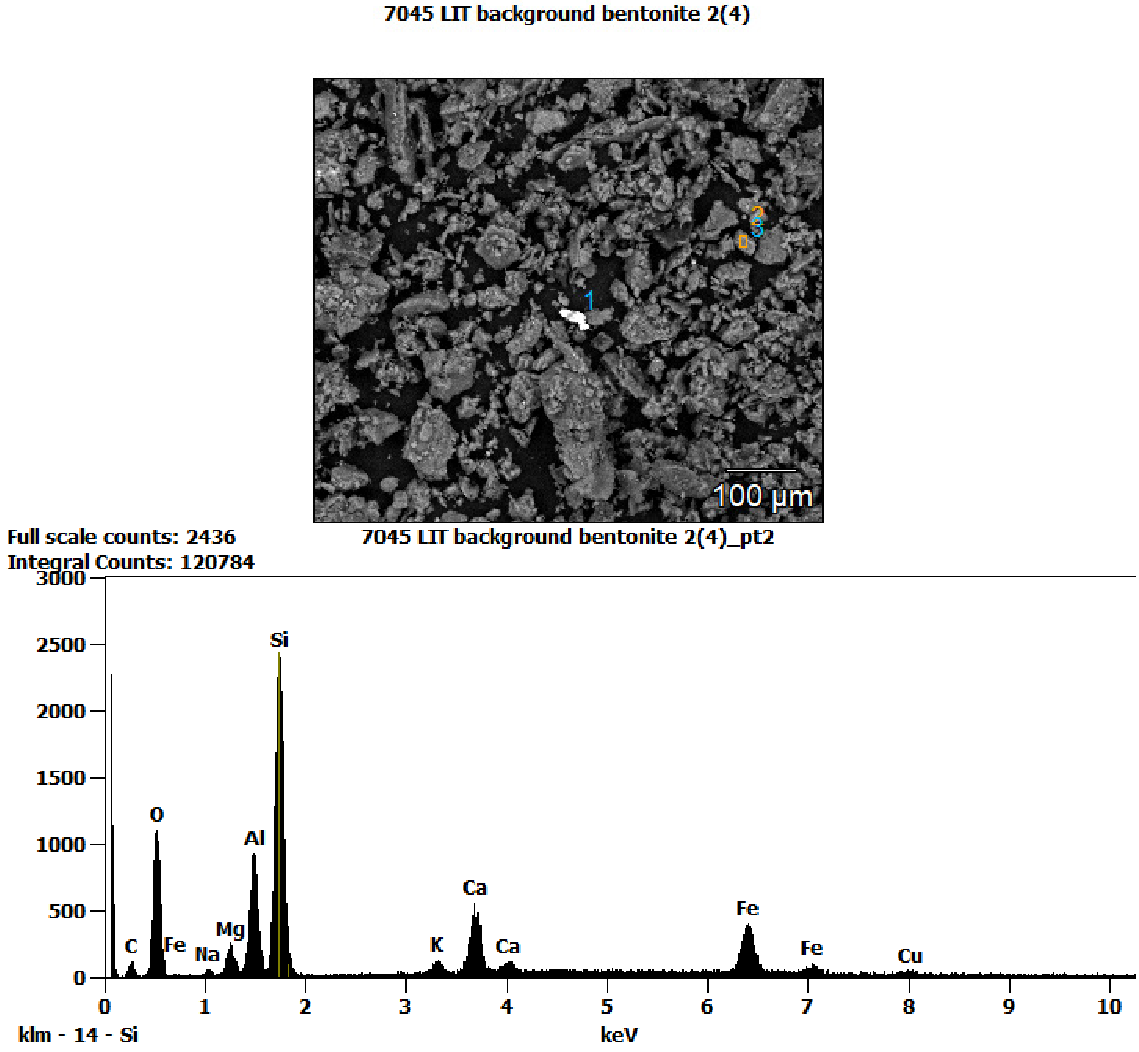

Fig. 4-13: SEM picture and EDX spectrum for an LIT sample

The powder bentonite samples were successively digested with hydrofluoric acid and aqua regia and submitted to (SF)-ICP-MS for elemental composition analysis with the same procedure used for the mock-up sample (see Section 4.1.2.2). Some residues left undissolved after the digestion were analysed using SEM-EDX and showed that they were mainly composed of $ZrSiO_4$ and TiO_2, known to be refractory minerals. In the dissolved fraction of the bentonite samples, the actinide tracers were always below the detection limit of (SF) ICP-MS, equal to approx. 10 pg/L. However, traces of ^{133}Ba and ^{137}Cs from former experiments were present and determined with gamma spectrometry. The elemental composition of LIT bentonite samples was compared to that of pristine bentonite. The main difference observed related to copper, manganese and vanadium contents (Tab. 4-1). These elements had the highest concentration in the second bentonite sample taken around 3 mm from the carbon steel mandrel. The concentrations of those elements in the first sample, which was around 1 cm away from the mandrel, was lower and comparable to that of the pristine bentonite sample. This finding indicated corrosion of the steel and diffusion of dissolved steel constituents through the bentonite.

Tab. 4-1: Concentrations of copper, iron, manganese and vanadium in two LIT bentonite samples and in pristine bentonite determined by (SF)ICP-MS after digestion in hydrofluoric acid and aqua regia. Sample 1 was taken in the middle of the bentonite ring while Sample 2 was taken in the vicinity of the carbon steel mandrel

Conc. in µg/g	Pristine bentonite	Sample 1 (ca. 10 mm from the carbon steel mandrel)	Sample 2 (ca. 3 mm from the carbon steel mandrel)
V	17.1 ± 0.3	12.8 ± 0.4	33.2 ± 0.2
Mn	324.1 ± 3.2	208.8 ± 2.1	854.5 ± 2.9
Fe	30,205.7 ± 205.4	22,944.8 ± 160.6	37,070.9 ± 189.1
Cu	15.3 ± 0.7	15.1 ± 0.6	43.4 ± 0.3

This "inactive" LIT sample also served to refine the abrasive peeling procedure that will subsequently be used to cut the radionuclide-spiked bentonite into thin segments of around 20 – 100 µm, in order to obtain diffusion profiles of the radionuclide tracers. Such forthcoming results will significantly help the interpretation of the observed ultra-trace-level near-field releases of the radionuclide tracers in the groundwater samples collected during the LIT (see following paragraph) and will allow for a comprehensive understanding of radionuclide migration through a bentonite geotechnical barrier.

4.3.2 Retention and Near-Field Release of ^{99}Tc, ^{233}U, ^{237}Np, ^{242}Pu and ^{241}Am in the LIT

During the approximately 4.5 years of the LIT, groundwater was regularly collected from two near-field boreholes placed at a distance of 4 cm from the LIT source (Noseck & Schäfer 2020). In these MW samples, composed of GGW mixed with a small proportion of bentonite porewater, the concentration of the conservative fluorescent tracer Amino-G (AGA) and the radionuclide tracers ^{99}Tc, ^{233}U, ^{237}Np, ^{242}Pu and ^{241}Am, originally emplaced in the bentonite as Tc(VII), U(VI), Np(V), Pu(III) and Am(III), was investigated. Considering the setup of LIT, a signal of the radionuclide tracers in the MW samples would account for a near-field release from the bentonite followed by the transport/retention through the shear zone under advective transport conditions. A detailed description of these analytical results is given in Quinto et al. (in preparation), while a summary and preliminary interpretation in the report is given as follows.

Fig. 4-14 shows extremely low concentrations of the ^{99}Tc tracer determined in the MW samples with values spanning from a maximum of $(1.2 \pm 0.6) \times 10^9$ atoms/mL at 206 days and down to $(4.5 \pm 1.2) \times 10^6$ atoms/mL at 1,600 days after the start of the experiment. Similar trends were observed for ^{233}U and ^{237}Np with a possible maximum in the first phase of the LIT and decreasing levels towards the end, while ^{242}Pu showed a more or less flat concentration profile. Levels higher than detection limits for ^{241}Am were determined in samples collected up to around 900 days, with concentrations generally lower than $(8.3 \pm 5.5) \times 10^4$ atoms/mL. Based on those analytical data collected over the 4.5 years, the fraction of radionuclide tracers in MW relative to the emplaced inventory corresponded to $\sim 8.5 \times 10^{-5}$ for ^{99}Tc, 3.4×10^{-4} for ^{233}U, 1.9×10^{-5} for ^{237}Np, 6×10^{-5} for ^{242}Pu and 2.4×10^{-5} for ^{241}Am, while the AGA recovery equalled $\sim 3.7 \times 10^{-2}$ (Noseck & Schäfer 2020). Whether the measured concentrations can be considered entirely as near-field releases from the LIT is a matter of discussion. In particular, the possible background from previous in-situ radionuclide tracer tests (Quinto et al. 2017) performed during the last 21 years in various dipoles intersecting the shear zone could play an important role by contributing to a "shear zone background". This "background" cannot be unequivocally estimated, since it can only be determined in GGW samples collected before or during the LIT in far-field boreholes located at a certain distance to the LIT. While the concentrations of most of the radionuclides in samples collected after around 700 days were close or below the respective "background" levels, the concentrations of ^{99}Tc lay significantly above the respective "background" levels of approx. 1.6×10^5 atoms/mL, indicating a clear release of ^{99}Tc from the bentonite source over the entire experimental period.

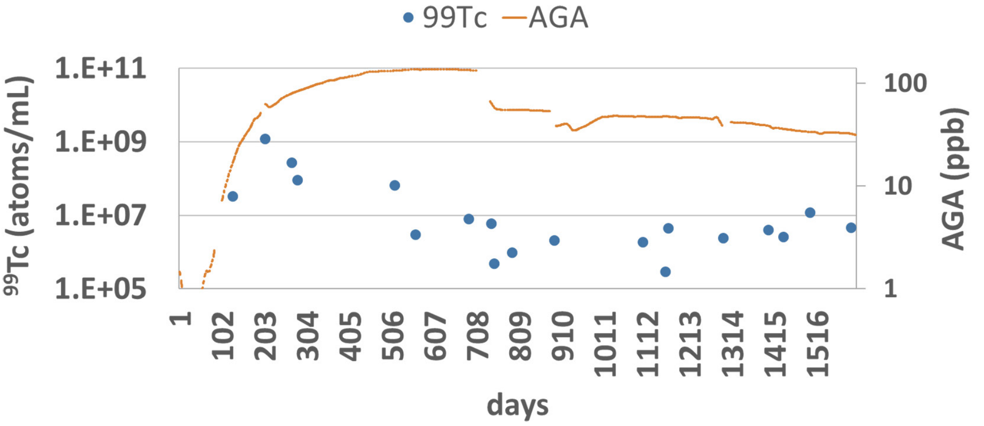

Fig. 4-14: Concentration of ^{99}Tc (atoms/mL) represented by blue spots and of the conservative tracer AGA (ppb) represented by the orange line in MW water samples. Both vertical axes are given with a logarithmic scale

However, the shape of the ^{99}Tc release curve differed from that of the conservative, non-sorbing tracer AGA. In fact, as shown in Fig. 4-14, the concentrations of ^{99}Tc (as well as of ^{233}U, ^{237}Np and ^{241}Am, not depicted here) significantly decreased after about 200 to 300 days. The concentration of AGA as a conservative non-sorbing tracer reached a maximum steady-state concentration after 400 to 500 days and decreased by 60% after 738 days due to an increase of the extraction rate of the MW samples from 20 to 50 µl/min (Noseck & Schäfer 2020). At this time, a clear decrease in the ^{99}Tc concentration could not be recognised, possibly due to the scatter in analytical data. The initial release curve shapes of the radionuclides could be ascribed to the inhomogeneous swelling in the early phase of bentonite saturation with the groundwater (Noseck & Schäfer 2020), possibly opening preferential transport pathways for the radionuclides and AGA. At the same time, redox conditions in the bentonite varied due to oxygen consumption that could have an impact mainly on the speciation of Tc and Np. The enhanced radionuclide retardation observed in the actual experiment after around 550 days would occur when the swelling of the fully saturated bentonite closed the pathways and the E_{hSHE} values decreased in bentonite porewater. It is important to note that the expected establishment of increasingly reducing conditions in the bentonite cannot be inferred from the evolution of the E_{hSHE} values determined in the MW samples (Noseck & Schäfer 2020) in the outflow, which showed three phases: a first phase characterised by positive values of E_{hSHE} until 1,400 days and with a maximum of around200 mV, a second phase of negative values of E_{hSHE} until 2,023 days with a minimum of – 280 mV and a third phase of positive values of E_{hSHE} until the end of the experiment with a maximum of around 230 mV. However, such E_{hSHE} values measured in the boreholes do not necessarily reflect the redox conditions within the bentonite. The obtained experimental data suggest that ^{233}U, ^{237}Np, ^{242}Pu and ^{241}Am were strongly captured by the bentonite. While trace fractions of ^{99}Tc, ^{233}U, ^{237}Np and ^{241}Am were released during the early phase when the bentonite was not fully saturated, for ^{99}Tc a steady state concentration was also established, pointing to the diffusive transport of a small fraction of non-reduced TcO_4^-. In this regard, the redox conditions appeared to be virtually different from those found in the mock-up experiment where a significant mobility could be stated for ^{237}Np and ^{233}U (see Section 4.2.2).

The forthcoming post-mortem analysis of the diffusion profiles of the radionuclide tracers through the bentonite of LIT will be a decisive step forward in the quantification of their retention in the bentonite.

5 Analysis of global fallout actinides at the GTS

In addition to in-situ radionuclide tracer tests, a further possibility to investigate the long-term behaviour of actinides in shear zones of the GTS could be the analysis of actinides from the global fallout, namely the worldwide deposition on the earth´s crust generated from the atmospheric testing of thermonuclear devices (H-bombs). H-bomb detonations occurred almost uninterruptedly between 1951 and 1980 and the most abundantly produced actinide nuclides were ^{236}U, ^{237}Np and ^{239}Pu with global fallout inventories of 2,800 to 3,108 kg, 1,500 kg and 900 to 1,698 kg, respectively (Denecke et al. 2018, Geckeis et al. 2019). The intensity of the global fallout varied each year, and the produced yearly inventories of ^{236}U, ^{237}Np and ^{239}Pu can be estimated as illustrated in Denecke et al. (2018). As a result, 31% of the total actinide global fallout inventories was shown to be released before the moratorium declared by the USA and the former USSR in 1958, the majority, namely 57% was released between 1961 and 1962, and finally 12% after 1963 as a consequence of the Partial Test Ban Treaty. The analysis of global fallout actinides in environmental systems relevant to the disposal of radioactive waste therefore has the potential to provide information on their behaviour over a time span of around 60 years to the present. Following these considerations, we decided to investigate global fallout of ^{236}U, ^{237}Np and ^{239}Pu at the GTS. Global fallout actinides are present in the environment at ultra-trace levels, representing the most abundant actinides, namely ^{236}U, ^{237}Np and ^{239}Pu, with a surface deposition density of 10^{12} – 10^{13} atoms/m^2 at the middle latitudes of the Northern Hemisphere (Denecke et al. 2018).

The GTS is an ideal location for studying the mobility of those radionuclides for the following reasons:

1. Located at an altitude of 1,730 m in the granitic rock of the Aar Massif in Switzerland, the GTS is far away from any source of nuclear contamination except global fallout.
2. The tunnel hosting the underground laboratory lies at a depth of around 450 m beneath the surface and provides several sampling sites for the collection of meteoric water migrating from the surface through fractures with different residence times.

It is evident that the interpretation of global fallout actinide behaviour in fractures at the GTS has to consider the given boundary conditions. At least in the upper zone close to the surface, oxidising conditions can prevail, and a redox gradient to more reducing conditions exists with increasing depth. This has an impact on actinide redox states, which in part will be different from the situation in a deep geological repository where reducing conditions exist. Taking those constraints into account, the analysis of actinide downward migration can provide valuable insight into their geochemical behaviour.

The GTS system can be schematised as composed by the compartments of soil, lake water and sediments, granodiorite fault gauge minerals and groundwater. A further compartment that can provide information, in particular on the geochemistry of U, is the secondary mineral Grimselite, $K_3Na[UO_2|(CO_3)_3]\cdot H_2O$, which forms as a result of the evaporation of groundwater over the granodiorite surface of the tunnel since it was excavated in 1983. Measurements of ^{236}U/^{238}U in samples of the Grimselite can provide insight on the origin of the U forming this mineral and as to whether a global fallout influence can be identified.

Initial information on the behaviour of global fallout actinides at the GTS could be obtained by comparing the concentrations of ^{236}U, ^{237}Np and ^{239}Pu in Grimsel groundwater samples with those in surface water samples collected from lake Grimsel at the surface. In Fig. 5-1, the concentration (number of atoms in a sample of 250 ml) of ^{236}U, ^{237}Np and ^{239}Pu measured in lake Grimsel and in six groundwater (GW) samples are depicted together with those determined in two procedure blanks (Blank_a and Blank_b). The groundwater samples, here named GW_G2, GW_C1, GW_B2, GW_Adus, GW_B5 and GW_F3, were collected at different locations of the Grimsel Test Site corresponding with the boreholes and intervals listed in Tab. 5-1.

Tab. 5.1: Denomination of the boreholes and intervals in which the Grimsel groundwater samples were collected

Sample	Borehole name	Interval name
GW_B5	BOUS 85.002-i5	3H-B5; Act-B5
GW_B2	BOUS 85.002-i2	3H-B2; Act-B2
GW_C1	BOSB 80.001	3H-C1; Act-C1
GW_ADUS	ADUS 96.001-i2	3H-ADUS-I2; Act-ADUS-I2
GW_F3	/	3H-F3; Act-F3
GW_G2	/	3H-G2; Act-G2

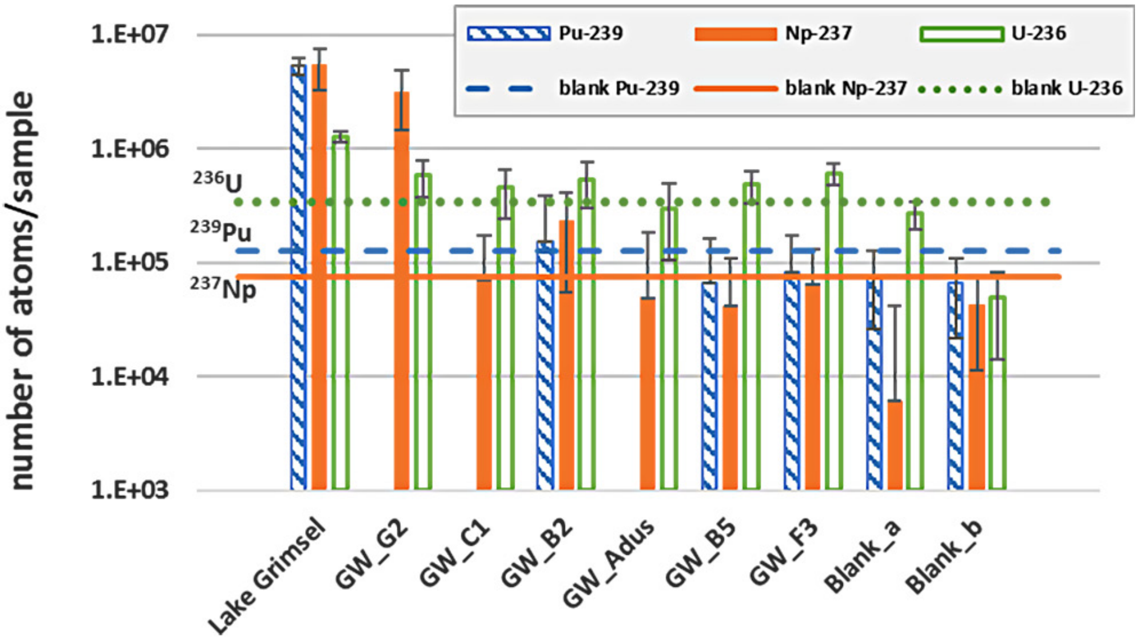

Fig. 5-1: Concentration of global fallout of ^{239}Pu (blue dashed column), ^{237}Np (red full column) and ^{236}U (green empty column) in Lake Grimsel, GW samples and in two procedure blanks (Blank_a and Blank_b) determined with AMS. Sample size is 250 ml. The horizontal lines depict the blank levels of ^{239}Pu (blue dashed line), ^{237}Np (red continuous line) and ^{236}U (green points line), see text

A clear global fallout signal is determined in the surface water sample from Lake Grimsel with concentrations of (1.3 ± 0.1) × 10^6, (5.4 ± 2.1) × 10^6 and (5.3 ± 0.9) × 10^6 atoms/250 ml for ^{236}U, ^{237}Np and ^{239}Pu, respectively. As shown in Fig. 5-1, the actinide levels determined in the GW samples are mostly consistent with those found in the procedure blanks, Blank_a and Blank_b, except for sample GW_G2 that presents a level of ^{237}Np, equal to (5.3 ± 0.9) × 10^6 atoms/250 ml, significantly higher than the blanks. In this sample, we then tried to determine ^{233}U in order to verify whether the detected ^{237}Np could originate from previous in-situ tracer tests in which ^{233}U and ^{237}Np were employed together with other actinide nuclides. However, the fact that no significant signal of ^{233}U was detected pointed to global fallout as the origin of ^{237}Np in sample GW_G2. Such preliminary results indicated the potential migration of global fallout ^{237}Np in the groundwater collected at the location G2.

After subtracting the highest level of each investigated actinide found in the procedure blanks from the levels of the corresponding actinides in the GW samples, we found a concentration of ^{236}U in GW_G2 and GW_F3 that was not consistent with the blank background within one sigma uncertainty, but remained very close to it. However, the possible determination of ^{236}U from global fallout in samples GW_G2 and GW_F3 had to be proven with further investigations. The sample of Grimselite, collected near the sampling location of the groundwater sample GW_Adus, presented a ^{236}U/^{238}U isotopic ratio of (8 ± 3) × 10^{-11}. The ^{236}U concentration in GW-F3 could also arise from "contamination" with uranium minerals.

As shown in Fig. 5-1, the measured levels of ^{239}Pu in GW_B2, GW_B5 and GW_F3 were consistent with the blank background and were equal to zero in GW_G2, GW_C1 and GW_Adus, i.e. no counts could be detected by AMS. This result supported the general view that Pu is rather immobile under environmental conditions, and in the present case was retained in the soil, lake sediments or in the fault gauge minerals of the GTS due to sorption. Pu in its tetravalent state often exists in colloidal state, which can enhance mobility. The fact that no fallout Pu was observed in GGW samples suggested that colloid-facilitated Pu transport was less relevant and/or filtration processes were active. On the other hand, the determination of ^{237}Np in GW_G2 and possibly of ^{236}U in GW_G2 and GW_F3 could be explained with a preferential migration of U(VI) and Np(V) as dissolved species.

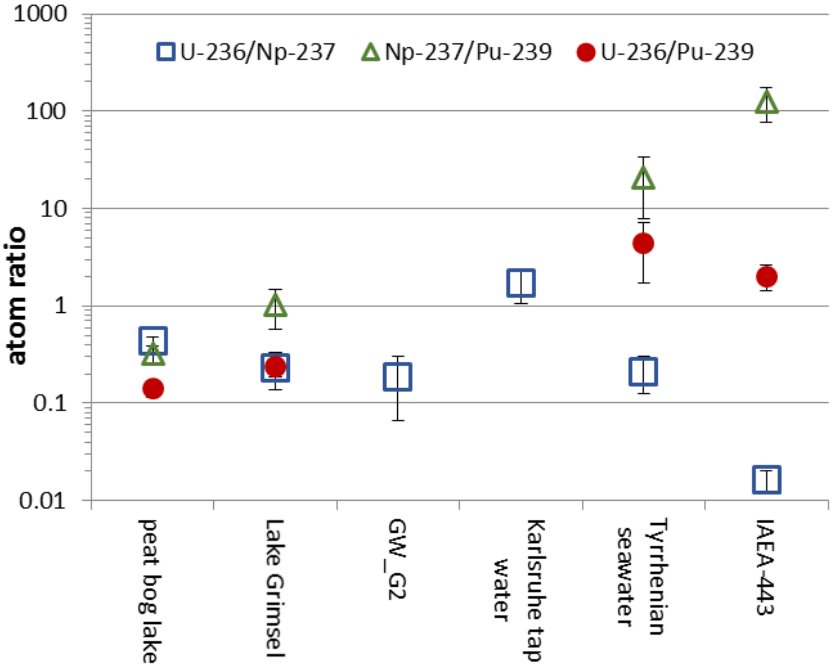

Fig. 5-2: $^{236}U/^{237}Np$, $^{237}Np/^{239}Pu$, and $^{236}U/^{239}Pu$ atomic ratios measured in different natural water samples (see text for description) (sample masses between 100 and 250 g). This figure shows how the observed atomic ratios reflect both the contamination source and the different behaviour of U, Np, and Pu in the investigated environmental system

Fig. 5-2 is an adaptation from Quinto et al. (2015) with the addition of two further samples from the actual study. It represents the $^{236}U/^{237}Np$, $^{237}Np/^{239}Pu$, and $^{236}U/^{239}Pu$ atomic ratios measured in different natural water samples and elucidates how these parameters are determined by the origin of the nuclear contamination. These are, for example, emissions from a nuclear fuel reprocessing plant in the case of the Seawater Reference Material IAEA-443, or the global fallout for samples from a peat bog lake. In addition, ratios are influenced by the different geochemical behaviours of U, Np and Pu in the various environmental systems. It is interesting to note that the $^{236}U/^{237}Np$ atom ratio in the groundwater sample GW_G2 equal to approx. 0.18, is similar to that found in the surface water sample of Lake Grimsel equal to approx. 0.23, as well as to the values found in the peat bog lake and the Tyrrhenian seawater samples, as shown in Fig. 5-2.

Such preliminary results are presently difficult to interpret, and more studies are needed to examine and verify the possible downward migration of global fallout actinides to certain regions of the GTS. However, they constitute a proof of concept for further investigations on global fallout actinides at the GTS as well as at other natural analogue systems.

The study of the possible migration of global fallout actinides at the GTS has the potential to complement the outcomes of in-situ radionuclide tracer tests and laboratory experiments, greatly extending the scale of time and space in which radionuclide behaviour can be investigated.

Such long-term and large-scale migration can provide an experimental observation for the far-field transport of the actinides after the bentonite engineered barrier system has failed and the released radionuclides in a water-conductive feature of the granodiorite rock undergo geochemical reactions in the ternary system of GGW/fault gauge minerals/colloids.

6 Model calculations

The modelling objectives within the framework of the Kollorado-e3 project focus on various aspects. Thermodynamic benchmark calculations are continued and expanded to an international group. The objective is to obtain a better understanding of the speciation of homologues and radionuclides under GTS field conditions, particularly under the conditions of the LIT, with the bentonite emplaced and resaturated in the Grimsel shear zone. The impact of near-field geochemical conditions and the role of accessory minerals on the bentonite erosion process is investigated by means of laboratory experiments and accompanied by modelling. A coupled flow and transport model is applied to describe the dissolution of gypsum minerals, the ion-exchange processes of the montmorillonite and the corresponding changes in chemical conditions in the fracture. Furthermore, a coupled code is applied to describe the ion-exchange processes in the LIT near-field and the evolution of the concentrations of major cations and trace elements (radionuclides). Further simulations of the radionuclide diffusion in the bentonite are performed to describe new available experimental data from the LIT and particularly the corresponding Mock-up experiments. Finally, the colloid-facilitated transport model, including kinetically controlled processes to describe the interaction among radionuclides, colloids and sediment matrix, is applied on the repository scale using data derived from CFM field and related laboratory experiments and accompanied modelling. These model calculations contribute to the qualification of the codes and set the basis for calculations with regard to the post-closure safety of deep geological repositories.

6.1 Benchmark calculation on thermodynamic databases

6.1.1 Background

The long-term In-situ Test (LIT) of the Colloid Formation and Migration project (CFM) at the Grimsel Test Site (GTS) was performed to investigate the generation of bentonite colloids and consequent radionuclide mobilisation within a well-defined and controlled shear zone in a crystalline rock. In this context, the knowledge about the radionuclide aqueous speciation is essential to understand whether a radionuclide is easily transported or can be immobilised by precipitation or uptake processes. The goal of the thermodynamic benchmark is to determine, through geochemical calculations, the aqueous speciation of seven elements, which have been used as radioisotope tracers (i.e. ^{75}Se(VI), ^{99}Tc(VII), ^{233}U(VI), ^{237}Np(V), ^{241}Am(III), Th(IV) and ^{242}Pu(IV)) in the LIT, across different water compositions representing the geochemical evolution during the LIT.

A first part of the benchmark, presenting the results of the two German groups from GRS and KIT-INE, has already been described in the report on the previous Kollorado-e2 project (Noseck & Schäfer 2020) and published in Montoya et al. (2022) this section summarises the benchmark results of all six partners, i.e. UJV, JAERI, GRS, KIT-INE, RWM, and CIEMAT. Details including all tables of thermodynamic data as well as calculations results and speciation of all considered radionuclides can be found in Noseck et al. (to be published). In the following, only a brief description of the benchmark and the key findings are described.

The simulations consider only reactions in thermodynamic equilibrium at 25 ºC and three different groundwater compositions (i.e. bentonite porewater, Grimsel groundwater and "mixed water" (MW)) with representative redox conditions of the LIT. The composition of the Grimsel groundwater (GGW) is described in Duro et al. (2006) and the bentonite porewater was used as given in Fernández et al. (2004). To reflect the differences between the initial conditions after emplacement of the bentonite source, when oxygen was still available, and the more reducing conditions expected to develop in the longrun of the experiment due to the existence of reducing mineral phases such as pyrite and siderite, a reducing and an oxidising bentonite porewater, BPWR and BPWO, respectively, were defined. Additional mixed water compositions (MWs) representing the interface between bentonite and the shear zone in the granite were calculated for all groups, i.e. a 10/90% mixture of BPWR and GGW, denoted as mixed-water-reducing (MWR) and a 10/90% mixture of BPWO and GGW, denoted as mixed-water-oxidising (MWO).

Five modelling groups used PHREEQC v.3 (Parkhurst & Appelo 2013) for their calculations, and one group used the code CHESS v.2.4 (van der Lee & De Windt 2002). To generate Pourbaix diagrams, either PhreePlot v.11 (2017 release) (Kinniburgh & Cooper 2011) or Geochemist Workbench 2015 (Bethke & Yeakel 2015) was applied.

Different thermodynamic databases were used in the assessment by the different groups, although all groups used the NEA Thermodynamic database (TDB) as a base for thermodynamic data selection. Group 1, Group 5 and Group 4 used the ThermoChimie v.9b database, updated in 2015 (Giffaut et al. 2014). Group 2 (Fujiwara et al. 2010) and Group 3 used their internal databases (Stockmann et al. 2017), which are mainly based on the updated PSI/Nagra Chemical Thermodynamic Database 12/07 (PSI/Nagra TDB 12/07) (Thoenen et al. 2014). The database of Group 2 database is also based on the PSI/Nagra Chemical Thermodynamic Database 12/07 and most of the selected values for tetravalent actinides have been taken from (Fujiwara et al. 2010) instead of those of the NEA. Group 6 used the CHESS database (EQ3) (Delany & Lundeen 1991), based on TermoChimie v.9b with regularly incorporation of NEA updates as well as updates from revision and new literature.

Group 1, Group 5, Group 3 and Group 6 used the Davies equation for the ionic strength correction, which is valid for aqueous solutions with ionic strengths <0.5 mol L^{-1}. Group 4 and Group 2 applied the Specific Ion Interaction (SIT) theory as ionic strength correction. This approximation gives good results for ionic strengths <2 mol L^{-1}.

6.1.2 Summary of results

The thermodynamic benchmark calculations were performed to determine the aqueous speciation of seven radionuclides mainly including actinides and fission products (i.e. ^{75}Se(VI), ^{99}Tc(VII),^{233}U(VI), ^{237}Np(V), ^{241}Am(III), Th(IV) and ^{242}Pu(IV)) in different water compositions representing the geochemical evolution through the in-situ experiment LIT at GTS. By comparing results of the six different modelling groups, key geochemical parameters affecting radionuclide transport could be identified.

Since the publication of a previous modelling exercise, thermodynamic databases have been further developed and harmonised. Particularly within the NEA TDB project, state-of-the-art thermodynamic data were summarised. All databases applied here are based on the NEA TDB, thereby highlighting the relevance and importance of this study. Particularly, the existence of new species such as ternary silica actinide complexes, ternary uranyl carbonate complexes or iron selenides has been proven and included, impacting for example the speciation and solubility of U, Pu, Am or Se in the systems investigated here.

Selenium solubility predictions are highly uncertain when the oxidation state is not known. This is particularly shown in the results of the less reducing waters, where the differences in Eh can cause differences in solubility of more than five orders of magnitude. Also important are assumptions about the solubility-limiting mineral phase, as well as uncertainties in the thermodynamic data. Whether or not to include polyselenides into the calculations is a decision that can impact solubility by more than one order of magnitude.

For **technetium**, the results of all groups agree rather well due to very similar thermodynamic data. The key factor impacting Tc solubility is the redox conditions. In the reducing waters in the LIT near-field, concentrations from 3 to $5 \cdot 10^{-9}$ mol/kg water are expected, whereas for oxidising conditions in the beginning of the experiment as well as in the mock-up tests, concentrations are expected to be high, i.e. $>10^{-3}$ mol/kg water.

In all systems, the differences in calculated maximum concentrations for **americium** are less than one order of magnitude. These differences are caused by uncertainties in thermodynamic data for stability constants of complexes (especially the ternary americium silica hydroxo complex, which is dominant in the bentonite porewater), assumptions about the solid phase and differences in pH values (mixed waters) due to different assumptions for mixing calculations. The highest concentrations occur in the nearly neutral bentonite porewater with values above 10^{-5} mol/kg water. With increasing pH, the solubility decreases, down to values between $5 \cdot 10^{-8}$ and $2 \cdot 10^{-7}$ mol/kg water in GGW, with slight variances depending on the selected solid phase Am(OH)3(am) or Am(CO3)(OH)(am).

The solubilities calculated for **thorium** are consistent with the thermodynamic data in all databases. The key impact factor on the maximum concentration is the selection of the solid phase, namely whether a fresh or aged amorphous ThO_2 phase is applied in the calculations. As reasons for selecting either the aged or the fresh species, the duration of the LIT (aged species) or conservativity in radionuclide transport calculations with respect to long-term safety assessment (fresh species) are given. Maximum thorium concentrations in all waters are expected to be in the range of 10^{-9} to 10^{-8} mol/kg water.

The speciation and solubility of **uranium** is complex and impacted by several factors. Thus, the concentration within the different waters but also between the different modelling groups varies by orders of magnitude. The major differences in the calculations by the different modelling groups are due to the selection of solubility-limiting solid species and to differences in the pH and Eh conditions calculated for the mixed waters. In addition, the ternary uranyl earth alkaline carbonate complexes dominate the speciation in all waters and increase the solubility by more than one order of magnitude, if considered in the database.

The **neptunium** solubilities are very similar, i.e. they are in the range of $1 \cdot 10^{-9}$ to $2 \cdot 10^{-9}$ mol/kg water, for all waters if amorphous NpO_2 is considered as a solubility-limiting phase. The presence of only Few different stability coefficients in the Group 2 database does not significantly impact the solubilities. The only deviations from this concentration range occur in the oxidising bentonite porewater in the case where the tetravalent NpO_2OH(am) is selected as the solubility-limiting phase (Group 2) or where the $NpO_2SiO(OH)_3$ complex, which is only considered in the database of Group 3, strongly contributes to the Np speciation.

The concentrations calculated for **plutonium** are rather low and the range between $1 \cdot 10^{-11}$ and $5 \cdot 10^{-10}$ mol/kg water for most waters. The only exception is BPWR, where the speciation is dominated by Pu(III) and the solubility range increased to $5 \cdot 10^{-10}$ to 10^{-8} mol/kg water.

The model comparison also showed the relevance of expert judgement in modelling decisions. The characteristics of solid phases directly impact the calculated maximum concentrations. This concerns the selection of different mineral phases as well as the selection of a crystalline, aged or fresh mineral phase of the same mineral. As an example of the former, uranium concentrations in more oxidising waters differ by up to three orders of magnitude, when different mineral phases (e.g. uranophane vs. schoepite) are selected. For ThO_2, as an example for the latter, it is recommended to use the value for the aged phase considering the 4.5 years duration of the LIT, resulting in reduced concentrations by a factor of five. Similarly, the inclusion/exclusion of mobile species leads to an increase/decrease of the solubility such as for the polyselenides in the case of selenium. All these modelling decisions need to be transparent and well justified.

In general, the calculations of all modelling groups agree well, and differences in results could always be traced back to differences in data or in modelling assumptions. This enhances confidence in TDBs and represents a sound basis for a planned second part of the modelling exercise, which will emphasise ion exchange and surface complexation processes on key mineral phases in the bentonite and the minerals of the shear zone/crystalline rock at the GTS.

Results from the benchmark calculations presented here will be verified by the recently launched analysis of the overcored material of the LIT, which, among other goals, is intended to identify radionuclide redox states and mineral phases in the bentonite and the adjacent granite.

6.2 Simulations of migration experiments, LIT and laboratory experiments

6.2.1 LIT near-field modelling

The in-situ LIT field experiment was active for 4.5 years between 2014 and 2018. One goal of the modelling work is to describe the near-field geochemistry around the bentonite source under the conditions of the LIT and characterise the impact of the flow in the adjacent fracture on the evolution of the geochemical conditions.

6.2.1.1 Modelling approach and input parameters

In accordance with the modelling goals, a 2D flow and transport model was developed using PHAST (version 3.4.0 – 12927, Parkhurst et al. 2010). A PhreeqC module implemented in this code describes the geochemical reactions. Of particular interest are the major ion concentrations and their behaviour during the LIT, in which the Grimsel groundwater (GGW) flows around the bentonite, which is expected to contain typical bentonite porewater after resaturation. The characteristics of both waters, as they are used in the simulations, is listed in Tab. 6-1.

The Febex bentonite contains, in addition to montmorillonite, 1 – 2% gypsum. The dissolution of the gypsum during the LIT released Ca^{2+} and SO_4^{2-} into the system, thereby increasing the ionic strength of the solution, which in turn impacted bentonite erosion and colloid stability, cf. Section 6.2.2. At the same time, cation exchange processes in the montmorillonite also influenced the composition of the solution. Among other things, it is to be investigated whether and how fast Ca^{2+} is removed from the solution by ion exchange processes and whether other elements are released in the process.

In a first step, a large geometrical model was developed based on the previous modelling approaches applied to field tests in the shear zone, see e.g. (Noseck et al. 2016) and (Huber et al. 2014). The extraction rate at the Pinkel defined the conditions of the flow field. The model area with all boundary conditions is illustrated in Fig. 6-1 and the parameters for the shear zone model are listed in Tab. 6-2.

Tab. 6-1: Properties and concentrations [mol/L] of bentonite porewater (Solution 1, Fernández et al. 2004) and Grimsel Groundwater (Solution 2, Alonso et al. 2005) used for the model calculations

	Solution 1 Bentonite porewater	**Solution 2 GGW**
pH	7.44	9.6
Na	3.9×10^{-1}	6.9×10^{-4}
K	3.0×10^{-3}	5.0×10^{-6}
Mg	9.7×10^{-2}	6.2×10^{-7}
Ca	8.2×10^{-2}	1.4×10^{-4}
Al	-	2.63×10^{-6}
Fe	-	3.0×10^{-9}
Mn	-	5.0×10^{-9}
Sr	7.3×10^{-4}	2.0×10^{-6}
Cl	7.3×10^{-1}	1.6×10^{-4}
HCO_3[a]	2.4×10^{-4}	4.5×10^{-4}
Si	1.8×10^{-4}	2.5×10^{-4}
SO_4	1.7×10^{-2}	6.1×10^{-5}
F	-	3.6×10^{-4}
Br	-	3.8×10^{-7}

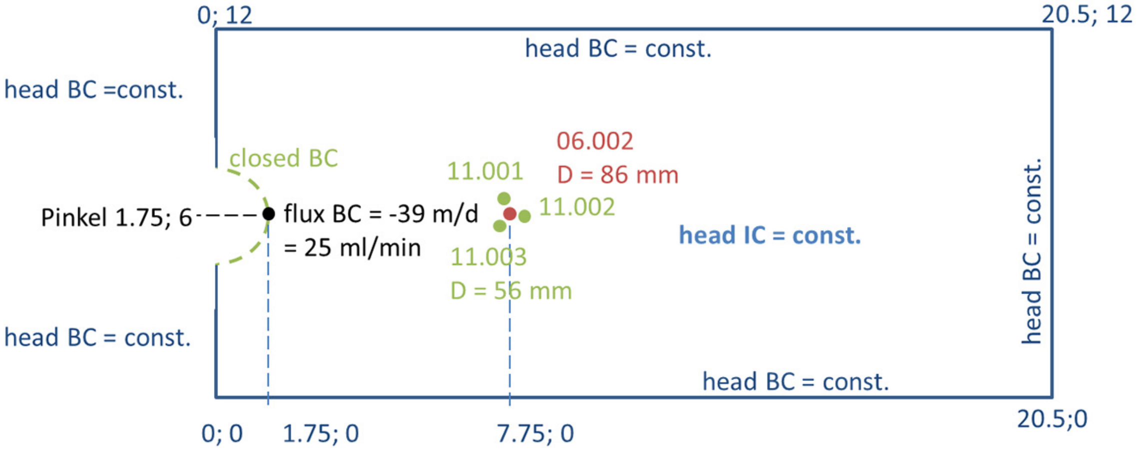

Fig. 6-1: Model area of a 2D flow simulation

If not stated otherwise, numbers correspond to [m]. Extraction (black), observation (green), and injection (red) boreholes are illustrated. BC corresponds to boundary conditions (green, blue), D to diameter, 06.002, 11.002, 11.001, and 11.003 identify boreholes, and IC stands for initial condition.

Tab. 6-2: Parameters for flow and transport in the fracture

Parameter	**Value**
Dimensionality	2D
Model thickness [m]	$5 \cdot 10^{-3}$
Dipole distance [m]	6.2
Porosity [-]	0.115
Dispersion length [m]	
• Longitudinal	0.3
• Transversal	0.1
Diffusion coefficient [m^2 s^{-1}]	$2.0 \cdot 10^{-11}$
Permeability [m^2]	$5.5 \cdot 10^{-11}$
Rock density [kg m^{-3}]	2,670
Temperature [K]	293.15

Results of the flow calculations for the large model are shown in Fig. 6-2.

Fig. 6-2 (top) shows the steady-state flow field related to the LIT conditions with an extraction of 25 mL/min at the Pinkel and an injection of 0.33 mL/min at CFM 06.002. Fig. 6-2 (bottom) shows the same flow field without injection at CFM 06.002.

This system then builds the basis for the fine-scale flow model.

Based on this larger model, a fine-scaled geometric model ("detailed model") was developed covering a model area of only 0.5 m x 0.5 m. The distance between the edges of the model area and the observation boreholes had to be large enough to avoid edge effects. The grid used had 100 nodes in the X direction and 100 nodes in the Y direction. Since PHAST is a code for 3D modelling, the 2D model was realised by only 3 nodes in the Z direction. The drill holes were included as circular subareas so that the hydraulic and chemical parameters could be specified. A bentonite ring was implemented in the central borehole CFM 06.002. After some test runs with different temporal discretisation, the time step for all calculations was set to one day. No significant changes of the forms of the breakthrough curves could be observed for calculations with time steps of five days and one day. All results are presented in 30-day time steps.

The flow conditions could be established by an outflow via the left boundary. The flow velocity at this left edge of the model area was derived from the steady-state conditions calculated by the large model with an average velocity of $-2.51 \cdot 10^{-07}$ m/s. This outflow was selected to meet the flow velocities from the large model in this area. The upper and lower borders are closed, and the right border is open. The resulting flow field is illustrated in Fig. 6-3.

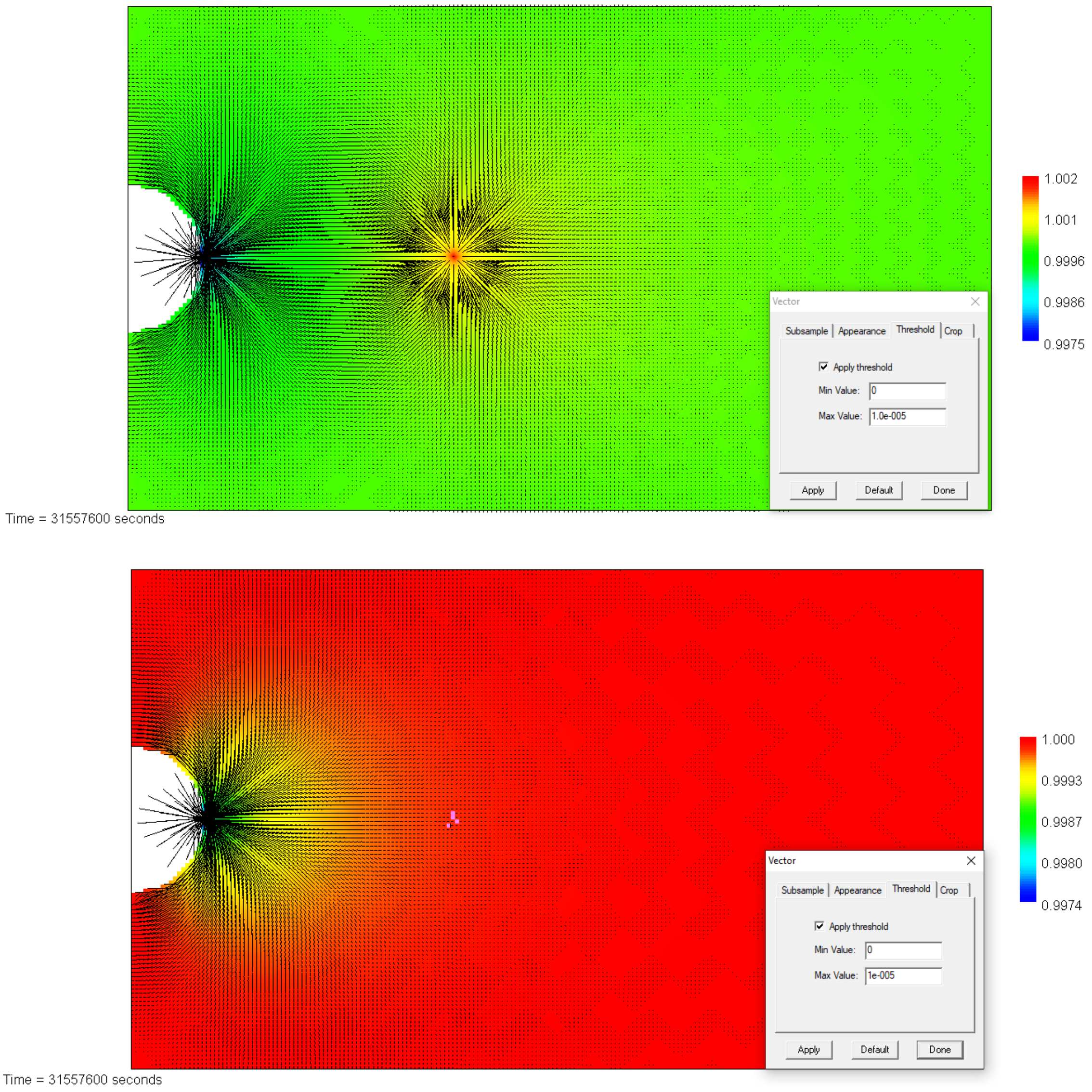

☑ Apply threshold

Min Value: 0

Max Value: 1.0e-005

Time = 31557600 seconds

☑ Apply threshold

Min Value: 0

Max Value: 1e-005

Time = 31557600 seconds

Fig. 6-2: Flow field with extraction rate at the Pinkel of 25 ml/min with (top) and without (bottom) injection of 0.33 mL/min at CFM 06.002

The flow is illustrated by the vectors and the fluid head [m] by the colour bar.

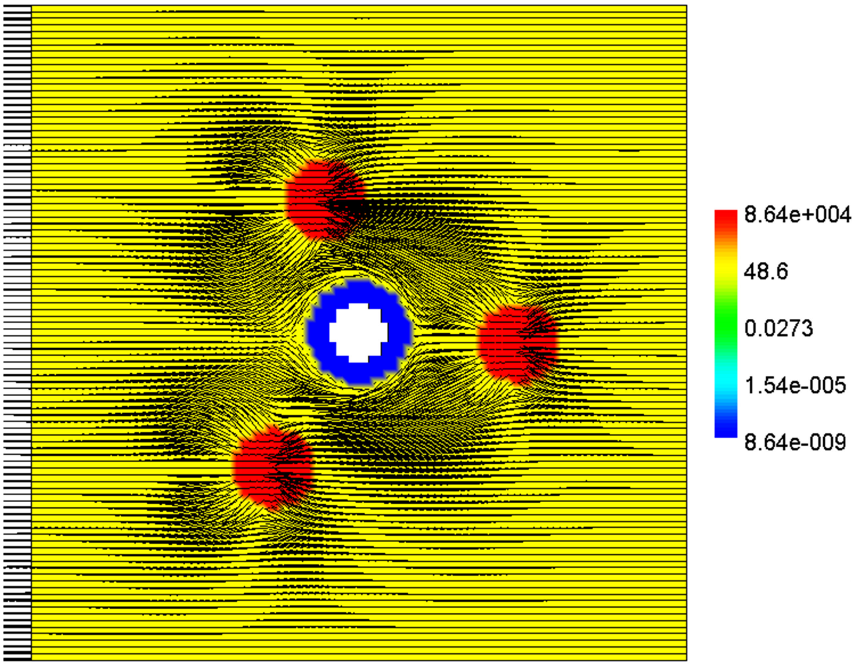

Fig. 6-3: Flow field in the detailed model with observation boreholes and bentonite ring. The flow is illustrated by the vectors and the hydraulic conductivity [m/d] by the colour bar

For the simulations, the bentonite was assumed to be fully saturated from the outset, so the saturation phase, which lasted about one month, was not simulated. The water content of the bentonite in this saturated state was 23.8 wt.% (Fernández et al. 2004). The saturated bentonite then also filled the entire cavity between the metal rod (shown as a closed boundary condition) and the borehole wall of CFM 06.002. Furthermore, a homogeneous bentonite ring without vials and without the slurries containing colloids and radionuclides was assumed. The composition of this bentonite was given as 99.2% montmorillonite and 0.015% gypsum (Fernández et al. 2004). Other equilibrium phases were not included here. In the model calculations, the gypsum content was increased as noted in the description of the calculation cases in Section 6.2.1.2. The hydraulic conductivity of bentonite was $1.0 \cdot 10^{-13}$ m/s (Lloret et al. 2004), and the porosity was assumed to be 0.48. Ion-exchange parameters were taken from (Fernández et al. 2004) and listed in Tab. 6-3.

Tab. 6-3: Parameters for ion exchange of Na^+, Ca^{2+} and Mg^{2+} (Fernández et al. 2004)

Ion exchange reaction	**Kc**	**Initial occupancies**	**[meq/kg]**
2Na-mont. + Ca = Ca-mont + 2Na	12.8	N_{Na}	270
2Na-mont. + Mg = Mg-mont + 2Na	10.7	N_{Ca}	330
Na-mont. + K = K-mont + Na	10.6	N_{Mg}	330
		N_K	23

Finally, for the transport model, it was considered that the observation boreholes had been filled with dummies to reduce the volume, as illustrated in Fig. 6-4. The figure also shows the coordinates of locations in the model area, where the temporal changes in the geochemical conditions are depicted for the evaluation of the results.

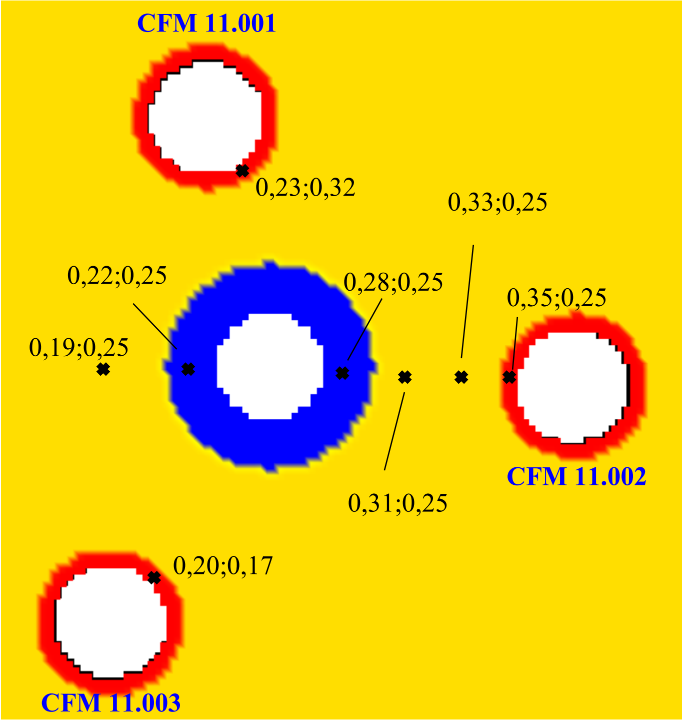

Fig. 6-4: Bentonite ring and observation boreholes, where the inner part is filled with dummies to reduce the volume

The black dots with the coordinates indicate the model observation spots, where chemical concentrations have been evaluated.

6.2.1.2 Modelling results

The calculations were performed over a modelling time of 4.5 years to cover the time frame of the LIT. The chemical processes, i.e. dissolution of gypsum and ionic exchange on the bentonite, were assumed to be in equilibrium. Three different calculation cases were considered. In order to investigate the impact of gypsum on the cation concentrations, for the first case, initial conditions in the bentonite were characterised as containing a content of 2% gypsum and the typical FEBEX bentonite porewater as listed in Tab. 6-1 (Fernández et al. 2004). In the second case, the initial conditions were assumed to be the same, except that the bentonite did not contain gypsum. The third case assumed 2% gypsum in the bentonite, as in the first case. An additional assumption was that the porewater in the bentonite was represented by Grimsel groundwater. This case was related to the experiment performed at FSU (see Section 2.1.2) to investigate the bentonite erosion under conditions where erosion rates are assumed to be highest (pessimistic assumption for the post-closure safety assessment).

The flow field and, as an example, 2D concentration distributions for Ca^{2+} are shown in Fig. 6-5. These are the concentrations calculated after 4.5 years, the timeframe of the LIT. In the fine-scale model, the flow field is determined by the boundary conditions on the left side originating from the extraction at the Pinkel as described above. However, the extraction rate at the CFM 11.002 observation borehole, which is three orders of magnitude lower than the flow rate at the Pinkel, also impacts the flow field to some extent. This is illustrated by the flow vectors in Fig. 6-5, which are very small (corresponding to a low flow velocity) in the area between the bentonite ring and the CFM 11.002 observation borehole. The pumping on the left of the observation borehole caused a flow in the opposite direction of the main flow field, thereby reducing the Darcy velocity in this area. Apart from the extraction rate at the observation hole, the relatively low flow on the right side of the bentonite was also due to the shielding effect of the low-permeable bentonite.

As a consequence of the flow conditions, the ion concentrations in the right half of the bentonite and in the space between CFM 06.002 and CFM 11.002 to the right of the bentonite remained higher than those at the other parts in the model area. In addition, gypsum remained in the system longer on the right-hand side, namely up to 300 days, while on the left-hand side, it completely dissolved much earlier because of the sharper gradient to the fissure. Thus, the areas to the right of the centre of the bentonite ring were enriched with SO_4^{2-} from the gypsum for longer.

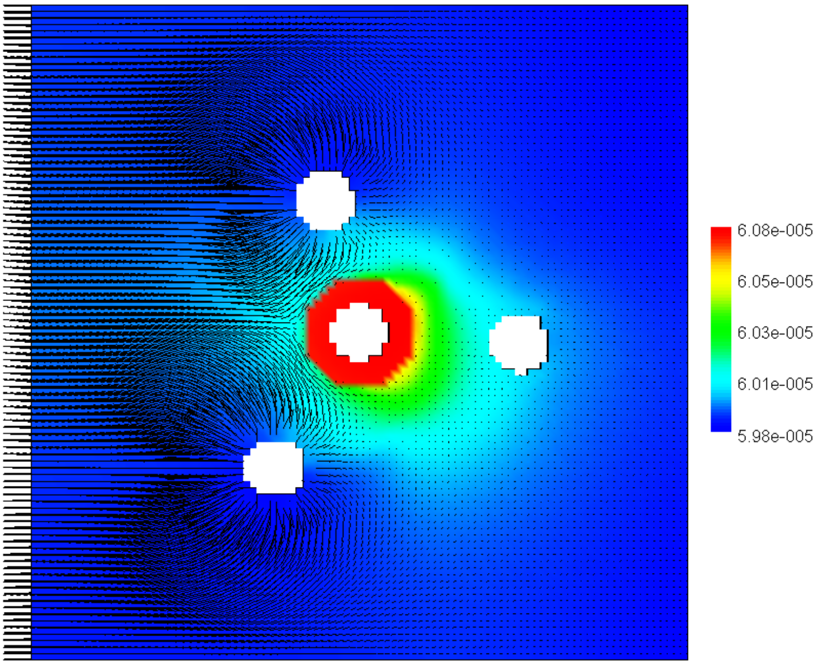

Fig. 6-5: Flow field indicated by the black arrows and distribution of SO_4^{2-} after a simulation time of 1,680 days

The concentrations of ions in solution and the occupancy of ion exchangers have been analysed in detail. Dissolution of gypsum and cation exchange processes are highlighted. The concentrations of sulphate, calcium, sodium, magnesium, chlorine and gypsum, as well as the ion exchanger concentrations CaX_2, NaX and MgX_2 and the pH value for the eight observation spots shown in Fig. 6-4 were recorded.

Fig. 6-6 shows the concentrations at the location 0.22;0.25. This is the first observation spot that is inside the bentonite. In the system with gypsum (left), the sulphate concentration increases for up to 60 days. The gypsum is no longer visible after 90 days within the scale used. The sulphate increase can therefore be explained by the presence of gypsum in the bentonite, which completely dissolved after less than 90 days from the start of the experiment. Ca^{2+} is also released from the gypsum. The Ca^{2+} concentration should also be slightly higher during the first 90 days than in the system without gypsum. However, the percentage of Ca^{2+} released from the gypsum is lower than that already present, since the initial Ca^{2+} concentration is much higher. In addition, the ion-exchange process reduces the Ca^{2+} concentration. In general, Ca^{2+}concentrations here decrease from a starting value. These initial concentrations, which are higher than the first two points, are the concentrations of the respective ions from the bentonite porewater (Fernández et al. 2004). The concentrations of the ions Mg^{2+} and Ca^{2+} drop particularly quickly in both systems. In the system without gypsum, sulphate is only present in the system up to the point in time of 270 days within the scale shown.

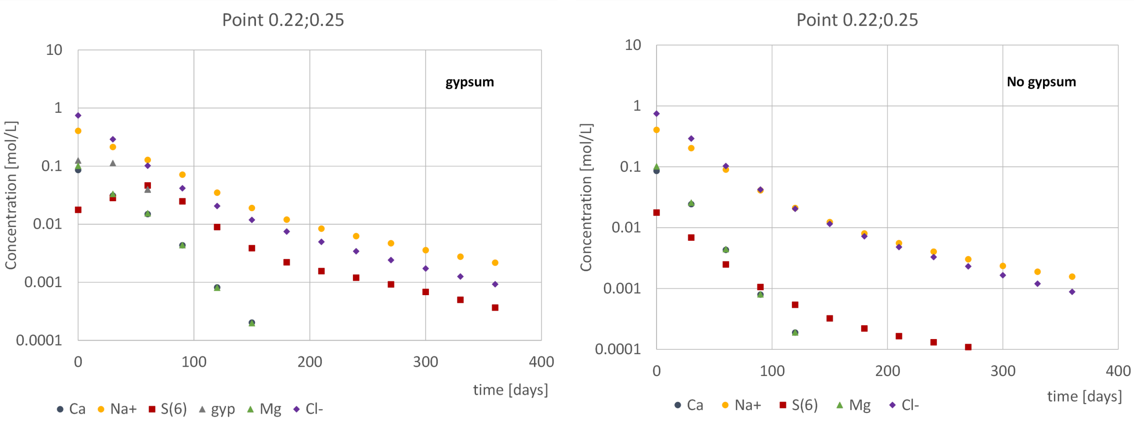

Fig. 6-6: Concentration of ions in solution for the system, with gypsum (left) and without gypsum (right) at observation spot 0.22;0.25 in the bentonite

Fig. 6-7 shows the concentrations of the dissolved ions at observation spot 0.28;0.25, i.e. in the bentonite. In the system with gypsum as the equilibrium phase, an increase in SO$_4^{2-}$, in the figures denoted as S(6) can be seen up to 180 days. This fits with the presence of gypsum in the system up to this point in time. In the right part of the bentonite ring, gypsum dissolution seems to have a much greater impact on ion concentrations. Due to the higher flow in the fracture to the left of the bentonite, the gypsum in the left part of the bentonite ring seems to be dissolved and transported away more quickly. The lower SO$_4^{2-}$ or Ca^{2+} concentration due to the stronger flow in the fracture on the left edge of the bentonite ring causes a higher gradient and thus stronger diffusion in the left part of the bentonite ring. The extraction at the CFM 11.002 borehole in combination with the generally lower flow on the right side of the bentonite, which is due to this side facing away from the extraction from the left, ensures that, on the right side of the bentonite ring, the Ca^{2+} and SO$_4^{2-}$ concentrations are higher in the gap. As a result, the gradient and diffusion on this side of the bentonite are lower, and gypsum is dissolved more slowly. The concentration of the other ions also decreases more slowly than at the observation spot 0.22;0.25. A kink can be seen on the curves of Ca^{2+} and Mg^{2+}between the time periods of 90 days and 180 days, which behave very similarly. Their gradient decreases and the concentrations fall more slowly. In the system without gypsum as the equilibrium phase, these slower falling curves cannot be observed, since no ions are released through the dissolution of gypsum.

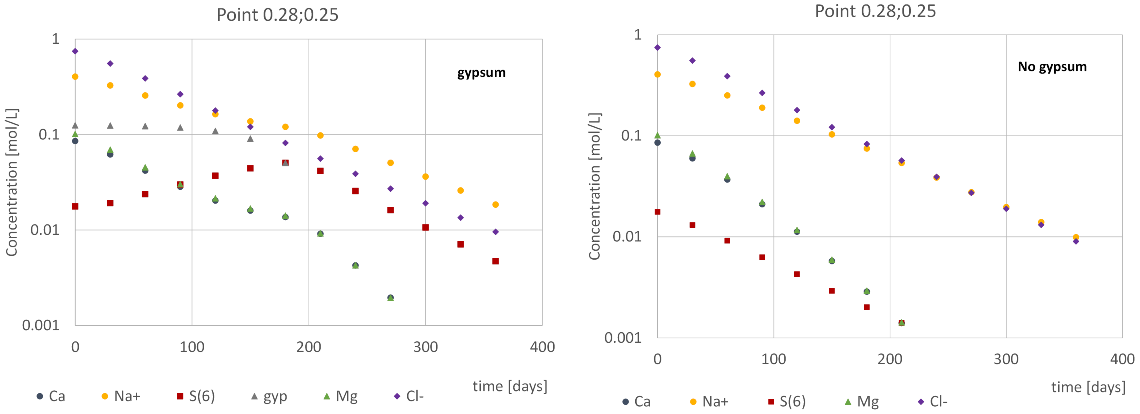

Fig. 6-7: Concentration of ions in solution for the system with gypsum (left) and without gypsum (right) at observation spot 0.28;0.25 in the bentonite

Fig. 6-8 shows the ion concentrations at observation spot 0.35;0.25 in the CFM 11.002 borehole, i.e. outside the bentonite. The curves show the course in the bentonite with a delay caused by transport. In the system with gypsum (left), the SO_4^{2-} slopes up to 180 days and then decreases, whereas the system without gypsum (on the right) shows a drop in the concentrations of all ions after 30 days. The curves for the cations Na^+, Ca^{2+} and Mg^{2+} decrease more slowly in the system with gypsum (left) than without gypsum (right). This could also be explained by the Ca^{2+} input by gypsum dissolution and its subsequent exchange with Na^+ and Mg^{2+} ions, increasing the concentration of all three ions in solution compared to the system without gypsum.

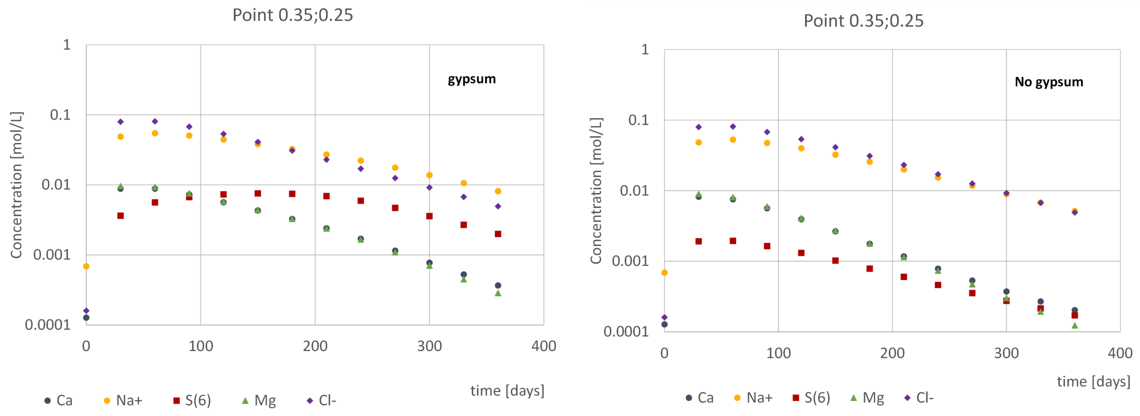

Fig. 6-8: Concentration of ions in solution for the system with gypsum (left) and without gypsum (right) in observation spot 0.35;0.25 outside the bentonite at the CFM 11.002 observation borehole

Fig. 6-9 shows the ion exchangers at observation spot 0.22;0.25 in the left half of the bentonite ring. A clear difference is visible between the system with gypsum (left) and without gypsum (right). In the system with gypsum, the Ca^{2+} content on the exchanger increased significantly within the first 90 days and stayed at a higher level afterwards compared to the system without gypsum (right). At the same time, the occupation of the NaX and, less clearly visible, of the MgX_2 exchangers were higher in the system without gypsum. Thus, in the system with gypsum, Na^+ and Mg^{2+} ions were released from the exchanger, while Ca^{2+} ions were taken up.

Fig. 6-10 shows the exchanger occupancy at the observation spot 0.28;0.25 in the right half of the bentonite ring. The general course of the exchanger is similar to those seen at spot 0.22;0.25. However, the increase of CaX_2 and the decrease of NaX and MgX_2 in the system with gypsum happened much more slowly here. This can be explained by the smaller gradients at the interface between bentonite and granite on the right side of the bentonite (cf. discussion above).

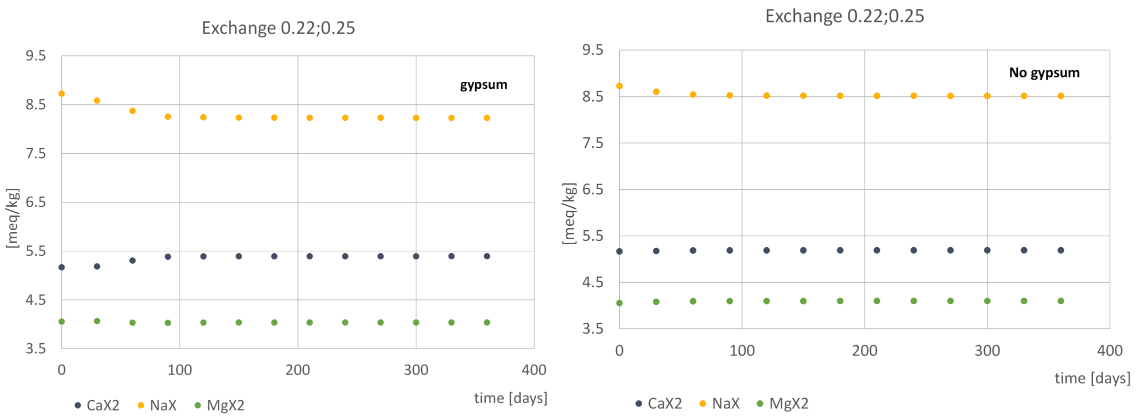

Fig. 6-9: Concentration of Ca, Na and Mg on the ion exchanger in the system with gypsum (left) and without gypsum (right) at observation spot 0.22;0.25 in the bentonite

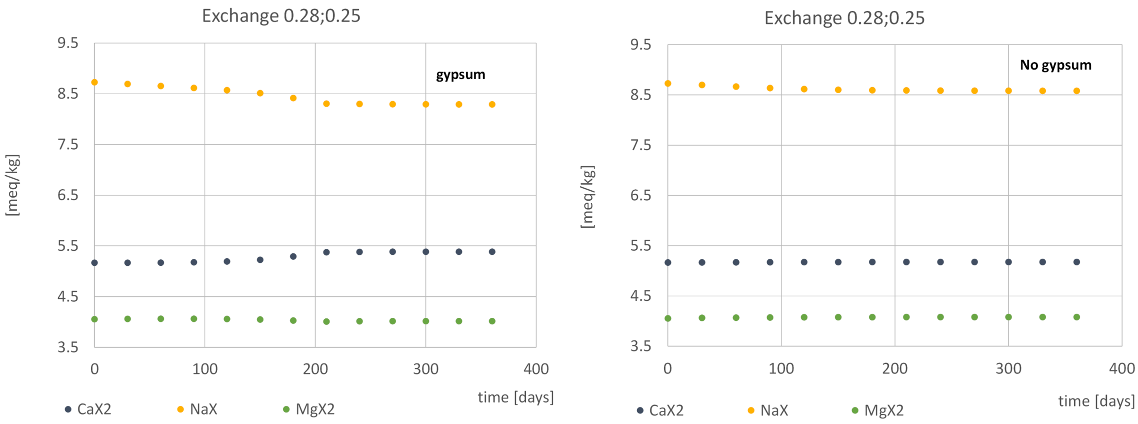

Fig. 6-10: Concentration of Ca, Na and Mg on the ion exchanger in the system with gypsum (left) and without gypsum (right) at observation spot 0.28;0.25 in the bentonite

While in the case of Ca^{2+}, ion exchange processes can be observed, through which Na^+ and partly probably also Mg^{2+} are released into the system, the SO_4^{2-} concentration is not reduced by such processes. Therefore, the Ca/SO_4ratios on different observation spots inside the model area are investigated to give evidence for ion exchange processes of Ca^{2+}.

Fig. 6-11 shows the Ca/SO_4 ratios at two observation spots in the shear zone for the system with gypsum, one on the left side and one on the right site of the bentonite source. The general course of the curves is similar: The ratio in the GGW is about 2. From this value, the ratio drops in both observation spots down to a value of 0.25. For the spot left of the bentonite source, this drop is much faster. After about 250 days, the ratio increases again and evolves back to the initial value after approx. 800 days. The curve for spot 0.35;0.25 at the observation borehole is delayed, i.e. it decreases more slowly down to the same value and increases again later back to the initial value. This can be explained by the impact of the flow conditions as described above.

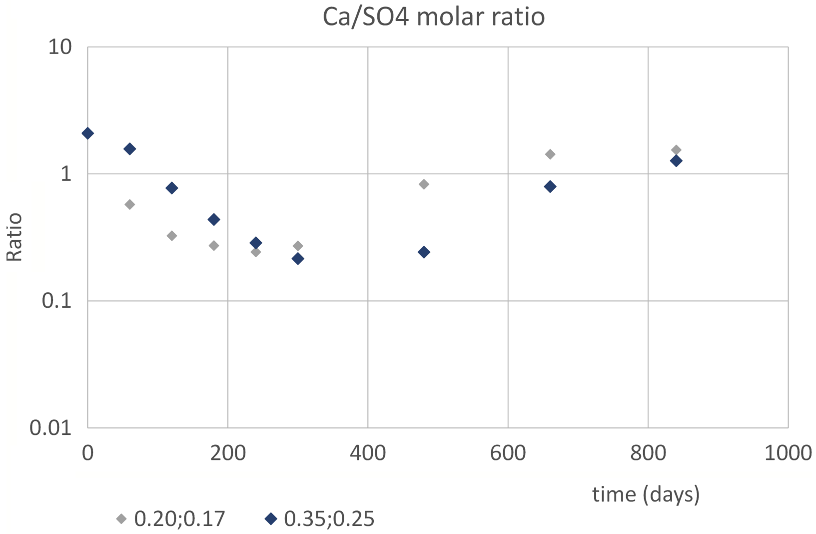

Fig. 6-11: Ratio of Ca^{2+} and SO_4^{2-} in solution in the fracture at the two observation spots 0.20;0.17 and 0.35;0.25 (observation borehole CFM 11.002)

When gypsum is dissolved, it is generally noticeable that the SO_4^{2-} concentration increases as a result, but the Ca^{2+} concentration increases significantly less. The initial concentration of Ca^{2+} in bentonite porewater is significantly higher than that of SO_4^{2-} (see Tab. 6-1). Thus, the effect of gypsum dissolution is more evident in the SO_4^{2-} concentration. Part of the Ca^{2+} released from the gypsum is exchanged by cation exchange processes, e.g. with Na^+ and Mg^{2+}. This can also explain the small concentration increases of Na^+ in the systems containing gypsum, as well as the change in the ion exchanger coverage (coverage with Ca increases, coverage with Na decreases). In the simulation models in this work, these exchange processes can only be seen up to the end of the first year of simulations at the latest, since the gypsum has completely dissolved by this time.

Finally, calculations were performed for the entire duration of the LIT, namely 4.5 years (1,680 days). The long-term distribution of the major ions in the model area is exemplarily shown for the area at the observation borehole CFM 11.002 in Fig. 6-12. The figure shows the early increase of major ion concentrations during the first 50 days caused by the high concentrations in the bentonite porewater, cf. also Fig. 6-7. Afterwards, the water is diluted by GGW flowing through the fracture, and concentrations of all ions are reduced, reaching the original concentration of GGW after about 800 days. The longer increase of SO_4^{2-} (S(6)), reaching its maximum at about 150 days, is caused by the dissolution of gypsum and the transport to the observation borehole. The concentration maximum of Ca^{2+} and SO_4^{2-} is about $9 \cdot 10^{-3}$ mol/l.

These results can be compared to experimental data from the LIT collected at the CFM 11.002 observation borehole by Rinderknecht (2017).

Fig. 6-13 shows the temporal evolution of the background-corrected concentrations of Ca^{2+} and SO_4^{2-} for about 500 days. No data is available for the first approx. 80 days, which roughly represents the phase of bentonite re-saturation. In the very beginning after the resaturation phase an increase of SO_4^{2-} and Ca^{2+} concentrations within a few days is visible. About 100 days after start of the LIT experiment the concentration of both ions decrease simultaneously, only that the

SO_4^{2-} concentrations are significantly higher. The maximum concentration increase against the background is between $5 \cdot 10^{-5}$ mol/L for Ca^{2+} and $1 \cdot 10^{-4}$ mol/L for SO_4^{2-}. This is about two orders of magnitude lower than the concentration values calculated by the model. The reason for this difference may result from the increased gypsum content of 2% in the model case compared to the average content of 0.015% gypsum in the FEBEX bentonite (Fernández et al. 2004), see description above. Concerning the temporal evolution of SO_4^{2-} and Ca^{2+} also in the model the SO_4^{2-} concentration appears to be higher than the Ca^{2+} concentration after 100 days until about 700 days. After 1,000 days the concentrations reach the GGW level. At least for the 500 days available from the LIT experiment the qualitative behavior of the simulation curve fits well.

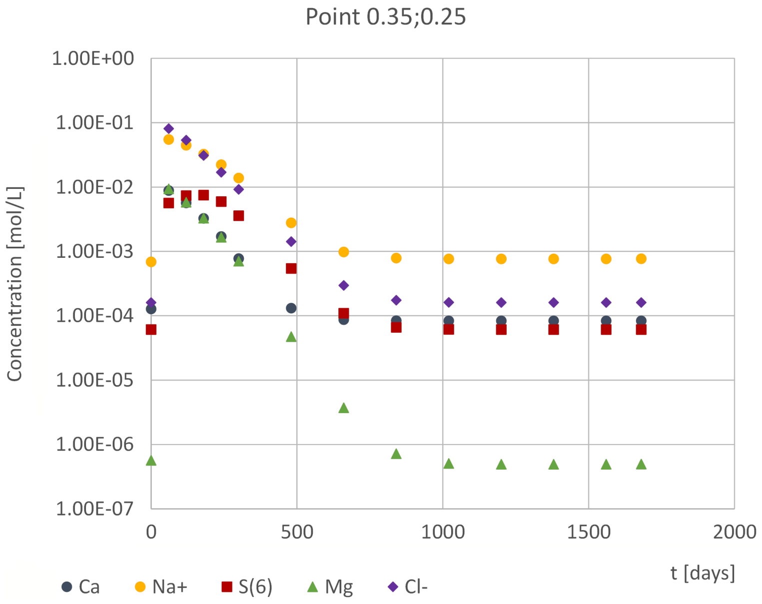

Fig. 6-12: Long-term evolution of major ions in the fracture exemplarily shown for the system with gypsum at observation spot 0.35;0.25 (CFM 11.002 observation borehole)

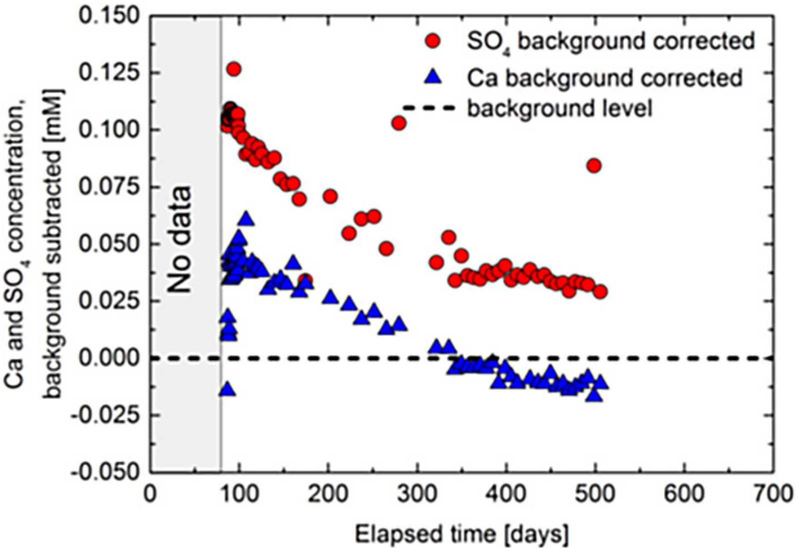

Fig. 6-13: Background-corrected Ca^{2+} and SO_4^{2-} concentrations in the Long-Term In-Situ Test (LIT) from

6.2.1.3 Summary and conclusions

In this work, a flow and transport model was developed to describe gypsum dissolution and ion exchange processes on montmorillonite within the framework of the LIT. In a first step, a coarse-scale (large-scale) model was developed based on experiences from previous modelling approaches to describe dipole field experiments. In the second step, a fine-scaled (detailed) model with a dimension of 0.5 m x 0.5 m was built, occupying the left edge of this model area with a flux boundary condition that reproduced the flow conditions simulated in the coarse-scale model in this area.

The transport calculations showed that the ion concentrations at the observation spots outside the bentonite increase initially. This can be explained by the influence of the more heavily mineralised bentonite porewater and partly also by the gypsum dissolution. The concentrations then decrease. The observation spots within the bentonite show falling concentrations of the ions from the beginning, caused by the concentration equalisation through diffusion of the bentonite. An exception is SO_4^{2-}, the concentration of which increases in the presence of gypsum. This elevation is of significantly longer duration on the right side of the bentonite. On the left side of the bentonite, the gradient to the fracture is sharper. As a result, ion exchange processes are less strong there than on the right-hand side of the bentonite. An increase in the Ca exchanger at early phases of the simulation explains the decrease in Ca^{2+} concentrations in the bentonite porewater. At the same time, the Na exchanger decreases. The Na^+ present in the bentonite is therefore exchanged by Ca^{2+}.

The model applied here is rather simple, particularly heterogeneities in the hydraulic parameters, such as permeability and porosity, of the shear zone have not been considered. Such heterogeneities were observed even in the direct vicinity of the bentonite source in the area where the observation boreholes are located. However, some general observations can be drawn from the model calculations. The gypsum dissolved within the first 90 – 180 days after the start of the simulation, which essentially increases the SO_4^{2-} concentration. On the other hand, no strong effect can be seen on the Ca^{2+} concentration. The Ca^{2+} concentration is mainly determined by the ion exchange processes. Within the bentonite, Ca^{2+} behaves very similarly to Mg^{2+}. In addition to the less sharp gradient at the right edge of the bentonite, the extraction rate used in the CFM 11.002 borehole also has a major impact on the transport processes. The increase in the SO_4^{2-}

concentration caused by the gypsum dissolution can still be observed in slightly increased concentrations after 4.5 years to the right of the bentonite ring at observation spots outside the bentonite. This can also be seen in the 2D representations of the ion concentrations in the model area, which show an uneven ion distribution around the bentonite ring. The presence of gypsum in the system no longer had any influence on the concentrations by the end of the 4.5-year simulation. Ca/SO_4 ratios at the various observation spots considered decreased at the beginning of the simulations. The ratios increase again and reach steady-state ratios of 1 after about 800 days. Further details of this investigation can be found in (Chemnitius 2021).

6.2.2 Simulation of geochemically changing conditions during bentonite erosion experiments

Bentonite erosion was studied by developing a flow and reactive transport model using PHAST (PHREEQC and HST3D) (Parkhurst et al. 2010) to simulate reactive solute transport and ion exchange of MX-80 bentonite in a saturated 2D fracture. It was intended to depict the erosion experiment at FSU Jena (see Section 2.1.2). In the reference case, the ion exchange between MX-80 and Grimsel groundwater was investigated. Variations were performed to study the influence of Ca enrichment of the GGW and of an increase of Ca availability due to gypsum as internal reservoir. Finally, a model variation was accomplished to investigate the flow field of the PHAST model.

6.2.2.1 Model development

The description of the experimental setup can be found in Section 2.1.2. Simplifications were necessary to transfer the experiment into a PHAST model. Initially, the bentonite, which is found in the centre of an open fracture, was 13 mm in diameter. During the experiment, the bentonite swelled into the fracture. PHAST cannot consider a change of geometry during one simulation. The reference case simulation was executed with a bentonite diameter of 61 mm (Fig. 6-14), that corresponds to the complete expansion into the fracture in the case of the Na-exchanged MX-80 sample that was preconditioned to 100% Na. As in the experiment (see Section 2.2.1.4), it is distinguished between the outer ring, inner ring and core. Not in the reference case but in the model variation, different properties were assigned for the different parts of the bentonite. In the experiment, the fracture had a height of 1 mm, and the bentonite had a height of 5 mm, so that as the bentonite expanded into the fracture, fresh bentonite became available as source for the expansion. For the model in PHAST, it was assumed that the total region had a height of 1 mm. The volume flow of 50 µL/min in the experiment was directly transferred to the model by defining a borehole as an injection point and an extraction point (highlighted in red in Fig. 6-14). A fracture size of 82 mm in length and width was used and discretised to cells with a length and width of 4 mm. The flow input parameters of the reference case are provided in Tab. 6-4.

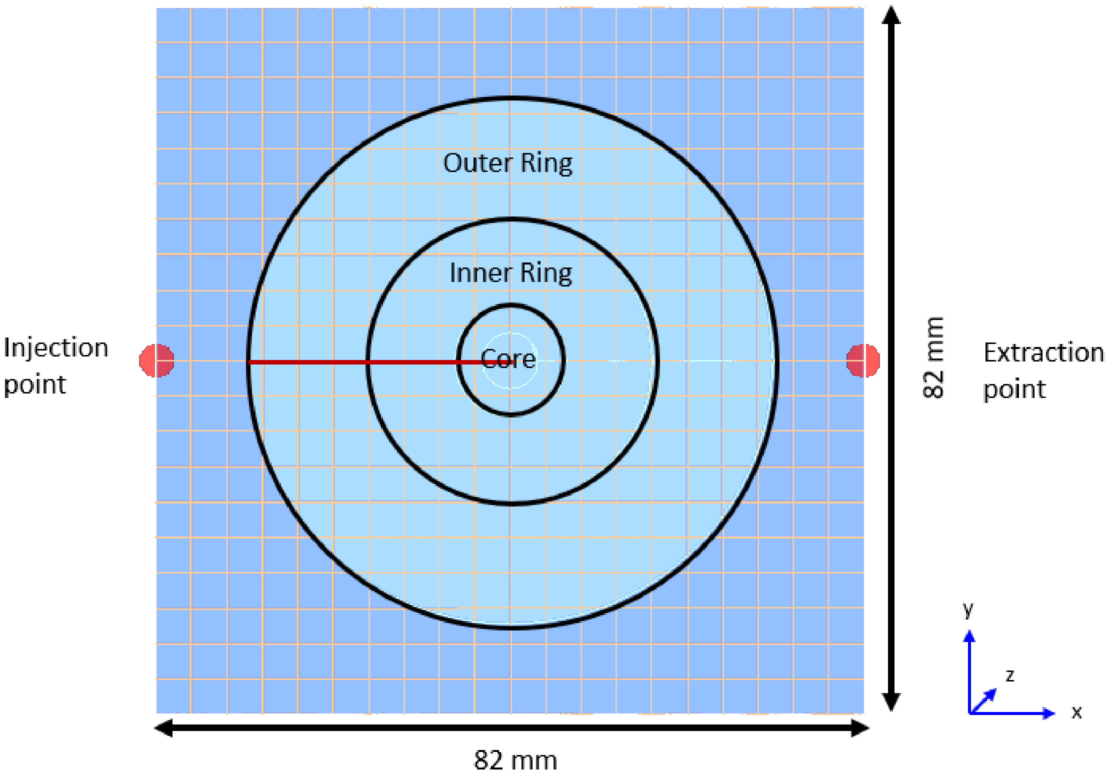

Fig. 6-14: Grid of the reference case with bentonite (diameter of 61 mm) in the centre of an open fracture

The bentonite is divided into three regions: core, inner ring, and outer ring, details see text. The fluid injection and extraction point are highlighted in red. results are depicted along the red line. Due to the relatively high flow in the fracture, the differences in the results between the left and right parts of the bentonite are low, and only results for the left part are shown.

Tab. 6-4: Input parameters (for the reference case)

Parameter	**Unit**	**Value**	**Reference**
Porosity (Fracture)	-	1.0	Assumption
Hydraulic Conductivity (Fracture)	m/s	10^{-4}	Assumption
Target density (Bentonite) ρ_t	kg/m³	1,630	Kiviranta & Kumpulainen (2011)
Mineral density ρ_m	kg/m³	2,700	Kiviranta & Kumpulainen (2011)
Porosity (Bentonite)	-	0.4	$1-\frac{\rho_t}{\rho_m}$
Hydraulic Conductivity (Bentonite)	m/s	10^{-13}	Zhang et al. (2023)
Model thickness	mm	1.0	Experiment
Model length	mm	82.0	Experiment
Model width	mm	82.0	Experiment
Diffusion coefficient	m²/s	$2.8 \cdot 10^{-10}$	van Loon (2014)
Longitudinal Dispersivity	mm	8.2	Assumption
Vertical Dispersivity	mm	0.82	Assumption
Horizontal Dispersivity	mm	0.82	Assumption

For the laboratory experiment at FSU Jena, bentonite samples were preconditioned in different ways, resulting in different types of bentonite samples (Section 2.1.1.4). The simulations were carried out for the MX-80 sample, which was exchanged to 100% Na. In the reference case with Grimsel groundwater (GGW) and in the variation with Ca-enriched GGW (Ca+GGW), the sample consisted of 100% of montmorillonite. In the variations with gypsum content, 10 wt.% quartz were added. For the calculation of the phase composition, the sample was considered saturated. The bentonite sample had an initial diameter of 13 mm and initial height of 5 mm. The sample expanded to a maximum diameter of 61 mm with a height of 1 mm (equal to the fracture). The volume increased from 0.67 cm³ (dry sample) to 2.8 cm³ (saturated sample). With a steady porosity of 0.4 and a sample mass of 1 g, there was 1.12 g water per saturated sample. Thus, the amount of montmorillonite in the reference case was 2.8 mol/kg water. For the variation with 2 wt.% gypsum content, 0.1 mol/kg water gypsum and 2.04 mol/kg water montmorillonite were defined. For the case of 5 wt.% gypsum, 0.26 mol/kg water gypsum and 1.97 mol/kg water montmorillonite were defined. The initial site composition was measured at the FSU Jena and the derived model input data are shown in Tab. 6-5 and Tab. 6-6. To determine the initial NaX value, the CEC was used instead of the measured Na concentration, due to the discussed uncertainties concerning this value (Tab. 6-5).

Experiments and simulations were carried out with the Grimsel groundwater and a Ca-enriched Grimsel groundwater when the former was used in the reference case. The main components are listed in Tab. 6-6 (measured in the laboratory of FSU Jena).

Ion exchange was defined as follows (Bradbury & Baeyens 2002):

$$2Na\text{-}clay + Ca^{2+} \leftrightarrow Ca\text{-}clay + 2Na^{+}$$

$$\frac{Ca}{Na} K_c = \frac{NCa}{N2Na} \cdot \frac{a2Na}{aCa} = 2.175 \text{ (mean value)}$$

$$Na\text{-}clay + K^{+} \leftrightarrow K\text{-}clay + Na^{+}$$

$$\frac{K}{Na} K_c = \frac{NK}{NNa} \cdot \frac{aNa}{aK} = 4.025 \text{ (mean value)}$$

$$2Na\text{-}clay + Mg^{2+} \leftrightarrow Mg\text{-}clay + 2Na^{+}$$

$$\frac{Mg}{Na} K_c = \frac{NMg}{N2Na} \cdot \frac{a2Na}{aMg} = 2.575 \text{ (mean value)}$$

Tab. 6-5: Initial site composition

Site type	[µg/g]*	[mol/kg water]**
NaX	19,918	0.681
CaX2	412	$8.08 \cdot 10^{-3}$
KX	60	$1.22 \cdot 10^{-3}$
MgX2	290	$9.37 \cdot 10^{-3}$

* Data provided by FSU Jena, **Model input derived for 0.88 g montmorillonite and 1.12 g water present in the saturated sample

Tab. 6-6: Main composition of the Grimsel groundwater (GGW) and the Ca-enriched Grimsel groundwater

Component	GGW [mol/L]	2 mmol Ca+GGW [mol/L]
Na	$3.65 \cdot 10^{-04}$	$3.65 \cdot 10^{-04}$
K	$5.14 \cdot 10^{-06}$	$5.37 \cdot 10^{-06}$
Mg	$1.02 \cdot 10^{-06}$	$1.02 \cdot 10^{-06}$
Ca	$2.02 \cdot 10^{-04}$	$2.11 \cdot 10^{-03}$
Mn	$1.86 \cdot 10^{-08}$	$1.80 \cdot 10^{-08}$
Sr	$1.51 \cdot 10^{-06}$	$1.65 \cdot 10^{-06}$
Cl	$1.66 \cdot 10^{-05}$	$3.82 \cdot 10^{-03}$
HCO_3	$4.80 \cdot 10^{-04}$	$4.80 \cdot 10^{-04}$
Si	$1.56 \cdot 10^{-04}$	$1.56 \cdot 10^{-04}$
$(SO_4)^{2-}$	$6.69 \cdot 10^{-05}$	$6.61 \cdot 10^{-05}$
F	$2.25 \cdot 10^{-04}$	$2.15 \cdot 10^{-04}$

6.2.2.2 Results

In the following, the results are discussed for the reference case and its variations. At first, the exchange sites were primarily occupied with sodium. During the experiment and model simulation, sodium was mainly exchanged for calcium. The results of the simulation in the reference case show that the exchange of Na for Ca mainly took place at the boundary of the bentonite (high CaX2 values), very little exchange occurred in the outer ring and no exchange took place in the inner ring and core (Fig. 6-15 and Fig. 6-16). The flow field (Fig. 6-15) showed that the inflowing solution mostly flowed around and only a small amount diffused through the bentonite. This was due to the very low hydraulic conductivity of the bentonite of 10^{-13} m/s. Therefore, less fresh solution from the injection point reached the bentonite, and only a small amount of Ca was available for the exchange. The Ca concentration of the bentonite porewater (Fig. 6-17) showed that initially, Ca was extracted from the GGW, but in the inner ring and core, only a very small amount of fresh solution followed. Fresh solution from the injection point only met the outer ring of the bentonite, where the exchanger occupation with Ca increased with time and, consequently, the Ca concentration increased and reached the GGW concentration when the exchange sites were completely occupied with Ca. Complementary Na concentration in solute initially increased to 18 mg/L, when GGW and bentonite reached equilibrium (Fig. 6-17). With increasing time, dissolved Na diffused out of the bentonite into the fracture being transported towards the extraction point and Na concentration in the porewater decreased. In comparison to the model simulation, the bentonite in the experiment swelled and expanded into the fracture during the first days and became a more porous material which was easier to flow through. Consequently, in the experiment, the bentonite was completely eroded after 35 days. The swelling process into the fracture and gradual increase of the hydraulic conductivity could not be represented in the PHAST model. An approximation was attempted using the model variant discussed below.

At first, the Ca concentration in the extraction point decreased sharply because the solution and the exchange sites were equilibrated, and Ca was instantly removed from the solution. Afterwards, when the exchange rate was smaller, the Ca concentration increased and tended towards the initial solution-concentration (Fig. 6-18). In contrast, the Ca concentration of the extracted solution of the experiment decreased more slowly but reached a comparable minimum concentration. In the experiment, the bentonite had eroded after 35 days, therefore the calcium concentration reached the initial GGW concentration at that time.

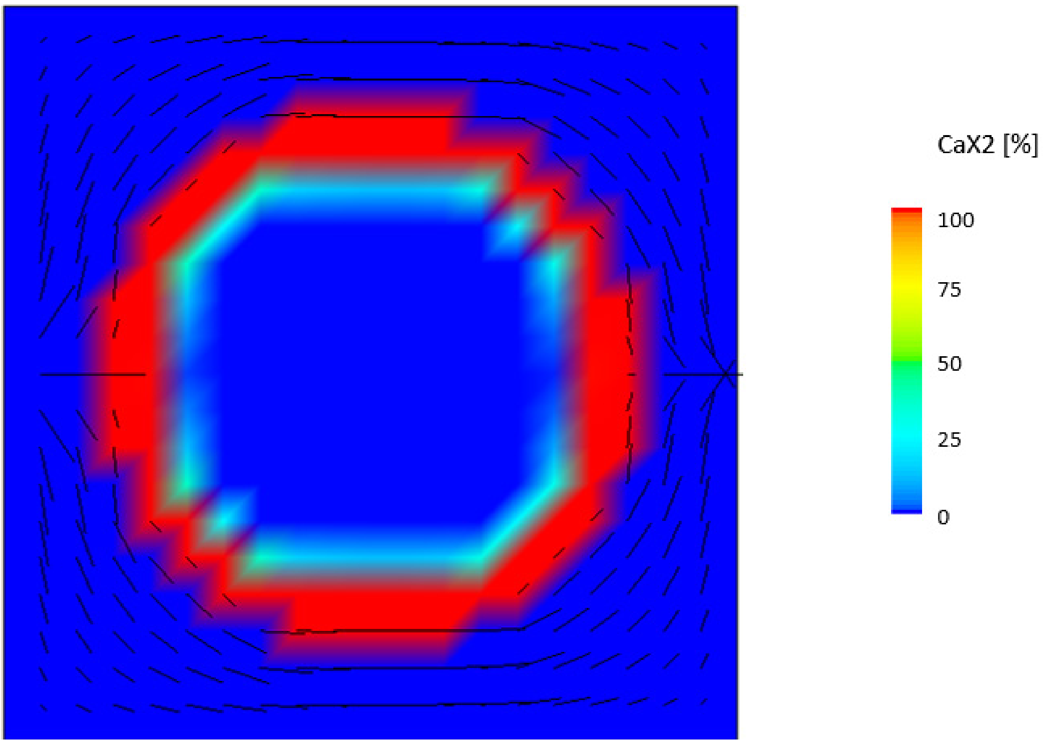

Fig. 6-15: CaX2 [%] of the reference case after 120 days and the flow field as vectors

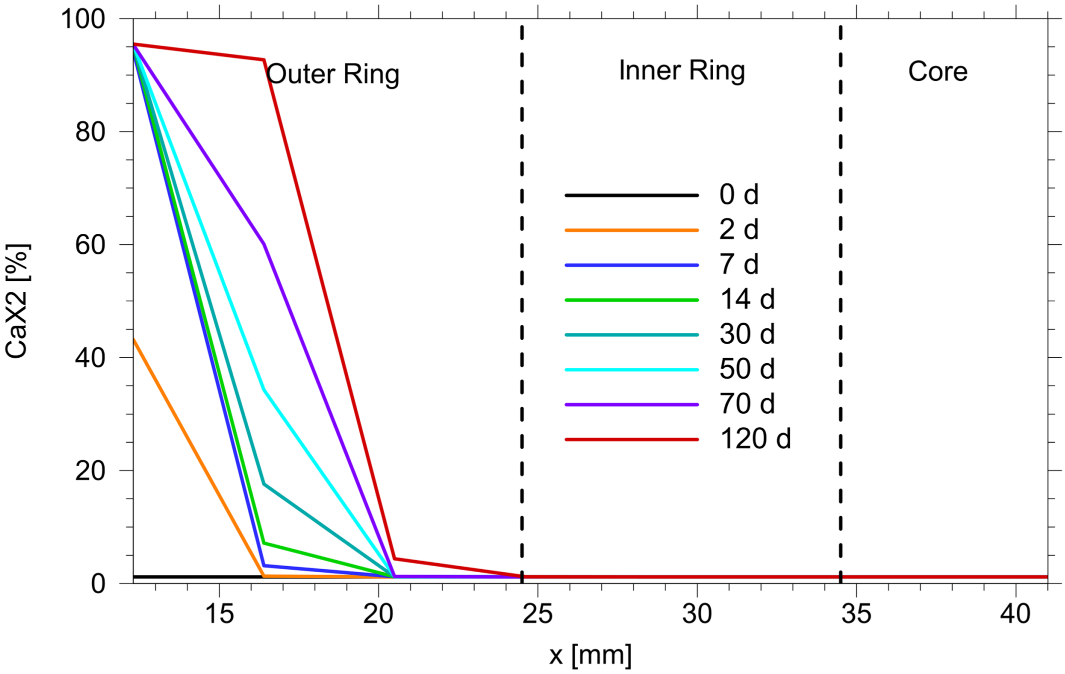

Fig. 6-16: Exchanger occupation with Ca (CaX2) [%] for the reference case along the red line in Fig. 6-14

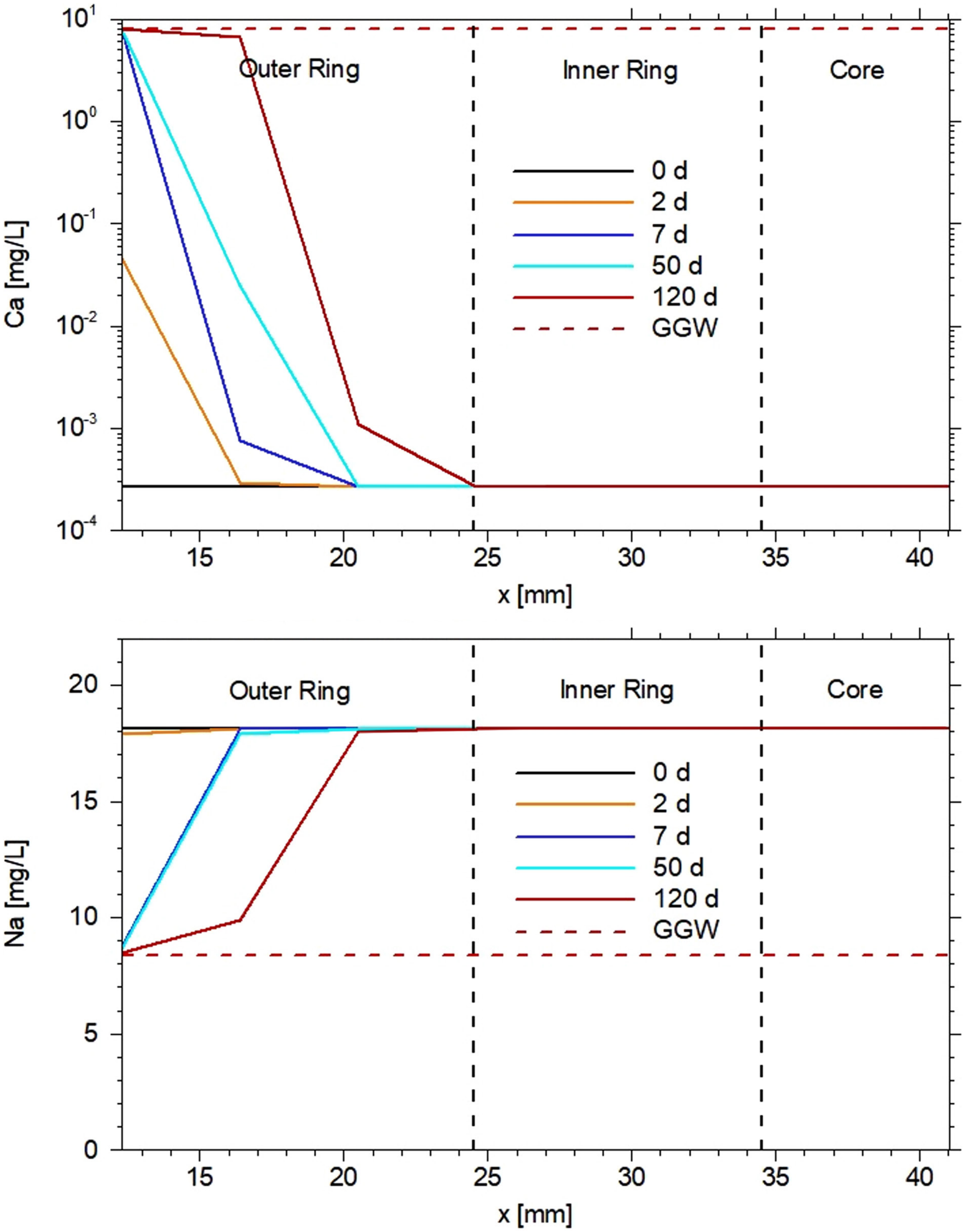

Fig. 6-17: Ca and Na concentrations of the bentonite porewater for the reference case

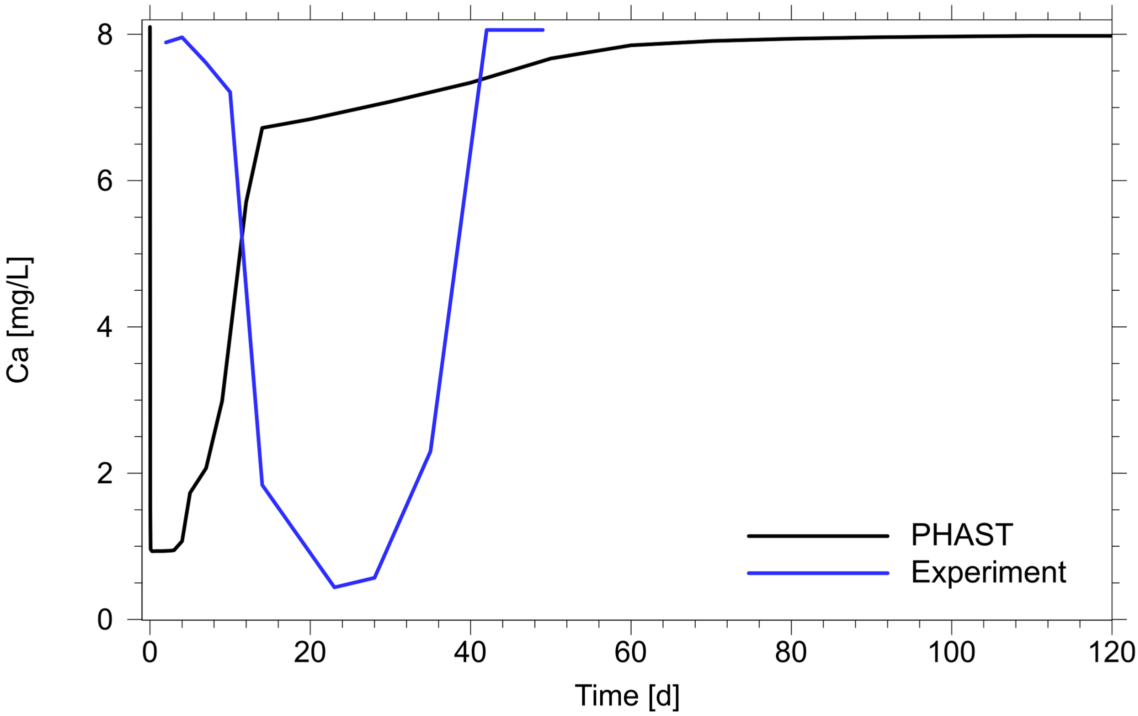

Fig. 6-18: Ca concentration in solute at the extraction point of the reference case (PHAST) compared to the Ca concentration of the extracted solution from the experiment

The initial solution is from the BOUS 85.003 extraction site and has a Ca concentration of 8.09 mg/L.

If the exchange sites have a higher Ca occupation, erosion is slower because of the reduced swelling properties of a Ca bentonite. When Ca occupies the interlayers of bentonite instead of Na, less water can intrude because interlayers are more cohesive. In conclusion, bentonite erosion is delayed due to the higher ionic strength of Ca. The Cation exchange process thus allows conclusions about the bentonite erosion process. The following discusses how erosion can be delayed and how erosion is affected by increased Ca concentration in solute and increased Ca availability due to an internal reservoir.

Influence of the Ca enrichment of the Grimsel groundwater

When the Grimsel groundwater is enriched by 2 mmol Ca, the higher availability of Ca causes increased exchanger occupation with Ca (Fig. 6-19). With increasing time, the exchange is retarded due to the small diffusion coefficient of Ca. After 120 days, Ca occupation increases up to 55% in the inner ring, whereas an increase of 0.01% takes place in the reference case. By increasing the Ca concentration of the GGW, the total exchange increased by a factor of two. When comparing the experimental and modelled data, the exchanger occupation with Ca is higher in the experiment (Fig. 6-20). In the experiment, more fluid intrudes into the inner ring and core due to swelling. Therefore, Ca availability and ion exchange are greater. Initially, the Ca concentration of the bentonite porewater (Fig. 6-21) is 10^{-2} mg/L and thus approximately two orders of magnitude higher than in the reference case. Due to the higher Ca concentration and the associated higher ionic strength, slower erosion is assumed. The Na concentration of the bentonite porewater is initially increased by 88 mg/L, when equilibrating with Ca-enriched GGW instead of GGW. Na concentration decreases with time when Na diffuses out of the bentonite towards the extraction point. Although the remaining Ca in solute is larger than in the reference case, Ca is not exchanged further because of the high Na concentration of the porewater, resulting in a competitive reaction between Na and Ca for the exchange sites.

Influence of accessory minerals

The influence of the accessory mineral gypsum on bentonite erosion was investigated for 5 wt.% and 2 wt.% gypsum in the bentonite.

Dissolution of gypsum increased the amount of calcium in the porewater. Most of the gypsum was dissolved when gypsum and the Grimsel groundwater were initially equilibrated. In the case of 5 wt.% gypsum, 75% dissolved. For the 2 wt.% gypsum, up to 95% dissolved (Fig. 6-22). After the initial equilibration, less fresh GGW was available, therefore dissolution was smaller after the initial equilibration, especially in the inner ring and core (Fig. 6-22). Gypsum was completely dissolved after 12 days in the case of 5 wt.% gypsum. In the case of 2 wt.% gypsum, it took 2.2 days. After gypsum dissolution, the exchanger occupation (CaX2) with Ca did not notably increase in the inner ring and core, so that the exchanger occupation in these areas was mainly determined by the dissolution of gypsum and not by the Ca present in the Grimsel groundwater (Fig. 6-23). Influx of Ca from the injection point only increased the exchanger occupation in the outer ring. After initial equilibration, the exchanger occupation in all bentonite regions was increased by 11%. In total, the exchange in the bentonite was three times larger for 5 wt.% gypsum and 60% higher for 2 wt.% gypsum compared to the reference case. In the case of 5 wt.% gypsum, 75% of gypsum was initially dissolved, therefore the calcium concentration in the porewater increased to 390 mg/L compared to the reference case (Fig. 6-24). Due to cation exchange and diffusion out of the bentonite, calcium concentration in the porewater decreased with time. After 12 days, gypsum was completely dissolved, and calcium concentration was not increased by the internal reservoir. After 30 days, the Ca concentration reached a stationary value in the inner ring and core, while the Ca concentration in the outer ring increased by the influx of GGW. At first, the Ca concentration of the porewater exceeded critical coagulation concentration (CCC) of 80.2 mg/L (Seher et al. 2020), thus it was assumed that no colloids formed. After two days, the Ca concentration at the boundary of the bentonite fell below CCC, and after 14 days, the Ca concentration was lower than CCC for all bentonite regions. Hence colloids could not coagulate after dissolution of gypsum was completed. Nevertheless, erosion was delayed due to the higher Ca concentration and related higher ionic strength in the porewater and the considerably higher exchanger occupation with calcium. The Na concentration in the porewater increased, too, due to the exchange reaction with Ca. Compared to the reference case, the Na concentration increased by a factor of 180 (Fig. 6-24). With time, Na diffused out of the bentonite and towards the extraction point, thus the concentration in the porewater decreased. After 30 days, the Na concentration in the inner ring and core reached a steady value that was equal to the concentration of the reference case. There was only a small decrease in the Na concentration after 30 days in the outer ring. The increased Na concentration resulted in a competitive reaction for the exchange with Ca. It was concluded that adding gypsum only had an effect for a short initial period when assuming an equilibrium dissolution reaction. In the experiment, gypsum dissolution took longer, so that it was reasonable to consider incorporating kinetic dissolution reactions in future modelling activities.

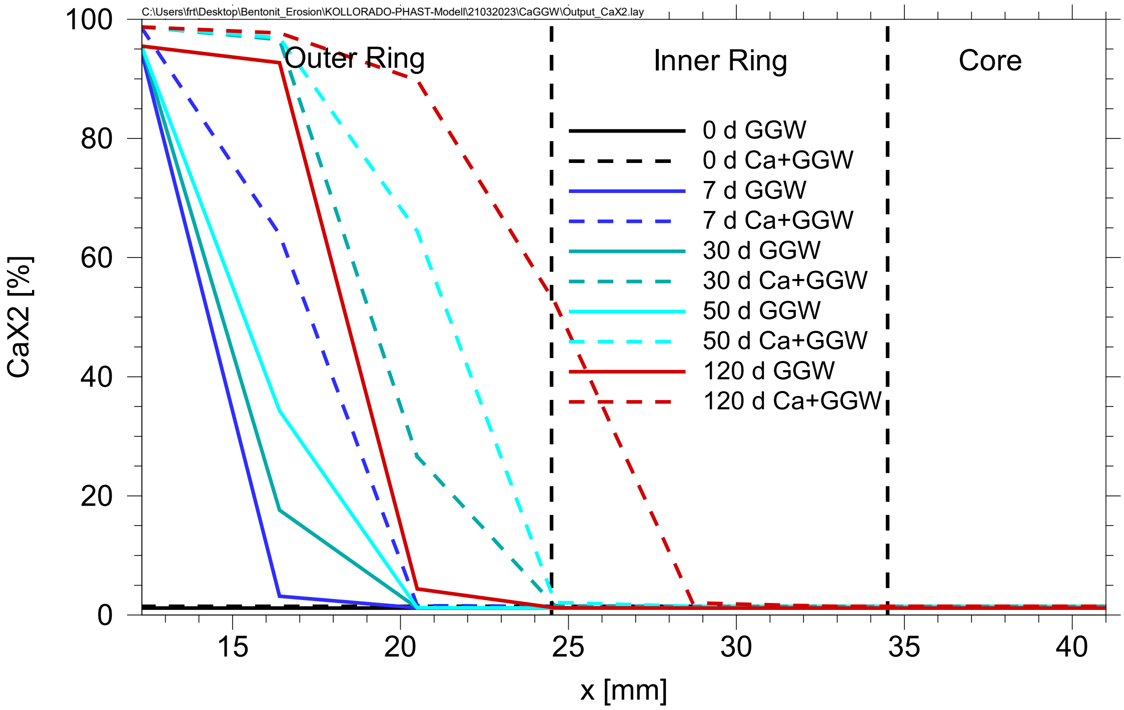

Fig. 6-19: Exchanger occupation with Ca (CaX2) [%] for the reference case (GGW, solid lines) and the variation with Ca-enriched Grimsel groundwater (Ca GGW, dashed lines)

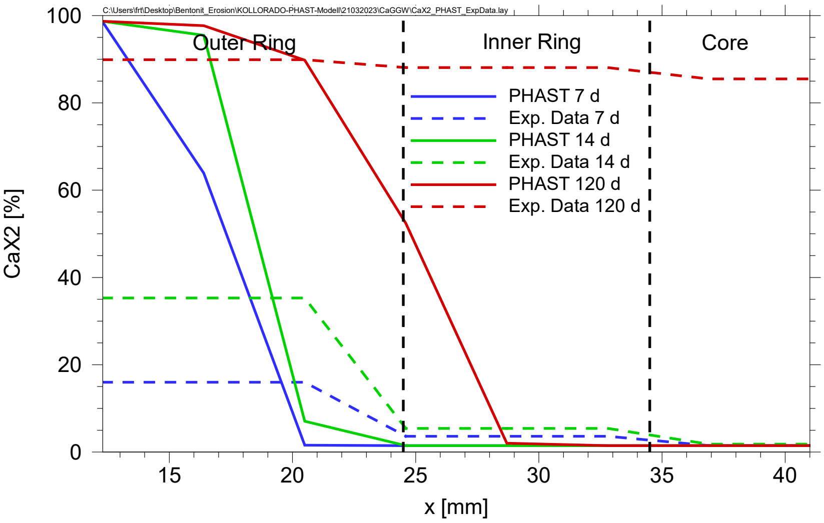

Fig. 6-20: Comparison of the exchanger occupation with Ca (CaX2) [%] for the simulation with Ca-enriched GGW (PHAST) and the experimental data

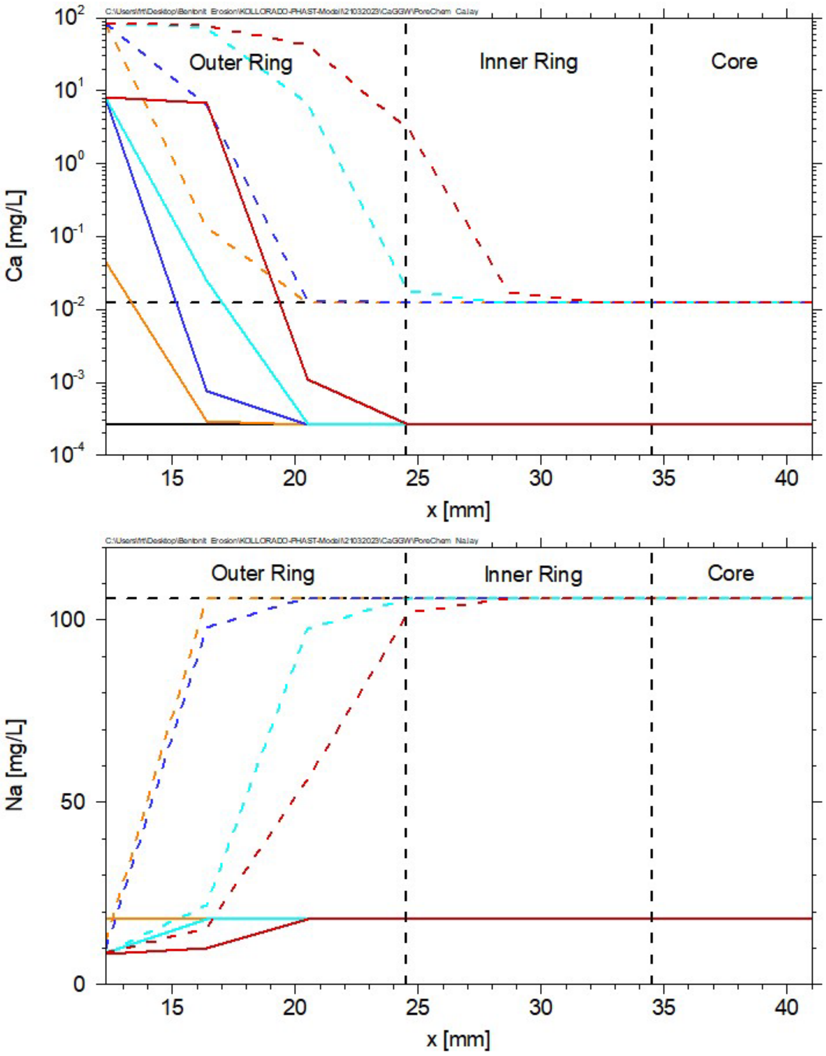

Fig. 6-21: Ca and Na concentrations of the bentonite porewater for the variation with Ca-enriched GGW (dashed lines) compared to the reference case (solid lines)

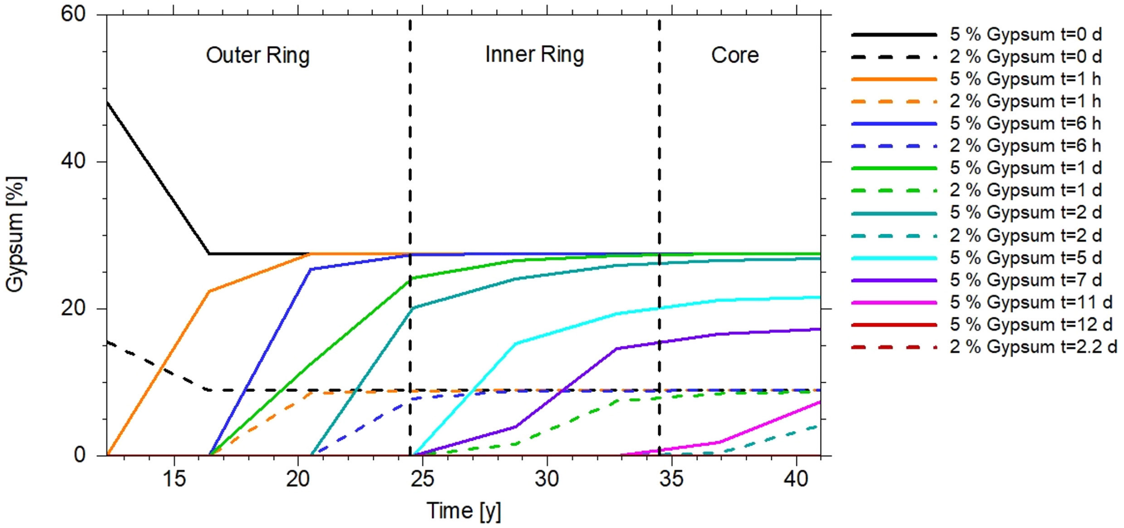

Fig. 6-22: Gypsum content [%] over time in the case of 5 wt.% (solid lines) and 2 wt.% gypsum (dashed lines) in the bentonite

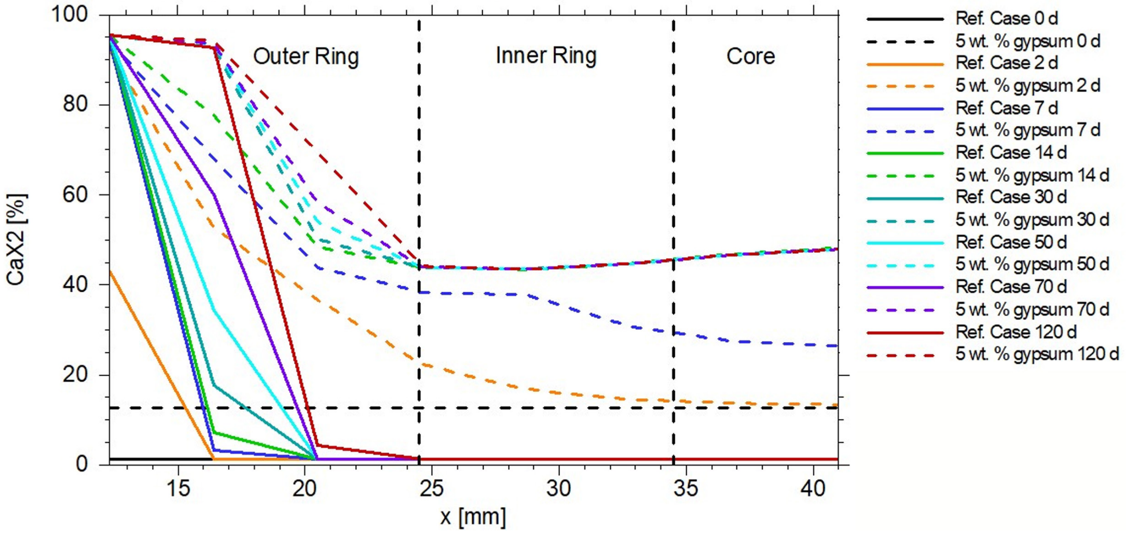

Fig. 6-23: Comparison of the exchanger occupation with Ca (CaX2) [%] for the reference case and the variation with 5 wt.% gypsum

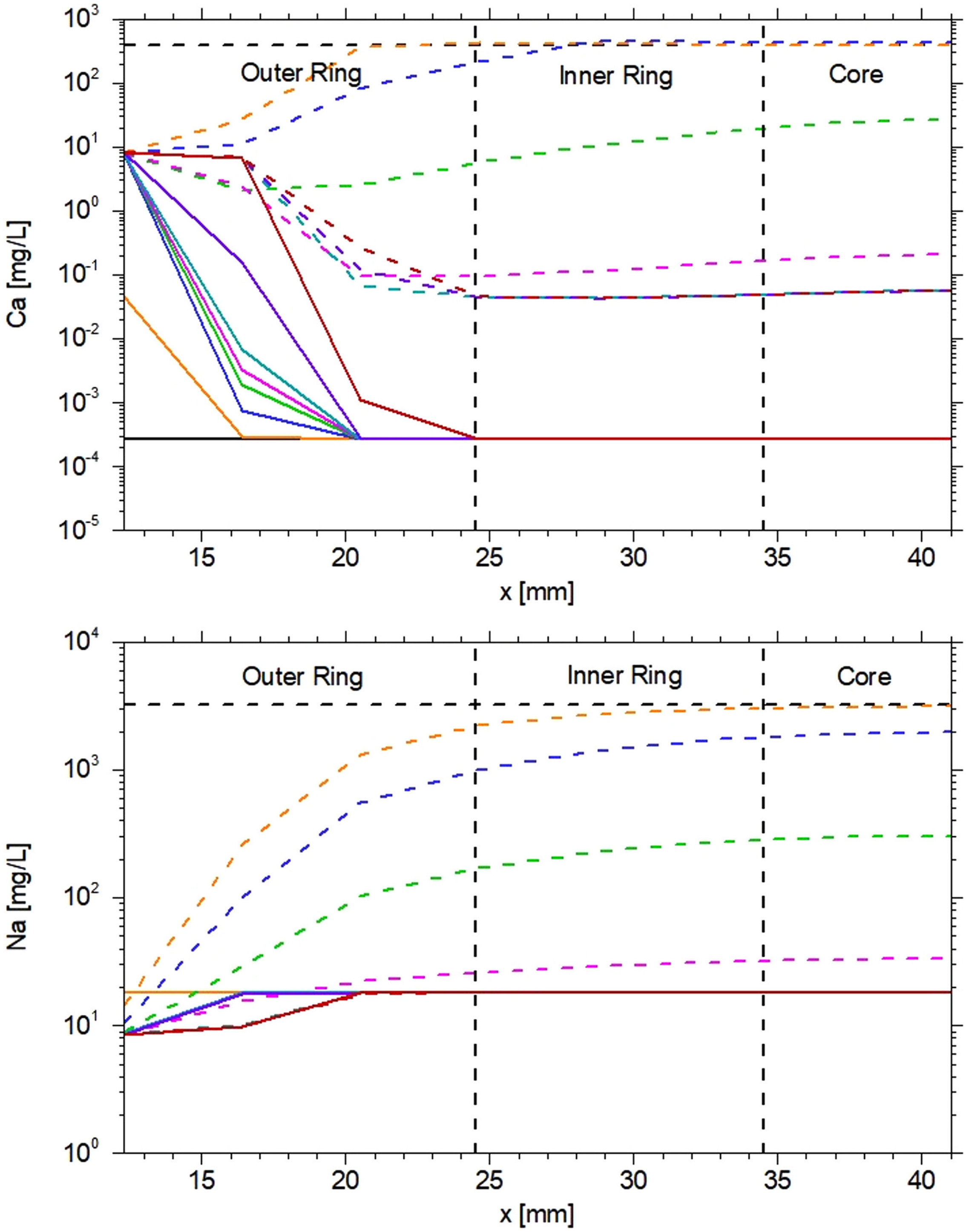

Fig. 6-24: Ca and Na concentrations [mg/l] of the bentonite porewater for the variation with 5 wt.% gypsum (dashed lines) compared to the reference case (solid lines)

Model variation

In a variation, the bentonite regions, i.e. core, inner ring, and outer ring, differed in their hydraulic conductivity. The core had a hydraulic conductivity of 10^{-13} m/s (as in the reference case), whereas the hydraulic conductivity of the inner ring was 10^{-08} m/s and that of the outer ring was 10^{-06} m/s instead of 10^{-13} m/s. The flow field showed that the solution could intrude in the outer and inner rings. Consequently, the Ca occupation of the exchange sites was noticeably higher after 120 days compared to Fig. 6-15 (Fig. 6-25). Implementation of gradual swelling leading to a higher hydraulic conductivity would thus lead to more Ca being exchanged as was the case in the experiment.

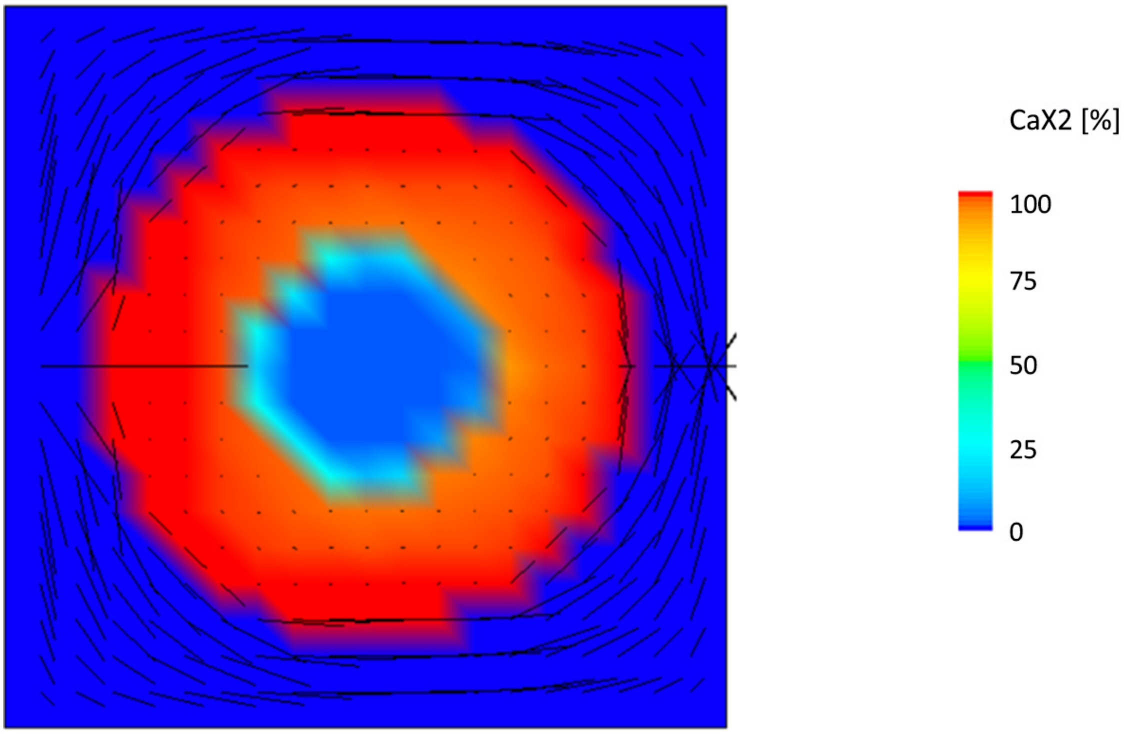

Fig. 6-25: CaX2 [%] of the model variation after 120 days and the flow field as vectors

6.2.2.3 Conclusion

Geochemically changing conditions during bentonite erosion experiments were studied by simulating ion exchange of swollen bentonite in an open fracture with a flow and reactive transport model using PHAST. It was observed that ion exchange strongly depends on fluid flow and calcium availability in solution. Using calcium-enriched Grimsel groundwater as contact solution, the exchange increased compared to using Grimsel groundwater. The exchange was in turn higher when adding gypsum to the bentonite and therefore increased the calcium concentration through an internal reservoir. These observed effects in the model are those also seen in the experiment: the increased exchange by adding gypsum to the system, i.e. the more gypsum is present, the higher is the amount of Ca in contact solution and therefore the exchanger occupation increases. As expected and observed in the experiment, this caused a delayed bentonite erosion. The experiment and the model agree that it is more efficient to bring a Ca-bearing mineral into the system than to increase the Ca concentration of the solution. Still, there are some deviations regarding the experimental and modelled data. The flow field and the accessibility of the exchange sites are different in the model compared to the laboratory experiments because swelling and expansion of the bentonite cannot be depicted in PHAST. For improvement of the simulations, the application of a high-resolution grid with consideration of continuous expansion of the bentonite into the fracture, coupled with flow and transport reactions, would be needed.

6.3 Radionuclide diffusion in bentonite for the LIT and Mock-up tests

Within the framework of the Kollorado-e2 project, predictive calculations were performed, describing the diffusion of the radionuclides inserted in glass vials into the LIT (Noseck & Schäfer 2020). The objective was to obtain an estimate on radionuclide movement within the bentonite. A schematic sketch of one of the four centre rings of the LIT is shown in Fig. 6-26. The status of the glass vials was uncertain. They could have broken due to the swelling pressure of the bentonite caused by water resaturation. In this case, radionuclide diffusion into the bentonite ring would have occurred from the areas where the vial wall was broken. If the glass vial did not break, radionuclide diffusion would definitely occur from the open part of the vial in the inner part of the bentonite ring. 1D diffusion models were applied: a planar diffusion model and a radial diffusion model. Neither type of models fully reflected the situation but gave indications on expected travel distances in the bentonite during the LIT.

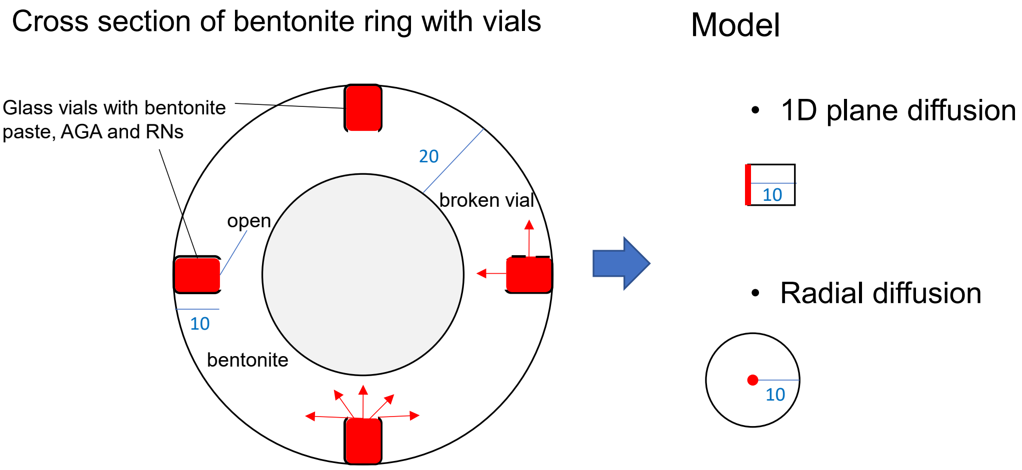

Fig. 6-26: Schematic cross-section of a bentonite ring with radionuclide-containing glass vials as used in the LIT as well as for the Mock-up experiments and the models applied for radionuclide diffusion (lengths are given in mm)

6.3.1 CLAYPOS transport code

The CLAYPOS module belongs to the RepoTREND program package, which is used for post-closure safety assessments of deep geological repositories for radioactive waste in Germany (Reiche 2016). CLAYPOS simulates one-dimensional radionuclide transport in low-permeable media either in cylindrical or in planar geometry (Rübel et al. 2007). It considers linear sorption and radioactive decay in decay chains. For each phase, the radioactive decay is calculated analytically for the dissolved/sorbed and the precipitated inventory, and the diffusive transport of the radionuclides is solved numerically. An implicit solution algorithm is used with a fixed width given for each phase. That means that the variable parameters are inserted with their values at the end of the examined phase for higher stability of the algorithm, i.e. negative concentrations are automatically avoided. The time derivative is replaced by an upwind difference and the spatial derivative is replaced by the central difference between the segments (Rübel et al. 2007). For the inner boundary conditions, two cases are distinguished. Supposing that the solubility limit has been reached (a), the boundary concentration is given, otherwise (b) a source is assumed. In order to also correctly represent the gradient at the inner and outer boundaries in the case of the stationary solution, the discretisation raster is extended into the inner/outer areas and the boundary condition is extrapolated. For the outer boundary condition of the radionuclide flux, the water volume flow in the aquifer is explicitly entered in the model. Since the volume flow in the aquifer can be very high and impossible to specify exactly in every case, an excessively high water flow can be entered into the model to simulate a zero concentration boundary condition (Rübel et al. 2007). The derivation of all the data used in the simulation calculations is discussed in detail in Noseck & Schäfer (2020). The data are compiled in Tab. 6-7 and Tab. 6-9.

Tab. 6-7: Data applied for the diffusion in bentonite of the LIT. Values in brackets for Mock-up test (if different from the LIT parameters)

	Value	**Unit**
Bentonite ring		
Transport pathway length	0.0375 (0.01)	m
Bentonite mineral density	2,760	kg m^{-3}
Bentonite dry density	1,435	kg m^{-3}
Total bentonite porosity	0.48	-
Liquid / mass ratio	0.3333	L/kg
Glass vial		
Bentonite mass per vial	0.111	g
Fluid volume per vial	1.11E-4	L
Porosity	0.734	-
Fracture		
Volume flow through fracture	1.0 (2.63E-2)	m^3 a^{-1}

Tab. 6-8: Compilation of radionuclide data

K_d values are taken from Bradbury & Baeyens (2010); effective diffusion coefficients are taken from van Loon (2014)

Radionuclide	**Inventory** [mol]	**K_d** [m^3/kg]	**Vial Initial concentration**	**Diffusion coefficient** D_{eff} [m^2/s]
^{45}Ca	1.49E-12	0.0027	3.64E-09	2.8E-10
^{75}Se(IV)	7.41E-14	0	6.67E-10	1.8E-11
^{75}Se(-II)				4.4E-11
^{99}Tc(VII)	5.38E-09	0	9.70E-09	1.8E-11
^{99}Tc(IV)		5		1.8E-10
^{137}Cs	6.23E-13	0.032	1.70E-10	1.5E-09
^{233}U(VI)	5.34E-10	51	9.62E-10	1.8E-10
^{233}U(IV)		293	1.64E-11	1.8E-10
^{237}Np(V)	1.08E-08	0.11	9.67E-07	1.8E-10
^{237}Np(IV)		375	2.60E-10	1.8E-10
^{241}Am	1.80E-12	9.5	1.71E-12	1.8E-10
^{242}Pu(IV)	3.75E-10	3002	1.13E-11	1.8E-10
^{242}Pu(III)		9.5	3.56E-10	1.8E-10

6.3.2 Long-Term In-situ Test (LIT)

During the Kollorado-e^3 project, an X-ray CT image of the overcored LIT became available, see Fig. 6-27. It showed that the MI shear zone did not exactly reach the location of the inner four rings with the radionuclide containing glass vials. The nearest distance of the water-conducting fracture to a glass vial was 37.5 mm. With this knowledge, updated calculations considering a planar transport on 37.5 mm instead of 10 mm were performed. In addition, the assumption of a constant radionuclide content in the vial was changed to a source, where the decrease of the inventory by diffusion out of the vial was considered. This was particularly important for mobile radionuclides, where a significant amount of its inventory was expected to be released during the 4.5-year duration of the LIT. The breakthrough curves for the non- or low-sorbing elements, namely Tc(VII) and Np(V) in their oxidised form, are shown in Fig. 6-28 for both the transport pathways of 10 mm and of 37.5 mm, respectively. The impact of the pathway was low for the non-sorbing Tc(VII). The maximum of the breakthrough curve occurred at the same point, only the concentration decrease of the curve was slightly faster for the shorter pathway. In the case of the low-sorbing Np, the difference was more pronounced. For a transport pathway of 10 mm, the breakthrough curve appeared after 1 month and reached its maximum after about 0.4 years, whereas for the transport pathway of 37.5 mm, the breakthrough curve was significantly delayed and did not reach its maximum within 1 year.

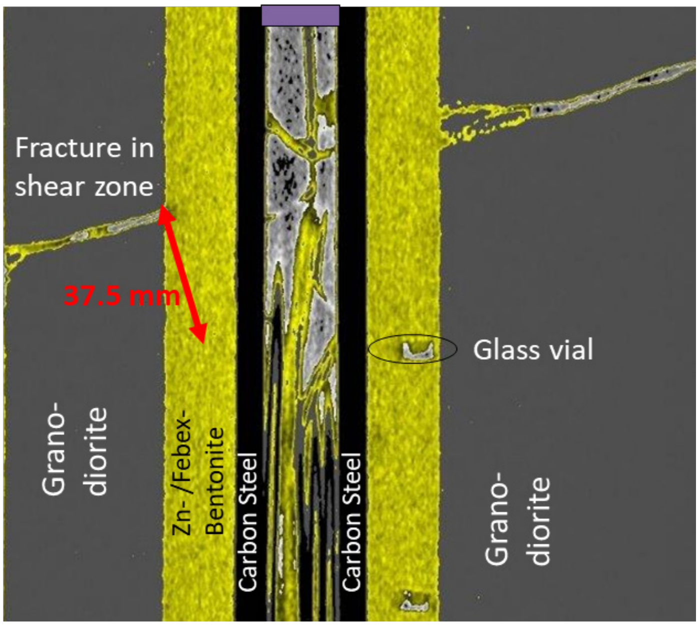

Fig. 6-27: Cross-section of X-ray CT scan of part of the core from LIT overcoring

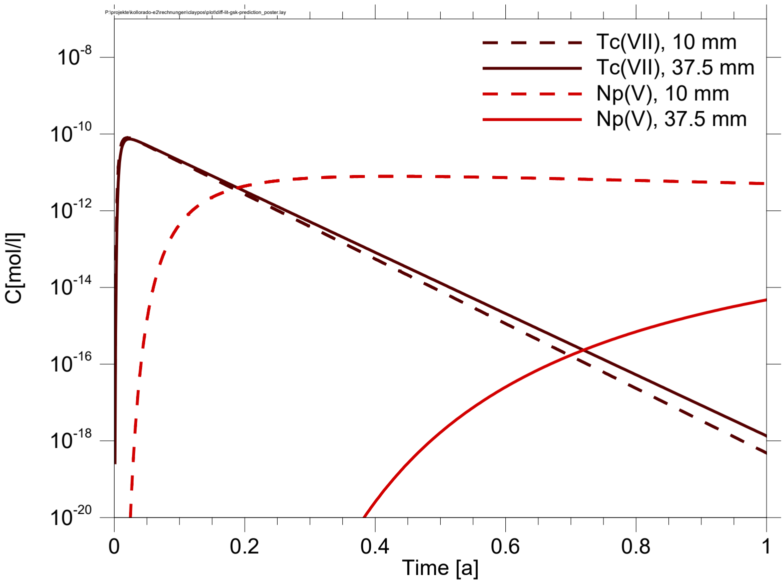

Fig. 6-28: Breakthrough curves for Tc (VII) and Np(V) (10 and 37.5 mm pathways)

In contrast, there was no observable difference for the transport of the strong-sorbing tri- and tetravalent actinides. The spatial distribution curves for a transport distance of 37.5 mm are shown in Fig. 6-29 and are similar to those calculated for 10 mm distance. The concentration of tetravalent radionuclides showed a sharp decrease within the first few mm (less than 4 mm). The content of Am(III) decreased by three orders of magnitude within the first 8 mm. The characterisation of the drill core, particularly the radionuclide diffusion profiles around the glass vials in the bentonite, are still under way. So far, no comparison is possible. Concerning Tc and Np, it is expected from the comparison of simulation and experiment that both occur in their reduced tetravalent form, since no significant amount of either tracer was observed during the LIT. A very small release of Tc, Am, Np and U at very early times cannot be explained by the diffusion process and is likely caused by some artefact at the start of the experiment, see Section 4.3.2.

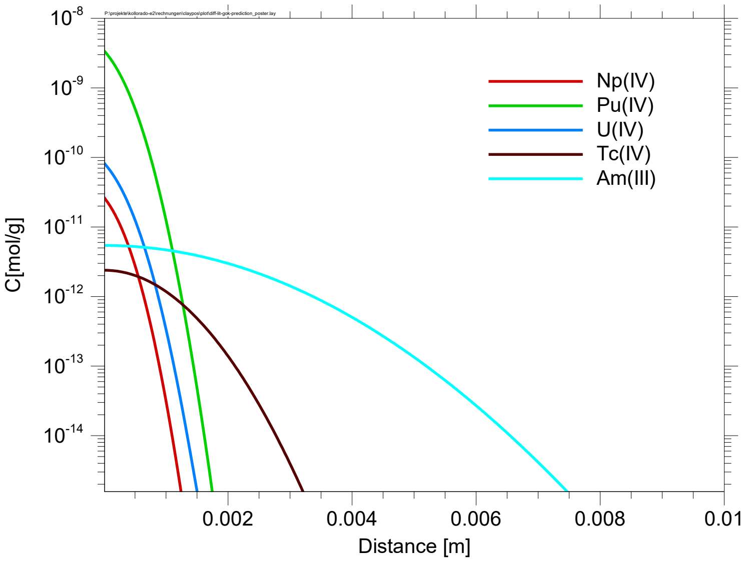

Fig. 6-29: Spatial distribution of tetravalent actinides(IV), Tc(IV) and Am(III) after 4.5 years

6.3.3 Mock-up Test

In addition to the LIT, results from the Mock-up test also became available. Therefore, the diffusion calculations were modified accordingly. The flow through the fracture in the mock-up experiment was 50 µl/min, corresponding to $2.63 \cdot 10^{-02}$ m^3/a. The flow through the fracture impacts the gradient in the bentonite and, naturally, the dilution of the breakthrough curves.

Fig. 6-30 shows the experimentally determined as open squares and the simulated breakthrough curves. For technetium, assumed to be in the oxidised state Tc(VII), the early increase of the experimental curve as well as the maximum of the experimental curve was successfully met. The concentrations of all three elements dropped below their detection limits. The breakthrough curves of Np(V) and U(VI) could only be matched by assuming K_d values of 0.02 and 0.05 m^3/kg, respectively, and considering a reduced release from the vial, specifically 4% of ^{233}U and 8% of ^{237}Np within 5 years.

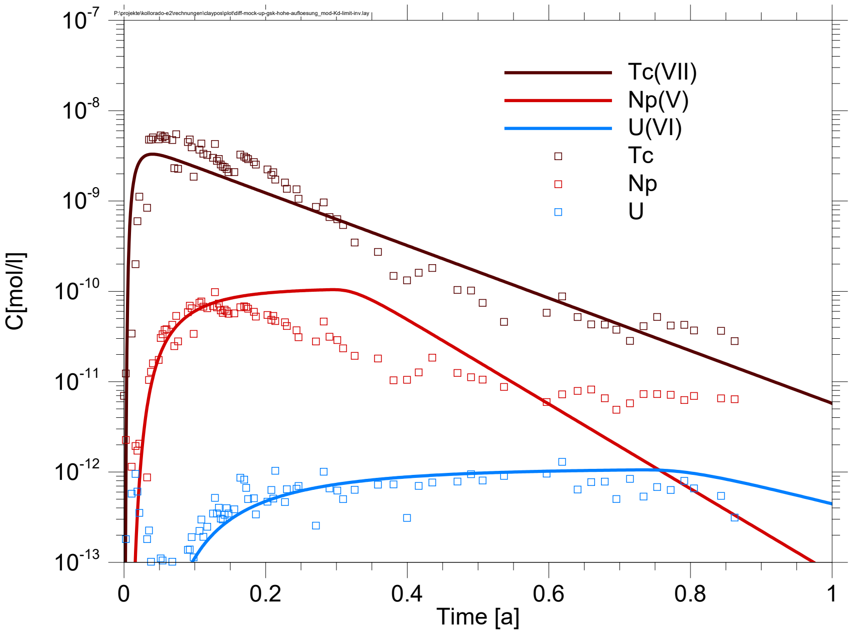

Fig. 6-30: Breakthrough curves for Tc, Np and U

Experiment = open squares and model = bold lines

Fig. 6-31 shows the measured spatial distributions in the bentonite ring out of the vial for ^{237}Np and ^{233}U as described in Section 4.2.2. These distributions are represented by plateaus of the concentrations between 1 and 10 ng/g for neptunium and between 0.1 and 1 ng/g for uranium. Technetium contents could not be detected in the vial. The simulated spatial distributions for all three radionuclides after 4.5 years are shown in Fig. 6-32. The very low profile of ^{99}Tc can be explained by its high mobility and would also explain that no ^{99}Tc could be detected in the bentonite ring from the mock-up test. After 4.5 years, the residual ^{99}Tc is far below the detection limit. Generally, the simulation supports the observation of a rather flat plateau concentration. An additional argument for the flat concentration profiles is the fact that the post-mortem analyses of the radionuclide profiles in the mock-up experiment were performed two years after the experiment was stopped (cf. Section 4.2.2), which could have contributed to an additional flattening due to still active diffusion processes. However, the absolute concentrations are significantly lower than the experimental concentrations, for ^{237}Np about one order of magnitude and for U about 3 orders of magnitude. These absolute concentrations are supposed to be mainly determined by the assumption of the mobile fraction (reduced release from U and Np from the vial, see above) and the distribution coefficient of the respective radionuclide in the bentonite ring.

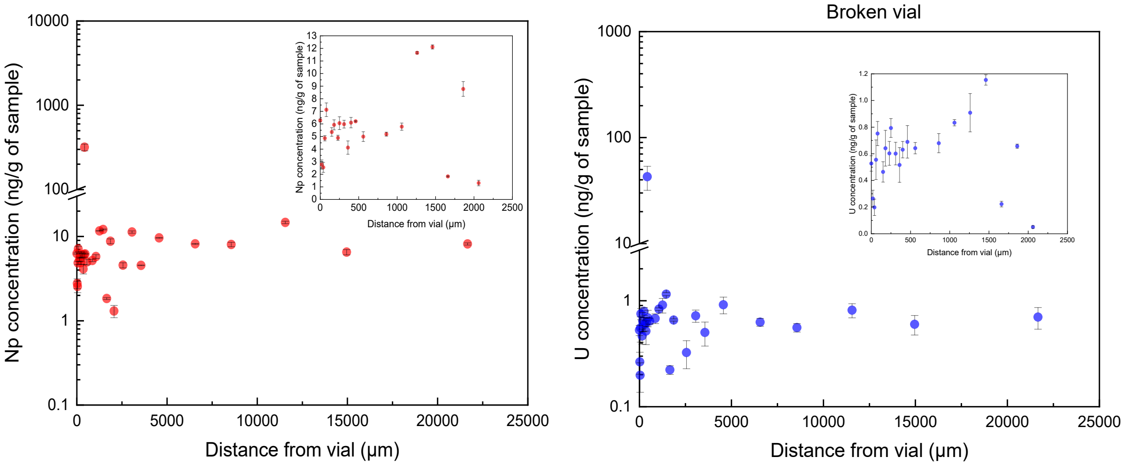

Fig. 6-31: Experimentally determined spatial distributions of Np (left) and U (right) in the bentonite ring outside the broken vial, cf. Section 4.2.2

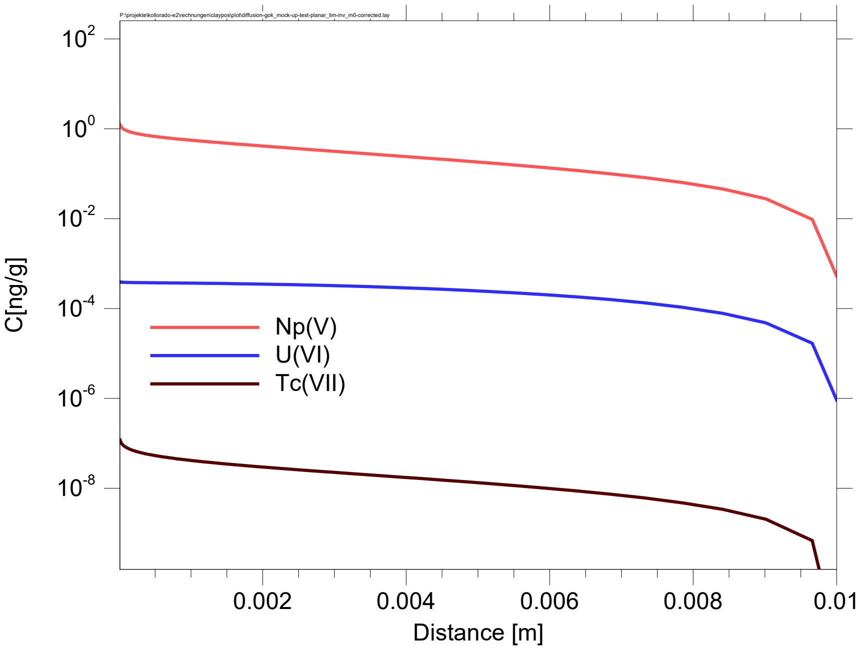

Fig. 6-32: Spatial distributions of Np(V), U(VI) and Tc(VII) calculated by the model

To investigate both effects, parameter variations with different mobile inventories of ^{237}Np and ^{233}U were performed first. The resulting breakthrough curves for the time frame of 5 years and the spatial distributions after 4.5 years are shown in Fig. 6-33. The qualitative difference in the curves, namely that ^{237}Np reaches a plateau concentration after 2.6 years – which is not the case for the ^{233}U curves – can be explained by the decay of the mother radionuclide ^{241}Am, which is available in the vial. The relatively short half-life of ^{241}Am of 423.2 years and the fact that it is very immobile in the system is decisive that during the few years of the LIT, a significant amount of ^{237}Np was continuously produced at the source, which then caused constant diffusion through the bentonite, resulting in a plateau of the breakthrough curve. On the other hand, the long half-life of ^{237}Np and its rather low distribution coefficient K_d (most of its content in the vial was released from the bentonite within one year) did not impact the concentration of the daughter nuclide ^{233}U during the life cycle of the LIT. This effect is also responsible for the differences in the spatial distributions of both radionuclides after 4.5 years, shown in Fig. 6-33 on the right. The profile of ^{237}Np after 4.5 years was independent on the considered mobile fraction in the vial whereas the ^{233}U distribution increased with along with an increase in the considered mobile fraction of its inventory, as expected. However, even for 100% mobility of U and Np, the absolute concentrations in the breakthrough curves did not match the simulated curves for increased mobile fractions of U and Np. The concentrations were lower by 2 orders of magnitude for U and 1 order for Np, respectively. Although the uranium profile increased, the assumption of an increased mobile U and Np fraction alone could not explain the differences between model and experiment.

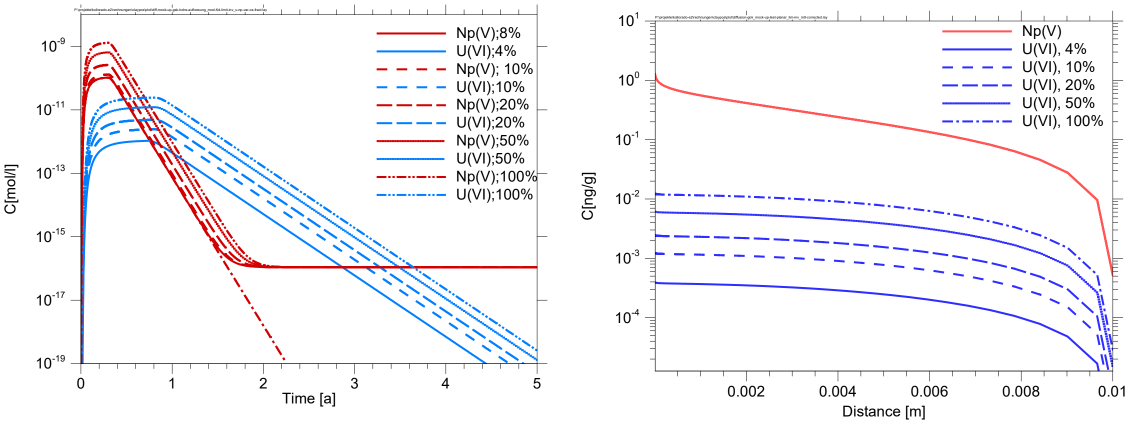

Fig. 6-33: Diffusion calculations for Mock-up test. Variation of the considered mobile fractions of ^{237}Np and ^{233}U denoted in%. Breakthrough curves (left; the red dash-dot line shows a calculation for 8% mobile ^{237}Np(V) without ^{241}Am inventory) and radial spatial distributions after 4.5 years (right)

Therefore, the impact of the K_d value was addressed next by means of a few parameter variations. Fig. 6-34 (left) shows the breakthrough curves for uranium with slightly increased K_d values for the diffusion through the bentonite. As the K_d value increases, the tailing of the breakthrough curve also increases, with the value at the 4.5-year time point rising by more than two orders of magnitude. This is directly reflected in the spatial distribution (Fig. 6-34, right) where the concentration plateau for uranium also increases by more than two orders of magnitude. Thus, the increase of the K_d value even over a small range from 0.05 to 0.07 m^3/kg has a strong impact resulting in a concentration plateau, in a region comparable with the one observed in the mock-up experiment. For ^{237}Np, the impact is not that strong since the plateau is mainly determined by radioactive decay of ^{241}Am in the range of the considered K_d values. The increase is related to an increase of the sorbed fraction in the bentonite leading to an increase of the concentration plateau.

The reference K_d values of 0.05 m^3/kg and 0.02 m^3/kg for uranium and neptunium, respectively, were selected to describe the observed breakthrough curves in Fig. 6-30. The model used here assumes a transport pathway of 10 mm from the open part of the vial to the outer rim of the bentonite, the interface to the artificial fracture. As described in Section 4.2, two vials in the mock-up experiment were broken. For these vials, the transport pathways to the artificial fracture were expected to be much shorter than 10 mm. Consequently, the K_d value to describe the radionuclide transports could be higher than the reference values, which could explain the differences in the observed and simulated concentration profiles for uranium and neptunium. As soon as more data become available, particularly for the concentration of ^{233}U and ^{237}Np in the vials (giving information about the source term), further calculations with superposition of different pathway lengths will be performed to better understand the observed profiles.

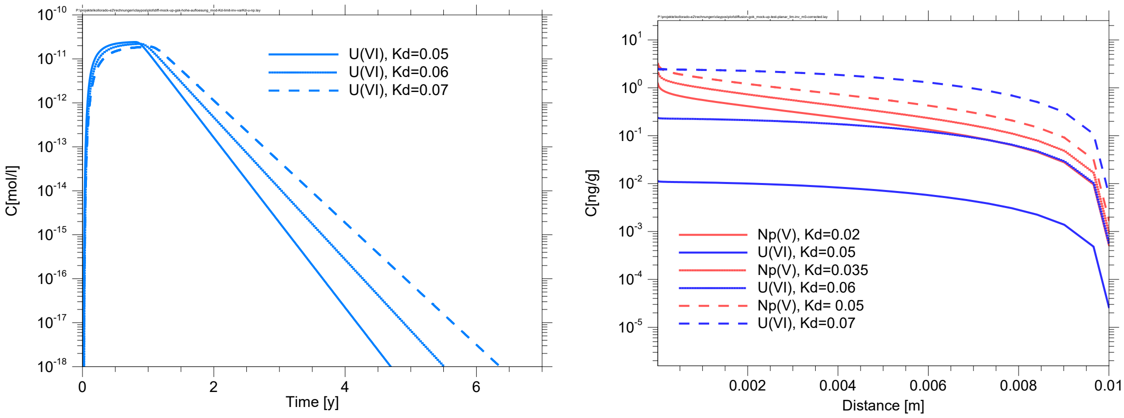

Fig. 6-34 Diffusion calculations for Mock-up test. Variation of the $K_d$values of ^{237}Np and ^{233}U. Left: Breakthrough curves for ^{233}U; Right: Concentration profiles of ^{237}Np and ^{233}U along the diffusion pathway

6.3.4 Summary and status

The characterisation of the overcored segment of the LIT is still ongoing. The X-ray CT showed that the fracture in the shear zone did not touch the inner four radionuclide-containing bentonite rings but occurred at a distance of 37.5 mm distance to one of the outer rings. Radionuclide diffusion profiles are not yet available. Very small releases of ^{99}Tc, ^{237}Np, ^{233}U and ^{241}Am were observed in the very beginning of the LIT, where those for ^{237}Np, ^{233}U and ^{241}Am lay in the range of the background and only ^{99}Tc levels clearly lay above background and detection limit concentrations (see Section 4.3.2). During the 4.5 years of the LIT, no further release of radionuclides from the bentonite source was observed. This indicates that Np and Tc were reduced to the tetravalent state and became rather immobile. The simulations even for an increased pathway of 37.5 mm from the nearest vial to the fracture indicated a breakthrough of non-sorbing Tc(VII) within the first month and for low sorbing Np(V) after about half a year.

The conditions of the mock-up test were different, since the $E_h$values were +250 mV. Under these conditions, breakthrough curves for ^{99}Tc, ^{237}Np and ^{233}U were observed, rising initially with peak maxima for Tc after 10 days and for Np after 50 days, respectively. U and Np profiles were present in a part of the bentonite ring, but no other radionuclides could be detected in this ring segment so far (see Section 4.2.2). The behaviour of the mobile ^{99}Tc could be well described, and the simulations indicated extremely low contents in the bentonite ring and the vial after 4.5 years. This explained why a spatial distribution in the bentonite could not be detected. The breakthrough curves for ^{237}Np and ^{233}U could be matched by the simulations, assuming that only a portion of both elements were mobile and that relatively low sorption values were used. Plateau-like distribution profiles in the bentonite, as observed for ^{233}U and ^{237}Np, were also expected from the simulations; however, the predicted concentrations were significantly lower than those observed experimentally. An explanation for the differences can be the difference in the model assumptions and the experimental conditions, particularly regarding the length of the diffusion pathway. In the model, the diffusion pathway length was 10 mm assuming that the vials were intact, whereas the evaluation of the experiment showed that two vials were broken (likely at the beginning of the experiment, when the bentonite was resaturated and swollen).As a consequence, the diffusion pathway were lower than assumed in the model calculations and K_d values for U and Np might have to be increased to describe the observed breakthrough curve out of the bentonite, causing much higher plateau concentrations which better matches the observed profiles.

When more experimental data are available, further simulations with modified assumptions will be performed.

6.4 Calculations on the repository system scale

This section describes the modelling work for colloid-facilitated radionuclide transport on the repository scale in a sheared granitic formation. Within the framework of the previous projects, i.e. Kollorado-e (Huber et al. 2016) and Kollorado-e^2 (Noseck & Schäfer 2020), simulation calculations were carried out for a repository constructed in granite. These calculations were applied to the concrete reference case of the Finnish Safety Case (Posiva OY 2012). The interaction parameters between radionuclides, colloids and fracture filling material were derived from previous laboratory and field experiments.

Here, the findings are to be transferred to colloid-carried transport for a potential German repository in crystalline rock. The work is based on repository systems for the concepts proposed by BGE in crystalline rock which have been developed as part of the CHRISTA-II project (Wolf et al. 2021). Data for the transport pathway are derived from the report on the potential geology in Germany (Mrugalla et al. 2020). The calculations are based on the specific radionuclide releases from the near-field used in the RESUS project (Becker et al. 2020).

The Basic assumption is that the colloids and radionuclides are released from the repository near-field. The modelling starts there and considers the transport to the geosphere. The model assumptions are based on expert assumptions and results from modelling of the various dipole experiments conducted at the GTS. All information on model assumptions and parameter values are given in Section 6.4.2 and the results are given in Section 6.4.3.

The transport is modelled with the RepoTREND code (Reiche 2016) particularly its FRAME and COFRAME modules (Reiche et al. 2014), see Section 6.4.1.

6.4.1 FRAME/COFRAME flow model

A three-dimensional rock body can be defined by its Area A [m^2] and length L [m] (see Fig. 6-35). Inside this rock body, water can flow with a volumetric flow Q [m^3·a^{-1}] through different fractures. Each fracture has a width of g_i [m] and an aperture of 2b [m]. With the assumption that all water-bearing fractures have the same total width of $\sum g_i$, the total area with flowing water is $2b \cdot \sum g_i$.

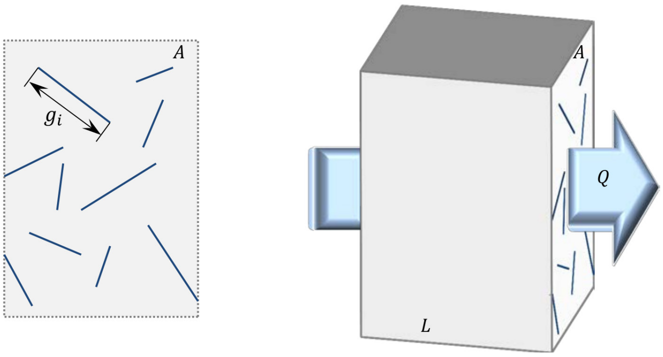

Fig. 6-35: Rock body containing water-bearing fractures

Reiche et al. (2014)

The FRAME/COFRAME flow model combines all fractures inside the rock body into one single fracture (see Fig. 6-36). The same volumetric flow Q as in the rock body is assumed in the fracture with length L, width $\sum g_i$ and aperture of 2b.

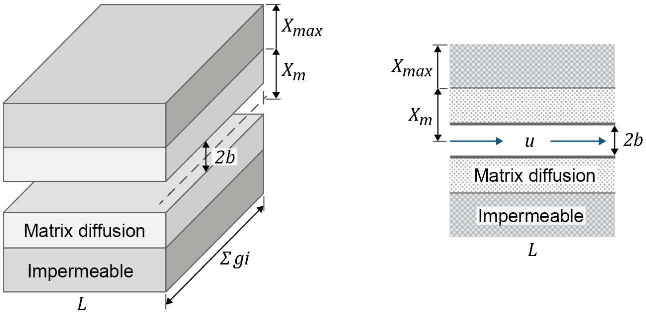

Fig. 6-36: Definition of model parameters for a planar geometry of the fractured medium

Reiche et al. (2014)

Inside the fracture, colloids and radionuclides can be transported with advective flow. a zone with matrix diffusion is located around the fracture. Here, only diffusive flow is calculated.

6.4.1.1 Contaminant transport and interactions

Within the fracture, FRAME/COFRAME can transport contaminants as Reiche et al. (2014) (see Fig. 6-37):

- Dissolved mobile contaminants in the fracture with a concentration $\mathbf{C_{fr}}$ [mol·m^{-3}] (fr for Radionuclide in the Fracture),
- Dissolved contaminants inside the porewater of the rock matrix with a concentration $\mathbf{C_{pr}}$ [mol·m^{-3}] (pr for Radionuclides in the rock matrix Pores),
- Sorbed contaminants on mobile colloids with a concentration $\mathbf{C_{cr}}$ [mol·m^{-3}] (cr for Radionuclides sorbed on mobile Colloids),

- Sorbed contaminants on the fracture surface with a concentration $\mathbf{S_{fr}}$ [mol·m^{-2}],
- Sorbed contaminants on pore walls of the rock matrix with a concentration $\mathbf{S_{pr}}$ given in contaminant mass per dried mass of the rock matrix [mol·kg^{-1}],
- Sorbed contaminants on immobile colloids with a concentration $\mathbf{S_{cr}}$ [mol·m^{-2}].

The colloids are given with two different components:

- Mobile colloids inside the fracture with a concentration $\mathbf{M_{Ccol}}$ [kg·m^{-3}],
- Immobile colloids sorbed on the fracture surface with a concentration $\mathbf{F_{Col}}$ [kg·m^{-2}].

The model has the following exchange processes:

- $\mathbf{Q_{fr}}$ sorption of in-fracture water-dissolved contaminants on the fracture surface,
- $\mathbf{Q_{c}}$ filtration and remobilisation of colloids on the fracture surface,
- $\mathbf{Q_{frm}}$ and $\mathbf{Q_{fri}}$ sorption of in-fracture water-dissolved contaminants on mobile and immobile colloids,
- $\mathbf{Q_{cr}}$ filtration and remobilisation of on-colloids sorbed contaminants due to the interaction of colloids with the fracture surface,
- $\mathbf{Q_{pr}}$ sorption of contaminants dissolved in the porewater of the rock matrix on the pore surface,
- $\mathbf{Q_{fp}}$ diffusive exchange between fracture and rock matrix.

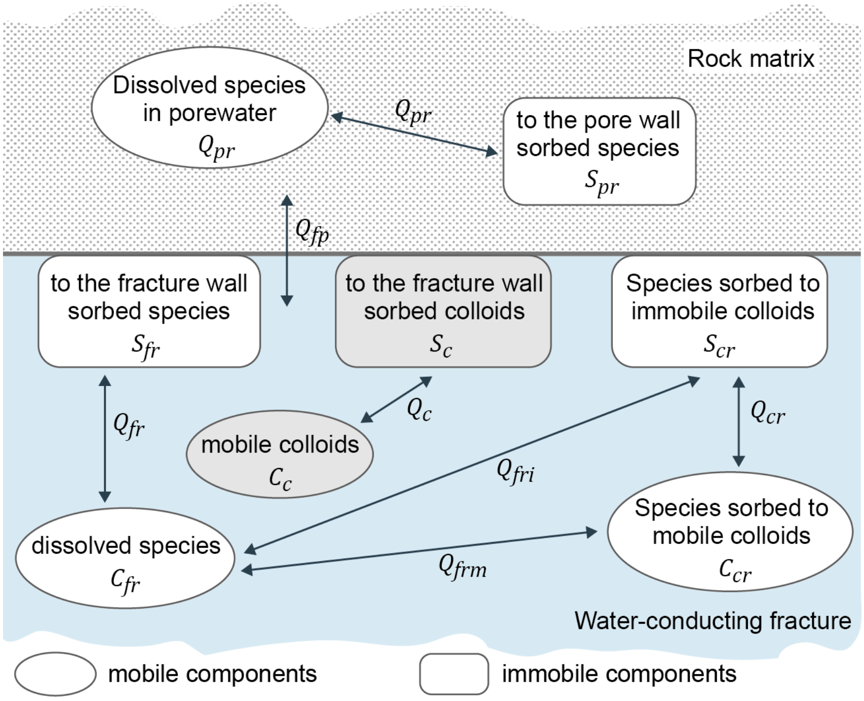

Fig. 6-37: Interaction between contaminants and colloids in COFRAME

Reiche et al. (2014)

Following the naming of components and interactions, the naming of the sorption coefficient on components is given with

- **K_{pr}** sorption coefficient on porous rock matrix [$m^3 \cdot kg^{-1}$],
- **K_{fr}** sorption coefficient on fracture surface [m],
- **K_{frm}** sorption coefficient for sorption on mobile colloids [$m^3 \cdot mol^{-1}$] and
- **K_{fri}** sorption coefficient for sorption on filtered colloids [$m^3 \cdot mol^{-1}$].

For calculations of kinetic, contaminant sorption, exchange rates are defined as

- **k_{fr}** exchange rate for kinetical contaminant sorption on the fracture surface [a^{-1}],
- **k_{frm}** exchange rate for kinetical contaminant sorption on mobile colloids [a^{-1}] and
- **k_{fri}** exchange rate for kinetical contaminant sorption on filtered colloids [a^{-1}].

6.4.2 Model assumptions and parameters

This chapter includes all model assumptions and parameters for the calculations.

In Germany, no site for a repository for high-level radioactive waste has been selected yet. The site selection process was only started a few years ago and considers three types of rocks, i.e. rock salt, clay stone and crystalline rock as potential host rock formations. In the past, research focused on rock salt formations and to some extent on clay formations. That is why not many data are available for granitic host rocks in Germany.

However, general information on fractures in granitic host rock is limited, too. Important international resources are data from underground laboratories, e.g., the Grimsel Test Site (Switzerland) or Äspö (Sweden) and the repository sites in Scandinavia , i.e., Olkiluoto (Finland) and Forsmark (Sweden). However, local conditions are different for each formation. That is why the information from these sites cannot simply be transferred to sites in Germany. A summary of currently available data for a granitic host rock in Germany is documented in Mrugalla et al. (2020). Within the CHRISTA-II project, generic models considered two different repository concepts, i.e. "multiple containing rock zone" and "(modified) mKBS-3" (Wolf et al. 2021). The choice of the presented data in the current report is always given for "mKBS-3" if not mentioned otherwise. Here a denser fracture network is assumed.

The assumption for the applied model is that a fracture connects the repository near-field with the geosphere. This means that there is a direct connection with the groundwater. This scenario is not valid for a repository for high-level radioactive waste since it would not be licensable. For the consideration of colloid-bound contaminant transport, it is an interesting scientific issue.

The fracture is assumed to be inside a planar granitic block with a cross-section area of 1 m^2 and a length of 1,000 m divided into **500 boxes**, each with a width of 20 m.

6.4.2.1 Fracture dimensions

The fracture aperture (2b in Fig. 6-36) can have a huge variability as shown in Fig. 6-38 (Mrugalla et al. 2020). For the model calculations, a value of **$5 \cdot 10^{-4}$ m** is used for the fracture aperture.

As fracture width ($\sum g_i$ in Fig. 6-36), the full width of the granitic block of **1 m** is assumed.

A fracture length is given for different rock formations by (Mrugalla et al. 2020) for a:

- Host rock with 10 to 1,000 m,
- A lamprophyre corridor between 10 and 100 m and
- The overburden between 10 and 100 m.

The assumption of a **1,000 m fracture** in a host rock is therefore plausible.

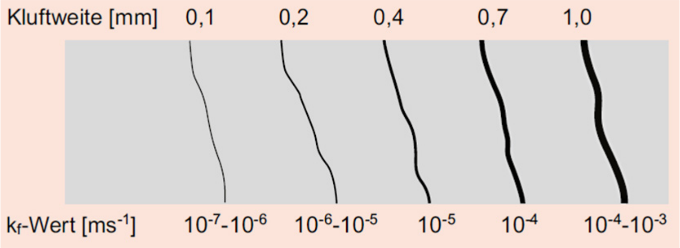

Fig. 6-38: Example of hydraulic conductivity for different fracture apertures in fractured rocks under the assumption of fracture distances of one metre

Sebastian (2018) cited in Mrugalla et al. (2020)

6.4.2.2 Flowrate

The site of a potential repository in crystalline rock and therefore conditions in the underground are not known. To model the effect of colloid transport, a Darcy flow rate of **$1 \text{ m} \cdot \text{a}^{-1}$** is defined.

It is assumed that the colloid velocity is the same as the Darcy flow rate.

6.4.2.3 Colloid release

The colloid release in a near-field of a repository is modelled based on the assumption of an intrusion of water with a low ionic strength. If the repository is located in northeast Germany, a huge amount of melting water could be available during transgression periods due to potential glaciations during cold climates in this area. If this water were to come into contact with the bentonite barrier, colloids could be released into the near-field (Seher et al. 2020).

colloid release is modelled with two different approaches: the first is a continuous release and the second is a release in glacial cycles (see explanation in Section 6.4.2.5). The first approach assumes a continuous inflow of meteoric water down to the disposal zone corresponding to a continuing warm climate. For the second approach, a ten-fold higher release rate is assumed based on high inflow of low mineralised glacial meltwater at the transition phase from cold to warm climates.

In Table 4-2 and Table 4-3, (Huber et al. 2016), the concentration of released colloids is given for geochemical conditions of the groundwater at the Grimsel test site with assumptions of:

- Fracture width ($\sum g_i$ in Fig. 6-36): 5 m,
- Fracture aperture (2b in Fig. 6-36): $1.47 \cdot 10^{-3}$ m,
- Flow velocity (v): 23 $m \cdot a^{-1}$,
- Flow rate (Q in Fig. 6-35): $1.6905 \cdot 10^{-1}$ $m^3 a^{-1}$
- Erosion rate of 0.0395 $kg \cdot a^{-1}$ (constant release) and 0.395 $kg \cdot a^{-1}$ (glacial cycles)

with colloid concentrations of $2.3366 \cdot 10^{-1}$ $kg \cdot m^{-3}$ for constant release and 2.3366 $kg \cdot m^{-3}$ for glacial cycles. This concentration can be recalculated for the current model setting (see Section 6.4.2.1 for fracture dimensions):

- Fracture width ($\sum g_i$ in Fig. 6-36): 1 m,
- Fracture aperture (2b in Fig. 6-36): $5 \cdot 10^{-4}$ m and
- Flow velocity (v):1 $m \cdot a^{-1}$
- Flow rate (Q in Fig. 6-35): $5 \cdot 10^{-4}$ $m^3 a^{-1}$

to a colloid release rate of **$1.1683 \cdot 10^{-4}$ $kg \cdot a^{-1}$** (constant release) or **$1.1683 \cdot 10^{-3}$ $kg \cdot a^{-1}$** (glacial cycles). For more details of the recalculation, see Appendix A.1.

6.4.2.4 Colloid filtration and remobilisation

Huber et al. (2016) used a filter coefficient of 0.333 m^{-1} and a remobilisation rate of 0.1095 h^{-1} to model in-situ experiments at the Grimsel test site. These values are used as starting point for the variation calculations in Section 6.4.3.2.

To only check the influence of the filter coefficient on the colloid release from the fracture system, the remobilisation was switched off and the filter coefficient was varied between $2 \cdot 10^{-3}$ m^{-1} and $2 \cdot 10^{-2}$ m^{-1}.

Tab. 6-9: Filter coefficient and rates as well as remobilisation rates

Parameter	**Value**	**Unit**	**Source**
Filter coefficient	0.333	m^{-1}	Huber et al. (2016), Tab. 3-3
Remobilization rate	0.1095	h^{-1}	
Filtration rate	0.01	h^{-1}	Huber et al. 2016, Fig. 3-17
Values for variation calculations			
Filter coefficient (without remobilization)	$2 \cdot 10^{-3}$, $6 \cdot 10^{-3}$, $2 \cdot 10^{-2}$	m^{-1}	This work

Filter coefficient λ_f [m^{-1}] and filtration rate k_{sc} [h^{-1}] can be converted into each other with the average colloid velocity u_c [$m{\cdot}s^{-1}$] using equation (6.1) as specified by Huber et al. (2016), p. 153). The filtration rate is given as

$$k_{sc} = \lambda_f \cdot u_c \tag{6.1}$$

Different filter coefficients and filtration rates are given in Huber et al. 2016, e.g. Tables 3-4, 3-6, 3-8 and Fig. 3-17). However, a time dependency for the filtration rate could not be found.

6.4.2.5 Glacial cycles

The glacial cycles are modelled after the time windows given in (Posiva OY 2012) as shown in Fig. 6-39. During these glacial cycles, a colloid release with a colloid release rate of $1.1683{\cdot}10^{-3}$ $kg{\cdot}a^{-1}$ is assumed. In a first attempt outside these cycles, no colloid release was modelled. However, this led to numeric problems, which is why a colloid release rate of $1{\cdot}10^{-5}$ $kg{\cdot}a^{-1}$ is set as a base concentration. this way, the numerical problems could be significantly improved. The used colloid concentration in the inflow waters at the left boundary of the fracture is given in Fig. 6-40.

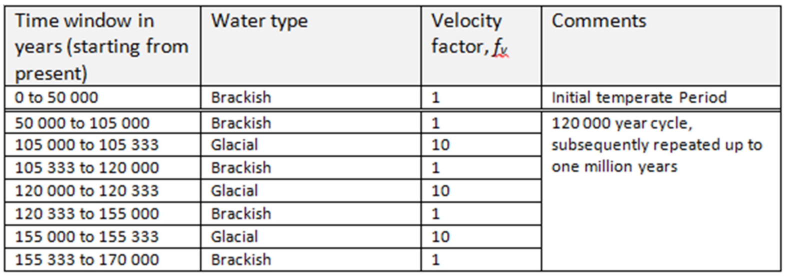

Time window in years (starting from present)	Water type	Velocity factor, f_v	Comments
0 to 50 000	Brackish	1	Initial temperate Period
50 000 to 105 000	Brackish	1	120 000 year cycle, subsequently repeated up to one million years
105 000 to 105 333	Glacial	10	
105 333 to 120 000	Brackish	1	
120 000 to 120 333	Glacial	10	
120 333 to 155 000	Brackish	1	
155 000 to 155 333	Glacial	10	
155 333 to 170 000	Brackish	1	

Fig. 6-39: Time window for glacial cycles

Posiva OY (2012) cited in Huber et al. 2016

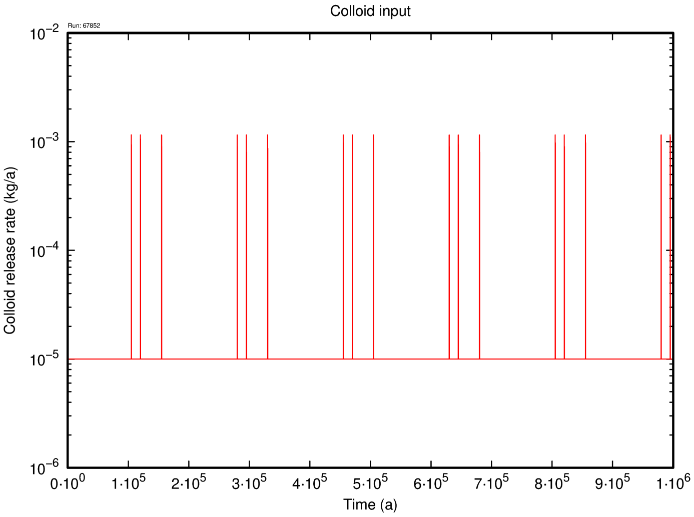

Fig. 6-40: Colloid release rate as input at the left border of the fracture in the model calculations with a colloid release in cycles

6.4.2.6 Sorption

The colloid-facilitated radionuclide transport is particularly interesting for the tri- and tetravalent radionuclides, since these typically strongly sorb on fracture material as well as on colloids. A substantial fraction of these radionuclides bound to colloids can significantly increase their transport if the colloids are mobile in the system.

FRAME/COFRAME includes two different parameters for the sorption of contaminants onto colloids and the walls of the fracture. First, a sorption coefficient K_{fr} [m] is used to calculate the sorption in a chemical equilibrium as well as a rate k_{fr} [a^{-1}] for a kinetic reaction.

In this study a generic fracture is used for the transport calculations. As a solution within the fracture, a solution with low ionic strength is assumed. Therefore, the sorption coefficients and rates used in the calculations for tri- and tetravalent as given in Tab. 6-10 are taken from results of the former Kollorado projects, where parameters have been derived from laboratory reversibility experiments with low ionised Grimsel Groundwater and fracture infill material. Some of These parameters applied have been modified to successfully describe interactions between radionuclides, colloids and matrix in the dipole field tests at GTS projects (Huber et al. 2016, Noseck & Schäfer 2020).

Tab. 6-10: Sorption coefficients and rates for tri- and tetravalent actinides

Parameter	**Value**	**Unit**	**Source/ Remark**
Interactions with colloids			
Sorption coefficient for trivalent elements (Am, Cm, Eu, Tb)	1,500	$m^3 \cdot kg^{-1}$	Huber et al. (2016), Tab. 3-3)
Sorption coefficients for tetravalent elements (Pu, Th, Hf)	1,600	$m^3 \cdot kg^{-1}$	
Sorption rate for Pu	45	a^{-1}	Huber et al. (2016), p. 171
Sorption rate for Am	71	a^{-1}	
Interaction with fracture filling material			
Sorption coefficient for Am	0.22	$m^3 \cdot kg^{-1}$	Noseck & Schäfer (2020), p. 87
Sorption coefficient for Pu	0.6	$m^3 \cdot kg^{-1}$	
Sorption rate for trivalent and tetravalent nuclides	$1 \cdot 10^6$	a^{-1}	Assumption that process is fast (in equilibrium)
Sorption coefficient for U (VI)	0.0038	$m^3 \cdot kg^{-1}$	Huber et al. (2016)

The sorption coefficients of the rock K_{fr}^* [$m^3 \cdot kg^{-1}$] are converted to the sorption coefficient of the fracture surface K_{fr} [m], the input parameter for the transport code COFRAME, according to equation 4.27 from (Reiche et al.) (Reiche et al. 2014)with fracture aperture b [m], porosity n_f^* [-] and density ρ_f^* [$kg \cdot m^{-3}$].

$$K_{fr} = b \cdot \frac{1-n_f^*}{n_f^*} \cdot \rho_{fr}^* K_{fr}^* \tag{6.2}$$

It is assumed that Am and Cm occur in their trivalent form and Th, Pu and Np occur in the tetravalent form. These assumptions are based on the conditions in the Grimsel groundwater at the research laboratory and the corresponding results from the thermodynamic benchmark calculations, cf. Section 6.1. Uranium has been assumed to occur in its oxidised form as U(VI). This has also been demonstrated in the thermodynamic benchmark calculations, which predict that the ternary complexes $Ca_2UO_2(CO_3)_3$ and $CaUO_2(CO_3)_3^{2-}$ stabilise the hexavalent form in solution. It is also supported by the reversibility experiments performed in (Huber et al. 2016).

Such assumptions must of course be confirmed or modified once a site-specific investigation is performed and the groundwater conditions at the respective site are known.

6.4.2.7 Fracture and rock matrix properties

Transport parameters and properties of the fractures and rock matrix are adopted from Huber et al. (2016) and given in Tab. 6-11.

Tab. 6-11: Transport parameters for calculations with FRAME/COFRAME

Huber et al. (2016), Tab. 3-2

Parameter	Value	Unit
Penetration depth	0.02	m
Rock porosity	0.05	
Rock density	2,670	kg·m^{-3}
Rock matrix diffusion coefficient	0.008	m^2·a^{-1}
Nuclide diffusion coefficient in fracture	0.03	m^2·a^{-1}
Colloid diffusion coefficient in fracture	0.003	m^2·a^{-1}

6.4.2.8 Dispersion length

A dispersion length of around 1/10 of the total length of the phenomenom is used (see measurements in Fig. 6-41). This means that for a fracture with a length of 1,000 m, the dispersion length should be set to 100 m. With this length, numerical problems occurred, which is why it was reduced to **50 m**.

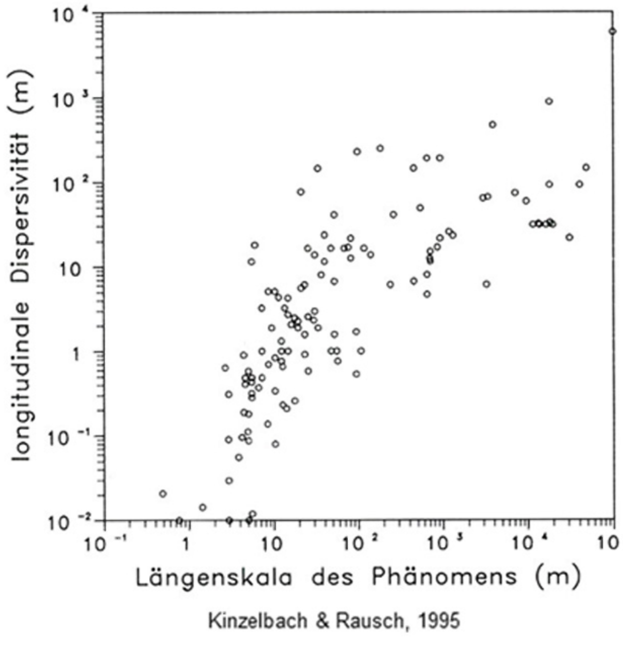

Fig. 6-41: Longitudinal dispersity against length of the phenomena

Kinzelbach & Rausch (1995)

6.4.2.9 Radionuclides

The radionuclide fluxes at the transition from near- to far-field for a generic repository in a granitic formation are modelled according to case K4 from the RESUS project (Becker et al. 2020). The radionuclide activity flux out of the bentonite into the fracture over time is shown in Fig. 6-42 and the considered radionuclides with their decay chains and half-lives are given in Tab. 6-13.

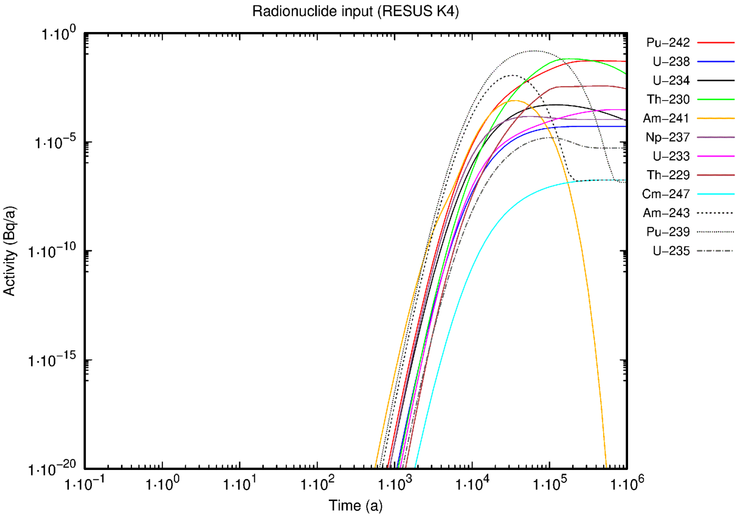

Fig. 6-42: Radionuclide activity flux in $Bq\cdot a^{-1}$ from the near-field over time from case K4 of the RESUS project (Becker et al. 2020) taken as input for the model calculations

Tab. 6-12: Used radionuclides and decay chains with half-lives

Decay chain nuclide	**Half-life** [a]	**Nuclide**	**Half-life** [a]	**Nuclide**
Uranium-Radium	Pu-242	$3.75 \cdot 10^{5}$	U-238	$4.468 \cdot 10^{9}$
	Th-234	$6.6 \cdot 10^{-2}$	U-234	$2.455 \cdot 10^{5}$
	Th-230	$7.54 \cdot 10^{4}$		
Neptunium	Am-241	$4.322 \cdot 10^{2}$	Np-237	$2.144 \cdot 10^{6}$
	U-233	$1.592 \cdot 10^{5}$	Th-229	$7.88 \cdot 10^{3}$
Uranium-Actinium	Cm-247	$1.56 \cdot 10^{7}$	Am-243	$7.37 \cdot 10^{3}$
	Np-239	$6.487 \cdot 10^{-3}$	Pu-239	$2.411 \cdot 10^{4}$
	U-235	$7.038 \cdot 10^{8}$	Th-231	$2.909 \cdot 10^{-3}$
	Th-227	$5.13 \cdot 10^{-2}$		

6.4.3 Results

6.4.3.1 Basic case

The basic case is calculated to get a better understanding of the modelled fracture system. The transport of radionuclides is calculated without colloids in the system (B1, colloid concentration = 0). For another basic case (B2), the interaction between colloids and radionuclides is switched off. As expected, both cases show the same concentrations in solution and on the fracture walls, therefore only the results of B1 are shown here.

Radionuclide transport without colloids (B1)

Basic case B1 is calculated without any colloids present in the system. The radionuclide concentration at the inflow location of the fracture (Fig. 6-43) shows the same characteristics as the input radionuclide flux shown in Fig. 6-42. The concentration of the radionuclides within the fracture in 100 m and 1,000 m as shown in Fig. 6-44. The sorption process on the fracture wall is calculated using the sorption coefficients and rates given in Tab. 6-10. The high sorption rate of $1 \cdot 10^6$ a^{-1} means that the sorption process is in equilibrium. In Fig. 6-44 (right side) it can be seen that, at the end of the fracture at 1,000 m, only U and its daughter nuclides are calculated. All the other radionuclides are retarded in the fracture system. The sorption coefficient of U is two orders of magnitude lower than for the other radionuclides. This can explain the observed behaviour.

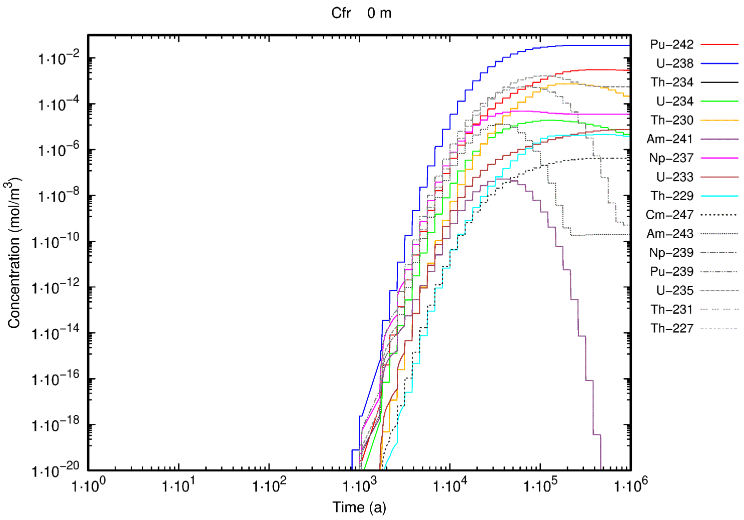

Fig. 6-43: Radionuclide concentration in solution (C_{fr}) inside the fracture over time (0 m, after the input into the fracture) for basic case B1 without colloids in the system

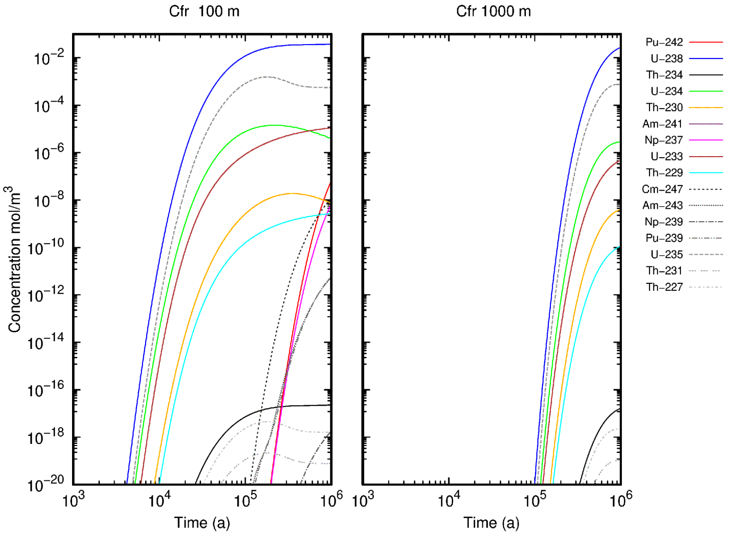

Fig. 6-44: Radionuclide concentration in solution (C_{fr}) 100 m within the fracture (left) and at 1,000 m at the end of the fracture (right) over time for basic case B1 without colloids in the system

6.4.3.2 Constant colloid release: no colloid filtration

The influence of colloids on the transport of radionuclides in the fracture system is tested with a constant input of colloids with a colloid release rate of $1.1683 \cdot 10^{-4}$ kg·a^{-1} as described in Section 6.4.2.3. All elements, except U, enter the system sorbed on the colloids. For uranium in the hexavalent state, no sorption on bentonite colloids was observed under the GGW conditions.

Transport without colloid filtration (CR1 and CR2)

As the first constant colloid concentration case, CR1 is modelled without colloid filtration. The increase in colloid concentration over time is shown in Fig. 6-45. Since no filtration of colloids is modelled, a constant colloid concentration is present inside the fracture after approx. 1,000 years.

Radionuclide concentrations on mobile colloids, in solution inside the fracture and on the fracture wall are shown in Fig. 6-46. Since no filtration of colloids is modelled, the concentration of radionuclides on immobile colloids is zero and therefore not shown.

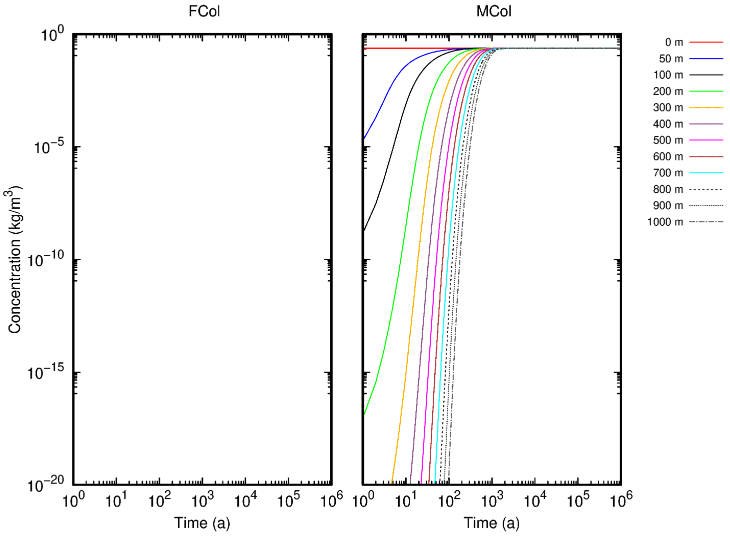

Fig. 6-45: Filtered colloids (F_{Col}, left) and mobile colloid concentration (M_{Col}, right) over time for different distances inside the fracture system for case CR1 without colloid filtration

Since no filtration of colloids is modelled, the concentration of filtered colloids is not calculated.

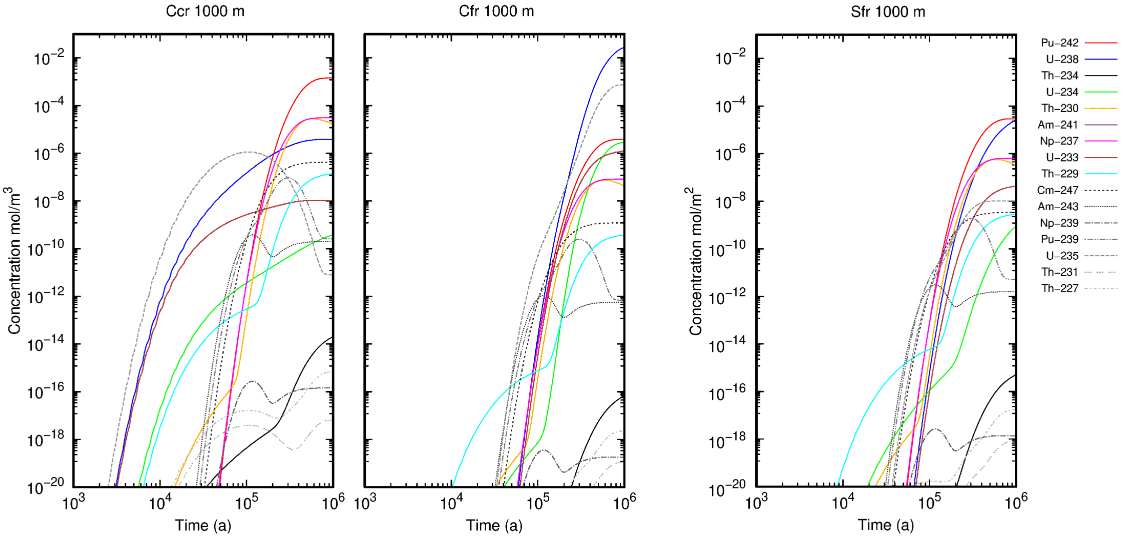

Fig. 6-46: Radionuclide concentration sorbed on mobile colloids (C_{cr}, left), in solution inside the fracture system (C_{fr}, middle) and on the fracture wall (S_{fr}, right) over time at a distance of 1,000 m at the end of the fracture for case CR1 without colloid filtration

The colour code in all figures is the same.

Fig. 6-46 (left side) shows that part of U is transported on the mobile colloids. This should not be observed, since there is a sorption coefficient of 0 $m^3 \cdot kg^{-1}$ and a kinetic exchange rate of 0 a^{-1} given for U sorption on colloids. An explanation of this observation is that the radioactive decay of other elements, which are sorbed on the colloids and represent uranium mother nuclides, build uranium which is still sorbed on the surface. The assumption of a desorption rate of 0 a^{-1} keeps the uranium on the surface. As a consequence, the U nuclides stay attached to the colloids although they should not be sorbed.

To test this assumption, the kinetic exchange rate of U on the colloids is set to 10^6 a^{-1} for case CR2. This value implies a fast desorption of the colloid-bound U formed by radioactive decay from the colloids. For this case, the radionuclide concentrations on mobile colloids, in solution and on the fracture wall are shown in Fig. 6-47, confirming the assumption. The high desorption rate drops the concentrations of the U nuclides on mobile colloids by several orders of magnitude. This change does not significantly alter the concentration of ^{238}U and ^{233}U in solution and on the fracture walls. However, for ^{234}U and ^{229}Th, the daughter nuclides of ^{238}U, the increase in concentration is modelled approx. 8,000 a later than in case CR1.

For all further model calculations, the kinetic exchange rate for U is set to 10^6 a^{-1}.

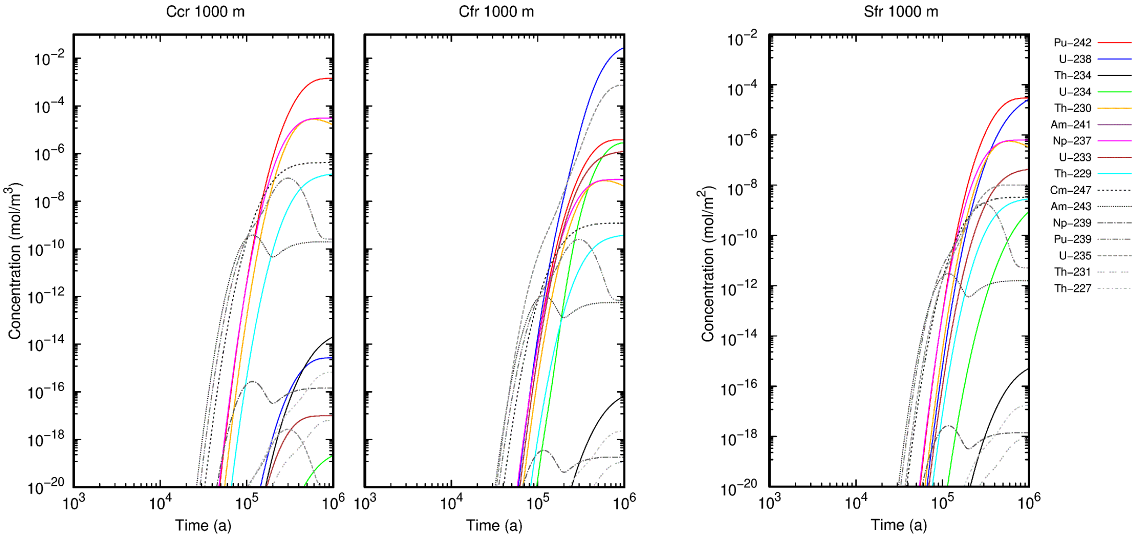

Fig. 6-47: Radionuclide concentration sorbed on mobile colloids (C_{cr}, left), in solution inside the fracture system (C_{fr}, middle) and on the fracture wall (S_{fr}, right) over time at a distance of 1,000 m at the end of the fracture for case CR2 with a sorption rate for U of 10^{-6} a^{-1}

The colour code in all figures is the same.

Compared to case B1 without any colloids in the system (see Fig. 6-48), not only U and its daughter nuclides arrive at the end of the fracture system. The other trivalent and tetravalent radionuclides travel through the system with the colloids and are also present after 1,000 m in the fracture system.

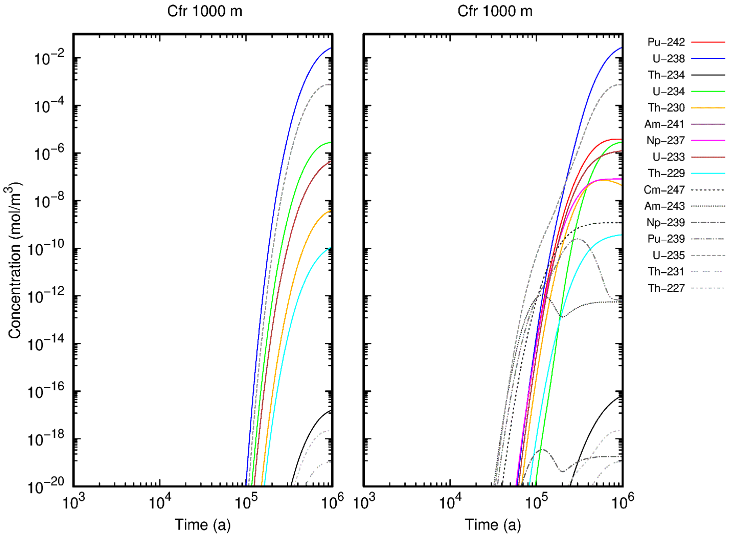

Fig. 6-48: Radionuclide concentration in solution in the fracture system (C_{fr}) over time at the end of the fracture (1,000 m) without colloids (left, result from B1 in Fig. 6-44) and with a sorption rate for U of 10^{-6} a^{-1} (right, result from case CR2)

6.4.3.3 Constant colloid release: with colloid filtration and variation of remobilisation

In Cases CR1 and CR2, colloid filtration is not considered. To test the influence of filtration and remobilisation, cases CR3 to CR7 are modelled.

Colloid filtration and remobilisation with data from CFM runs (CR3)

To investigate the influence of colloid filtration and remobilisation on the transport inside the fracture system, the filter coefficient and remobilisation rates used in modelling the CFM runs 10-01 and 12-02 (Huber et al. 2016) are used for case CR3.

The colloid concentration for mobile and immobile colloids is shown in Fig. 6-49. Since the mobile colloids are filtered, the concentration of immobile colloids increases inside the fracture until an equilibrium is reached after approx. 1,000 years. After this time, the concentration of the mobile colloids does not change anymore, either. This can be explained by the fast remobilisation rate of the CFM runs.

The main difference to the calculations without colloid filtration in cases CR1 and CR2 is the increase in radionuclide concentration on immobile colloids (Fig. 6-51, left side). Due to the remobilisation, formerly immobile colloids can reach the end of the fracture after traveling 1,000 m.

All other radionuclide concentrations on mobile colloids, inside the fracture system and on the walls of the fracture show the same behaviour and concentration range as in case CR2 (see Fig. 6-50, Fig. 6-51 and in direct comparison with C_{fr} in Fig. 6-52 as well as C_{cr} in Fig. 6-53).

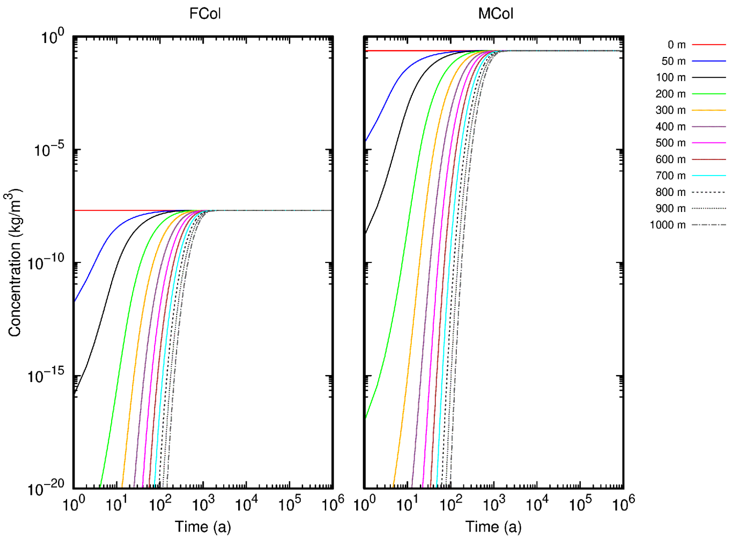

Fig. 6-49: Filtered colloids (F_{Col}, left) and mobile colloid concentration (M_{Col}, right) over time for multiple locations inside the fracture system for case CR3 with a filter coefficient and remobilisation from Huber et al. (2016) as described in Section 6.4.2.4

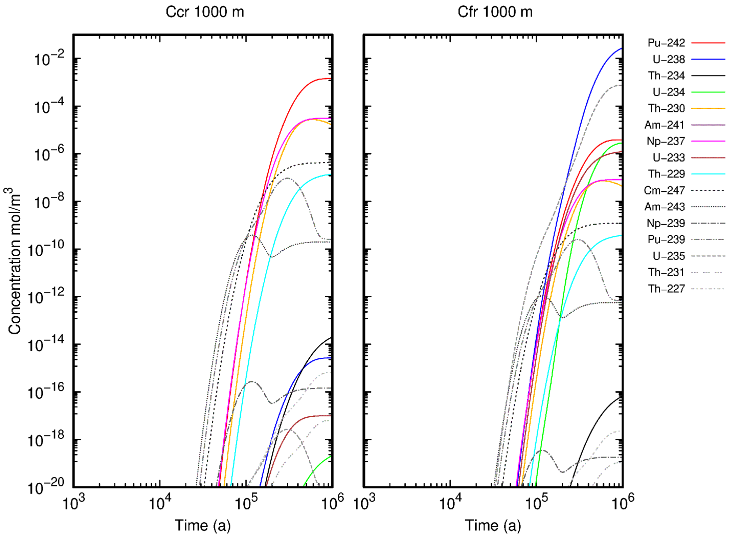

Fig. 6-50: Concentration of radionuclides sorbed on mobile colloids (C_{cr}, left) and dissolved in solution inside the fracture system (C_{fr}, right) over time at the end of the fracture for case CR3 with a filter coefficient and remobilisation from Huber et al. (2016) as described in Section 6.4.2.4

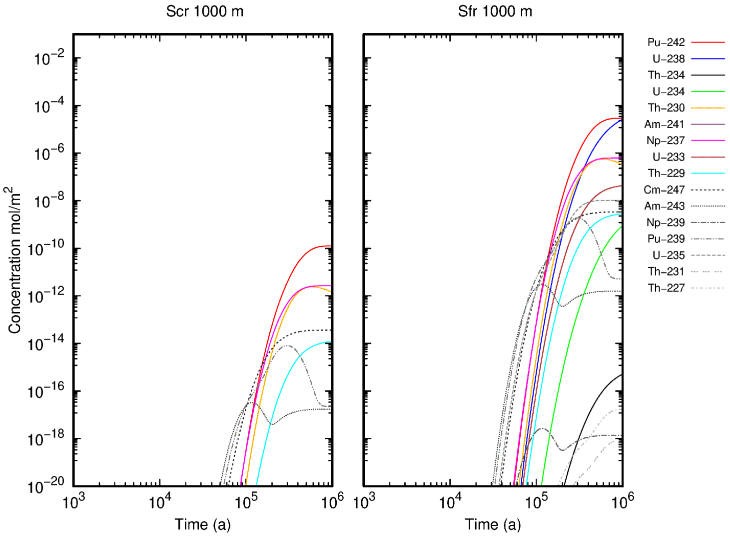

Fig. 6-51: Concentration of radionuclides sorbed on immobile mobile colloids (S_{cr}, left) and on the fracture wall (S_{fr}, right) over time at the end of the fracture for case CR3 with a filter coefficient and remobilisation from Huber et al. (2016) as described in Section 6.4.2.4

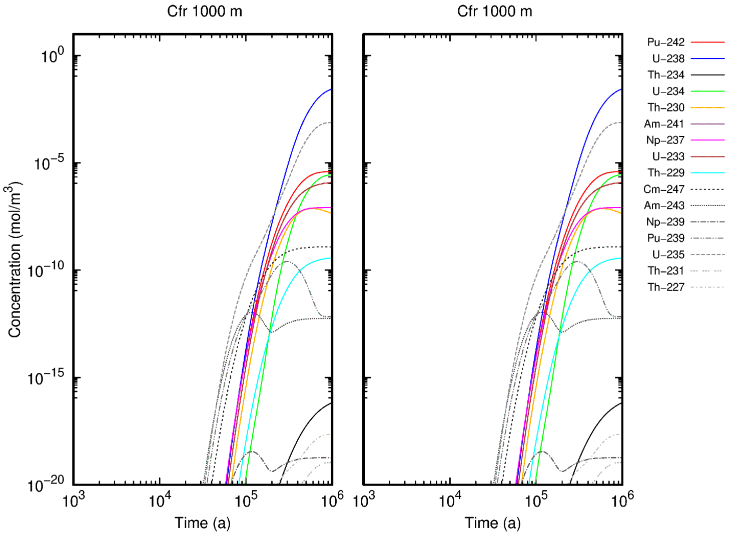

Fig. 6-52: Radionuclide concentration dissolved in solution inside the fracture system (C_{fr}) over time at the end of the fracture (1,000 m) without colloid filtration (left, results from case CR2 in Fig. 6-47) and with colloid filtration and remobilisation (right, result from case CR3 in Fig. 6-50)

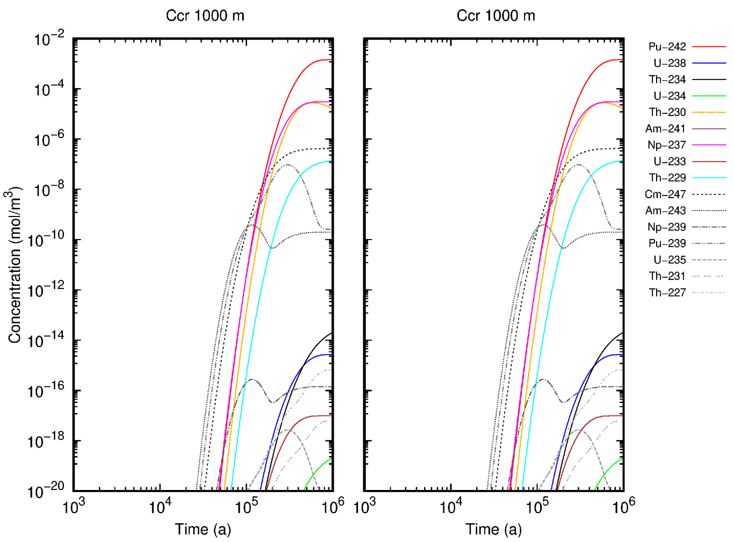

Fig. 6-53: Concentration of radionuclides sorbed on mobile colloids (C_{cr}) over time at the end of the fracture (1,000 m) without colloid filtration (left, results from case CR2 in Fig. 6-47) and with colloid filtration and remobilisation (right, result from case CR3 in Fig. 6-50)

Colloid filtration without remobilisation (CR4)

The filtration rate and the remobilisation of colloids can be varied. Calculations with remobilisation in case CR3 showed that colloids will impact the radionuclide transport if the remobilisation rate is high. To check remobilisation has an impact or not in case CR4, the remobilisation rate is set to zero. As can be seen in Fig. 6-54 (right), the concentration of mobile colloids decreases with the length of the fracture. After 600 m, no significant amount of colloids ($>1\cdot10^{-20}$ $kg\cdot m^{-3}$) is calculated. The accumulation of colloids over time can be seen in Fig. 6-54 (left) where the concentration of colloids increases over time.

Since the colloids are filtrated throughout transport pathway, they do not facilitate any radionuclide transport. Only uranium and its daughter nuclides in solution occur after one million years at the end of the pathway with the same breakthrough curves as in case B1 without any colloids present (Fig. 6-55).

To identify parameter ranges of the filtration rate, where an impact on the radionuclide transport is expected, parameter variations of the filtration rate have been performed. To be able to model the influence of colloids on the transport of radionuclides inside the fracture, the filter coefficient needs to be changed or a remobilisation needs to be modelled.

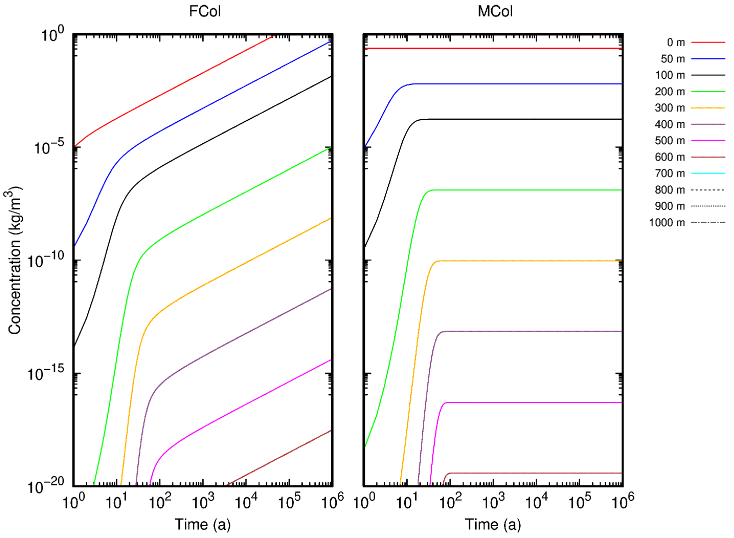

Fig. 6-54: Filtered colloids (F_{Col}, left) and mobile colloid concentration (M_{Col}, right) over time for multiple locations inside the fracture system for case CR4 with a filter coefficient from Huber et al. (2016) as described in Section 6.4.2.4, and no colloid remobilisation

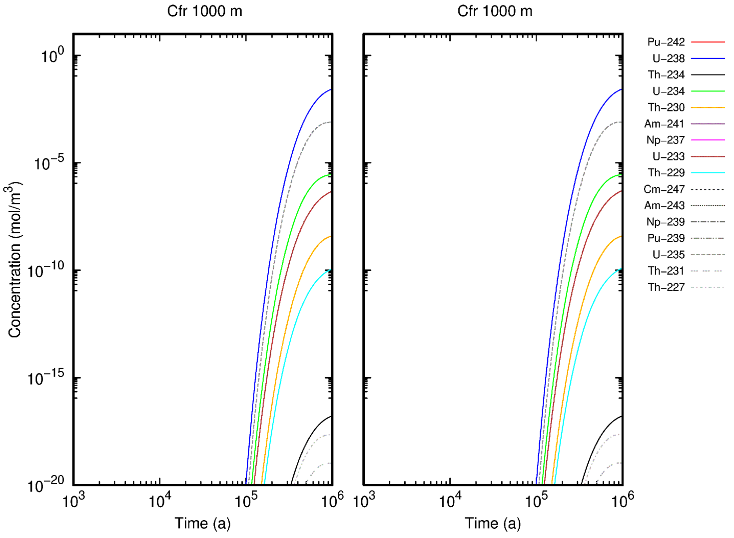

Fig. 6-55: Radionuclide concentration dissolved in solution inside the fracture system (C_{fr}) over time at the end of the fracture (1,000 m) without colloids (left, results from case B1 in Fig. 6-44) and with colloid filtration without remobilisation (right, result from case CR4)

Colloid filtration with recalculated filter coefficient $2 \cdot 10^{-3}$ m^{-1} (CR5)

Since no significant concentration of colloids reaches the end of the fracture system without a remobilisation in case CR4, another filter coefficient needs to be defined. A filter coefficient is a property of the fracture system. The filter coefficient of 0.333 m^{-1} taken from CFM runs 10-01 and 12-02 allowed for modelling these runs in a dipole of the Grimsel test site with a length of 6.2 m. The current fracture system has a length of 1,000 m.

As a first approximation, under the assumption that the same number of colloids are filtered in the 1,000 m fracture than in the CFM runs, the filter coefficient from Grimsel is used and recalculated after equation (6.3).

$$\begin{gathered} 6.2\,m \cdot 0.333\,\frac{1}{m} = 2.0646 \\ {}^{2.0646}/_{1{,}000\,m} = 2.0646 \cdot 10^{-3}\,\frac{1}{m} \longrightarrow 2 \cdot 10^{-3}\,\frac{1}{m} \end{gathered} \tag{6.3}$$

For a filter coefficient of $2 \cdot 10^{-3}$ m^{-1} in case CR5, a reduction of colloid concentration within the fracture is modelled (Fig. 6-56). Compared to case CR4, where all the colloids are filtered in the fracture and C_{cr} concentrations are zero at the end of the fracture at 1,000 m, colloids reaching the end of the fracture and a radionuclide concentration on mobile and immobile colloids are observed for CR5 (Fig. 6-57).

Compared to case CR3 where the transport of colloids is not reduced by filtration, the same concentration of U and its daughter nuclides can be calculated (Fig. 6-58). For all the other nuclides, which are associated with the colloids, a reduction of concentration is seen. This is also accompanied by a later increase in concentration approx. 80.000 years later than in case CR3.

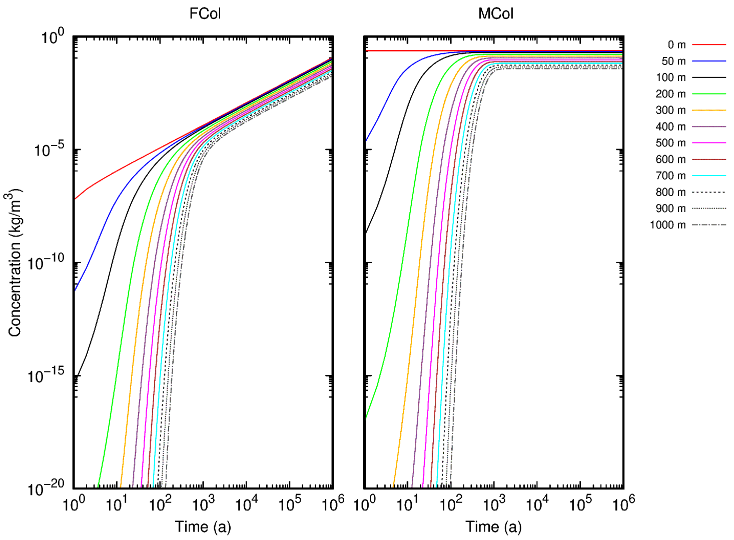

Fig. 6-56: Filtered colloids (F_{Col}, left) and mobile colloids (M_{Col}, right) over time for multiple locations inside the fracture system for case CR5 with a filter coefficient of $2 \cdot 10^{-3}$ m^{-1} and no colloid remobilisation

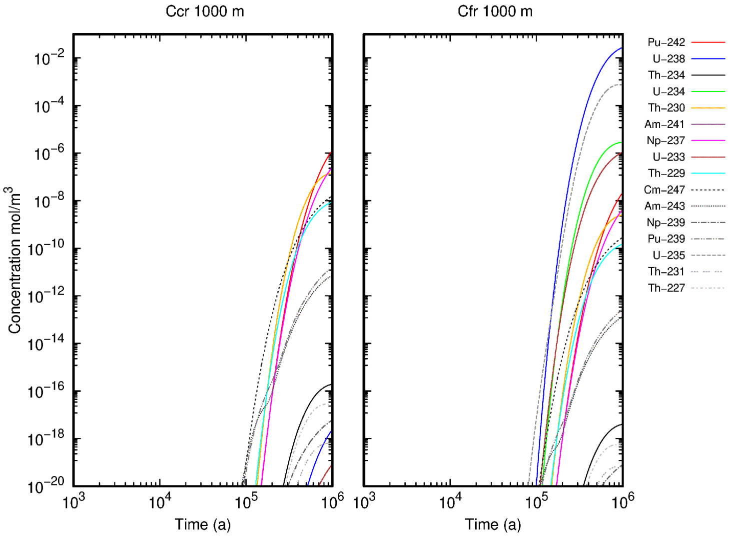

Fig. 6-57: Radionuclide concentration sorbed on mobile colloids (C_{cr}, left) and dissolved in solution inside the fracture system (C_{fr}, right) over time at the end of the fracture for case CR 5 with a filter coefficient of $2 \cdot 10^{-3}$ m^{-1} and no colloid remobilisation

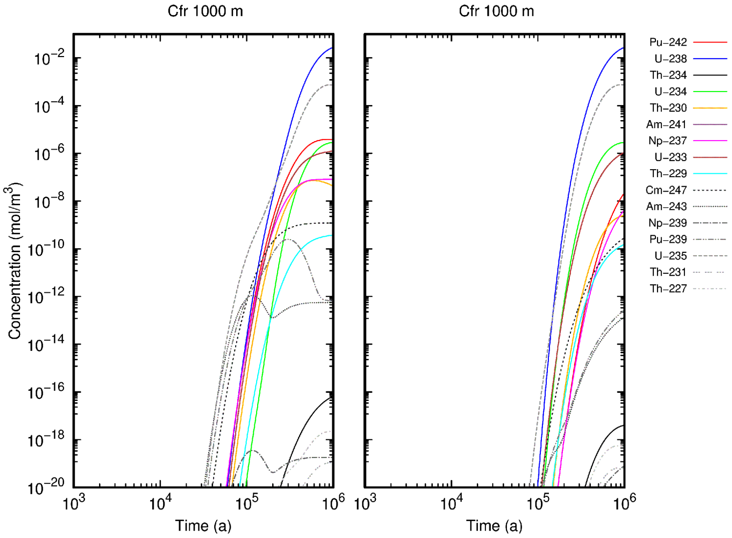

Fig. 6-58: Radionuclide concentration dissolved in solution inside the fracture system (C_{fr}) over time at the end of the fracture (1,000 m) with colloid filtration and remobilisation (left, result from case CR3 in Fig. 6-50) and a filter coefficient of $2 \cdot 10^{-3}$ m^{-1} and no colloid remobilisation (right, result from case CR5 in Fig. 6-57)

Colloid filtration factor 10-fold higher than CR5 (CR6)

Since the filter coefficient has a significant impact on the colloid facilitated transport of radionuclides, it was increased by a factor of 10 to $2 \cdot 10^{-2}$ m^{-1} in case CR6.

Due to the increase of the filter coefficient, fewer colloids are released from the fracture system (Fig. 6-59). On these mobile colloids, only Th nuclides (^{230}Th, ^{229}Th and ^{234}Th) are calculated at the end of the fracture after 1,000 m (Fig. 6-60 left). This is due to the differences in sorption coefficients for Th and U (see Tab. 6-10). As in the previous cases B1 and CR4, only U nuclides and their daughter nuclides can be calculated in solution (Fig. 6-60 right). All other nuclides associated with the colloids are retarded within the fracture. The calculated concentration in solution is the same as in case B1, which did not include any colloids (Fig. 6-60, compare centre and right).

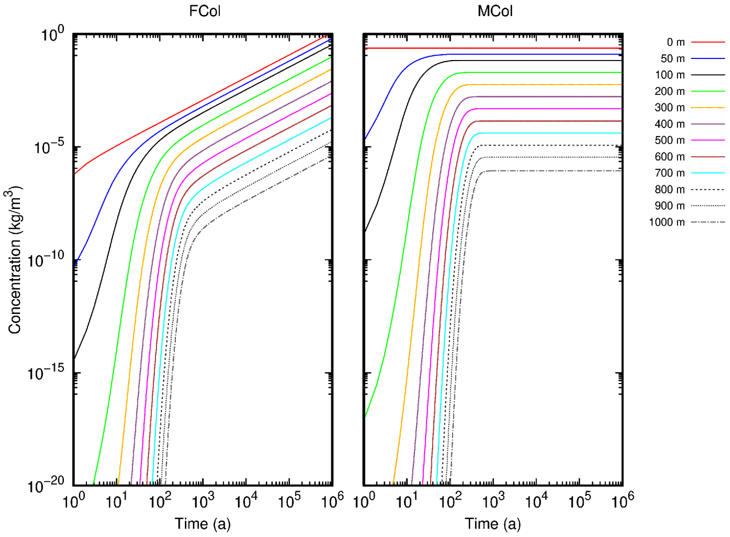

Fig. 6-59: Filtered colloids (F_{Col}, left) and mobile colloids (M_{Col}, right) over time for multiple locations inside the fracture system for case CR6 with a filter coefficient of $2 \cdot 10^{-2}$ m^{-1} and no colloid remobilisation

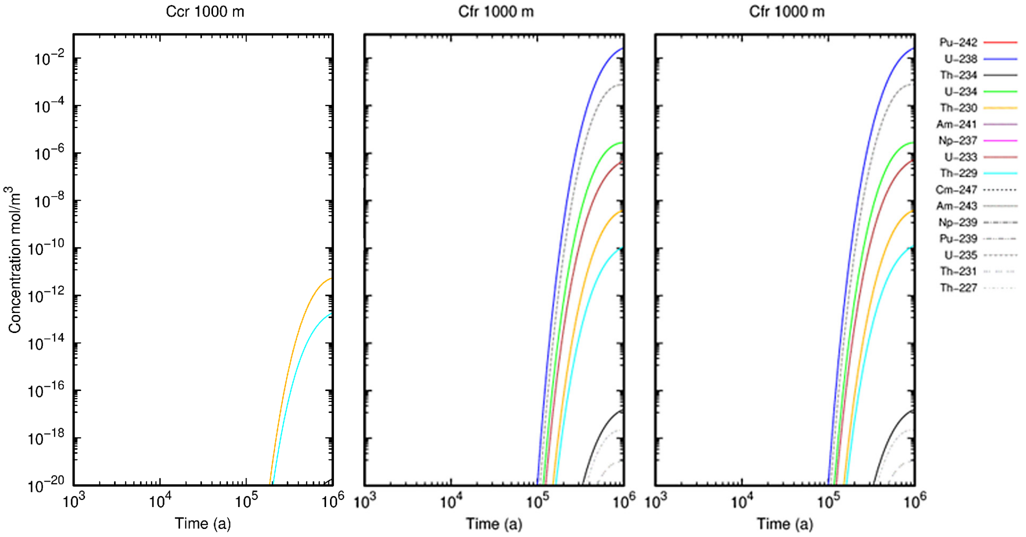

Fig. 6-60: Radionuclide concentration sorbed on mobile colloids (C_{cr}, left, results from CR6) and in solution in the fracture system (C_{fr}) over time at the end of the fracture (1,000 m)

Results from B1 without colloids (middle, see Fig. 6-44) and from CR6 (right) with a filter coefficient of $2 \cdot 10^{-2}$ m^{-1} and no colloid remobilization.

Colloid filtration set to $6 \cdot 10^{-3}$ m^{-1} (CR7)

Case CR6 shows that a high filter coefficient leads to no colloids released from the fracture. To test where a boundary value for the filter coefficient could be, the filter coefficient was set to $6 \cdot 10^{-3}$ m^{-1} in case CR7 as a value between $2 \cdot 10^{-3}$ m^{-1} (CR5) and $2 \cdot 10^{-2}$ m^{-1} (CR6).

With a filter coefficient of $6 \cdot 10^{-3}$ m^{-1}, the concentration of colloids in the fracture (Fig. 6-61) lies in between the value for cases CR5 and CR6. Although a higher concentration of colloids is transported within the fracture, the same behaviour of the concentration in solution at the end of the fracture at 1,000 m is calculated as for cases B1 and CR6 (Fig. 6-62). But in case CR7, ^{247}Cm and ^{243}Am increase above a concentration of 10^{-20} mol·l^{-1} for a time >$3 \cdot 10^{5}$ a.

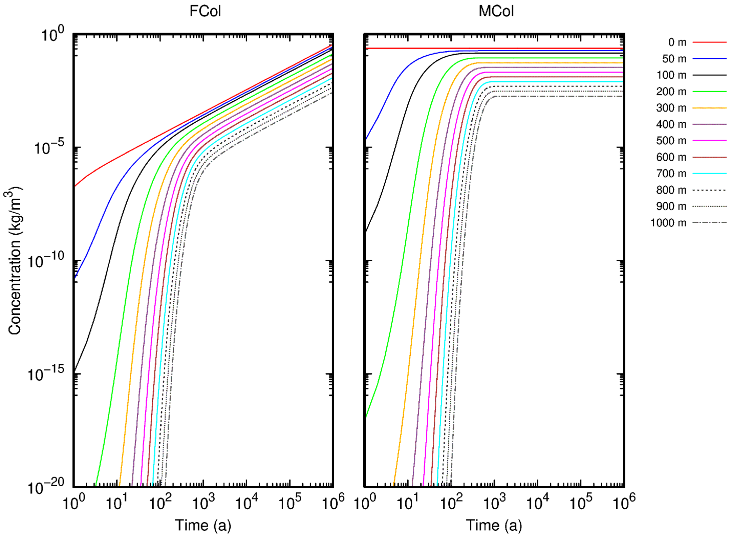

Fig. 6-61: Filtered colloids (F_{Col}, left) and mobile colloids (M_{Col}, right) over time for multiple locations inside the fracture system for case CR7 with a filter coefficient of $6 \cdot 10^{-3}$ m^{-1} and no colloid remobilisation

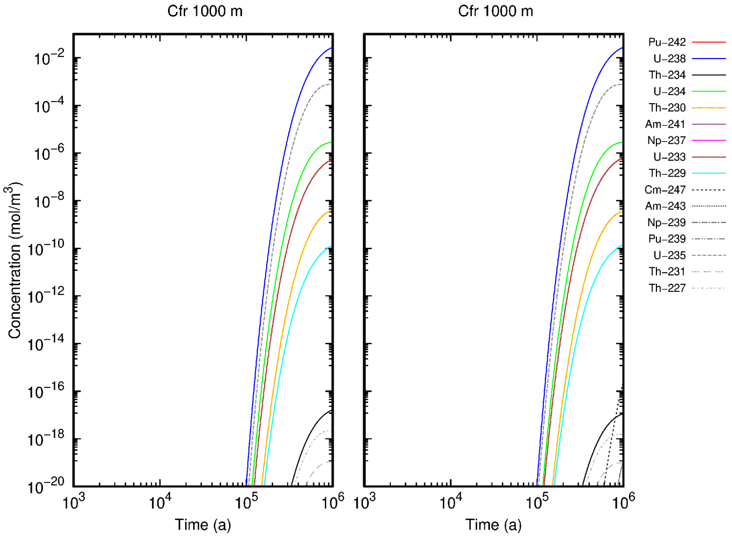

Fig. 6-62: Radionuclide concentration in solution in the fracture system (C_{fr}) over time at the end of the fracture (1,000 m) with a filter coefficient of $2 \cdot 10^{-2}$ m^{-1} and no colloid remobilisation (left, result from CR6 in Fig. 6-60) and with a filter coefficient of $6 \cdot 10^{-3}$ m^{-1} and no colloid remobilisation (right, results from CR7)

6.4.3.4 Constant colloid release: reduction of sorption on colloids

Besides the filter coefficient, the sorption of radionuclides on colloids also influences their transport within the fracture system. To test the influence of the sorption for transport, the sorption coefficients given in Tab. 6-10 were lowered by a factor of 10, resulting in a K_d value of 150 $m^3 \cdot kg^{-1}$ for trivalent and 160 $m^3 \cdot kg^{-1}$ for tetravalent radionuclides.

The cases for the reduction of the sorption coefficient are based on:

- **Case CR3 with a filter coefficient and remobilisation from Huber et al. (CR8)** and
- **Case CR5 with a filter coefficient of $2 \cdot 10^{-3}$ m^{-1} and no colloid remobilisation (CR9)**.

In cases CR3 and CR5, radionuclides were transported with the colloids through the fracture system. Not only U and its daughter nuclides, but also the trivalent and tetravalent radionuclides associated with the colloids were found.

Lowering sorption coefficients for tri- and tetravalent radionuclides by a factor of 10 reduces the concentration of radionuclides on the colloid surface. This behaviour can be seen in concentrations of mobile colloids and in solution inside the fracture in Fig. 6-63 and Fig. 6-64 for case CR3 compared to CR8 as well as in Fig. 6-65 and Fig. 6-66 for case CR5 compared to CR9, respectively.

In case CR8, the colloids are remobilised within the fracture system. However, due to the lower sorption coefficient, the impact of colloids on the radionuclide transport is reduced and the radionuclides (e.g. Am-241 and Np-237) arrive much later at the end of the pathway with reduced concentration. Due to the reduced sorption coefficient of radionuclides on colloids, the ratio of free dissolved and mobile colloid-bound radionuclides increases by a factor of ten. For U and its daughter nuclides, only small differences can be seen for very low concentrations before 10^5 years, caused by the artefact discussed for case CR2.

Case CR9 is modelled without remobilisation. Therefore, only negligible colloid concentration reaches the end of the fracture system at 1,000 m. Together with the reduction of the sorption coefficient, no trivalent and tetravalent radionuclides on mobile colloids and in solution above a concentration of $>10^{-20}$ $mol \cdot m^{-3}$ are observed at the end of the transport pathway. The concentration of Th on the mobile colloids in Fig. 6-66 can be explained by sorption of these elements from solution (where U is transported, and Th nuclides are formed through radioactive decay of uranium isotopes) onto the colloids.

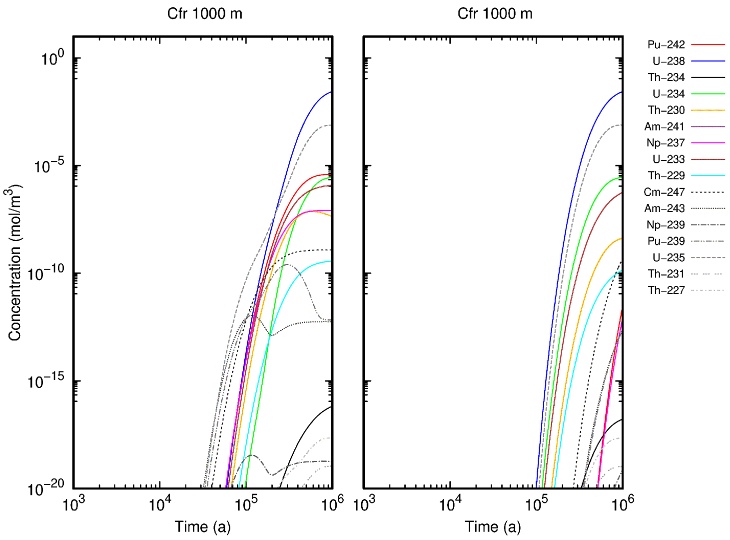

Fig. 6-63: Radionuclide concentration in solution in the fracture system (C_{fr}) over time at the end of the fracture (1,000 m) with a filter coefficient and remobilisation from Huber et al. (2016) (left, result from CR3 in Fig. 6-50) and the same input but with reduction of the sorption coefficients (right, results from CR8)

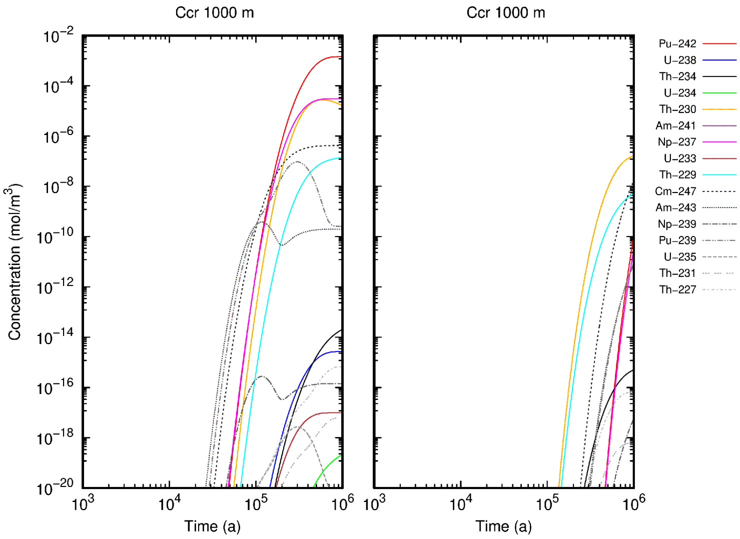

Fig. 6-64: Radionuclide concentration sorbed on mobile colloids (C_{cr}) over time at the end of the fracture (1,000 m) with a filter coefficient and remobilisation from Huber et al. (2016) (left, result from CR3 in Fig. 6-50) and the same input but with reduction of the sorption coefficients (right, results from CR8)

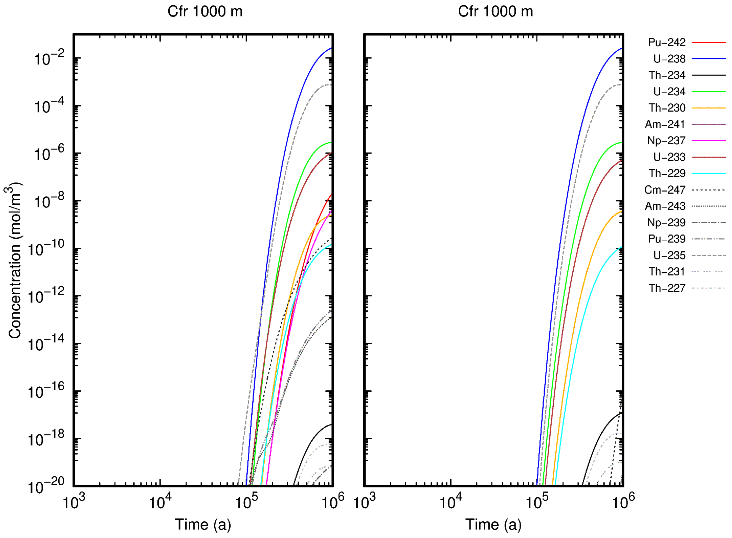

Fig. 6-65: Radionuclide concentration in solution in the fracture system (C_{fr}) over time at the end of the fracture (1,000 m) with a filter coefficient of $2 \cdot 10^{-3}$ m^{-1} and no colloid remobilisation (left, result from CR5 in Fig. 6-57) and the same input but with reduction of the sorption coefficients (right, results from CR9)

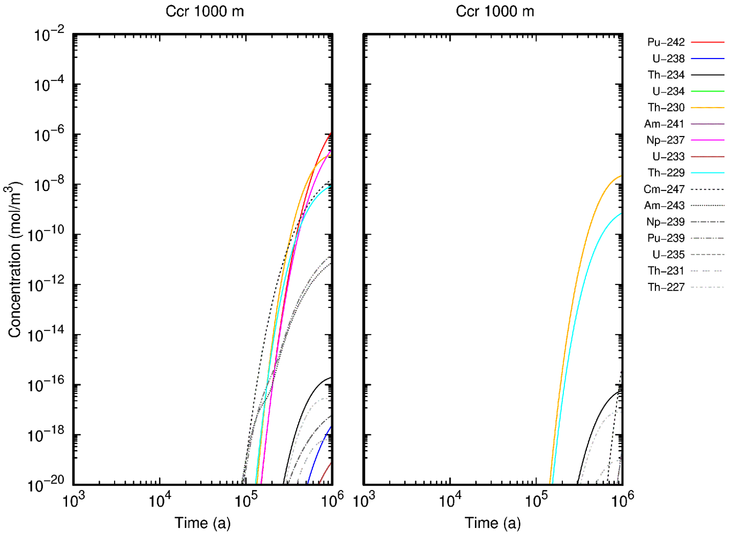

Fig. 6-66: Radionuclide concentration sorbed on mobile colloids (C_{cr}) over time at the end of the fracture (1,000 m) with a filter coefficient of $2 \cdot 10^{-3}$ m^{-1} and no colloid remobilisation (left, result from CR5 in Fig. 6-57) and the same input but with reduction of the sorption coefficients (right, results from CR9)

6.4.3.5 Colloid release in glacial cycles

A deep geological repository for high-level radioactive waste could have freshwater intrusions which are related to glacial cycles (description see Section 6.4.2.5). In the following cases, the periodic release of colloids into the fracture system following the glacial cycles is modelled.

As a first case (GC0), the colloid release was only modelled in the periods given in Fig. 6-39, where brackish water enters the system. In between these periods, no colloid release was assumed. This case had numerical difficulties. To reduce these numerical problems, a basic colloid release rate was set to $1 \cdot 10^{-8}$ kg·a^{-1} for the glacial periods in case GC1. The resulting colloid release rate over time is shown in Fig. 6-67. With this basic concentration, COFRAME is able to calculate a colloid transport. But as can be seen in Fig. 6-68, there are still numerical problems that lead to negative colloid concentrations resulting in gaps of the lines in a logarithmic plot.

Colloid filtration with recalculated filter coefficient 2·10^{-3} m^{-1} (GC2)

For case GC2, the base colloid release rate increased to $1 \cdot 10^{-5}$ kg·a^{-1} as given in Section 6.4.2.5. Also, the same filter coefficient as case CR5 with a value of $2 \cdot 10^{-3}$ m^{-1} and no remobilisation is used. The resulting colloid concentration within the fracture (Fig. 6-69) shows variations during the times of freshwater intrusion. But no gaps are visible in this plot.

At the end of the fracture system after 1,000 m, radionuclide concentrations can be calculated for mobile and immobile colloids as well as in solution and on the fracture walls (Fig. 6-70 and Fig. 6-71). Th concentrations increase when the first release of colloids arrives at the end of the fracture system. All the next release cycles are also reflected in the concentrations.

The differences in arrival time can also be seen in comparison to case CR5 with the same transport parameters but a constant input of colloids (Fig. 6-72 and Fig. 6-73). Arrival times of radionuclides in solution (C_{fr}, Fig. 6-72) and on mobile colloids (C_{cr}, Fig. 6-73) are the same at approx. 10^5 a. However, the concentrations on case GC2 are higher compared to CR5.

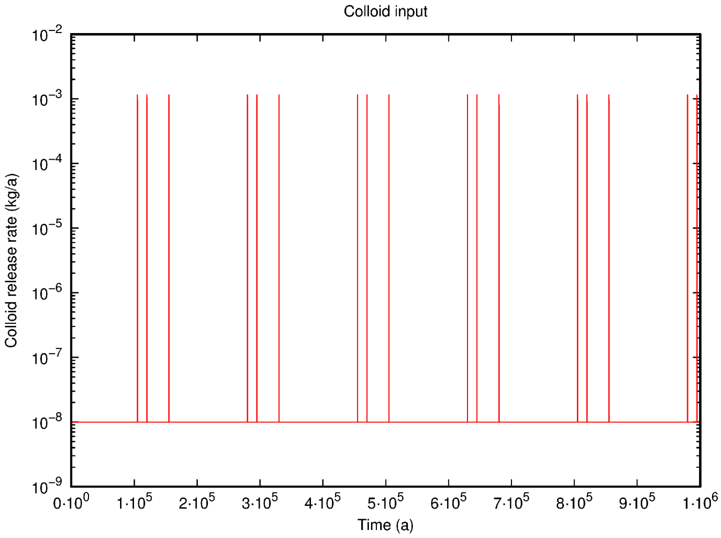

Fig. 6-67: Colloid release rate with a Fig. 6-40 lower concentration of $1 \cdot 10^{-8}$ kg·a^{-1} compared to in between freshwater intrusions for case GC1

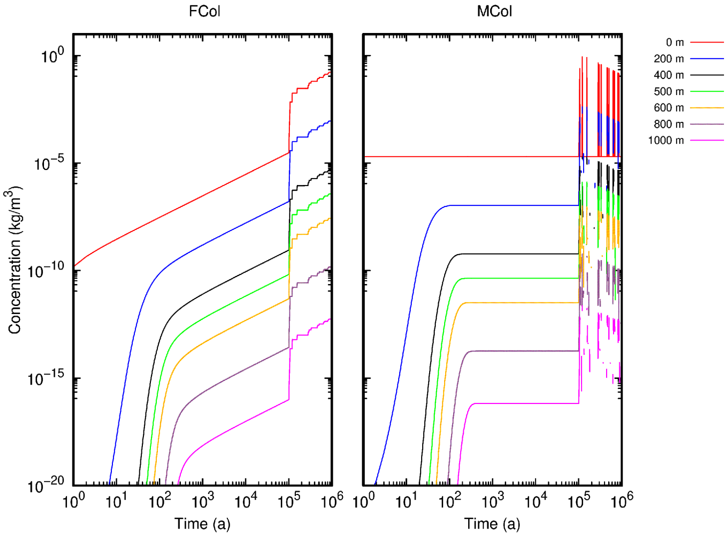

Fig. 6-68: Filtered colloids (F_{Col}, left) and mobile colloids (M_{Col}, right) over time for multiple locations inside the fracture system for the input concentration given in Fig. 6-67, a filter coefficient of $6 \cdot 10^{-2}$ m^{-1} and no colloid remobilisation in case GC1

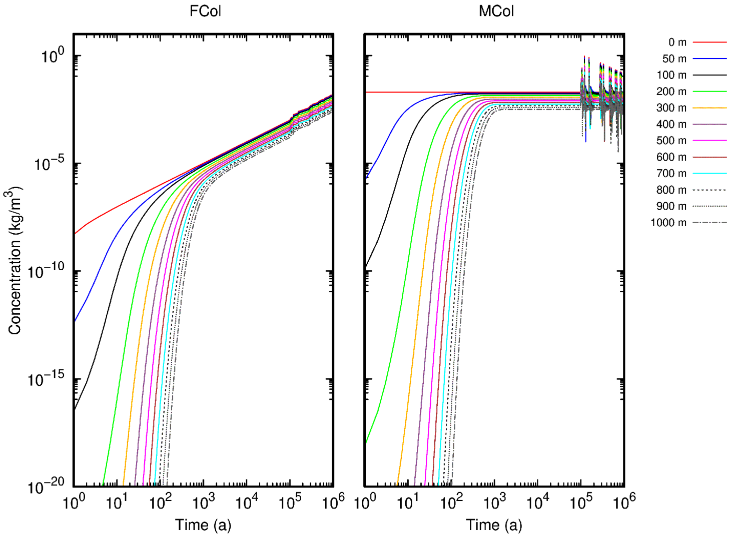

Fig. 6-69: Filtered colloids (F_{Col}, left) and mobile colloids (M_{Col}, right) over time for multiple locations inside the fracture system for the colloid release concentration given in Fig. 6-40, a filter coefficient of $2 \cdot 10^{-3}$ m^{-1} and no colloid remobilisation in case GC2

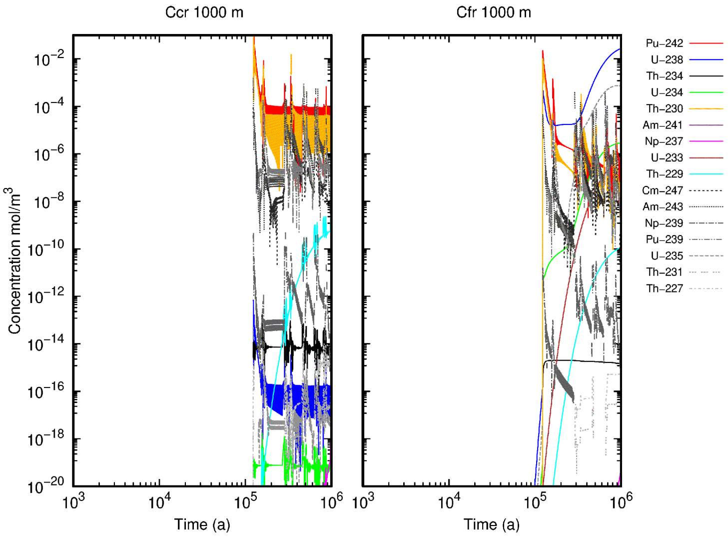

Fig. 6-70: Radionuclide concentration sorbed on mobile colloids (C_{cr}, left) and dissolved in solution inside the fracture system (C_{fr}, right) over time at the end of the fracture for case GC2 with colloid in cycles, a filter coefficient of $2 \cdot 10^{-3}$ m^{-1} and no colloid remobilisation

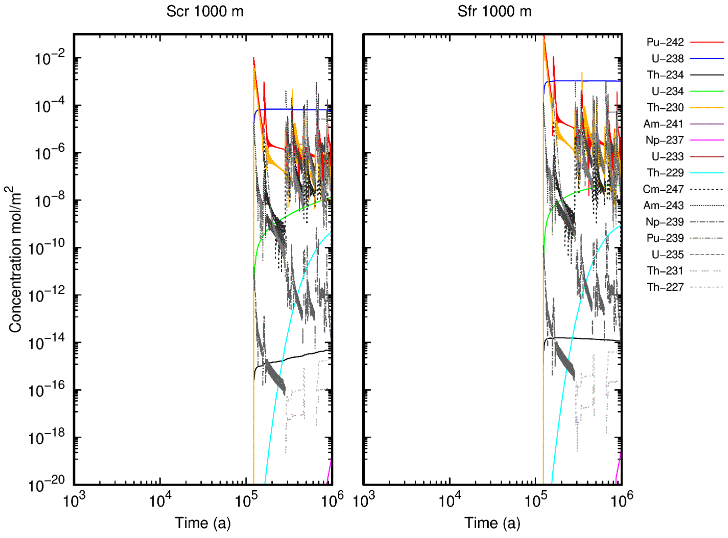

Fig. 6-71: Radionuclide concentration sorbed on immobile mobile colloids (S_{cr}, left) and on the fracture wall (S_{fr}, right) over time at the end of the fracture for case GC2 with colloid in cycles, a filter coefficient of $2 \cdot 10^{-3}$ m^{-1} and no colloid remobilisation

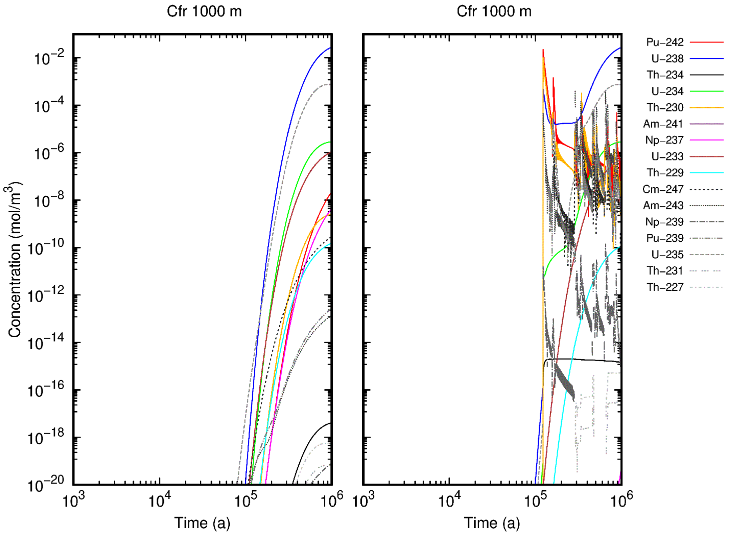

Fig. 6-72: Radionuclide concentration dissolved in solution inside the fracture system (C_{fr}) over time at the end of the fracture (1,000 m) with a filter coefficient of $2 \cdot 10^{-3}$ m^{-1} and no colloid remobilisation (left, result from CR5 in Fig. 6-57) and the same input but with colloid release in glacial cycles (right, results from GC2)

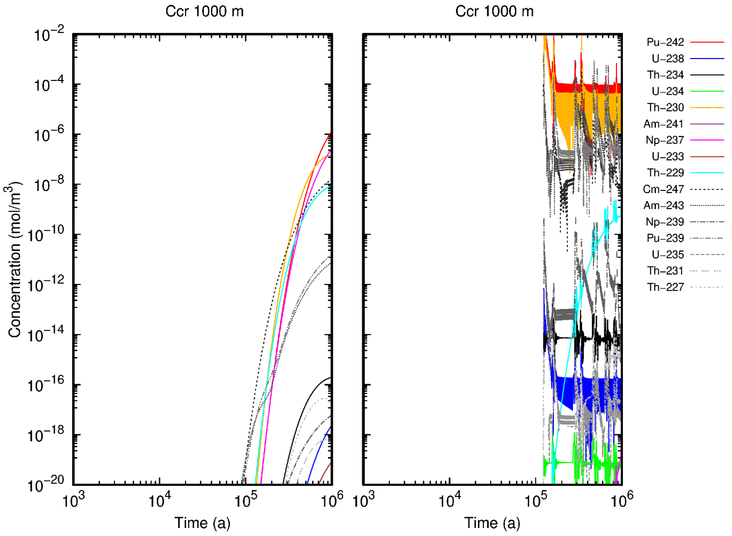

Fig. 6-73: Radionuclide concentration sorbed on mobile colloids (Ccr) over time at the end of the fracture (1,000 m) with a filter coefficient of $2 \cdot 10^{-3}$ m^{-1} and no colloid remobilisation (left, result from CR5 in Fig. 6-57) and the same input but with reduction of the sorption coefficients (right, results from GC2)

6.4.4 Summary and conclusions

Calculations of colloid-facilitated radionuclide transport in crystalline rock on the repository scale have been performed assuming a transport pathway of 1000 m through a planar-like fracture. Since only scarce information is available for crystalline rock systems in Germany, various assumptions with respect to the hydrogeological conditions and properties of the crystalline formations have been made. The radionuclide inflow from the bentonite buffer has been taken from a recent study performed for a potential repository in crystalline rock in Germany.

The modelling cases with constant colloid release into the fracture system show that U isotopes, which are not associated with colloids, and their daughter nuclides are found in all cases after 1,000 m at the end of the fracture. This is due to the sorption coefficient on the fracture-filling material, which is much lower for U than for the other nuclides (Fig. 6-74, CR6 second to the left). In the absence of colloids, the trivalent and tetravalent radionuclides do not reach the end of the pathway after 1,000 years since they are strongly retarded by sorption on fracture filling material (Fig. 6-74, B1 left). when they do enter the fracture system associated with the colloids, they can only be observed at the end of the pathway after less than one million years, when enough colloids have been transported through the fracture and when the sorption onto these colloids is high enough (Fig. 6-74, CR5 third to the left and CR8 right).

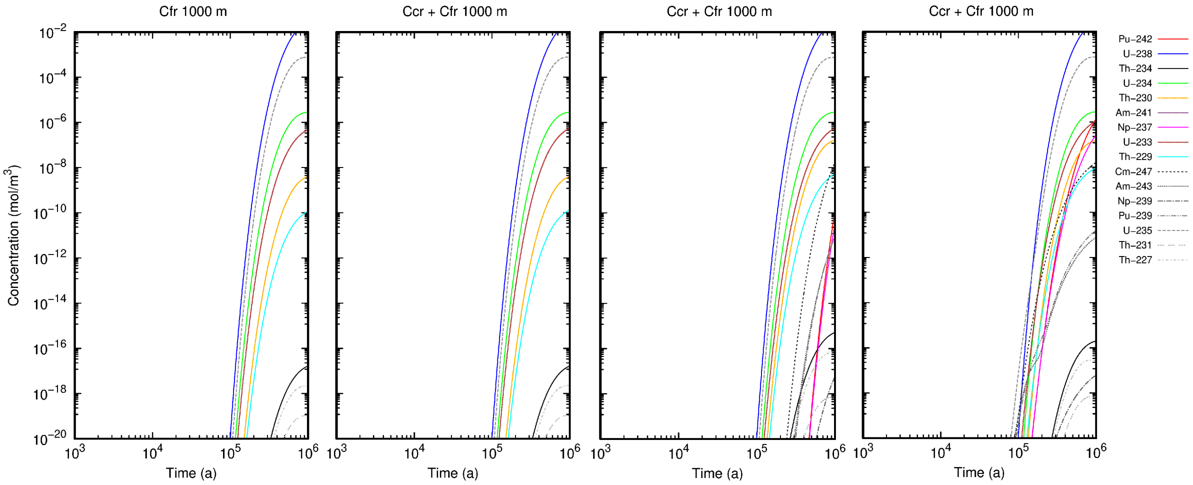

Fig. 6-74: Radionuclide concentration in solution (Cfr) over time at the end of the fracture (1,000 m) for the base case where radionuclides are transported without colloids (left, B1) and the sum of the radionuclide concentration sorbed on mobile colloids (Ccr) together with Cfr for case CR6 with a filter coefficient of $2 \cdot 10^{-2}$ m^{-1} and no colloid remobilisation (second to the left), case CR5 with a filter coefficient of $2 \cdot 10^{-3}$ m^{-1} and no colloid remobilisation (third on the left) and Case CR8 with filter coefficient and remobilisation from Huber et al. (2016) but with reduction of the sorption coefficients (right)

The colour code in all figures is the same.

The important processes for colloid-facilitated radionuclide transport in the modelled cases are therefore the sorption/desorption processes of the radionuclides onto the colloids and the process of filtering (and, if occurring, remobilisation) of these colloids in the fracture system. Typical filtration rates observed in the field tests at GTS would lead to a strong filtration of colloids and thus do not facilitate the transport of radionuclides, unless remobilisation occurs.

The release of colloids into the fracture system following the glacial cycles and modelling possible freshwater intrusions into the repository system were calculated in cases GC1 and GC2 (Section 6.4.3.5). Due to numerical problems, the concentration of colloids between the glacial cycles cannot be set to zero. A basic colloid concentration needs to be modelled.

The maximum colloid concentration entering the fracture system during freshwater intrusions is higher compared to the constant release. This leads to a higher concentration of radionuclides at the end of the fracture system compared to the constant release.

The results of the constant colloid release show that variations of filter coefficient and sorption coefficient could lead to higher colloid concentrations and therefore a higher concentration of radionuclides associated with colloids. The effect of these parameters on the colloid-facilitated transport for release in glacial cycles should be tested with further modelling.

7 Summary and conclusions

Bentonite erosion

Summarising the key findings, we aimed for a contribution and transferability of the small-scale laboratory experiments to the large-scale in-situ i-BET setup. The same base material was applied for both the i-BET project and the artificial fracture cell erosion experiments (Bara-Kade bentonite, Na-dominated natural wyoming bentonite, comparable to MX-80) and both were brought into contact with GTS groundwater. The comparison is biased by *inter alia* differences in fracture material (acrylic glass vs. granite) and surface roughness. Differences were also observed concerning the hydro-chemical evolution of the systems with Ca release observed in the i-BET system. Measured average colloidal particle concentrations were similar for the artificial fracture cell experiments (5.1 ± 1.6E+08 particles/mL) and the i-BET setup (CFM18.001: 1.6 ± 0.1E+08; CFM18.002: 1.7 ± 0.1E+08; CFM18.003: 1.5 ± 0.1E+08 particles/mL). However, a tendency towards larger particle-size distributions was observed for the laboratory experiments over time, while the i-BET setup had an opposite trend. Erosion rates in the same order of magnitude could be approximated for both the artificial MX-80 reference setup with 0.25 ± 0.11 kg/m²/a and the i-BET setup with approx. 0.2 to 0.5 kg/m²/a, although the fracture orientation is different. Na-exchanged montmorillonites from different sources (here, MX-80 or GMZ-001) developed different swelling and erosion behaviour with GMZ 001-derived Na-mnt showing generally higher erosion. As expected, the contact pressure depended on the smectite/ montmorillonite content and the exchangeable cation composition with higher pressures for the Na form.

Increasing amounts of soluble Ca- containing accessory minerals reduced the swelling ability of the respective samples via calcium cation exchange. In the case of the artificial Na-mnt samples, 2 wt.% of added hemihydrate were insufficient to supply the gel with an adequate amount of calcium, thus leading to an increased clay erosion, whereas ≥5 wt.% of added Ca carrier was sufficient. Non-reactive accessory mineral quartz (10 or 20 wt.%) powder with average grain size of 2 µm had no impact on the swelling or erosion behaviour.

Compared to literature data, no uniform picture exists to date concerning accessory minerals and will be a topic for further investigations.

Radionuclide migration

Post-mortem characterisation of samples from LIT and respective Mock-up experiments have been started. Respective sample preparation methods were developed to (i) take samples from the experimental segments that are as undisturbed as possible and (ii) to analyse tracer radionuclides down to lowest concentration levels using mass spectrometric methods in post-mortem and collected water samples from the LIT. In samples from the outflow of LIT, only the lowest actinide concentrations close to the background levels of the site (partly originating from earlier tracer tests) and detection limits of the method could be discovered. Only for ^{99}Tc, could significant concentrations be detected, albeit at an ultra-trace level. A concentration of (4.5 ± 1.2) × 10^{6} atoms/mL (corresponding to 7.5 × 10^{-15} mol/L) after 1,600 days demonstrates a continuous "bleeding" of ^{99}Tc from the source, which can be explained by a small fraction of oxidised technetium existing as mobile and non-sorbing TcO_4^- species. For the actinides Np and Pu, low mobility of the tetravalent redox states can be assumed.

In mock-up bentonite samples taken from the vicinity of tracer vials, ^{237}Np and ^{233}U diffusion profiles could be experimentally determined. Even though data are scattered pointing to spatially variable abundance of strongly sorbing minerals and possible preferential pathways existing in the early experimental phase where the bentonite was not yet saturated, a more or less flat diffusion profile was established. Those results clearly demonstrate the less reducing conditions in the mock-up experiment compared to the in-situ test, leading to significant fractions of oxidised species such as hydroxo or carbonate complexes of $^{237}NpO_2^{+}$ and $^{233}UO_2^{2+}$, respectively. Data at least qualitatively confirm the outcome of diffusion calculations and suggest the establishment of steady-state conditions.

Global fallout actinides at the GTS

For the first time, actinide nuclides derived from global fallout, namely ^{236}U, ^{237}Np and ^{239}Pu were analysed in a series of six GW samples collected at different locations of the GTS together with a surface water sample from Lake Grimsel. This study represented a proof of concept for the investigation of the possible downward migration of actinides mainly generated during the atmospheric testing of H-bombs during the early 1960s from the surface down to the GTS. While the surface water sample from Lake Grimsel carried clear signals of global fallout in the form of ^{236}U, ^{237}Np and ^{239}Pu, among the six investigated GW samples, ^{236}U and ^{237}Np were determined at the ultra-trace levels of 10^5 and 10^6 atoms/250 mL in one sample, respectively, and potentially originated from global fallout. in another sample, ^{236}U lay similarly above a blank background. Levels of ^{239}Pu were consistent with or below blank background in all GW samples, possibly reflecting the affinity of Pu(IV) to be retained in the soil, lake sediments or in the fault gouge material of the GTS due to sorption as well as filtration processes for colloid-associated Pu. At the same time, a preferential migration of U(VI) and Np(V) as dissolved species from the surface down to the two GW samples can be inferred. Furthermore, a sample of the secondary mineral Grimselite presented a $^{236}U/^{238}U$ isotopic ratio of $(8 \pm 3) \times 10^{-11}$ that could also indicate a slightly enhanced isotopic abundance for ^{236}U with respect to its natural levels. These preliminary results must be proven with further investigations, which are currently planned. However, this proof-of-concept study demonstrates our analytical capability to make use of the study of global fallout actinides at the GTS as a natural analogue system, thereby greatly extending the scale of time and space in which radionuclide behaviour can be investigated.

Modelling results

The speciation of the radionuclides, for example their redox state, is of crucial importance for their mobility, solubility and interaction with colloids in systems in the near- and far-fields of a repository in crystalline rock. To check (i) the influence of the geochemical conditions on radionuclide speciation and (ii) the applicability of the currently available databases, benchmark calculations for the speciation and solubility of six radionuclides used in the LIT, i.e. $^{75}Se(VI)$, $^{99}Tc(VII\ )$, $^{233}U\ (VI)$, $^{237}Np(V)$, $^{241}Am(III)$, $^{242}Pu(IV)$ and $^{232}Th(IV)$ have been performed in bentonite porewater, Grimsel groundwater and mixed water that form at the bentonite/crystalline rock interface. The first results of two modelling groups have already been published (Montoya et al. 2021). By comparing results of the six different modelling groups, key geochemical parameters affecting radionuclide transport could be identified. In general, the calculations of all modelling groups agree well. Few differences arose in the calculation of maximum concentrations for radionuclides, which are required for the planning of radionuclide tracer cocktails for in-situ experiments. These differences are mainly caused by different solubility-determining solid phases and their crystallinity, which the respective experts suggested as relevant for their calculations. A publication of the results of all six modelling groups involved is currently in preparation (Noseck et al. 2024, to be published). The extended thermodynamic benchmark exercise demonstrates the importance of thermodynamic model calculations but also shows that the robustness and traceability of the underlying data must be critically questioned. An "expert judgement" is often required but must then be justified in a transparent and comprehensible manner. This is of great value for discussions and predictions of radionuclide behaviour in selected systems beyond the project.

The characterisation of the overcored segment of the LIT is still under way. The X-ray CT showed that the fracture in the shear zone did not hit the inner four radionuclide-containing bentonite rings but occurs at a distance of 37.5 mm to one of the outer rings. Radionuclide diffusion profiles are not yet available. Simulated spatial profiles for tri- and tetravalent actinides did not change if a longer transport pathway of 37.5 mm from the nearest vial to the fracture is considered, this still being in the mm range after 4.5 years. The simulations for non-sorbing Tc(VII) and low sorbing Np(V) indicate breakthrough curves within the first month and for low-sorbing Np(V) after about half a year for the extended pathway of 37.5 mm. Since neither Np nor Tc were detected in significant amounts, they are expected to have been reduced to the tetravalent state, as they are rather immobile as described above. The conditions of the mock-up test are different, since the Eh values are in the range of +250 mV. Under these conditions, breakthrough curves for ^{99}Tc, ^{237}Np and ^{233}U have been observed. They initially increased, with peak maxima for Tc after 10 and for Np after 50 days, respectively. U and Np profiles in a part of the bentonite ring are available, but other radionuclides could not be detected in this ring segment so far. The behaviour of the mobile ^{99}Tc can be well described and the simulations indicate extremely low contents in the bentonite ring out of the vial which would explain why no spatial distribution was detected in the bentonite. The breakthrough curves for ^{237}Np and ^{233}U and their plateau-like profiles can be met by the simulations, assuming only part of both elements are mobile. However, the predicted concentrations in the plateau-like distribution profiles are significantly lower than the experimentally observed ones. An explanation for the differences can be due to the difference in the model assumptions and the experimental conditions, particularly, regarding the length of the diffusion pathway. In the model, intact vials and a diffusion pathway length of 10 mm were assumed, whereas the evaluation of the experiment showed that two vials were broken (likely at the beginning of the experiment, when the bentonite was resaturated and swollen). Based on these findings, increased K_d values for U and Np, may need to be applied, causing much higher plateau concentrations matching the observed profiles. When more experimental data are available, further simulations with modified assumptions will be performed.

Bentonite erosion was studied by simulating ion exchange of bentonite in an open fracture with a flow and reactive transport model using PHAST. It was observed that ion exchange and bentonite erosion strongly depend on fluid flow and calcium availability in solution. Using a calcium-enriched Grimsel groundwater as contact solution, the exchange increased in comparison with non-enriched Grimsel groundwater. The exchange was in turn higher when adding gypsum to the bentonite and thereby increasing the calcium concentration through an internal reservoir. These observed effects in the model are also seen in the experiment: the increased exchange and delayed erosion by adding gypsum to the system. the more gypsum is present, the higher is the amount of Ca in contact solution and therefore the exchanger occupation increased. The experiment and the model agree that it is more efficient to bring a Ca-bearing mineral into the system than to increase the Ca concentration of the solution. Still, there are some deviations regarding the experimental and modelled data. The flow field and the accessibility of the exchange sites are different in the model compared to the laboratory experiments because swelling and expansion of the bentonite cannot be depicted in PHAST. Bentonite erosion is a complex process for modelling and further work would be needed to model a high-resolution grid with continuous expansion of the bentonite into the fracture, coupled with flow and transport reactions.

Based on the results from this study and previous studies, calculations of colloid-facilitated radionuclide transport in crystalline rock on the repository scale have been performed assuming a transport pathway of 1000 m through a planar-like fracture. Since only scarce information is available for crystalline rock systems in Germany, various assumptions with respect to the hydrogeological conditions and properties of the crystalline formations have been made. The radionuclide inflow from the bentonite buffer has been taken from a recent study performed for a potential repository in crystalline rock in Germany. The modelling cases with constant colloid release into the fracture system show that U isotopes, which are not associated with colloids, and their daughter nuclides are found in all cases after 1,000 m at the end of the fracture. This is due to the sorption coefficient on the fracture-filling material, which is much lower for U than for the other nuclides. In the absence of colloids, the tri- and tetravalent radionuclides do not reach the end of the pathway after 1,000 years since they are strongly retarded by sorption on fracture-filling material. In the case when they enter the fracture system associated with the colloids, they can only be observed at the end of the pathway after less than one million years, when enough colloids have been transported through the fracture and when sorption onto these colloids is high enough. The main uncertainty is the conceptual description of colloidal transport across a fracture as a porous medium. The filter coefficient for porous media on which the calculations are based is decisive for the extent of colloidal transport.

8 References

Agus, S.S. & Schanz, T. (2008): A method for predicting swelling pressure of compacted bentonites. Acta Geotechnica 3/2, 125-137. DOI: 10.1007/s11440-008-0057-0.

Alonso, E.E., Alcoverro, J., Coste, F., Malinsky, L., Merrien-Soukatchoff, V., Kadiri, I., Nowak, T., Shao, H., Nguyen, T.S., Selvadurai, A., Armand, G., Sobolik, S.R., Itamura, M., Stone, C.M., Webb, S.W., Rejeb, A., Tijani, M., Maouche, Z., Kobayashi, A., Kurikami, H., Ito, A., Sugita, Y., Chijimatsu, M., Börgesson, L., Hernelind, J., Rutqvist, J., Tsang, C.-F. & Jussila, P. (2005): The FEBEX benchmark test: case definition and comparison of modelling approaches. International Journal of Rock Mechanics and Mining Sciences 42/5-6, 611-638. DOI: 10.1016/j.ijrmms.2005.03.004.

Alonso, U., Missana, T., Fernández, A.M. & García-Gutiérrez, M. (2018): Erosion behaviour of raw bentonites under compacted and confined conditions: Relevance of smectite content and clay/water interactions. Applied Geochemistry 94, 11-20. DOI: 10.1016/ j.apgeochem.2018.04.012.

Alonso, U., Missana, T., Gutiérrez, M.G., Morejón, J., Mingarro, M. & Fernández, A.M. (2019): CIEMAT studies within POSKBAR project. Bentonite expansion, sedimentation and erosion in artificial fractures. Svensk Kärnbränslehantering AB SKB. (Technical Report, TR-19-08), available online at https://www.skb.se/publikation/2493587/TR-19-08.pdf.

Becker, D.-A., Bertrams, N., Bollingerfehr, W., Frenzel, B., Krumpholz, M., Maßmann, J., Mayer, K.-M., Mönig, J., Müller-Hoeppe, N., Reinhold, K., Rübel, A., Schubarth-Engelschall, N., Simo, E., Thiedau, J., Weber, J.R. & Wolf, J. (2020): Grundlagen zur Bewertung eines Endlagersystems in einer Kristallinsgesteinsformation mit Einschluss der Radionuklide durch technische und geotechenische Barrieren. RESUS. (GRS-577). Gesellschaft für Anlagen- und Reaktorsicherheit (GRS) gGmbH, status as of October 13, 2020.

Bethke, C.M. & Yeakel, S. (2015): The Geochemist´s Workbench. GWB Essentials Guide. Version 10.0. Aqueous Solutions, LLC.

Bouby, M., Kraft, S., Kuschel, S., Geyer, F., Moisei-Rabung, S., Schäfer, T. & Geckeis, H. (2020): Erosion dynamics of compacted raw or homoionic MX80 bentonite in a low ionic strength synthetic water under quasi-stagnant flow conditions. Applied Clay Science 198, 105797. DOI: 10.1016/j.clay.2020.105797.

Bradbury, M.H. & Baeyens, B. (2002): Porewater chemistry in compacted re-saturated MX-80 bentonite. Physico-chemical characterisation and geochemical modelling. Nagra Technical Report NTB 01-08).

Bradbury, M.H. & Baeyens, B. (2010): Sorption Data Bases for Generic Swiss Argillaceous Rock Systems. Nagra Technical Report NTB 09-03.

Brandt, F. & Bosbach, D. (2001): Bassanite ($CaSO4·0.5H2O$) dissolution and gypsum ($CaSO4·2H2O$) precipitation in the presence of cellulose ethers. Journal of Crystal Growth 233/4, 837-845. DOI: 10.1016/S0022-0248(01)01637-2.

Bruno, J., Duro, L., Rollind, C. & Guimerà, J. (2000): Prediction of the solubility and speciation of RN in Febex and Grimsel waters. QuantiSci, Barcelona, Spain.

Caballero, E., Jiménez de Cisneros, C., Huertas, F.J., Huertas, F., Pozzuoli, A. & Linares, J. (2005): Bentonites from Cabo de Gata, Almería, Spain: a mineralogical and geochemical overview. Clay Minerals 40/4, 463-480. DOI: 10.1180/0009855054040184.

Carr, B. & Wright, M. (2013): Nanoparticle tracking analysis. Innovations in Pharmaceutical Technology 26, 38-40.

Carr, B. & Wright, M. (2014): Nanoparticle Tracking Analysis. A review of the first 1000 reports of applications and usage of the Nanoparticle Tracking Analysis. Malvern Panalytical, available online at https://www.malvernpanalytical.com/en/learn/knowledge-center/whitepapers/wp150320ntabook.

CASEA GmbH (2013): Alpha AGR 40. Produktdatenblatt. CASEA GmbH, available online at https://www.casea-gips.de/fileadmin/user_upload/casea2020/downloads_DE/produktdatenblaetter/Produktdatenblatt_Alpha_AGR_40.pdf, status as of 22.12.23.

CASEA GmbH (2018): Micro A. Produktdatenblatt. CASEA GmbH, available online at https://www.casea-gips.de/fileadmin/user_upload/casea2020/downloads_DE/produktdatenblaetter/Produktdatenblatt_Micro_A.pdf, status as of 22.12.23.

Chemnitius, M. (2021): Simulationsrechnungen zu geochemischen und Transport-Prozessen im Nahbereich einer Bentonitbarriere in einem Feldexperiment im Felslabor Grimsel, Schweiz. Masterarbeit. Georg-August-Universität Göttingen.

Chen, L., Liu, Y.M., Wang, J., Cao, S.F., Xie, J.L., Ma, L.K., Zhao, X.G., Li, Y.W. & Liu, J. (2014): Investigation of the thermal-hydro-mechanical (THM) behavior of GMZ bentonite in the China-Mock-up test. Engineering Geology 172, 57-68. DOI: 10.1016/j.enggeo.2014.01.008.

Chen, Y.-G., Zhu, C.-M., Ye, W.-M., Cui, Y.-J. & Wang, Q. (2015): Swelling pressure and hydraulic conductivity of compacted GMZ01 bentonite under salinization–desalinization cycle conditions. Applied Clay Science 114, 454-460. DOI: 10.1016/j.clay.2015.06.033.

Christensen, A.N., Olesen, M., Cerenius, Y. & Jensen, T.R. (2008): Formation and Transformation of Five Different Phases in the CaSO 4 −H 2 O System: Crystal Structure of the Subhydrate β-CaSO 4 ·0.5H 2 O and Soluble Anhydrite CaSO 4. Chemistry of Materials 20/6, 2124-2132. DOI: 10.1021/cm7027542.

Dai, Z., Kan, A.T., Shi, W., Zhang, N., Zhang, F., Yan, F., Bhandari, N., Zhang, Z., Liu, Y., Ruan, G. & Tomson, M.B. (2017): Solubility Measurements and Predictions of Gypsum, Anhydrite, and Calcite Over Wide Ranges of Temperature, Pressure, and Ionic Strength with Mixed Electrolytes. Rock Mechanics and Rock Engineering 50/2, 327-339. DOI: 10.1007/s00603-016-1123-9.

Daniels, K.A., Harrington, J.F., Milodowski, A.E., Kemp, S.J., Mounteney, I. & Sellin, P. (2021): Gel Formation at the Front of Expanding Calcium Bentonites. Minerals 11/2, 215. DOI: 10.3390/min11020215.

Degueldre, C., Longworth, G., Moulin, V. & Vilks, P. (1990): Grimsel Test Site. Grimsel Colloid Exercise An inernational intercomparison exercise on the sampling and characterisation of groundwater colloids. Nagra Technical Report NTB 90-01.

Delany, J.M. & Lundeen, S.R. (1991): The LLNL thermochemical data base. revised data and file format for the EQ3/6 package. (Technical Report, UCID-21658). Lawrence Livermore National Lab LLNL.

Delavernhe, L., Steudel, A., Darbha, G.K., Schäfer, T., Schuhmann, R., Wöll, C., Geckeis, H. & Emmerich, K. (2015): Influence of mineralogical and morphological properties on the cation exchange behavior of dioctahedral smectites. Colloids and Surfaces A: Physicochemical and Engineering Aspects 481, 591-599. DOI: 10.1016/ j.colsurfa.2015.05.031.

Denecke, M.A., Bryan, N., Kalmykov, S., Morris, K. & Quinto, F. (2018): Sources and Behaviour of Actinide Elements in the Environment. *In:* Gibson, J.K. & Jong, W.A. de (eds.): Experimental and theoretical approaches to actinide chemistry. Wiley, Hoboken, NJ, 378-444.

DIN (2002): Geometrical Product Specifications (GPS) - Indication of surface texture in technical product documentation.

Dohrmann, R., Genske, D., Karnland, O., Kaufhold, S., Kiviranta, L., Olsson, S., Plötze, M., Sandén, T., Sellin, P., Svensson, D. & Valter, M. (2012): Interlaboratory CEC and Exchangeable Cation Study of Bentonite Buffer Materials: I. Cu(II)-triethylenetetramine Method. Clays and Clay Minerals 60/2, 162-175. DOI: 10.1346/CCMN.2012.0600206.

Duda, R., Rejl, L. & Slivka, D. (1990): Minerals (in Czech). Aventinum, Prague, available online at https://www.mindat.org/loc-7944.html.

Dundon, M.L. & Mack, E. (1923): The solubility and surface energy of calcium sulfate. Journal of the American Chemical Society 45/11, 2479-2485. DOI: 10.1021/ja01664a001.

Duro, L., Grivé, M., Cera, E., Gaona, X., Domènech, C. & Bruno, J. (2006): Determination and assessment of the concentration limits to be used in SR-Can. (Technical Report, TR-06-32). Svensk Kärnbränslehantering AB SKB.

EndlSiUntV (2020): Verordnung über Anforderungen an die Durchführung der vorläufigen Sicherheitsuntersuchungen im Standortauswahlverfahren für die Endlagerung hochradioaktiver Abfälle of October 6, 2020, status as of October 6, 2022. BGBl. I, 2094.

Engelhardt, W. (1960): Der Porenraum der Sedimente. (Mineralogie und Petrographie in Einzeldarstellungen, 2). Springer Berlin Heidelberg, Berlin, Heidelberg, s.l.

Eriksson, R. & Schatz, T. (2015): Rheological properties of clay material at the solid/solution interface formed under quasi-free swelling conditions. Applied Clay Science 108, 12-18. DOI: 10.1016/j.clay.2015.02.018.

Fernández, A.M., Baeyens, B., Bradbury, M. & Rivas, P. (2004): Analysis of the porewater chemical composition of a Spanish compacted bentonite used in an engineered barrier. Physics and Chemistry of the Earth 29/105-118. DOI: 10.1016/j.pce.2003.12.001.

Fernández, A.M., Cuevas, J. & Rivas, P. (2000): Pore Water Chemistry of the Febex Bentonite. MRS Proceedings 663. DOI: 10.1557/PROC-663-573.

Fernández, A.M., Missana, T., Alonso, U., Rey, J.J., Sánchez-Ledesma, D.M., Melón, A. & Robredo, L.M. (2017): Characterisation of Different Bentonites in the Context of BELBAR Project (Bentonite Erosion: Effects on the Long Term Performance of the Engineered Barrier and Radionuclide Transport). (CIEMAT Report), Madrid, Spain.

Filipe, V., Hawe, A. & Jiskoot, W. (2010): Critical evaluation of Nanoparticle Tracking Analysis (NTA) by NanoSight for the measurement of nanoparticles and protein aggregates. Pharmaceutical research 27/5, 796-810. DOI: 10.1007/s11095-010-0073-2.

Fujiwara, K., Kitamura, A. & Yui, M. (2010): JAEA Thermodynamic database for performance assessment of geological disposal of high-level and TRU radioactive wastes. Refinement of thermodynamic data for tetravalent thorium, uranium, neptunium and plutonium [in Japanese]. (JAEA-Review, 2009-059), available online at https://jopss.jaea.go.jp/search/servlet/search?5023059&language=1.

Geckeis, H., Schäfer, T., Hauser, W., Rabung, T., Missana, T., Degueldre, C., Möri, A., Eikenberg, J., Fierz, T. & Alexander, W.R. (2004): Results of the colloid and radionuclide retention experiment (CRR) at the Grimsel Test Site (GTS), Switzerland – impact of reaction kinetics and speciation on radionuclide migration. Radiochimica Acta 92/9-11, 765-774. DOI: 10.1524/ract.92.9.765.54973.

Geckeis, H., Zavarin, M., Salbu, B., Lind, O.C. & Skipperud, L. (2019): Evironmental Chemistry of Plutonium. *In:* Clark, D.L., Geeson, D.A. & Hanrahan, R.J. (eds.): Plutonium handbook. 2nd ed. (3). American Nuclear Sociedty, La Grange Park, Illinois, USA, 1979-2118.

Giffaut, E., Grivé, M., Blanc, P., Vieillard, P., Colàs, E., Gailhanou, H., Gaboreau, S., Marty, N., Madé, B. & Duro, L. (2014): Andra thermodynamic database for performance assessment: ThermoChimie. Applied Geochemistry 49, 225-236.
DOI: 10.1016/ j.apgeochem.2014.05.007.

Gisinger, J. (2022): GTS iBET Experiment, Monitoring and maintenence Update, 01/01/21 - 19/12/22. (A 1588-89). Solexperts AG.

Hole, P., Sillence, K., Hannell, C., Maguire, C.M., Roesslein, M., Suarez, G., Capracotta, S., Magdolenova, Z., Horev-Azaria, L., Dybowska, A., Cooke, L., Haase, A., Contal, S., Manø, S., Vennemann, A., Sauvain, J.-J., Staunton, K.C., Anguissola, S., Luch, A., Dusinska, M., Korenstein, R., Gutleb, A.C., Wiemann, M., Prina-Mello, A., Riediker, M. & Wick, P. (2013): Interlaboratory comparison of size measurements on nanoparticles using nanoparticle tracking analysis (NTA). Journal of nanoparticle research : an interdisciplinary forum for nanoscale science and technology 15/12, 2101. DOI: 10.1007/s11051-013-2101-8.

Hoo, C.M., Starostin, N., West, P. & Mecartney, M.L. (2008): A comparison of atomic force microscopy (AFM) and dynamic light scattering (DLS) methods to characterize nanoparticle size distributions. Journal of nanoparticle research : an interdisciplinary forum for nanoscale science and technology 10/S1, 89-96. DOI: 10.1007/s11051-008-9435-7.

Horwitz, E., Dietz, M.L., Chiarizia, R., Diamond, H., Maxwell, S.L. & Nelson, M.R. (1995): Separation and preconcentration of actinides by extraction chromatography using a supported liquid anion exchanger: application to the characterization of high-level nuclear waste solutions. Analytica Chimica Acta 310/1, 63-78. DOI: 10.1016/0003-2670(95)00144-O.

HPF (2015): SIKRON® Quarz. Stoffdaten. HPF, Frechen, available online at https://www.quarzwerke.com/fileadmin/quarzwerke/pdf/HPF_Broschueren/HPF_Produktuebersicht.pdf.

Huber, F., Noseck, U. & Schäfer, T. (eds.) (2014): Colloid/nanoparticle formation and mobility in the context of deep geological nuclear waste disposal. Project KOLLORADO-2 Final Report. Karlsruher Institut für Technologie KIT. (KIT Scientific Report, 7645).

Huber, F.M., Noseck, U. & Schäfer, T. (eds.) (2016): Stability of compacted bentonite for radionuclide retardation – Experiments and modelling. Project Kollorado-e Final Report. Karlsruher Institut für Technologie KIT, Karlsruhe.

Hulett, G.A. (1901): Beziehungen zwischen Oberflächenspannung und Löslichkeit. Zeitschrift für Physikalische Chemie 37U/1, 385-406. DOI: 10.1515/zpch-1901-3722.

IAEA (2013): Characterization of Swelling Clays as Components of the Engineered Barrier System for Geological Repositories. Results of an IAEA Coordinated Research Project 2002–2007. (IAEA-TECDOC-1718). International Atomic Energy Agency IAEA, available online at https://www-pub.iaea.org/MTCD/Publications/PDF/TE-1718_web.pdf.

Karnland, O. (2010): Chemical and mineralogical characterization of the bentonite buffer for the acceptance control procedure in a KBS-3 repository. (Technical Report, TR-10-60). Svensk Kärnbränslehantering AB SKB, available online at https://www.skb.se/upload/publications/pdf/TR-10-60.pdf.

Karnland, O., Olsson, S. & Nilsson, U. (2006): Mineralogy and sealing properties of various bentonites and smectite-rich clay materials. (SKB Technical Report, TR-06-30). Svensk Kärnbränslehantering AB SKB, available online at https://www.skb.se/publication/1419144/TR-06-30.pdf.

Kaufhold, S., Shao, H., Wang, J., Liu, Y., Zhang, Q., Xie, J., Li, N., Schäfer, T., Pingel, J.L., Czaikowski, O., Zhang, C.-L., Geckeis, H., Wang, Q., Chaudhry, A.A., Konietzky, H., Nagel, T., Düsterloh, U. & Zhao, J. (2023): Reanalysis of BRIUG THM Mock-up Test (ELF-China-Pilot). (Deutsch-Chinesische Entsorgungsforschung, Pilotprojekt).

Kinniburgh, D.G. & Cooper, D.M. (2011): PhreePlot. Creating graphical output with PHREEQC, available online at http://www.phreeplot.org/, status as of 28.3.23.

Kiviranta, L. & Kumpulainen, S. (2011): Quality control and characterization of bentonite materials. (POSIVA Report, Working Report 2011-84). Posiva OY, Finnland.

Klimchouk, A. (1996): The dissolution and conversion of gypsum and anhydrite. International Journal of Speleology 25/3/4, 21-36. DOI: 10.5038/1827-806X.25.3.2.

Koll, D., Busser, C., Faestermann, T., Gómez-Guzmán, J.M., Hain, K., Kinast, A., Korschinek, G., Krieg, D., Lebert, M., Ludwig, P. & Quinto, F. (2019): Recent developments for AMS at the Munich tandem accelerator. Nuclear Instruments and Methods in Physics Research Section B: Beam Interactions with Materials and Atoms 438, 180-183. DOI: 10.1016/j.nimb.2018.05.002.

Kumpulainen, S. & Kiviranta, L. (2011): Mineralogical Chemical and Physical Study of Potential Buffer and Backfill Materials from ABM Test Package 1. (Working Report 2011-41). Posiva OY.

Kunze, P., Seher, H., Hauser, W., Panak, P.J., Geckeis, H., Fanghänel, T. & Schäfer, T. (2008): The influence of colloid formation in a granite groundwater bentonite porewater mixing zone on radionuclide speciation. Journal of Contaminant Hydrology 102/3-4, 263-272. DOI: 10.1016/j.jconhyd.2008.09.020.

Kuusela-Lahtinen, A., Sinnathamby, G., Mendez, J., Sołowski, W.T., Gallipoli, D., Pintado, X. & Korkiala-Tanttu, L.K. (2016): Estimation of water retention behaviour of MX-80 bentonite partially saturated with saline solution. E3S Web of Conferences 9, 11006. DOI: 10.1051/e3sconf/20160911006.

Lanyon, B., Schneeberger, R. & Blechschmidt, I. (2018): In-rock Bentonite Erosion Test (I-BET): Site Selection and Bentonite Source. GTS Phase VI - CFM Phase III. Nagra Arbeitsbericht NAB 18-29.

Lebedev, A.L. (2015): Kinetics of gypsum dissolution in water. Geochemistry International 53/9, 811-824. DOI: 10.1134/S0016702915070058.

Lebedev, A.L. & Kosorukov, V.L. (2017): Gypsum solubility in water at 25°C. Geochem. Int. 55/2, 205-210. DOI: 10.1134/S0016702917010062.

Liu, J. & Neretnieks, I. (2006): Physical and chemical stability of the bentonite buffer. (SKB Rapport, R-06-103). Svensk Kärnbränslehantering AB SKB, available online at https://skb.se/upload/publications/pdf/R-06-103.pdf.

Liu, Y., Xu, G., Liu, S. & Chen, Z. (2004): Study on compatibility and swelling property of buffer/backfill material for HLW repository. (Management of Radioactive Waste, and non-Radioactive Waste from Nuclear Facilities, S12).

Liu, Y.M. & Wen, Z.J. (2003): An investigation of the physical properties of clayey materials used in nuclearwaste disposal at great depth. Mineral Rocks 23/4, 42-45.

Lloret, A., Romero, E. & Villar, M.V. (2004): FEBEX II Project. Final report on thermo-hydro-mechanical laboratory tests. (10/2004). ENRESA.

Mächtle, W. (2007): Centrifugation in Particle Size Analysis. *In:* Meyers, R.A. (ed.): Encyclopedia of Analytical Chemistry. Wiley.

Malvern Panalytical (2017): Basic Principles of Nanoparticle Tracking Analysis – Q&A. Malvern Panalytical, available online at https://www.materials-talks.com/basic-principles-of-nanoparticle-tracking-analysis-qa/, status as of September 13, 2022.

Mehrabi, K., Nowack, B., Arroyo Rojas Dasilva, Y. & Mitrano, D.M. (2017): Improvements in Nanoparticle Tracking Analysis To Measure Particle Aggregation and Mass Distribution: A Case Study on Engineered Nanomaterial Stability in Incineration Landfill Leachates. Environmental science & technology 51/10, 5611-5621. DOI: 10.1021/acs.est.7b00597.

Meier, L.P. & Kahr, G. (1999): Determination of the cation exchange capacity (CEC) of clay minerals using the complexes of copper(II) ion with triethyleneteramine and tetraethylenepentamine. Clay and Clay Minerals 47/3, 386-388.

Missana, T., Alonso, U., Albarran, N., García-Gutiérrez, M. & Cormenzana, J.-L. (2011): Analysis of colloids erosion from the bentonite barrier of a high level radioactive waste repository and implications in safety assessment. Physics and Chemistry of the Earth, Parts A/B/C 36/17-18, 1607-1615. DOI: 10.1016/j.pce.2011.07.088.

Missana, T., Alonso, U., Fernández, A.M. & García-Gutiérrez, M. (2018): Colloidal properties of different smectite clays: Significance for the bentonite barrier erosion and radionuclide transport in radioactive waste repositories. Applied Geochemistry 97, 157-166. DOI: 10.1016/j.apgeochem.2018.08.008.

Montoya, V., Noseck, U., Mattick, F., Britz, S., Blechschmidt, I. & Schäfer, T. (2022): Radionuclide geochemistry evolution in the Long-term In-situ Test (LIT) at Grimsel Test Site (Switzerland). Journal of hazardous materials 424/D, 127733. DOI: 10.1016/ j.jhazmat.2021.127733.

Moreno, L., Liu, L. & Neretnieks, I. (2011): Erosion of sodium bentonite by flow and colloid diffusion. Physics and Chemistry of the Earth, Parts A/B/C 36/17-18, 1600-1606. DOI: 10.1016/j.pce.2011.07.034.

Möri, A. & Blechschmidt, I. (2006): CFM Experiment. Structural geological model. Nagra Arbeitsbericht NAB 06-18.

Möri, A. (ed.) (2004): The CRR final project report series I. Description of the Field Phase - Methodologies and Raw Data Grimsel Test Site Investigation Phase V. Nagra Technical Report NTB 03-01.

Mrugalla, S., Frenzel, B., Krumbholz, M., Sönnke, J., Stark, L. & Weitkamp, A. (2020): CHRISTA-II. Beschreibung der generischen geologischen Modelle für die Endlagerkonzepte „multipler ewG“ und „mKBS-3“ Ergebnisbericht. Bundesanstalt für Geowissenschaften und Rohstoffe BGR. (B3.3/B50112-56/2021-0001/002), Hannover.

Müller-Vonmoos, M. & Kahr, G. (1983): Mineralogische Untersuchungen von Wyoming Bentonit MX-80 und Montigel. Nagra Technischer Bericht 83-12.

Neretnieks, I., Liu, L. & Moreno, L. (2009): Mechanisms and models for bentonite erosion. (Technical Report, TR-09-35). Svensk Kärnbränslehantering AB SKB, available online at https://www.skb.com/publication/1989990/TR-09-35.pdf.

Neretnieks, I., Moreno, L. & Liu, L. (2017): Clay erosion – impact of flocculation and gravitation. (Technical Report, TR-16-11). Svensk Kärnbränslehantering AB SKB, available online at https://skb.se/publikation/2487954/TR-16-11.pdf.

Norrfors, K.K., Bouby, M., Heck, S., Finck, N., Marsac, R., Schäfer, T., Geckeis, H. & Wold, S. (2015): Montmorillonite colloids: I. Characterization and stability of dispersions with different size fractions. Applied Clay Science 114, 179-189. DOI: 10.1016/ j.clay.2015.05.028.

Noseck, U., Flügge, J., Reimus, P., Cvetkovic, V., Lanyon, G.W., Schäfer, T. & Blechschmidt, I. (2016): Modelling of tracer, colloid and radionuclide/homologue transport for dipole CFM 06.002 – Pinkel surface packer. Colloid Formation and Migration Project Grimsel Test Site Investigation Phase VI. Nagra Technical Report NTB 16-06.

Noseck, U. & Schäfer, T. (eds.) (2020): Integrity of the bentonite barrier for the retention of radionuclides in crystalline host rocks -experiments and modeling. Project KOLLORADO-e2 Final Report. (KIT Scientific Working Papers, 140). Karlsruher Institut für Technologie KIT, Karlsruhe.

OECD-NEA (2013): The Nature and Purpose of the Post-Closure Safety Cases for Geological Repositories. (Radioactive Waste Management, NEA/RWM/R(2013)1). Organisation for Economic Co-Operation and Development - Nuclear Energie Agency OECD-NEA, available online at https://oecd-nea.org/jcms/pl_19258/the-nature-and-purpose-of-the-post-closure-safety-cases-for-geological-repositories.

Palandri, J.L. & Kharaka, Y.K. (2004): A compilation of rate parameters of water-mineral interaction kinetics for application to geochemical modeling. (Open file report 2004-1068). U.S. Geological Survey USGS, available online at https://apps.dtic.mil/sti/pdfs/ADA440035.pdf.

Parkhurst, D.L. & Appelo, C.A.J. (2013): Description of input and examples for PHREEQC version 3. A computer program for speciation, batch-reaction, one-dimensional transport, and inverse geochemical calculations. (U.S. Geological Survey Techniques and Methods 6-A43). U.S. Department of the Interior; U.S. Geological Survey (USGS), Denver.

Parkhurst, D.L., Kipp, K.L. & Charlton, S.R. (2010): PHAST version 2-A program for simulating groundwater flow, solute transport, and multicomponent geochemical reactions. (Techniques and Methods, 6-A35). U.S. Geological Survey USGS, available online at https://pubs.usgs.gov/tm/06A35/pdf/TM6-A35.pdf.

Posiva OY (2012): Safety case for the disposal of spent nuclear fuel at Olkiluoto. Synthesis 2012. (POSIVA Report, 2012-12). Posiva Oy, Eurajoki, Finland, available online at http://www.posiva.fi/files/2987/Posiva_2012-12web.pdf, status as of February 24, 2016.

Posiva OY & SKB (2017): KBS-3H System Design Phase 2011−2016: Final Report. (Posiva SKB Report 06). Posiva OY & Svensk Kärnbränslehantering AB SKB, available online at https://www.skb.com/publication/2489077/Posiva+SKB+Report+06.pdf.

Quinto, F., Blechschmidt, I., Faestermann, T., Hain, K., Korschinek, G., Kraft, S., Lanyon, B., Plaschke, M., Schäfer, T., Steier, P. & Geckeis, H. (in preperation): Retention and Ultra-Trace Near-Field Release of 99Tc, 233U, 237Np, 242Pu and 241Am from the Long-Term In-Situ Test at the Grimsel Test Site (Switzerland) investigated with AMS. Environmental science & technology.

Quinto, F., Blechschmidt, I., Garcia Perez, C., Geckeis, H., Geyer, F., Golser, R., Huber, F., Lagos, M., Lanyon, B., Plaschke, M., Steier, P. & Schäfer, T. (2017): Multiactinide Analysis with Accelerator Mass Spectrometry for Ultratrace Determination in Small Samples: Application to an in Situ Radionuclide Tracer Test within the Colloid Formation and Migration Experiment at the Grimsel Test Site (Switzerland). Analytical chemistry 89/13, 7182-7189. DOI: 10.1021/acs.analchem.7b01359.

Quinto, F., Busser, C., Faestermann, T., Hain, K., Koll, D., Korschinek, G., Kraft, S., Ludwig, P., Plaschke, M., Schäfer, T. & Geckeis, H. (2019): Ultratrace Determination of 99Tc in Small Natural Water Samples by Accelerator Mass Spectrometry with the Gas-Filled Analyzing Magnet System. Analytical chemistry 91/7, 4585-4591.
DOI: 10.1021/ acs.analchem.8b05765.

Quinto, F., Golser, R., Lagos, M., Plaschke, M., Schäfer, T., Steier, P. & Geckeis, H. (2015): Accelerator Mass Spectrometry of Actinides in Ground- and Seawater: An Innovative Method Allowing for the Simultaneous Analysis of U, Np, Pu, Am, and Cm Isotopes below ppq Levels. Analytical chemistry 87/11, 5766-5773. DOI: 10.1021/acs.analchem.5b00980.

Rahimi, M., Dehghani, F., Rezai, B. & Aslani, M.R. (2012): Influence of the roughness and shape of quartz particles on their flotation kinetics. International Journal of Minerals, Metallurgy, and Materials 19/4, 284-289. DOI: 10.1007/s12613-012-0552-z.

Reiche, T. (2016): RepoTREND. Das Programmpaket zur integrierten Langzeitsicherheitsanalyse von Endlagersystemen Version 4.5 (Stand März 2016). (GRS-Bericht, GRS-413). Gesellschaft für Anlagen- und Reaktorsicherheit (GRS) gGmbH, Braunschweig, available online at https://www.grs.de/sites/default/files/pdf/grs-413.pdf, status as of February 19, 2020.

Reiche, T., Noseck, U. & Schäfer, T. (2016): Migration of Contaminants in Fractured-Porous Media in the Presence of Colloids: Effects of Kinetic Interactions. Transport in Porous Media 111/1, 143-170. DOI: 10.1007/s11242-015-0585-7.

Reiche, T., Noseck, U. & Wolf, J.W. (2014): Modellierung des Schadstofftransports in geklüftet-porösen Medien unter Berücksichtigung von Kolloiden mit den Transportprogrammen FRAME und COFRAME. Gesellschaft für Anlagen- und Reaktorsicherheit (GRS) gGmbH. (GRS-333), Braunschweig, available online at http://www.grs.de/node/2487.

Rinderknecht, F.R. (2017): Bentonite erosion and colloid mediated transport of radionuclides in advection-controlled systems. Dissertation. Karlsruher Instituts für Technologie KIT, Karlsruhe. Fakultät für Chemie und Biowissenschaften.

Rolnick, L.S. (1950): The stability of gypsum and anhydrite in the geological environment. Massachusetts Institute of Technology (MIT).

Rösli, U. (2021): GTS iBET Experiment, Monitoring and maintenence Update, 01/01/21 - 04/10/21. (A 1588-86). Solexperts AG.

Rübel, A., Becker, D.-A. & Fein, E. (2007): Radionuclide transport modelling. Performance assessment of repositories in clays. (GRS-228). Gesellschaft für Anlagen- und Reaktorsicherheit (GRS) gGmbH, Braunschweig.

Saveyn, H., Baets, B. de, Thas, O., Hole, P., Smith, J. & van der Meeren, P. (2010): Accurate particle size distribution determination by nanoparticle tracking analysis based on 2-D Brownian dynamics simulation. Journal of colloid and interface science 352/2, 593-600. DOI: 10.1016/j.jcis.2010.09.006.

Schäfer, T., Geckeis, H., Bouby, M. & Fanghänel, T. (2004): U, Th, Eu and colloid mobility in a granite fracture under near-natural flow conditions. Radiochimica Acta 92/9-11, 731-737. DOI: 10.1524/ract.92.9.731.54975.

Schatz, R.E., Hansen, E.E., Hedström, M., Alonso, U., Fernández, A.M., Bouby, M., Heck, F., Geyer, F. & Schäfer, T. (2015): WP2 partners final report on bentonite erosion. BELBaR. European Commission EC.

Schatz, T., Kanerva, N., Martikainen, J., Sane, P., Olin, M., Seppälä, A. & Koskinen, K. (2013): Buffer Erosion in Dilute Groundwater. (POSIVA 2012-44). Posiva OY, available online at https://inis.iaea.org/collection/NCLCollectionStore/_Public/45/087/45087745.pdf?r=1.

Schlickenrieder, L., Lanyon, G.W., Kontar, K. & Blechschmidt, I. (2017): Colloid Formation and Migration Project: Site instrumentation and initiation of the long-term in-situ test. Grimsel Test Site Investigation Phase VI. Nagra Technical Report NTB 15-03.

Schneeberger, R., Berger, A., Herwegh, M., Eugster, A., Kober, F., Spillmann, T. & Blechschmidt, I. (2016): Geology and structure of the GTS and Grimsel region. GTS Phase VI - LASMO. Nagra Arbeitsbericht NAB 16-27.

Schneeberger, R., Blechschmidt, I., Kontar, K., Lanyon, B., Rösli, U. & Steiner, P. (2019a): As-built report for the In Situ Bentonite Erosion Test (i-BET). GTS Phase VI - CFM. Nagra Arbeitsbericht NAB 19-20.

Schneeberger, R., Kober, F., Lanyon, G.W., Mäder, U.K., Spillmann, T. & Blechschmidt, I. (2019b): Grimsel Test Site: Revisiting the site-specific geoscientific knowledge. Nagra Technical Report NTB 19-01.

Schneeberger, R., Kontar, K., Rösli, U., Blechschmidt, I. & Lanyon, B. (2018): I-BET – Hydraulic characterization of the I-BET site. GTS Phase VI – CFM Phase 3. Nagra Arbeitsbericht NAB 18-32.

Sebastian, U. (2018): Gesteinskunde. Springer Berlin Heidelberg, Berlin, Heidelberg.

Seher, H., Geckeis, H., Fanghänel, T. & Schäfer, T. (2020): Bentonite Nanoparticle Stability and the Effect of Fulvic Acids: Experiments and Modelling. Colloids and Interfaces 4/2, 16. DOI: 10.3390/colloids4020016.

SKB (2011): Long-term safety for the final repository for spent nuclear fuel at Forsmark. Main report of the SR-Site project. (SKB Technical Report, TR-11-01). Svensk Kärnbränslehantering AB SKB, Stockholm, Sweden.

Slaughter, M. & Earley, J.W. (1965): Mineralogy and Geological Significance of the Mowry Bentonites, Wyoming.

Smith, P., Schatz, T., Reijonen, H. & Hellä, P. (2017): Chemical Erosion and Mass Redistribution of Bentonite in a KBS-3H Repository. (Posiva 2016-12). Posiva OY.

Steier, P., Forstner, O., Golser, R., Kutschera, W., Martschini, M., Merchel, S., Orlowski, T., Priller, A., Vockenhuber, C. & Wallner, A. (2010): 36Cl exposure dating with a 3-MV tandem. Nuclear Instruments and Methods in Physics Research Section B: Beam Interactions with Materials and Atoms 268/7-8, 744-747. DOI: 10.1016/j.nimb.2009.10.020.

Steudel, A. (2009): Selection strategy and modification of layer silicates for technical applications. Universität Karlsruhe UKA. (Karlsruher Mineralogische und Geochemische Hefte - Schriftenreihe des Instituts für Mineralogie und Geochemie, 36).

Steudel, A. & Emmerich, K. (2013): Strategies for the successful preparation of homoionic smectites. Applied Clay Science 75-76, 13-21. DOI: 10.1016/j.clay.2013.03.002.

Stockmann, M., Schikora, J., Becker, D.-A., Flügge, J., Noseck, U. & Brendler, V. (2017): Smart Kd-values, their uncertainties and sensitivities. Applying a new approach for realistic distribution coefficients in geochemical modeling of complex systems. Chemosphere 187, 277-285. DOI: 10.1016/j.chemosphere.2017.08.115.

Stoll, M., Huber, F.M., Darbha, G.K., Schill, E. & Schäfer, T. (2016): Impact of gravity, collector surface roughness and fracture orientation on colloid retention kinetics in an artificial fracture. Journal of colloid and interface science 475, 171-183. DOI: 10.1016/ j.jcis.2016.04.045.

Sun, D., Zhang, J., Zhang, J. & Zhang, L. (2013): Swelling characteristics of GMZ bentonite and its mixtures with sand. Applied Clay Science 83-84, 224-230. DOI: 10.1016/ j.clay.2013.08.042.

Svensson, D., Dueck, A., Nilsson, U., Olsson, S., Sandén, T., Lydmark, S., Jägerwall, S., Pedersen, K. & Hansen, S. (2011): Alternative buffer material. Status of the ongoing laboratory investigation of reference materials and test package 1. (Technical Report, TR-11-06). Svensk Kärnbränslehantering AB SKB, available online at https://www.osti.gov/ etdeweb/servlets/purl/22059298.

Syvitski, J.P.M. (2007): Principles, Methods and Application of Particle Size Analysis. Cambridge University Press.

Thoenen, T., Hummel, W., Berner, U. & Curti, E. (2014): The PSI/Nagra Chemical Thermodynamic Database 12/07. (PSI-Bericht, 14-04). Edited by Paul Scherrer Institut (PSI), Villingen, Switzerland.

Tributh, H. & Lagaly, G.A. (1986): Aufbereitung und Identifizierung von Boden- und Lagerstättentonen; 2. Korngrößenanalyse und Gewinnung von Tonsubfraktionen. GIT Labor Fachzeitschrift, 771-776.

van der Lee, J. & De Windt, L. (2002): CHESS Tutorial and cookbook.

van Loon, L.R. (2014): Effective Diffusion Coefficients and Porosity Values for Argillaceous Rocks and Bentonite: Measured and Estimated Values for the Provisional Safety Analyses for SGT-E2. Nagra Technical Report 12-03.

Winkler, S.R., Steier, P., Buchriegler, J., Lachner, J., Pitters, J., Priller, A. & Golser, R. (2015): He stripping for AMS of 236U and other actinides using a 3 MV tandem accelerator. Nuclear Instruments and Methods in Physics Research Section B: Beam Interactions with Materials and Atoms 361, 458-464. DOI: 10.1016/j.nimb.2015.04.029.

Wolf, J., Becker, D.-A., Flügge, J., Frank, T. & Johnen, M. (2021): Bewertung des sicheren Einschlusses von Radionukliden in Endlagersystemen im Kristallingestein. Ergebnisse aus dem Vorhaben CHRISTA-II. Gesellschaft für Anlagen- und Reaktorsicherheit (GRS) gGmbH. (GRS-685), available online at https://www.grs.de/sites/default/files/2022-09/GRS-658.pdf.

Xie, M., Miehe, R., Kasbohm, J., Herber, H.-J., Meyer, L. & Ziesche, U. (2012): Bentonite Barriers – New Experiments and State of the Art. Bentonite as Barrier Material for the Sealing of Underground Disposal Sites Final Report. Gesellschaft für Anlagen- und Reaktorsicherheit (GRS) gGmbH. (GRS-300), available online at https://www.grs.de/sites/default/files/publications/GRS-300.pdf.

Ye, W.-M., Chen, Y.-G., Chen, B., Wang, Q. & Wang, J. (2010): Advances on the knowledge of the buffer/backfill properties of heavily-compacted GMZ bentonite. Engineering Geology 116/1-2, 12-20. DOI: 10.1016/j.enggeo.2010.06.002.

Ye, W.M., Cui, Y.J., Qian, L.X. & Chen, B. (2009): An experimental study of the water transfer through confined compacted GMZ bentonite. Engineering Geology 108/3-4, 169-176. DOI: 10.1016/j.enggeo.2009.08.003.

Ye, W.M., He, Y., Chen, Y.G., Chen, B. & Cui, Y.J. (2016): Thermochemical effects on the smectite alteration of GMZ bentonite for deep geological repository. Environmental Earth Sciences 75/10. DOI: 10.1007/s12665-016-5716-0.

Ye, W.M., Wan, M., Chen, B., Chen, Y.G., Cui, Y.J. & Wang, J. (2013): Temperature effects on the swelling pressure and saturated hydraulic conductivity of the compacted GMZ01 bentonite. Environmental Earth Sciences 68/1, 281-288. DOI: 10.1007/s12665-012-1738-4.

Yoshida, H., Takeuchi, M. & Metcalfe, R. (2005): Long-term stability of flow-path structure in crystalline rocks distributed in an orogenic belt, Japan. Engineering Geology 78/3-4, 275-284. DOI: 10.1016/j.enggeo.2005.01.002.

Zaier, I., Billiotte, J., Charmoille, A. & Laouafa, F. (2021): The dissolution kinetics of natural gypsum: a case study of Eocene facies in the north-eastern suburbs of Paris. Environmental Earth Sciences 80/1. DOI: 10.1007/s12665-020-09275-x.

Zhang, C.-L. (2020): ELF-China Project. Definition of Reference Materials for THM Experiments. Gesellschaft für Anlagen- und Reaktorsicherheit (GRS) gGmbH.

Zhang, C.-L., Rogalski, A., Zehle, B. & Hertes, U. (2023): Investigation of Claystone / Bentonite Mixtures as Barrier Material for Geological Disposal of Radioactive Waste. Gesellschaft für Anlagen- und Reaktorsicherheit (GRS) gGmbH. (GRS-703).

App. A Laboratory-scale erosion experiments

A.1 Colloid release

Colloid release is recalculated with the input parameters of Huber et al. (2016) and the assumptions of a fracture width of 5 m, a fracture aperture of $1.47 \cdot 10^{-3}$ m, a flow rate of 23 $m \cdot a^{-1}$, and a constant release rate of 0.0395 $kg \cdot a^{-1}$:

Flow-through area: $A = 5m \cdot 1.47 \cdot 10^{-3}m = 7.35 \cdot 10^{-3}m^2$

Flow-through rate $Q = A \cdot v = 7.35 \cdot 10^{-3}m^2 \cdot 23\frac{m}{a} = 1.6905 \cdot 10^{-1}\frac{m^3}{a}$

Colloid concentration in release solution $c = \frac{r}{Q} = \frac{3.95 \cdot 10^{-2}\frac{kg}{a}}{1.6905 \cdot 10^{-1}\frac{m^3}{a}} = 2.3366 \cdot 10^{-1}\frac{kg}{m^3}$

The model calculations in this report are made with the assumptions of a fracture width of 1 m, a fracture aperture of $5 \cdot 10^{-4}$ m, and a flow rate of 1 $m \cdot a^{-1}$. Applying the above colloid concentration, we can recalculate to:

Flow-through area: $A = 1m \cdot 5 \cdot 10^{-4}m = 5 \cdot 10^{-4}m^2$

Flow-through rate $Q = A \cdot v = 5 \cdot 10^{-4}m^2 \cdot 1\frac{m}{a} = 5 \cdot 10^{-4}\frac{m^3}{a}$

Rate of colloid release $r = Q \cdot c = 5 \cdot 10^{-4}\frac{m^3}{a} \cdot 2.3366 \cdot 10^{-1}\frac{kg}{m^3} = 1.1683 \cdot 10^{-4}\ \frac{kg}{a}$

Since Huber et al. (2016) used a release rate for glacial cycles that was higher by a factor of ten, the colloid release rate in that case is set to $1.1683 \cdot 10^{-3}$ $kg \cdot a^{-1}$.

A.2 C0 values of the erosion experiments

Raw bentonite

MX-80 – BOUS regular GGW

Na	8.4	±	0.05
Ca	8.09	±	0.04
K	0.021	±	0.005
Mg	0.0248	±	0.0002
Cl	0.59	±	0.01
SO4	6.43	±	0.05

MX-80 – BOUS 2 mmol/L Ca

Na	8.442	±	0.03
Ca	84.5	±	0.4
K	0.21	±	0.002
Mg	0.02442	±	0.00011
Cl	135.4	±	0.4
SO4	6.35	±	0.04

GMZ-001 & GMZ-24-200 – Pinkel GGW

Na	17.9	±	0.02
Ca	5.86	±	0.02
K	0.141	±	0.002
Mg	0.014	±	0.00003
Cl	7.5	±	0.03
SO4	6.47	±	0.03

100% MX-80 Na-mnt – C0 concentrations

100% MX-80 Na-mnt – BOUS regular

Fig. 3-14	Na	8.4	±	0.05
	Ca	8.09	±	0.04
	K	0.021	±	0.005
	Mg	0.0248	±	0.0002
Fig. 3-15	Cl	0.59	±	0.01
	SO4	6.43	±	0.05

100% MX-80 Na-mnt – BOUS 2 mmol/L Ca

Fig. 3-14	Na	8.442	±	0.03
	Ca	84.5	±	0.4
	K	0.21	±	0.002
	Mg	0.02442	±	0.00011
Fig. 3-15	Cl	135.4	±	0.4
	SO4	6.35	±	0.04

Case 3: Na-mnt + SiO2 – C0 concentrations

MX-80 80/90 Na-mnt + SiO2 – BOUS regular

Fig. 3-27	Na	8.4	±	0.05
Fig. 3-28	Ca	8.09	±	0.04
Fig. 3-29	K	0.021	±	0.005
Fig. 3-30	Mg	0.0248	±	0.0002
Fig. 3-31	Al	0.015	±	0.001
	Si	4.38	±	0.03
Fig. 3-32	Cl	0.59	±	0.01
	SO4	6.43	±	0.05

MX-80 80/90 Na-mnt + SiO2 – BOUS 2 mmol/l Ca

Fig. 3-27	Na	8.442	±	0.03
Fig. 3-28	Ca	84.5	±	0.4
Fig. 3-29	K	0.21	±	0.002
Fig. 3-30	Mg	0.02442	±	0.00011
Fig. 3-31	Al	0.026	±	0.004
	Si	4.37	±	0.01
Fig. 3-32	Cl	135.4	±	0.4
Fig. 3-27	SO4	6.35	±	0.04

GMZ-001 90 Na-mnt + SiO2 – Pinkel

Fig. 3-27	Na	17.9	±	0.02
Fig. 3-28	Ca	5.86	±	0.02
Fig. 3-29	K	0.141	±	0.002
Fig. 3-30	Mg	0.014	±	0.00003
Fig. 3-31	Al	0.02	±	0.001
	Si	5.8	±	0.042
Fig. 3-32	Cl	7.5	±	0.03
Fig. 3-27	SO4	6.47	±	0.03

Na-mnt + SiO2 + Cacarrier – C0 concentrations

MX-80 Na-mnt + SiO2 + Cacarrier – Pinkel GGW 1

Fig. 3-47	Na	17.9	±	0.03
Fig. 3-48	Ca	5.86	±	0.02
Fig. 3-49	K	0.141	±	0.002
Fig. 3-50	Mg	0.014	±	0.00003
Fig. 3-51	Al	0.01875	±	0.00002
	Si	5.91	±	0.015
Fig. 3-52	Cl	6.85	±	0.03
Fig. 3-53	SO4	4.88	±	0.025

GMZ-001 Na-mnt + SiO2 + Cacarrier – Pinkel GGW 2

Fig. 3-47	Na	17.65	±	0.071
Fig. 3-48	Ca	5.735	±	0.035
Fig. 3-49	K	0.135	±	0.001
Fig. 3-50	Mg	0.02155	±	0.003
Fig. 3-51	Al	0.019855	±	0.001
	Si	5.8	±	0.042
Fig. 3-52	Cl	6.28	±	0.028
Fig. 3-53	SO4	5.965	±	0.078